Semiconductors, Vol. 37, No. 5, 2003, pp. 493–518. Translated from Fizika i Tekhnika Poluprovodnikov, Vol. 37, No. 5, 2003, pp. 513–538.

REVIEW

Artificial GeSi Substrates for Heteroepitaxy: Achievements and Problems

Yu. B. Bolkhovityanov*, O. P. Pchelyakov, L. V. Sokolov, and S. I. Chikichev

Institute of Semiconductor Physics, Siberian Division, Russian Academy of Sciences, ul. Akademika Lavrent'eva 13, Novosibirsk, 630090 Russia

**e-mail: bolkhov@isp.nsc.ru*

Submitted October 22, 2002; accepted for publication November 30, 2002

Abstract—It is desirable to have a set of substrates which are based on Si and ensure growth of heterostructures with various lattice parameters in order to develop electronic devices composed of semiconductor materials whose epitaxial growth is reasonably well developed. Such substrates are typically referred to as artificial. In this paper, a comparative analysis of various methods for the fabrication of artificial substrates (heterostructures), in which the relaxation of stresses is based on the introduction of misfit dislocations, is performed. Based on published and new experimental data, the mechanisms for attaining a low density of threading dislocations in plastically relaxed films represented by heterostructures composed of GeSi and an Si buffer layer grown at low temperatures are analyzed. The problems and results of another group of methods for obtaining artificial substrates which gained favor recently and become known as "compliant" or "soft" substrates are discussed. The most important electrical parameters of Si and GeSi films grown on artificial substrates are considered. © *2003 MAIK "Nauka/Interperiodica".*

1. INTRODUCTION

The term "artificial substrate" is used to denote a heterostructure that is grown epitaxially on an Si (or GaAs) substrate and has new valuable characteristics: a perfect crystal structure and surface smoothness which differ only slightly from those of the initial substrate; however, an artificial substrate differs radically from an initial substrate in its lattice parameter. Perfect heterostructures based on GeSi/Si make it possible to significantly improve the characteristics of devices produced conventionally on Si substrates (for details, see the reviews [1–3]). Another special feature of these heterostructures consists in the fact that they can be used as artificial substrates for the growth of GaAs, which could result in compatibility of the devices based on silicon technology with optoelectronic devices based mainly on GaAs. The most important components for ensuring this compatibility are Ge_xSi_{1-x} buffer layers, which make it possible to form completely relaxed, perfect layers of Ge–Si solid solution with x as large as unity; as a result, the formation of epitaxial Ge/Si structures with a low defect concentration becomes possible.

The physical mechanism which underlies the epitaxial transition of one material to another with differing lattice constants and is used in conventional methods consists in the relaxation of elastic strains in a thin layer of new material by introducing misfit dislocations (MDs). However, the introduction of MDs gives rise to so-called threading dislocations, which are dislocation-loop segments that emerge at the surface of an epitaxial layer. In order to reduce the density of threading dislocations, one conventionally uses either buffer layers with the lattice varying across the layers or so-called dislocation filters composed of stressed superlattices.

The main requirements imposed on the above substrates are (i) small thickness of the film in which plastic relaxation occurs; (ii) a perfect crystal structure, which is mainly assessed from the threading-dislocation density; and (iii) low roughness of the heterostructure surface.

Recently, a number of methods for the production of new artificial substrates referred to as "compliant" and "soft" ones have been suggested. When these substrates are used, it is assumed that a completely different physical mechanism is in effect: redistribution of stresses between the pseudomorphic layer and thin (compliant) substrate–membrane; as a result, the pseudomorphic layer relaxes elastically without the formation of MDs and, correspondingly, without generation of threading dislocations.

2. PLASTIC RELAXATION OF HETEROSTRUCTURES AS A CLASSICAL METHOD FOR THE FORMATION OF ARTIFICIAL SUBSTRATES

2.1. Basic Points of the Plastic-Relaxation Theory for Artificial Substrates

It is well known that plastic relaxation of mismatch stresses in GeSi/Si films is mainly attained by the introduction of 60° dislocations over the inclined {111} glide planes (see, for example, [3]). The initial stage of plastic relaxation of a pseudomorphic film is shown schematically in Fig. 1. The relaxation sets in with the

1063-7826/03/3705-0493$24.00 © 2003 MAIK "Nauka/Interperiodica"

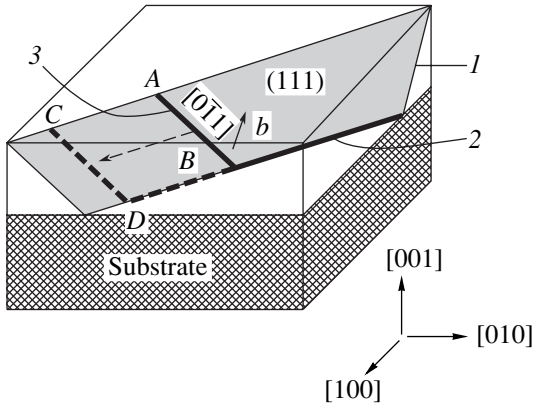

Fig. 1. Schematic representation of plastic relaxation in a (*1*) stressed film via formation of (*2*) misfit dislocations and (*3*) threading dislocations related to them.

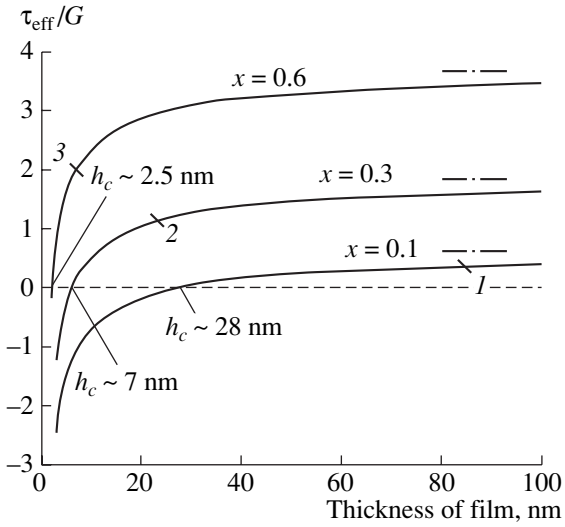

Fig. 2. Calculated normalized effective shear stress as a function of the Ge_xSi_{1-x}/Si(001) film thickness for $x = 0.1$, 0.3, and 0.6. The dash-and-dot lines correspond to the largest values of τ_{eff}/G for $h \longrightarrow \infty$.

formation of a 60° dislocation that can glide in the (111) plane, which is inclined to the interface. The dislocation consists of a segment lying in the interface (the misfit dislocation) and a segment *AB* that emerges at the film surface (the threading dislocation). Plastic relaxation of the film occurs owing to an increase in the length of this MD (segment *BD*) via the motion of a threading segment *CD* in the glide plane. The passage of the dislocation loop through a part of the film reduces plastic strains in this part. Correspondingly, the problem of obtaining perfect and completely relaxed GeSi/Si films can be separated into two subproblems: (I) the attainment of an acceptable rate of film relaxation (reduction of residual elastic strains as the film thickness increases) by introducing MDs and (II) the minimization of the number of threading dislocations. To a certain extent, these two subproblems are contradictory since introduction of MDs occurs via the passage of threading dislocations through the film volume and an increase in the rate of plastic relaxation by increasing the MD density brings about an increase in the density of threading dislocations.

The concept of an effective (excess) shear stress τ_{eff} is used in the studies concerned with the introduction of threading dislocations and their propagation in stressed films (see, for example, [4]); this shear stress governs the processes of MD generation and threading-dislocation propagation in stressed films and is defined by the following expression for a film with thickness *h*:

$$\tau_{eff} = S\left[\frac{2G(1+\nu)}{(1-\nu)}\right]\varepsilon - \frac{Gb(1-\nu\cos^2\alpha)\cos\phi}{4\pi h(1-\nu)}\left(\ln\frac{\beta h}{b}+1\right). \quad (1)$$

The first term on the right-hand side in formula (1), $[2G(1 + \nu)/(1 - \nu)]\varepsilon$, represents the driving force of plastic relaxation and is equal to the biaxial stress in the film. Here, *G* and ν are the shear modulus and the Poisson ratio, respectively; and ε is the elastic strain. The quantity $S = \cos\lambda\cos\phi$ is introduced in order to account for the effect of the stress component along the threading-dislocation motion and is referred to as the Schmidt factor. Here, ϕ is the angle between the glide plane and the normal to the interface; and λ is the angle between the Burgers vector *b* of dislocation and the perpendicular to the line of intersection of the dislocation's glide plane with the interface (this perpendicular lies in the interface plane). The second term on the right-hand side of formula (1) represents the shear-stress component that impedes the propagation of threading dislocations [5]. This component is calculated from the work required to form a unit length of a new MD. In this term, α is an angle between the Burgers vector and the dislocation line. The quantity β is referred to as the dislocation-core parameter and is set (according to recent data) equal to 0.76 for 60° dislocations in a GeSi system [6]. The critical thickness h_c is determined from the equality of τ_{eff} to zero at the initial stage of plastic relaxation, in which case $\varepsilon = f$ (*f* is the lattice-parameter mismatch); thus, we have

$$h_c = \frac{b(1-\nu\cos^2\alpha)}{8\pi f(1+\nu)\cos\lambda}\left(\ln\frac{\beta h_c}{b}+1\right). \quad (2)$$

This expression was first derived by Matthews and Blakeslee in 1974 [7] on the basis of the balance of forces acting on a threading dislocation. The model [7] referred to as the force balance model is very popular among researchers, and the publication [7] has been cited about 2000 times in scientific literature.

When the film thickness exceeds h_c, the value of τ_{eff} becomes positive; as a result, MDs can now originate and propagate. In Fig. 2, we show the dependences of

dimensionless effective shear stress τ_{eff}/G on the Ge_xSi_{1-x} film thickness for $x = 0.1$, 0.3, and 0.6. As the film thickness increases, the dependences tend to the value of $[2(1 + \nu)/(1 - \nu)]\varepsilon$, which is proportional to x. It is well known that, in almost all situations, films grow to thicknesses which greatly exceed the critical thickness corresponding to the origination of the first MDs [3, 8]. For illustration, the points that are marked by numbers and correspond to the film thicknesses equal to $3h_c$ are indicated for each curve in Fig. 2. It can be seen that the effective shear stress increases appreciably as the fraction of Ge in the pseudomorphic film increases, which is bound to affect the rates of MD generation and the propagation of corresponding threading segments.

Houghton [4] suggested the following semiempirical expression for the MD generation rate:

$$\frac{dN(t)}{dt} = N_0\tau_{eff}^n \exp\left(-\frac{W_n}{kT}\right). \quad (3)$$

Here, N_0 is an adjustable parameter, which [4] characterizes the initial density of the sites for the most probable generation of MDs (this density differs for dissimilar Si substrates); and W_n is the activation energy for MD generation and is equal [4] to about 2.5 eV. On the basis of experimental data [4], the exponent n is equal to 2.5. Thus, comparing the Ge_xSi_{1-x} films with $x = 0.1$ and 0.3, taking into account Fig.2, and using expression (3), we may state that the generation rate of MDs in the films with $x = 0.3$ should be at least an order of magnitude higher than that in the films $x = 0.1$. Correspondingly, the density of threading-dislocation pairs should also be higher.

The final threading-dislocation density depends both on the density of generated MDs and on the velocity of propagation of corresponding threading segments. According to the widely accepted concepts [9] adapted to the threading-dislocation glide in a stressed film [4], the velocity of dislocation motion can be represented as

$$V_d = V_0(\tau_{eff})^m \exp(-E_\nu/kT), \quad (4)$$

where V_0 is a constant, E_ν is the activation energy for the motion of dislocations by gliding, and the value of m seems to range from unity to two (see, for example, [10]). Consequently, as τ_{eff} increases, the velocity of motion of the MDs' threading branches increases as well. Expression (4) is valid for the initial stage of relaxation. The emerging MD network retards the threading-dislocation motion [6] owing to interaction between local stress fields of dislocations [11].

Under equilibrium conditions and in the absence of barriers, MDs are introduced as long as the thickness of pseudomorphic films exceeds h_c. Stresses in the film are reduced, the critical thickness increases, and MDs are no longer introduced. The film thickness should be increased again in order to introduce a new portion of MDs. Thus, in an ideal situation, the film should plastically relax gradually as its thickness increases. Residual elastic strains can be expressed as

$$\varepsilon(t) = f - b_{eff}\rho(t), \quad (5)$$

where b_{eff} is the component of the Burgers vector along the normal which lies in the interface plane and is perpendicular to the line of intersection of the glide plane with the interface plane, $\rho(t)$ is the linear density of dislocations, and, according to Hu [12],

$$\varepsilon(t) = f\frac{h_c}{h(t)} \quad \text{for} \quad h \geq h_c. \quad (6)$$

In Fig. 3, this dependence of residual elastic strains on the film thickness is shown by the solid line. This equilibrium theoretical dependence corresponds to the largest possible decrease in residual elastic strains as the thickness of GeSi heterostructures increases (based on the highest relaxation rate). As has been mentioned in many publications (see, for example, [3, 4, 8]), the experimentally determined critical thickness exceeds, in the majority of cases, the calculated one (Fig. 3). We may introduce two critical thicknesses: theoretical or equilibrium critical thickness h_c and experimental critical thickness h_c(exptl). A persistent difference between these two critical thicknesses which has been observed

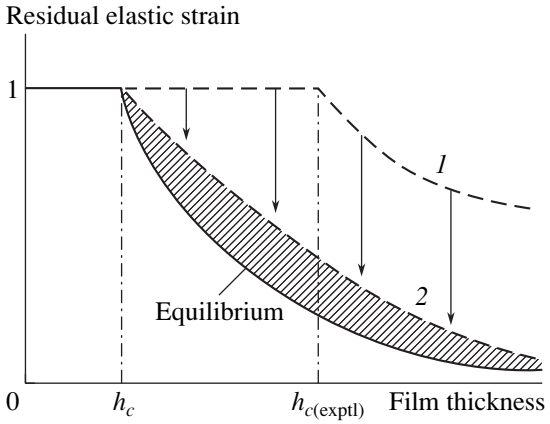

Fig. 3. Schematic illustration of mechanisms governing a decrease in residual elastic strains due to plastic relaxation of the film with an increase in the film thickness. The solid line represents thermodynamic equilibrium in the absence of barriers to the introduction of misfit dislocations; dashed line *1* corresponds to kinetic hindrance to misfit-dislocation generation and to threading-dislocation glide (low growth temperatures), and dashed line *2* represents an experimental quasi-equilibrium dependence (after the prolonged annealing of the heterostructure). Vertical arrows indicate the behavior of relaxation in the course of annealing (the transition from dependence *1* to dependence *2*). Critical thicknesses are also indicated: h_c stands for the thickness calculated according to the Matthews–Blakeslee model [7], and h_c(exptl) denotes the experimental thickness (h_c(exptl) far exceeds h_c if the films are grown at comparatively low temperatures). The hatched lines illustrate the persistent difference between experimental data and the curve calculated for barrierless conditions of introducing misfit dislocations.

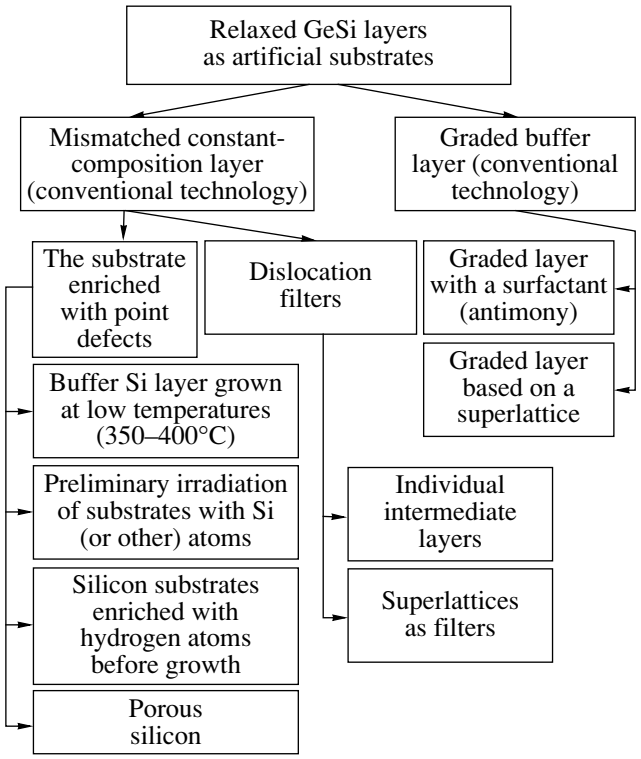

Fig. 4. Classification of the methods for growing plastically relaxed GeSi films, which are conducive to a decrease in the density of threading dislocations in the heterostructure.

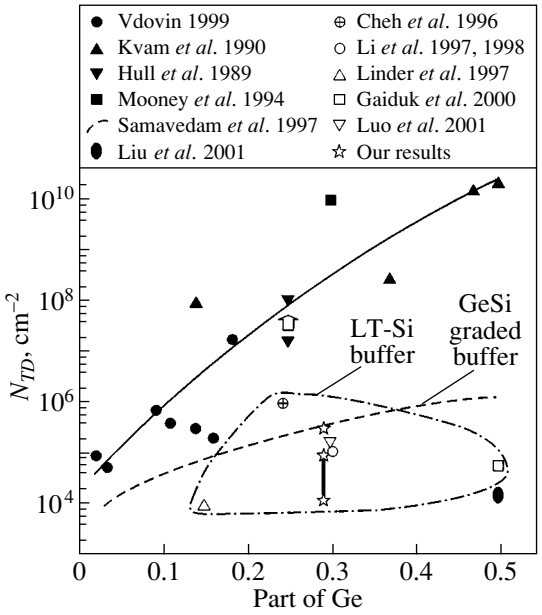

Fig. 5. The density of threading dislocations in Ge_xSi_{1-x}/Si(001) films according to various sources. The solid line approximates the data on the growth of layers with a steplike composition in accordance with conventional technology [16–19] (see text). The dashed line represents the density of threading dislocations in layers using a graded buffer layer [31]. The dash-and-dot line encircles the data on the growth of GeSi layers on an LT-Si buffer [20–22, 24–27, 44]. The filled oval corresponds to a graded Si buffer layer with a surfactant (Sb) [62].

experimentally indicates that various potential barriers play an important role in retarding MD introduction during the growth of semiconductor films. Elevated growth temperatures and postgrowth heat treatments of heterostructures make it possible to approach the equilibrium conditions of MD generation. For example, special studies performed by Houghton *et al.* [13] for Ge_xSi_{1-x} solid solutions with x = 0.01–0.15% showed excellent agreement between experimental data and the results of calculations reported by Matthews and Blakeslee [7, 14].

Expression (2) derived for equilibrium conditions defines a certain basic parameter h_c which depends only on the mechanical properties of the specific pair of materials forming the heterostructure, on the degree of mismatch, and on the crystallographic orientation of the interface plane. This parameter is used by researchers as a certain borderline in thicknesses. If the film thickness is smaller than h_c, the pseudomorphic film is thermodynamically stable and MDs are not introduced into it; otherwise, the film is in a metastable state. The onset and rate of plastic relaxation of pseudomorphic films with thicknesses in this range depend on new parameters: on the temperature and duration of the heat treatment of the heterostructure (Fig. 3, dependence *1*) and on characteristics of the films' growth (growth rate, two-dimensional mechanism of growth, role of impurities, and so on). Correspondingly, h_c(exptl) for a specific heterostructure is a drifting quantity which depends on these new parameters. In order to remove (if possible) the restrictions imposed on plastic relaxation of pseudomorphic films, one either has to grow the films at a high temperature [15] or subject the films to postgrowth annealing at elevated temperatures. Nevertheless, as numerous published data indicate (they will be cited in Subsection 2.3), the experimental dependence of the degree of plastic relaxation of a heterostructure on the thickness deviates appreciably from the theoretical (equilibrium) dependence; the former runs systematically above the latter when the aforementioned methods of heterostructure formation are used.

2.2. Comparative Analysis of Various Methods for the Fabrication of Artificial GeSi Substrates

Figure 4 illustrates a classification of the methods for growing GeSi films on Si substrates; these methods are classified according to technical procedures that make it possible to form heterostructures with acceptable structural characteristics. The method involving the growth of films with constant composition is simplest and will be considered first.

The dislocation structure of relaxed films of Ge_xSi_{1-x} solid solutions on Si(001) substrates has been studied in detail for the last 15 years. A typical threading-dislocation density in constant-composition films and its dependence on the Ge fraction x are shown in Fig. 5 based on published data [16–27]. This density is unacceptably high (10^8–10^9 cm^{-2}) for applications in

$Ge_{0.3}Si_{0.7}$ layers. The most widely used temperature for growing such heterostructures is 550°C. We will refer to this variant of growth as the standard. A high density of threading dislocations in these heterostructures is caused by a high density of MDs, each of which is connected to the surface by a pair of "arms" (threading dislocations). According to Hull *et al*. [16], the density of threading dislocations in such a sample is on the order of 10^7 cm^{-2} (correspondingly, the density of generated MDs is on the same level) even at the earliest stages of plastic relaxation, where the degree of this relaxation does not exceed 1%. At the end of the relaxation process, the density of threading dislocations increases to 10^8 cm^{-2} (see the lower and upper inverted filled triangles connected by arrow in Fig. 5).

In order to decrease the threading-dislocation density in a heterostructure, one has to use buffer layers with a varying lattice constant with either a steplike or linear increase in the content of the new component of the solid solution. For more than 30 years, this method was found to be the most appropriate one for growing heterostructures to be used as artificial substrates. Thus, this method is used, for example, to commercially fabricate arrays of light-emitting diodes based on GaAsP/GaAs heterostructures. The basic results of studying these heterostructures were published as far back as the late 1960s [28, 29]. The successful growth of GeSi/Si heterostructures with a gradual variation in the composition of the buffer layer was initiated by Fitzgerald *et al*. [30]. Data on the threading-dislocation density in a graded Ge_xSi_{1-x} buffer layer [31] are shown in Fig. 5. The method for growing relaxed heterostructures with a graded buffer layer yields satisfactory results, since a small composition gradient is chosen (~0.1 Ge fraction per μm); there is only a small elastic strain in the buffer layer at each instant of time. If the parameters of composition variation in the graded buffer layer are chosen properly, the most favorable conditions will be ensured for the generation and propagation of MDs [8, 32, 33]: (i) relatively low stresses in the graded layer (these stresses depend on the gradient steepness) lead to about a low generation rate of MDs; (ii) the MDs are distributed over the entire thickness of the layer with varying composition, which appreciably reduces the effect of blocking a moving threading dislocation by an orthogonally positioned MD; and (iii) a stressed surface region in the growing graded layer gives rise to and continuously supports the driving force for the threading-dislocation glide. In addition to these special features, Shiryaev *et al*. [34] introduce the concept of self-organization for an MD network in a buffer layer with varying composition. It is assumed [34] that it is this factor that is responsible for a low density of threading dislocations at the heterostructure surface, since the ordering of the dislocation network increases the probability of annihilation for threading dislocations.

Unfortunately, the advantages of transition layers with a varying lattice constant gradually become drawbacks as present-day requirements imposed on heterostructures become more and more stringent. Since a small composition gradient is chosen (equal to about 0.1 Ge fraction per μm), then (I) the buffer layers will be thick (1–10 μm), which increases both the growth duration and the consumption of expendable materials (when analyzing the prognosis for the wide use of heterostructures, König [35] noted that a buffer layer with a thickness of about 100 nm would have been ideal from an economical standpoint); (II) the surface roughness, which increases with increasing thickness and can amount to no less than 30–40 nm [36], represents a serious problem in using the layers in modern technology; and (III) the dislocation density of 10^6–10^7 cm^{-2} observed in Ge_xSi_{1-x} solid solutions on Si with $x > 0.5$ is still too high.

2.2.1. Methods based on the modification of the structural properties of Si substrate

Recently, several new methods for forming artificial substrates have been developed; these methods make it possible to significantly improve the results obtained using the standard variant based on fabrication of the buffer layers which have a steplike distribution of composition. First of all, we should mention the use of an Si layer preliminarily grown at low temperatures (LT-Si), which yields good results even if the GeSi films with constant composition are grown on Si substrates [20–24]. At present, this method is best developed among the group of methods (Fig. 4) for which saturation of the substrate with point defects in order to use them as sources of MDs is common. The main methods of this group are represented in the left-hand column in Fig. 4. These methods include preliminary irradiation of the substrate with Si and other ions [37], saturation of the substrate with hydrogen atoms before film growth [38], and use of porous silicon as the substrate material [39]. This group of methods is represented in more detail in Fig. 6 in combination with the characterization of artificial substrates with respect to three main parameters characterizing the structure quality: the relaxation rate, the final degree of smoothness of the heterostructure surface, and the crystal-structure quality. A comparative assessment according to the rate of plastic relaxation is given on the basis of the data reported in cited publications. These data were compared with the results obtained for similar layers grown by the standard steplike method.

Preliminary bombardment of Si substrates with Si ions (method *b* [37] in Fig. 6) is conducive to an increase in the rate of plastic relaxation in GeSi layers; however, this method offers no advantages for the structural quality of corresponding heterostructures over standard steplike growth. Method *c* (see Fig. 6) suggested by Holländer [40, 41] is inconvenient in that hydrogen is implanted into silicon substrate after the growth of the GeSi layer, which should remain pseudomorphic. This layer relaxes plastically only after

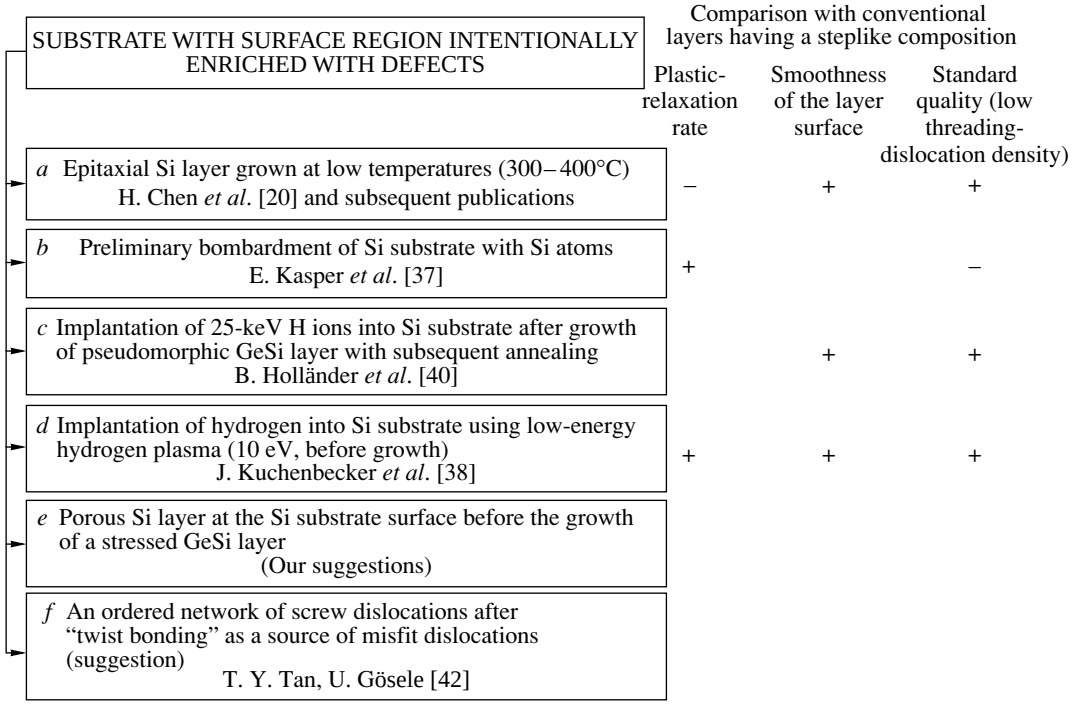

Fig. 6. A group of methods based on the preliminary formation of point defects at the substrate boundary and their comparison with conventional methods using three parameters: the rate of plastic relaxation, density of threading dislocations, and surface smoothness.

annealing of the heterostructure. Such a sequence of operations significantly restricts the potential of this method with respect to both layer thickness and composition. Methods *e* and *f* (Fig. 6) rely on the use of substrate composed of either an artificially formed layer of porous silicon or a spacer involving screw dislocations introduced by the method of bonding with misorientation (so-called twist bonding) [42] (this technology will be considered in more detail in Subsection 3.2). However, these methods have not been tested yet.

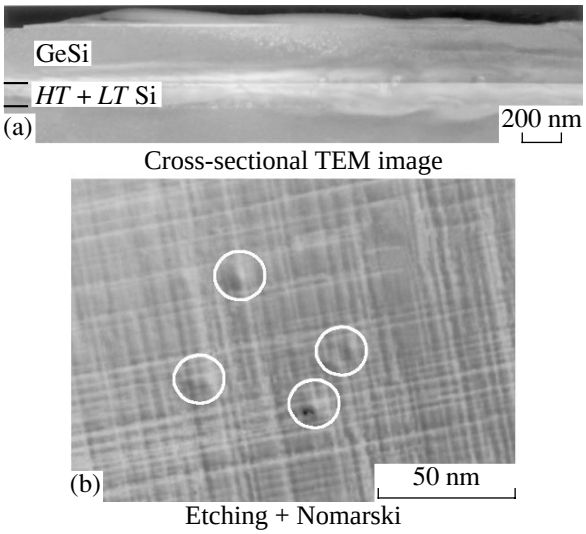

Fig. 7. Electron-microscope image of (a) a cross section of a 300-nm-thick $Ge_{0.29}Si_{0.71}$/Si(001) sample with a 50-nm-thick low-temperature silicon (LT Si) underlayer and (b) the sample surface after treatment in the Schimmel etchant. The circles outline the dislocation pits. The cross-sectional TEM image was obtained by A.K. Gutakovskiĭ.

Judging from the characteristics of the comparison given in Fig. 6, methods *a* and *d* involving the use of a buffer layer grown at low temperatures and saturation of the substrate with hydrogen are most promising. However, the latter method has been reported in only a single publication [38] and its further validation and development are required.

The method of growth of a GeSi layer on a preliminarily formed LT-Si buffer layer was reported in [20–24]; in particular, it was shown that completely plastically relaxed 0.5-μm-thick $Ge_{0.3}Si_{0.7}$ films on Si(001) substrates can be obtained with a threading-dislocation density no higher than 10^5 cm^{-2}. Data on the threading-dislocation density in structures with LT-Si underlayers were reported in [20–27] and are outlined in Fig. 5. An appreciable decrease in the threading-dislocation density (even compared with heterostructures based on graded buffer layers) is observed in GeSi/Si structures with an LT-Si underlayer. In addition, the thickness of a heterostructure with an LT-Si layer is much smaller (cf. 0.5 and 3 μm for $x = 0.3$). In Fig. 7a, we show a cross-sectional electron-microscope image of a 300-nm-thick $Ge_{0.29}Si_{0.71}$ sample grown on a 50-nm-thick LT-Si layer. One can see MDs in the interface plane, whereas

threading dislocations are not observed. An optical microphotograph of the GeSi layer surface for the same sample after treatment in Schimmel etchant is shown in Fig. 7b [43]. Estimation of the threading-dislocation density on the basis of electron and optical microscopy methods yields 10^4–10^5 cm^{-2}. Since low-temperature molecular-beam epitaxy (MBE) proceeds in significantly nonequilibrium conditions, it is reasonable to assume [21] that the layers grown at a low temperature contain a high concentration of intrinsic point defects, which can represent the main factor conducive to the formation of GeSi with a low density of threading dislocations. Ideas about mechanisms that are conducive to reducing the threading-dislocation density in GeSi films grown on a low-temperature buffer layer are numerous (see Subsection 2.3 for details).

As will be clear from what follows, the main contribution to relaxation in the majority of heterostructures is made by MDs that multiply from a single source. The misfit dislocations, which are closely spaced as a result of the prolonged operation of such a source and have identical Burgers vectors, are largely responsible for the increased roughness of the film surface; this roughness is represented by relatively high hillocks, which act as pinning sites for threading dislocations. According to Fitzgerald *et al*. [31, 32], this mechanism for immobilization of threading dislocations represents one of the main obstacles to the formation of perfect GeSi films based on graded layers. A thick graded buffer layer is necessary to reduce the density of MD sources (see above). At the same time, such a layer ensures plastic relaxation with a small number of secondary sources owing to a high multiplication rate of dislocations; as a result, we have an unacceptable (by today's standards) roughness of the GeSi layer surface and a relatively high density of threading dislocations. The films grown on an LT-Si buffer layer have less pronounced roughness of the surface [22, 44]. It is assumed that this effect is caused by a more uniform distribution of dislocation sources when an LT-Si buffer is used and, correspondingly, by a lower degree of multiplication of each of these sources.

2.2.2. Dislocation filters

Studies aimed at reducing the density of threading dislocations using so-called dislocation filters, which are represented by layers with different structural characteristics, have a long history [45] and have mostly been restricted to the growth of III–V solid-solution films [46–49] and GaAs/Si heterostructures [50–52]. It is assumed that the filtering properties of separate stressed layers are based on the phenomenon of bending of threading dislocations subjected to tangentially directed forces [45], which is similar to what happens when an MD is formed from a dislocation penetrating from the substrate (see the Matthews model [53]). It would seem reasonable to use a system of stressed layers [a stressed superlattice (SL)] rather than a single stressed layer in order to further reduce the density of threading dislocations. However, the initial explanation for the filtering effect of an SL by the bending of threading dislocations due only to stresses is incomplete and somewhat contradictory in the context of recent data. Indeed, a stressed layer is conducive to bending of threading dislocations; however, it is known that stress-compensated and even unstressed SLs (of the $In_xGa_{1-x}As/In_xAl_{1-x}As$ type) are also efficient dislocation filters [47, 50]. It is assumed [52] that a built-in electric field in an SL with layers which differ appreciably in their electrical parameters is an important parameter of interaction between threading dislocations and the SL. This interaction gives rise to instability of the dislocation segment and is conducive to an increase in the probability of forming a double kink in the dislocation line, thus increasing the velocity of motion of dislocations in the tangential direction.

The use of stressed layers as dislocation filters can be illustrated by the following results. Takano *et al*. [54] grew GaAs films on Si substrates with an $In_xGa_{1-x}As$ intermediate layer (with x as large as 0.15). This layer has a larger lattice parameter than that of GaAs and, as a result, reduces the threading-dislocation density to 10^6 cm^{-2}. Thus, this density decreased by almost two orders of magnitude compared to the situation where there was no intermediate layer. For the same purpose, Sakai *et al*. [55] used a 5-nm-thick Si film introduced into a $Ge_{0.3}Si_{0.7}$ layer on Si(001). Luo *et al*. [56] used an intermediate layer with a thickness of 50 nm. In both cases, a decrease in the threading-dislocation density by about two orders of magnitude was observed.

Unstressed separate layers also act as efficient dislocation filters. For example, Osten and Bugiel [57] grew a $Ge_{0.3}Si_{0.7}$ solid solution on Si(001) using intermediate layers with 10, 15, 20, and 25% of Ge. The density of threading dislocations in the top layer was 10^7 cm^{-2}. After a lattice-matched GeSiC ternary solid solution was inserted into each GeSi solid-solution intermediate layer, the density of threading dislocations decreased to a value lower than 10^5 cm^{-2}. A similar decrease in the density of threading dislocations was observed by Huang *et al*. [58]. In this case, a 100-nm-thick $Ge_{0.2}Si_{0.8}$ solid-solution layer grown on Si(001) at 500°C was inserted into the midsection of a 400-nm-thick layer of the same composition but grown at 750°C. The characteristic features of the last two examples were related to the fact that the so-called insertions had the same lattice parameter as the main layer and, despite the absence of additional bending forces for threading dislocations, acted as dislocation filters. These examples are indicative of a more complex interaction between threading dislocations and additional layers whose properties differ only slightly from those of the main overgrown material.

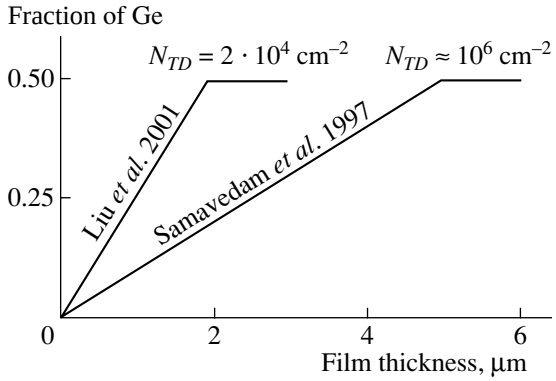

Fig. 8. Linear increase in the Ge fraction in the buffer layer: the data reported by Samavedam *et al.* [31] correspond to conventional technology and those reported by Liu *et al.* [60–62] were obtained using antimony as a surfactant. A schematic representation.

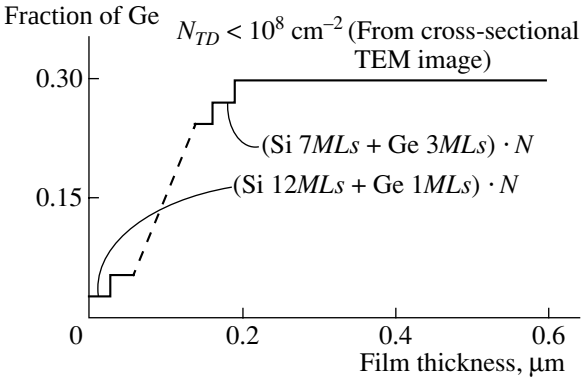

Fig. 9. An illustration of using a buffer layer with a short-period superlattice (according to Obata *et al.* [64]).

2.2.3. Development of gradient methods

As mentioned above, the method of using a graded buffer layer is presently most widely used to obtain artificial substrates. Fitzgerald *et al*. [31, 32, 36, 59] have shown that a comparatively high density of threading dislocations (~10^6 cm^{-2} for x = 0.3–0.5 and higher for $x \sim 1$) is attributable to the stoppage (or capture) of moving dislocations by hillocks and depressions on the rough surface. The characteristics of this method can be improved by lowering the roughness of the growth surface. Impressive results were obtained [60–62] by using a monatomic Sb layer, which stabilized the planarity of the growth surface, in addition to using the composition gradient. Antimony is a surfactant, exerts a smoothing effect on the growth surface, and, owing to segregation, remains at the surface during the entire process of growth. Using this method, Liu *et al*. [60–62] managed to appreciably increase the steepness of the gradient in the buffer layer and simultaneously improve the structural characteristics of such artificial substrate. The surface roughness amounted to 2–5 nm (it was 15 nm on the reference-sample surface without using Sb) [61]. In Fig. 8, we show schematically the characteristics of the samples [60–62] compared to those obtained in the standard variant developed by Samavedam [31].

Another method for improving the characteristics of artificial substrates consists in the use of so-called short-period graded SLs [63–66]. Figure 9 illustrates the distribution of the GeSi composition over the depth in this sample [64]. The transition graded layer consists of packs of short-period SLs based on Ge and Si monolayers whose average composition (x) increases as the buffer-layer thickness increases. The fractions of Ge in extreme monolayers are illustrated in Fig. 9. The use of graded SLs makes it possible to reduce appreciably the necessary thickness of the graded layer (in the case under consideration, the reduced thickness is 0.2 μm, as compared with 3 μm in the conventional variant illustrated in Fig. 8), retain or improve the smoothness of the growth surface, and, supposedly, decrease the density of threading dislocations. The attained improvement of these characteristics can be attributed to two factors. It is known that intermediate Si layers in an SL exert a smoothing effect [67–69]. Accordingly, the surface smoothness of artificial substrates with SLs is improved by an order of magnitude compared with conventional structures with a smooth composition gradient (for example, the surface roughness can be reduced by 1–2 nm according to Rahman *et al*. [65, 66]. Further, it is reasonable to assume that the presence of abrupt interfaces between adjacent SL layers, which differ significantly in their composition and lattice parameter, should be conducive to the generation of MDs and, especially, to the propagation of threading segments (see above). Obata *et al.* [64] evaluated the structural perfection of artificial substrates from the absence of threading dislocations in an electron-microscope photograph of a cross section with a length of 1 μm, which sets the detection threshold for threading dislocations at 10^8 cm^{-2}. At the same time, estimations of the threading-dislocation density from images obtained using atomic-force microscopy [66] yield values on the order of 10^5 cm^{-2} or smaller for this density.

Thus, by analyzing modern methods for the formation of artificial substrates, which are based on the plastic relaxation of layers with a differing lattice parameter, we should accept the following three methods as the comparatively developed and most promising. These methods rely on the use of (i) LT-Si buffer layers, (ii) graded layers with Sb as a surfactant, and (iii) graded superlattices; these methods can be combined. For example, Bozzo *et al.* [70] reported the use of a graded GeSi buffer layer terminated by a dislocation filter based on an SL. The threading-dislocation densities in $Ge_{0.25}Si_{0.75}$ layers on Si were reduced to 10^3–10^5 cm^{-2}.

2.3. Possible Mechanisms for the Attainment of a Low Density of Threading Dislocations in Plastically Relaxed Films using GeSi/LT-Si Heterostructures as an example

2.3.1. Relaxation rate and initial density of misfit dislocations

As mentioned above, under the plastic-relaxation rate we mean the rate of decrease in residual elastic strains as the film thickness increases. Figure 10 shows the dependence of the normalized value of residual elastic strain in the $Ge_{0.3}Si_{0.7}$/Si(001) film on the film thickness; this dependence was calculated using the Hu equilibrium model [12] [see expression (6)]. Theoretical dependences based on the generally and widely recognized Gillard–Nix–Freund (GNF) model [6] for x = 0.35 are also shown. In the GNF model, a so-called blocking potential of the MD orthogonal network is introduced; the stress field of this potential is calculated taking into account the edge and screw components of 60° MDs. This potential decreases the effective thickness of a growing stressed film and thus decreases the driving force for the propagation of threading dislocations. The hatched area corresponds to the region in which the dependences calculated for four combinations of the Burgers vectors are found. Experimental points are taken from the data reported in [6] and also in other publications [26, 27, 55, 71, 72]. It can be seen that the dependences calculated according to the GNF model are, in general, close to the majority of experimental data; however, these data persistently fall above the results of calculations. Some experimental points deviate appreciably in the direction of either smaller or larger values of residual elastic strain. This is related to special features of growth of specific GeSi films and will be discussed below.

As can be seen from Fig. 10, 100-nm-thick GeSi films grown on an LT-Si buffer layer relax by no more than 15–20% despite prolonged heat treatments at 800–900°C. However, the degree of relaxation increases abruptly as the thickness of the solid-solution film increases. For example, Fig. 11 shows (in the same coordinates as in Fig. 10) two groups of experimental data on the plastic relaxation of $Ge_{0.3}Si_{0.7}$/Si(001) films grown on an LT-Si buffer layer at temperatures of 350°C [26, 27] and 550°C [22, 24]. An abrupt increase in the degree of plastic relaxation in such films is observed even at growth temperatures if the film thickness exceeds 100 nm. Annealing additionally reduces the residual elastic strains in these films.

It is generally accepted that the major part of plastic relaxation of stressed films occurs owing to an increase in the density of MDs due to their multiplication. Beanland [73] draws attention to two waves of plastic relaxation in a stressed layer. The first relaxation wave propagates in the case of a small layer thickness, is caused by primary sources, and, according to different estimations, accounts for 10–20% of complete plastic relaxation. The second wave develops on the basis of sec-

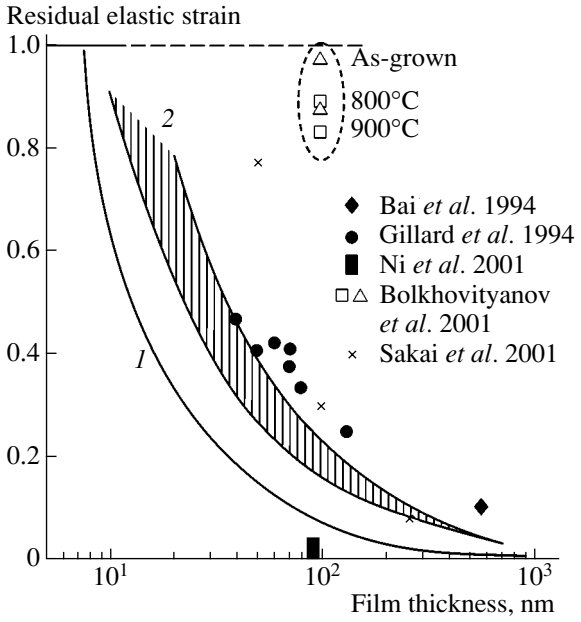

Fig. 10. Normalized residual elastic strains in Ge_xSi_{1-x}/Si(001) films in relation to the film thickness. Comparison of the results of calculations with experimental data. Curve *1* corresponds to the Hu [12] equilibrium model, and hatched area *2* represents a group of dependences calculated by Gillard *et al.* [6]. Experimental points are taken from relevant publications [6, 55, 71, 72]. The dashed oval outlines experimental points that correspond to slowly relaxing Ge_xSi_{1-x}/LT-Si/Si(001) films [26, 27].

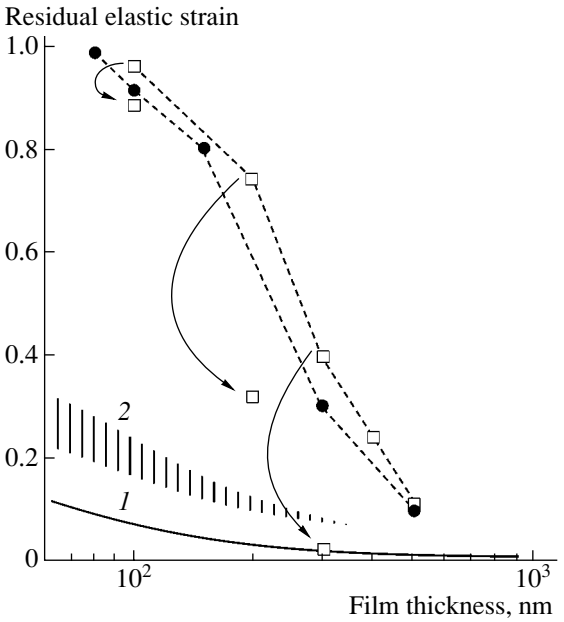

Fig. 11. Normalized residual elastic strains in $Ge_{0.3}Si_{0.7}$/Si(001) films grown on a low-temperature Si buffer layer in relation to the GeSi film thickness. Filled circles correspond to the data reported by Li *et al.* [22, 24]. Squares represent the data obtained by Bolkhovityanov *et al.* [26, 27]. Curved arrows indicate a decrease in residual elastic strains as a result of annealing heterostructures for 1 h at 800°C. Dependences *1* and *2* are part of those shown in Fig. 10.

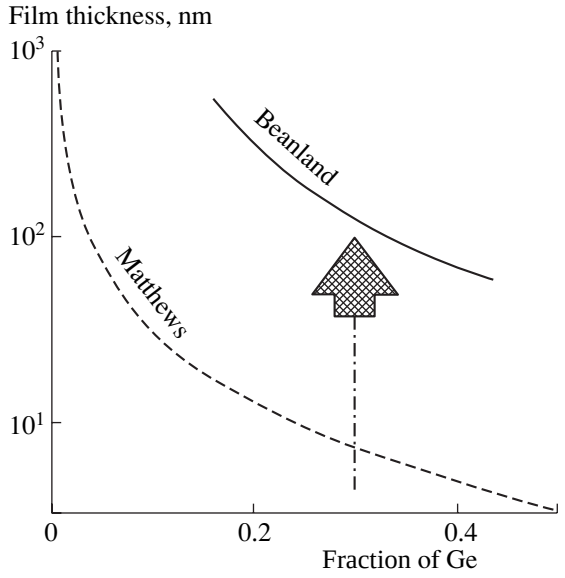

Fig. 12. The critical thickness for the onset of operation of the Frank–Read dislocation source as a function of the GeSi film composition (as calculated by Beanland [73]). Comparison with the conventional dependence of the critical thickness for introducing misfit dislocations on the film composition as derived by Matthews and Blakeslee [7, 14].

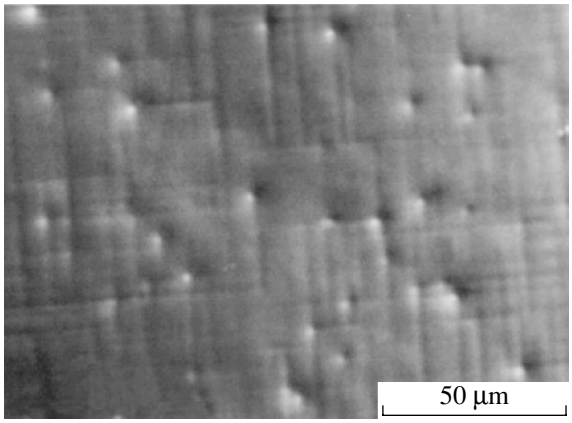

Fig. 13. Threading dislocations (pits) on the $Ge_{0.29}Si_{0.71}$/Si(001) layer surface after treatment in the Schimmel etchant. The GeSi layer thickness is 100 nm; the growth temperature, 350°C; and the degree of plastic relaxation, 5%.

ondary sources related to various variants of the multiplication of dislocations.

According to Beanland [73], the necessary condition for the initiation of secondary sources is that the film thickness exceed the critical one. Figure 12 shows the calculated [73] film thickness for which the Frank–Read source can be effective (and, correspondingly, for which the MD multiplication can occur); this dependence is drawn against the "background" of the curve for the critical thickness of MD introduction [7, 14]. It can be seen that the estimated film thickness corresponding to the onset of MD multiplication is no smaller than 100 nm (the arrow in Fig. 12) for Ge_xSi_{1-x}/Si(001) structures with x close to 0.3. Thus, 100-nm-thick $Ge_{0.3}Si_{0.7}$/LT-Si/Si(001) films, the special features of plastic relaxation of which are illustrated in Fig. 10, have a thickness no larger than that necessary for the actuation of mechanisms of plastic relaxation via the multiplication of MDs; furthermore, the density of primary centers of MD generation is low. Figure 13 shows an optical microphotograph of the surface of a 100-nm-thick $Ge_{0.29}Si_{0.71}$/Si(001) film grown at 350°C [26, 27]. Traces of steps related to MDs and pits corresponding to threading dislocations are observed on the film surface after treatment of the sample in a solution of Schimmel etchant [43]. Taking into account that the degree of plastic relaxation in this film is no greater than 5%, we may assume that the threading-dislocation density of about 10^5 cm^{-2} corresponds to nearly the same density of MDs. This density is two orders of magnitude lower than the threading-dislocation density in GeSi films (triangles connected with the arrow in Fig. 5) grown under standard conditions; in the latter case, the degree of relaxation is no greater than 1% [16]. Consequently, when GeSi films are grown at low temperatures (in the case under consideration, at 300°C), the MD and threading-dislocation density are lower by two orders of magnitude than those in standard films [16]; at the same time, the rate of threading-dislocation glide is higher in the former case since the degree of plastic relaxation is greater. As can be seen from Fig. 11, plastic relaxation of the main portion of elastic strain occurs in thicker films (200 and 300 nm), which can be naturally related to the multiplication of MDs.

It is reasonable to assume that, in order to increase the rate of plastic relaxation in the films to the value exceeding that in conventional films (see dependences *2* in Fig. 10), it is necessary to increase significantly the density of generation sites for MDs. This assumption is validated by the experimental dot (a filled rectangle) shown in Fig. 10 and taken from the publication by Ni *et al.* [71]. Ni *et al.* [71] and Bauer *et al.* [74] showed that the relaxation rate is very high in a GeSi layer grown at a relatively low temperature (150°C) and subjected to subsequent annealing; experimental results reported in the above publications corresponded to nearly 100% relaxation for a 90-nm-thick layer. Apparently, these results are related to the fact that the layer was initially grown at a temperature which was close to the amorphization temperature [71] for the growing layer. Such a layer contains a high concentration of point defects sufficient for the generation of MDs with a high density. At the same time, the threading-dislocation density in such layers, which was determined from analysis of electron-microscope images [74], exceeded 10^{10} cm^{-2}. Thus, an ultrahigh concentration of defects in a GeSi layer is conducive to the formation of MDs with a high density and, correspondingly, to a high rate

of plastic relaxation. However, as a result, one obtains a high density of threading dislocations.

We may assume that optimal growth conditions should exist for the formation of relaxed GeSi films with a low density of threading dislocations. For example, Luo *et al.* [44] showed that an LT-Si buffer layer grown at 400°C is most appropriate for subsequent epitaxy of GeSi layers with a low density of threading dislocations. Studies based on electron–positron annihilation spectroscopy [75–77] showed that the layers grown using the low-temperature (200–400°C) epitaxy of silicon and its solid solutions with germanium contain a high concentration of vacancy-type defects ($\sim 10^{17}$–10^{18} cm^{-3}). According to Ueno *et al*. [77], the largest vacancy cluster (containing more than ten vacancies) was observed in an Si layer grown at 400°C. It is at this temperature that the discoverers of this method (Chen *et al*. [20]) for obtaining GeSi films with a low threading-dislocation density grew the LT-Si buffer layer.

2.3.2. The rate of motion of threading dislocations

The magnitude of residual elastic strains should be approximately the same in the layers with a high density of "short" MD segments and in the layers with a low density of extended MDs. However, it is evident that the threading-dislocation density is bound to be higher in the former case. Consequently, it is preferable to combine a low MD generation rate with a high propagation velocity for threading dislocations. Thus, it is necessary to be able to control both processes separately. It is worth noting that, in the majority of studies concerned with a discussion of mechanisms which are conducive to the formation of heterostructures with a lowered threading-dislocation density, attention was primarily focused on the assumption that annihilation of threading dislocations is enhanced; the possibility of increasing the glide rate of these dislocations was not considered at all. It is reasonable to assume that the presence of a high concentration of vacancy-type defects [77], which diffuse from the LT-Si layer and accumulate in the vicinity of MDs, can decrease the dislocation-core energy [78] in a structure with an LT-Si underlayer. Additional arguments can be found in the publication by Fedina *et al*. [79], where it was shown experimentally that, under conditions of a high concentration of point defects, microregions with an absence of dangling bonds were formed, whereas the defect-displacement vector decreased. As a result, the linear tension of an MD extended section [i.e., the right-hand side of expression (1)] decreases; correspondingly, the propagation velocity of threading dislocations increases. The data on the increase (by two orders of magnitude) in the rate of motion of dislocations in silicon saturated with hydrogen can serve as indirect evidence in support of the above mechanism [80].

Additional confirmation of the fact that this mechanism is feasible can be obtained by paying attention again to the experimental point (filled rectangle in Fig. 10) reported by Ni *et al.* [71]. As can be seen from Fig. 10, this experimental point lies significantly lower than the relevant dependence for equilibrium critical values of thickness calculated according to the Hu model [12]; i.e., this point lies in the region where a 100% degree of relaxation is energetically unfavorable. If the data reported in [71, 74] are reliable, this inconsistency between experiment and the dependence calculated according to the Hu model [12] can be attributed to a significant decrease in the work needed for the formation of a new MD of unit length [the right-hand side of expression (1)]. In these conditions, according to expression (1), critical values of thickness for the introduction of MDs become smaller than those in conventionally grown GeSi layers. In addition, a new calculated dependence for critical thicknesses is bound to run below the standard one shown in Fig. 10.

The aforementioned assumptions relate an increase in the motion rate of threading dislocations to variation in the effective shear stress τ_{eff} in expression (4). Another possibility can be also considered. A variation in the glide velocity of dislocations can also be related to variation in the activation energy of this process. As is well known, the widely accepted model of dislocation motion is the model based on the formation of double [81] and single kinks in dislocations. Due to thermal fluctuations or the effect of stresses, a double kink (DK) can originate in the dislocation line. After attaining a critical size, the DK dissociates into two single kinks, which propagate in different directions; this ultimately results in the transition of the dislocation line to a neighboring valley of the energy profile. Thus, the rate of glide of dislocation is controlled by the kink-formation energy F_k and the height of the energy barrier for the migration of the kink W_m. The activation energy E_v of dislocation motion in expression (4) consists of two components: the activation energy for formation of a double kink and the activation energy for kink migration, i.e., $E_v = 2F_k + W_m$. Measurements of the motion rate for dislocations in stressed structures were used to reveal that the activation energies for the motion of 60° dislocations E_v are equal to about 2.2 eV for Si and GeSi [4, 16, 82, 83]. These activation energies are much lower in GaAs: 0.89–1.3 eV for α dislocations and 1.24–1.57 eV for β dislocations [82]. In our opinion, these data for GaAs were the main reasons why good results were achieved earlier in producing high-quality artificial substrates made of III–V compounds and were more dependable than in the case of GeSi. Gottschalk *et al.* [84] summarized experimental data on F_k and W_m in Si: W_m = 1.2–1.8 eV and F_k = 0.4–0.7 eV.

These energies were measured and calculated for Si and GaAs in the conventional crystalline state. However, they may decrease if the growing layer contains a high concentration of point defects. Correspondingly, the rate of motion of threading dislocations may increase. For example, Öberg *et al.* [82] noted that, according to both experimental data and the results of

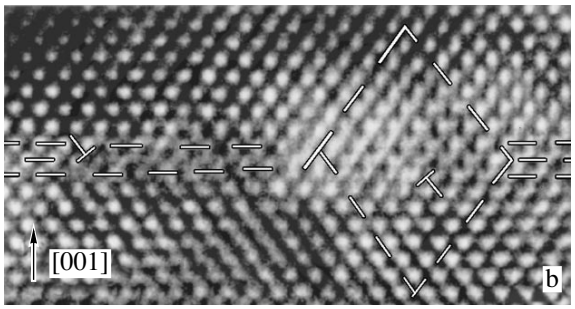

Fig. 14. An HREM image of a dislocation dipole in the (001) plane. A Burgers contour encloses the right-hand core of the dislocation dipole. The initial mismatch amounts to 0.9%. The photograph was made available to us by L. Fedina (reproduced with permission of the authors [88]).

calculations, the activation energy for the motion of dislocations is lower in doped silicon. Yamashita *et al.* [80] reported that the activation energy for the glide of dislocations decreased from 2.2 to 1.2 eV and the rate of their motion increased by two orders of magnitude after silicon was enriched with atomic hydrogen. Therefore, a decrease in both F_k and W_m under the effect of a high concentration of point defects can be considered a reasonable assumption. It is noteworthy that a thin layer inserted into the main film and having a different composition [54–57] or a spacer grown at low temperatures [58] can play the same role as defects; i.e., these layers can increase the probability of the formation of a double kink in the dislocation line and can thus increase the rate of motion of threading dislocations. It was also observed [54–57, 58] that the threading-dislocation density is lower in films with inserted foreign layers than in films without these layers.

2.3.3. Improvement of conditions for the annihilation of threading dislocations

The rate of annihilation of threading dislocations can increase owing to an increase in the radius of interaction between threading dislocations that move in closely spaced glide planes; this effect can also be related to a high concentration of point defects [37]. Typically, stressed layers are grown at temperatures such that the climb of dislocations can be ignored. A high concentration of point defects formed as a result of either irradiation or growth of a low-temperature buffer layer increases the probability of the inclusion of this mechanism for the climb of dislocations in the process of annihilation of threading dislocations which propagate in closely spaced glide planes. An assumption about the origination of an ordered network of threading dislocations at the initial stage of plastic relaxation also relies on the emergence of additional conditions which are conducive to the annihilation of threading dislocations [25, 41]. Trinkaus *et al.* [41] assume that there is a certain ordering of threading dislocations as a result of their generation at microvoids formed after implantation of hydrogen into a preliminarily grown and initially pseudomorphic GeSi layer, whereas Gaiduk *et al.* [25] and then Bolkhovityanov *et al.* [26, 27] suggested a more elegant model; the latter will be considered in detail in the next subsection.

2.3.4. An ordered network of threading dislocations

It is assumed that a silicon underlayer grown at low temperatures and enriched with point defects can serve as a source for the origination and development of an ordered misfit-dislocation network. The significance of ordering lies in the fact that this network should be formed of single-type dislocations; reactions between these dislocations should be energetically favorable and lead to the annihilation of threading dislocations. The issue concerning the properties of the sources required for the generation of misfit dislocations is most important in this context.

It is reasonable to assume that, as the density of primary heterogeneous MD-generation sources related to various inhomogeneities in the substrate surface decreases, the main sources of MD generation become associations of intrinsic defects at the heterostructure interface. The number and atomic structure of these associations are governed by the conditions of low-temperature growth of the Si buffer layer and by the properties of the adjacent portion of a stressed GeSi layer (or by the structural state of Si substrate after irradiation). It is known [85, 86] that annealing of silicon containing a high concentration of point defects gives rise to specific rodlike defects in {311} planes. These defects are oriented along the ⟨110⟩ directions and are composed of interstitial atoms located in the {311} planes in the form of a hexagonal Si monolayer. Under certain conditions, the rodlike defects become the sources of dislocation loops [87]. The formation first of vacancies in the plane parallel to the interface and then of dipoles of 60° dislocations was observed after direct irradiation of pseudomorphic GeSi/Si(001) layers with electrons in a high-resolution electron microscope (HREM) (Fig. 14) [88].

Heterogeneous sources of dislocations at the substrate surface are formed before the onset of growth of the stressed layer and exist irrespective of the presence of this layer. These sources are activated both when the temperature is elevated and when the thickness of the pseudomorphic layer is increased beyond the critical thickness; as a result, it is generally assumed that a complete set of dislocations is formed in the relaxing film. Clusters composed of point defects are initially absent in the LT-Si (or (LT-GeSi) layers and appear only under certain conditions, in particular, when there is a field of internal stresses in the course of growing the stressed layer. We may assume that the diversity of the crystallographic shapes of these clusters becomes limited when they are formed in the presence of a biaxial stress field. Under conditions of a plane-stressed state of the heterosystem, the clusters become ordered with

respect to both the crystallographic orientation and spatial distribution. As a result, the formed clusters have a specific crystallographic orientation and are conducive to the generation of a more limited variety of MDs; in other words, as Gaiduk *et al.* note [25], "a self-assembled network of primary dislocations is formed." In this case, the annihilation rate of threading dislocations is bound to increase drastically compared to the conventional case (a decrease in the density of threading dislocations is inversely proportional to the film thickness [89]), which ultimately brings about a lower density of threading dislocations.

Thus, under the effect of self-organization of the primary MD network we mean the following sequence of events: point defects, which are present in the LT-Si and (or) LT-GeSi layers, are grouped into clusters in the vicinity of the interface during the growth of the pseudomorphic GeSi layer; the 60° MDs are then generated on the basis of these clusters. The determining factor of this process is the fact that the above structural rearrangements occur under the effect of a stress field of the growing pseudomorphic solid-solution layer. Despite the apparent consistency of the model, which implies ordering of MDs at the initial stage of formation of the dislocation network and, as a consequence, an increase in the probability of threading-dislocation annihilation, direct observations indicating that this mechanism is plausible are lacking in the available publications.

2.4. Basic Methods for the Fabrication of Artificial Substrates Based on Plastic Relaxation of Heterostructures

Thus, after more than 20 years of attempts to grow perfect GeSi/Si heterostructures with constant-composition films, the crystalline quality of these structures leaves much to be desired. This manifests itself in a high threading-dislocation density, which increases with an increasing Ge fraction (see the solid line in Fig. 5). As the mismatch between the lattice parameters of the film and substrate becomes more significant, the glide rate for threading dislocations increases; however, the number of these dislocations increases as well. In our opinion, the observed high density of threading dislocations is governed by the relation between the density of generated MDs and the velocities of propagation of threading segments in GeSi heterostructures grown under similar conditions (standard Si substrates and conventional growth conditions of GeSi films); the terms of the above relation have common driving forces, and the relation itself varies within a narrow range.

Recently, new methods for treating substrates have been developed and new conditions of film growth have been suggested; these innovations made it possible to affect the above processes independently, which resulted in the improvement of the crystalline quality of grown GeSi films. For example, the density of the centers for the heterogeneous generation of MDs can be reduced significantly by thorough preepitaxial treatment of the substrate surface and by overgrowth of the Si buffer layer (with a thickness of 50–100 nm); this layer moves the GeSi/Si interface away from the substrate surface. As follows from the above discussion, the rate of the threading-dislocation propagation can be increased by a number of methods. These methods include introducing point defects into the substrate and the interfacial region of the heterostructure and the formation of "insertions" within the heterostructure in the form of separate layers or superlattices. The efficiency of these methods in increasing the rate of threading-dislocation glide has been observed so far only in experiments in which the Si substrate is enriched with hydrogen atoms [80]. In other cases, the effect of these methods is within reasonable assumptions based on the analysis of experimental data related to efforts to improve the structural properties of the heterostructure.

The data listed in Table 1 make it possible to correlate the new methods with possible mechanisms for reducing the threading-dislocation density, which were discussed above. It can be seen that, in the majority of cases, explaining the positive effect of a certain factor will be tentative. Thus, these new methods require more thorough experimental studies with the aim of gaining insight into specific mechanisms that bring about an improvement in the structural properties of relaxed GeSi films.

Nevertheless, if we combine the analysis of the aforementioned experimental data with basic concepts of the theory of plastic relaxation in heteroepitaxial films, we can envisage the following methods that are conducive to a decrease in the density of threading dislocations in relaxed films and to an acceptable morphological quality of these films:

(I) The MD density caused by the activation of primary centers of MD generation should be low (~10^4–10^5 cm^{-2}), which is ensured by thorough preepitaxial treatment of the substrate surface, absence of contaminants during growth, and overgrowth of an Si buffer layer.

(II) It is necessary to satisfy the conditions for the activation of threading-dislocation motion and for an increase (or retention at the same level) of the propagation of these dislocations. Suggested methods consist in introducing a high concentration of point defects and forming additional inhomogeneities in growing films by introducing separate layers with a different composition or superlattices.

(III) It necessary to provide conditions for an increase in the probability of annihilation of threading dislocations (presumably, a high concentration of point defects and ordering of the dislocation network can be conducive in this respect).

(IV) Special attention should be paid to ensuring a two-dimensional mechanism of growth and planarity of the growth surface. These requirements can be met by

Table 1. The factors that are conducive to decreasing the density of threading dislocations in relaxed layers with lattice-parameter mismatch and realization of these factors in various methods

Method	Factor						
	a decrease in the density of primary misfit dislocations	an increase in the propagation rate of threading dislocations	promotion of threading-dislocation annihilation	an ordered misfit-dislocation network conducive to threading-dislocation annihilation	a decrease in the capture of threading dislocations by a rough surface	a decrease in the immobilization of threading dislocations by misfit dislocations	number of publications
1. Graded buffer (conventional technology)	Experiment and theory [8, 32, 33]	Constant rate expected on the basis of the model [33]		Assumption [34]		Expected on the basis of the model [33]	>10
2. Graded buffer with Sb as a surfactant	Expected on the basis of the model [33]	Constant rate expected on the basis of the model [33]			Reduction of roughness, experiment [61]	Expected on the basis of the model [33]	3
3. Graded buffer based on short-period superlattices	Expected on the basis of the model [33]	Should be expected on the basis of assumptions [52]			Circumstantial evidence, this review	Possible, since misfit dislocations reside in different planes	4
4. Filters based on superlattices		Assumption [52]	Assumption [8, 52]				2
5. Individual inserted layers		Assumption, this review	Assumption [45]		Assumption [55]		4
6. Buffer layer grown at a low temperature	Experiment [26, 27]	Assumption based on circumstantial evidence [79], this review	Assumption [37]	Assumption [25–27]	Assumption [22, 24]		>10
7. Enrichment of silicon substrate with hydrogen		Experiment [80]					2
8. Implantation of hydrogen under the pseudomorphic GeSi layer with subsequent annealing				Assumption [41]			3

inserting thin layers of either a pure Si layer or short-period (graded) SLs into the film or by using antimony as a surfactant.

The conditions of growth of heterostructures intended for use as artificial substrates should be chosen on the basis of the aforementioned special features.

3. "COMPLIANT" AND "SOFT" SUBSTRATES: EXPECTATIONS AND REALITY

3.1. Basic Concepts

The idea of using a compliant substrate is based on the effect related to redistribution of elastic strains between the pseudomorphic layer and the substrate if the thickness of the latter is comparable to the thickness of the growing layer (see, for example, the monograph [90]). In Fig. 15, we show the schematic representation of a structure in which this effect can be used. It is assumed that a thin membrane, which serves as a compliant substrate, can move freely in the lateral direction without, however, losing contact with the thick supporting substrate. Strains in the pseudomorphic layer, with allowance made for the substrate thickness, can be written as [90]

$$\varepsilon_f = \frac{d_0}{d_0 + h}\varepsilon_0, \quad (7)$$

where d_0 and h are the thicknesses of the compliant substrate and the layer, respectively; and ε_0 is the total elastic strain in the case of a thick substrate. The smaller the thickness of the substrate–membrane, the smaller the total strain in the layer.

The term "compliant substrate" was introduced into scientific literature by Lo [91]. It was assumed that, under certain conditions (for example, a small thickness of the membrane), the elastic strain in a growing pseudomorphic film decreases as the film thickness increases. In this case, the introduction of MDs into the films becomes energetically unfavorable at any film thickness; correspondingly, the process of plastic relaxation of stresses in the growing film may not set in at all. Since the idea of using a compliant substrate was quite clear and promised real advantage in improving the crystalline quality of growing films with a differing lattice parameter, it was rapidly accepted by the scientific community; specifically, experiments with various materials were conducted [92–104], theoretical calculations of the critical thickness and relaxation of stressed films [105–109] were performed, and the relevant reviews were published [3, 110–114].

3.2. Technical Realization

To date, two variants of fabricating compliant substrates have become known and implemented.

(I) The first variant relies on the use of silicon-on-insulator (SOI) substrates [94, 95]. In these structures, a silicon layer on oxide is thinned and becomes a thin membrane (substrate) for the growth of the heteroepitaxial film, whereas the oxide layer is treated as a viscous spacer, which ensures sliding of the heterostructure with respect to the main substrate. In addition, other methods for the formation of an amorphous viscous spacer between the main substrate and the membrane have been used. These methods include (i) the implantation of B into the SiO_2 layer in order to reduce its viscosity [98] and (ii) the bonding of the GeSi/Si heterostructure to the Si substrate using a SiO_2 intermediate layer [100]. Recently, Luo *et al*. [99] reported the use of a compliant substrate with an underlayer of borosilicate glass for the growth of a Ge_xSi_{1-x} solid-solution film with $x = 0.25$. This underlayer was formed by ion implantation of B and O into the buried SiO_2 layer. With respect to the threading-dislocation density in GeSi films, the result reported in [99] was comparable to the best data obtained in other studies using thick graded buffer layers or silicon buffer layers grown at low temperatures.

In a version of this method used for III–V compounds, a GaAs/AlGaAs/GaAs heterostructure is bonded via an intermediate layer (which will play the role of a "soft" substrate in what follows) to the supporting substrate [93, 96, 97]. The heterostructure substrate and the AlGaAs layer are then dissolved in different etchants [AlGaAs is used as a stopper layer in etching the GaAs substrate according to the well-known technology for the fabrication of photocathodes (see, for example, [115])]. The remaining GaAs film on the "soft" underlayer is treated as a compliant membrane in the course of growing stressed InGaAs films.

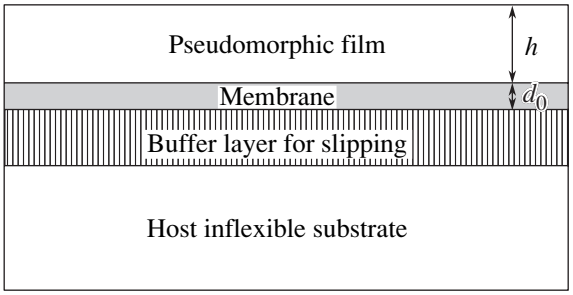

Fig. 15. A schematic heterostructure model including a thin membrane which can slide over the supporting substrate.

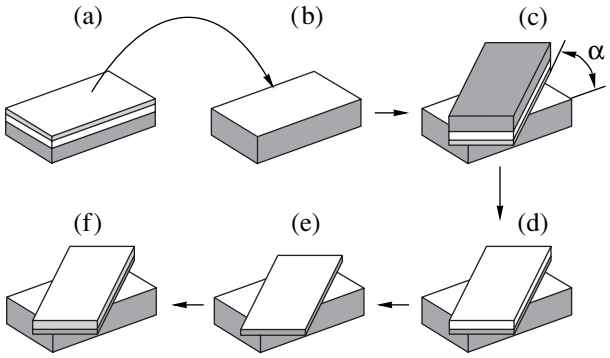

Fig. 16. Schematic representation of the formation of a compliant substrate according to the twist-bonding technology: (a) a preliminarily grown GaAs/AlGaAs/GaAs heterostructure, (b) a supporting GaAs substrate, (c) bonding of a and b by welding with rotation by an angle α, (d) etching off of the GaAs substrate, (e) etching off of the stopping AlGaAs layer (the compliant-substrate structure is finally formed), and (f) an InGaAs layer is grown on the compliant substrate.

(II) The second variant consists in bonding with misorientation (the so-called twist bonding) [42, 101–104]. In this case, the GaAs/AlGaAs/GaAs heterostructure is bonded directly to the GaAs substrate (without intermediate layers), with the crystallographic orientations of the components of the bonded pair being different. In the ideal case, twist boundaries with a weakened bond structure and an ordered network of screw dislocations are formed between joined wafers. Eventually (as illustrated in Fig. 16), the GaAs substrate and the AlGaAs stopper layer are etched off in the same way as in the previous variant. It is assumed that, in the course of subsequent growth of a stressed layer on a thin GaAs layer, the latter is compliant since the region containing screw dislocations is conducive to the sliding of the GaAs layer over the supporting substrate [101]. Ejeckam *et al*. [101] reported on the efficiency of using

such a substrate in their pioneering studies concerned with the heteroepitaxy of InSb on GaAs. In this case, the lattice-parameter mismatch amounts to 14.7%. According to Ejeckam *et al*. [101], it is possible to reduce the density of threading dislocations to 10^6 cm^{-2}.

It is noteworthy that both methods are based on bonding technology, which is sophisticated and costly. It seems that the method based on the use of a viscous amorphous layer, which is formed "automatically" during the growth of crystalline strontium titanium oxide, is more promising [116]. The authors of the latter publication, in attempting to improve quality of a GaAs/Si structure, introduced an additional $SrTiO_3$ layer between the Si substrate and GaAs film. This layer has a lattice parameter which is intermediate between those of Si and GaAs; this circumstance is conducive to a more gradual (two-stage) transition from Si to GaAs. In addition, it has been found [116] that oxygen diffusing from $SrTiO_3$ into the Si substrate forms a SiO_x amorphous spacer in the substrate; it is believed [116] that this spacer gives rise to the effect of compliance. This method was used to grow GaAs layers on Si substrates that were 12 inches in diameter; the authors state that the properties of these layers were no different from those of homoepitaxial GaAs.

3.3. Mechanisms of Relaxation

It has been demonstrated repeatedly that the structural quality of relaxed films grown on compliant substrates is indeed higher than in the case of films grown otherwise; the relevant results are summarized in published reviews [112–114]. However, the relaxation mechanism based on redistribution of elastic strains between the film and elastic membrane (or a region with decreased elastic constants, e.g., a region of porous silicon) cannot be dominant, even though this mechanism is suggested in the majority of publications. In fact, if the film on the substrate initially grows pseudomorphically and then relaxes elastically without the formation of MDs, the strain in this film is transferred to the compliant membrane. The final lateral size of the film after elastic relaxation should be larger than the initial size (larger by the magnitude of mismatch). Consequently, if the substrate size is reasonable, both the epitaxial film and the membrane should slide unimpeded over the inflexible substrate by large distances (by fractions of a millimeter, or by several millimeters in the case of 12-in. wafers). Despite a large body of experimental data and the analysis of it in relevant publications, sliding of an extended relaxing film over the substrate was not detected.

Typically, the interface between the membrane and substrate involves a number of various defects (steps, inclusions, impurities, and so on), which hinders the free sliding of a membrane by large distances and makes this slide impossible without detachment of the heterosystem from the inflexible substrate. The same problem also persists in the case of plastic relaxation of the membrane if the processes of introduction, glide, and interaction of dislocation half-loops are confined to the compliant ("soft") intermediate layer. The process of slide of the layer–membrane pair over the inflexible substrate should set in at different (random) sites of the substrate surface, which must inevitably result in the counterslide of separate regions and the formation of a cellular structure. In addition, the regions of perfect material are expected to alternate with folds, cracks, or highly imperfect zones.

It has been shown recently [117, 118] that relaxation of stressed films on a viscous substrate occurs via elastic extension of the film due to the film's slide over the above spacer only if the latter has a small lateral size. For example, Yin *et al*. [117], when studying the characteristics of relaxation of 30-nm-thick pseudomorphic $Ge_{0.3}Si_{0.7}$ islands connected to the Si substrate via a layer of borosilicate glass, found that the mesa islands relax in the course of annealing; this relaxation is mainly due to buckling. Relaxation of elastic strains in these islands as a result of slide of the film over the interface has been observed to prevail over buckling only at the corners of the islands with diameters ranging from 10 to 20 μm. Tezuka *et al.* [118] showed that GeSi mesa islands which were 5 μm or less in diameter and had been grown on SOI substrates relaxed completely without the formation of MDs as a result of annealing at 1000–1200°C. This is evidenced by the absence of so-called cross hatches, which are markings of dislocations' outcrop. However, extended regions (with sizes of 300 μm or larger) of GeSi films on the same substrate contain surface cross hatches, which constitutes direct evidence that these layers are plastically relaxed.

The use of continuous intermediate porous buffer layers, which are expected to act as "lubricants", is inefficient in the context of the conventional interpretation of the phenomenon of compliance. Since the porous layer is rigidly linked to the main Si substrate, such a layer cannot freely slide over the supporting substrate. The porous layer has low mechanical strength and is more likely to be used as a plastically relaxing membrane. The forming of small-sized mesa regions made of porous silicon and covered with a thin silicon membrane seems to be the most appropriate method for realizing the idea of a compliant substrate [119]. These mesa regions have a small Young's modulus (at least an order magnitude smaller than the Young's modulus of solid silicon [120]) and can accommodate strains in the heterosystem; in addition, the small sizes of these regions make elastic relaxation possible due to distortion of the crystal lattice of porous silicon, since the variation in the absolute dimensions of the film does not exceed fractions of a micrometer. Corresponding calculations were carried out by Novikov *et al*. [119]. Figure 17 illustrates the effect of the width of a porous mesa strip (L = 5, 10, and 30 μm) with a thickness h_{mesa} = 1 μm on the degree of elastic relaxation in a $Ge_{0.3}Si_{0.7}$ layer. It can be seen that the layer grown on 30-μm-wide porous Si mesa strip ($h_{mesa}/L \sim 0.03$) is virtually

unsusceptible to elastic relaxation. The "softness" of the mesa strip is caused by its porosity and begins to manifest itself only when the transverse size of the mesa-strip decreases and its height increases, i.e., when the ratio h_{mesa}/L (the aspect ratio) increases.

Thus, the mechanism of elastic relaxation in a stressed film due to the sliding of this film over a viscous substrate can be efficient only at small distances in the mesoscopic range, i.e., in the situation where the film is of the island type owing either to its formation (so-called quantum dots [121]) or if it was grown on intentionally formed mesa islands.

On the basis of the above discussion, we should consider the mechanisms of plastic relaxation in films grown on "compliant" substrates. The main contribution to a reconsideration of relaxation mechanisms in such films was made by Kästner and Gösele [113]. They returned again to plastic relaxation of strains as an alternative to elastic relaxation and suggested a modified concept of plastic relaxation; this concept consists in the following. The conventional variant of formation of MDs at the interface between a stressed film and a substrate–membrane is illustrated in Fig. 18a. If there is an amorphous or amorphized spacer near the interface, an MD sinks in this spacer (Fig. 18b); this phenomenon is caused by the fact that an MD is pulled from the film–membrane interface by forces which are similar to image forces acting on the dislocation line near the film surface. As in the case of a free surface, a dislocation leaves a step at the interface between the membrane and the "lubricating" layer (see dashed lines in Fig. 18). The additional energy caused by the origination of such a step is much lower than the MD energy at the interface (similarly to what happens in the case of a free surface). The difference between the above two energies represents the driving force for the displacement of an MD to the interface between the membrane and "lubricating" layer. Correspondingly, the work spent on the MD formation decreases.

Since the retarding forces inhibiting the propagation of threading dislocations decrease [see expression (1)], the critical thickness for the introduction of MDs decreases rather than increases, as follows from calculations based on the model of redistribution of elastic strains between the film and a compliant membrane. In this case, the velocity of motion of threading dislocations increases, which contributes to a decrease in the density of these dislocations. A similar situation is possible if porous silicon or a system of screw dislocations after the twist-bonding procedure are used as "lubricating" layers. Experimental verification of these two cases is lacking at present; therefore, these methods are listed as suggestions. In the latter case, a periodic network of strains in the vicinity of the interface between the stressed film and the membrane can serve [42, 111] as the site of origination for an ordered network of MDs, which is conducive to the annihilation of threading dislocations.

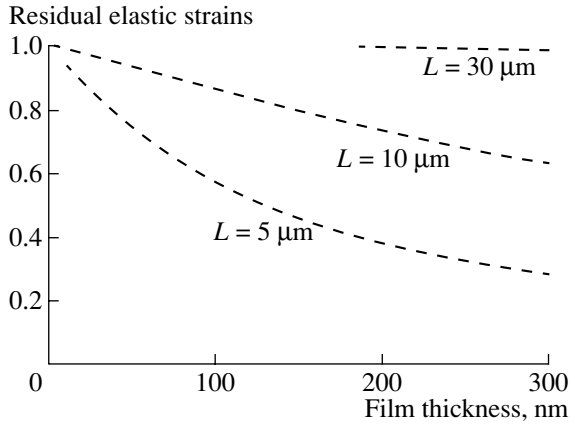

Fig. 17. The behavior of elastic relaxation of strains in GeSi film grown on a porous silicon strip with a thickness of 1 μm and a width L as a function of the film thickness [119].

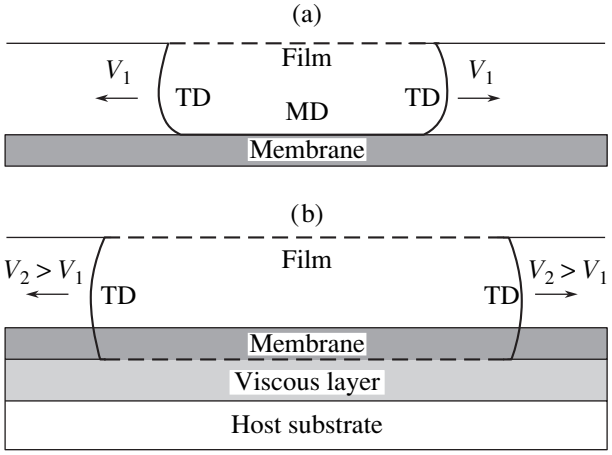

Fig. 18. "Disappearance" of a misfit dislocation in a heterostructure grown on the substrate–membrane, which is positioned on a viscous amorphous spacer (according to Kuastner and Gösele [113]). TD stands for threading dislocation; and MD, for misfit dislocation.

Recently, Pei *et al.* [122] also suggested the idea of "pulling" MDs from the interface between the stressed film and Si membrane to the interface between the Si membrane and SiO_2. By growing GaAs on SOI substrates with thinned Si membranes 100 and 200 nm thick, it was possible to attain the smallest half-width of the X-ray rocking curve (128″) for GaAs films grown on Si [122].

Thus, we return again to the concept of modifying the plastic-relaxation mechanism; this concept was outlined above in Subsection 2.4 and consists in the following. In heterosystems with intermediate layers (grown at low temperatures or subjected to ion bombardment) including viscous spacers, the velocity of propagation of threading dislocations increases. As a result, the relation (between the generation rate of MDs and the velocity of propagation of threading disloca-

Table 2. The basic characteristics of SiGe/Si heterostructure bipolar transistors

Manufacturer	Transit-time frequency for the base, f_T (GHz)	Maximum frequency of oscillation, f_{max} (GHz)	Design parameter of complementary MOS transistors (μm)
AMSINT	35	30	0.8
AMTEL	30, 50	50, 50	0.35
AMTEL	30, 50, 80	30, 70, 90	0.5
AMTEL	40, 70	50, 80	0.21
Daimler Chrysler	156	80	
Hitachi	76	180	0.25
IBM	47	50	0.35
IBM	48, 90	72, 105	0.18
Infineon	75	80	0.25
Lucent	72	116	0.25
Motorola	48, 75	100, 65	0.25
National Semiconductor	30		0.35
NEC	73	61	0.18
Philips	45	43	
ST Micro	52	71	0.35
Texas Instrument	50		0.35

tions) determined for heterosystems with a steplike transition from the substrate to the film and conducive to a high resulting density of threading dislocations (10^7–10^{10} cm^{-2}) is impaired. As a result, an opportunity arises to control each of these parameters separately, which makes it possible to reduce the threading-dislocation density to a value smaller than 10^5–10^6 cm^{-2}.

4. ELECTRICAL PROPERTIES OF SIGE FILMS ON ARTIFICIAL SUBSTRATES

First of all, we should mention the continuing and growing use of the GeSi solid solution in so-called heterostructure bipolar transistors (HBTs) based on GeSi/Si heterostructures. It is evident that heterostructures without MDs (i.e., with a pseudomorphic base) are necessary for HBTs. It is also noteworthy that the SiGe/Si-based HBTs have been brought into commercial production and more than ten leading companies are already producing (or will be producing in the near future) ultrahigh-frequency integrated circuits based on HBTs. The most important characteristics of Si–Ge HBTs are listed in Table 2 [123]. At present (May 2002), the best characteristics of SiGe/Si HBTs are f_T = 207 GHz and f_{max} = 285 GHz [124].

The set of electrical parameters for the Ge_xSi_{1-x} solid solution, which are of interest from the standpoint of device applications (as for any semiconductor), is rather wide. Undoubtedly, the most important of these parameters are the concentration and mobility of free charge carriers. The product of these quantities defines the conductance of the undepleted channel in a metal–oxide–semiconductor (MOS) transistor (or in a field-effect transistor with modulation doping) or the conductance of the base of a HBT; i.e., this product represents one of the most important characteristics of a device. If we consider optoelectronic applications of SiGe/Si heterostructures, we realize that, in this case, the most important parameter (along with the concentration and mobility of the charge carriers) is the concentration of nonradiative-recombination centers related to the point and linear defects in the structure. For example, if the dislocation density in Si and Ge single crystals is lower than 10^6 cm^{-2}, it virtually does not affect the electron and hole mobility; in contrast, the effect of this density on the lifetimes τ_n and τ_p of minority charge carriers is appreciable even if the dislocation density is as low as 10^3 cm^{-2}. Notably, $\tau_n(\tau_p) \sim N_{disl}^{-1}$ [125], whereas the absolute value of $\tau_n(\tau_p)$ depends heavily on the impurity type and the doping level.

Even more conclusive evidence of the effect of isolated dislocations on the properties of the *n*-Si/*p*-GeSi *p*–*n* heterojunction was obtained in the course of unique *in situ* studies using a transmission electron microscope [126]. Figure 19a shows the dependence of a reverse current on the number of misfit dislocations in the heterojunction plane. Dislocations were introduced into the structure (see the inset in Fig. 19) by heating the sample directly in the column of a transmitting electron microscope; the current–voltage characteristic of the structure (after cooling to 300 K) was also measured *in situ*. Similar correlations were also obtained using traditional methods (Fig. 19b) [127].

4.1. Electrons

A major contribution to the development of the technology for growing Ge_xSi_{1-x} films on an intermediate buffer layer with a varying composition was made by the team of researchers headed by Fitzgerald [30–32, 36, 59]. The fabrication of Ge_xSi_{1-x} solid-solution films with a low dislocation density ($N_{disl} \le 10^6$ cm^{-2}) was originally reported in 1991 [30]. Rapid thermal chemical-vapor deposition was used [30] to grow the films at a substrate temperature of 900°C; the composition gradient in the buffer layers amounted to 10% of the Ge content per micrometer of depth [30]. Unprecedented low densities of threading dislocations were obtained in these structures: $(4 \pm 0.5) \times 10^5$ cm^{-2} for $x = 0.23$ and $(3 \pm 2) \times 10^6$ cm^{-2} for $x = 0.5$. Shortly thereafter, high mobility of electrons in similar layers grown by MBE on a graded buffer layer was reported [128]. A two-dimensional electron gas (2DEG) was formed in a quantum well (QW) fabricated from pure silicon (a 15-nm-thick pseudomorphic Si film) using the method of modulation doping to introduce an Sb donor impurity (~10^{18} cm^{-3}) into the 40-nm-thick $Ge_{0.30}Si_{0.70}$ top layer; a 10-nm-thick spacer made of undoped solid solution with the same composition was used. According to the results of Hall effect measurements in the van der Pauw configuration (assuming that the Hall factor is equal to unity), the 2DEG density was 1.2×10^{12} cm^{-2} at 300 K and 7.8×10^{11} cm^{-2} at $T < 77$ K. The electron mobility in this gas was equal to 9600 cm^2 V^{-1} s^{-1} at 77 K and 96000 cm^2 V^{-1} s^{-1} at 4.2 K.

Over the last ten years, the number of publications concerned with the electrical properties of 2DEG and two-dimensional hole gas (2DHG) in modulation-doped SiGe/Si heterostructures has exceeded several hundred; therefore, we refer the reader to the comprehensive reviews [1, 2, 129–131] which illuminated the current state in this field up to 2000, we will mention only the most important and recent relevant publications.

The advent of artificial GeSi substrates with a low density of threading dislocations and the use of these substrates to form 2DEG and 2DHG with high mobilities of charge carriers (μ_n = 180000–200000 cm^2 V^{-1} s^{-1} at T = 4.2 K and $\mu_p \ge$ 17000 cm^2 V^{-1} s^{-1} at T = 40 K [132]) necessitated a comprehensive theoretical analysis of scattering mechanisms in the SiGe heterostructure. Monroe *et al.* [133] analyzed the following mechanisms that can limit the low-temperature mobility in a 2DEG: (i) scattering by "remote" donors, which are separated from 2DEG by a spacer made of undoped solid solution; (ii) scattering by background impurities; (iii) scattering at roughness of the heterointerface; (iv) scattering at the fluctuations of the solid-solution composition; and (v) scattering by dislocations penetrating into the channel from a completely relaxed graded-gap buffer layer. Comparison with experimental data made it possible to state [133] that threading dislocations (if their density was lower than 10^6 cm^{-2}) did not limit the mobility in 2DEG (and 2DHG) and that the first four mechanisms were the most important. It was shown [134] that, if the mean amplitude of the heterointerface roughness (to be more specific, the amplitude of the corresponding Fourier component of the roughness spectrum) exceeded 1.2 nm, the electron mobility was no higher than 10^5 cm^2 V^{-1} s^{-1} at $T = 0.4$ K in a 30-nm-thick SI QW with a 2DEG density of 5×10^{11} cm^{-2} (Fig. 20). A similar problem was considered in more detail by Yutani and Shiraki [135]; the dependence of electron mobility on the channel thickness was studied.

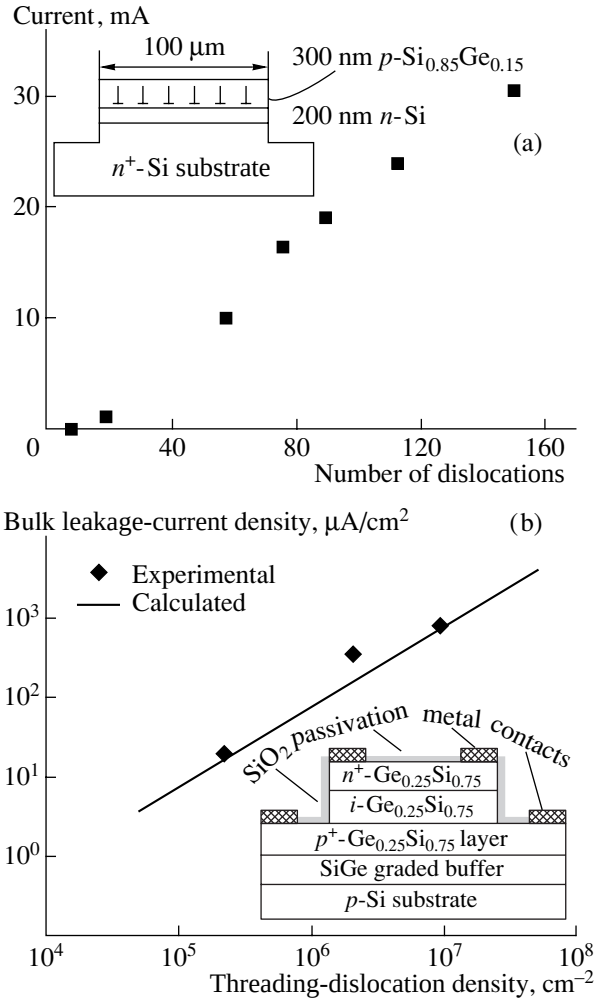

Fig. 19. (a) Dependence of reverse current through the *n*-Si/*p*-SiGe heterojunction on the number of misfit dislocations which intersect a 1-cm-long segment of the heteroboundary; the measurements were performed using an electron microscope; the heterojunction was biased by 0.5 V [123]. (b) Dependence of the leakage current in the bulk of the $Si_{0.25}Ge_{0.75}$ *p*–*i*–*n* diode (see the inset) on the density of dislocations threading from the graded-gap buffer layer [124].

Ismail *et al.* [136] noted that the role of misfit dislocations was underestimated by Monroe *et al.* [133].

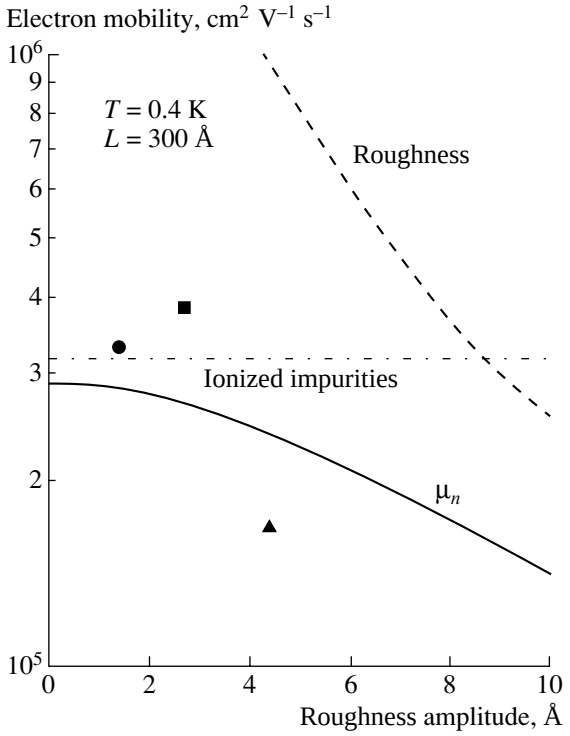

Fig. 20. The electron mobility in pseudomorphic Si films (d = 7–8 nm, n_s = 5–6 × 10^{11} cm^{-3}, T = 0.4 K) grown on thick relaxed buffer layers with the final composition of $Si_{0.7}Ge_{0.3}$ as a function of the roughness amplitude for a heteroboundary with a lateral correlation length of 30 nm. The circle, square, and triangle correspond to experimental data. Theoretical results: dashed line represents the contribution of roughness; the dash-and-dot line, the contribution of scattering by ionized impurities; and the solid line was calculated taking into account both mechanisms.

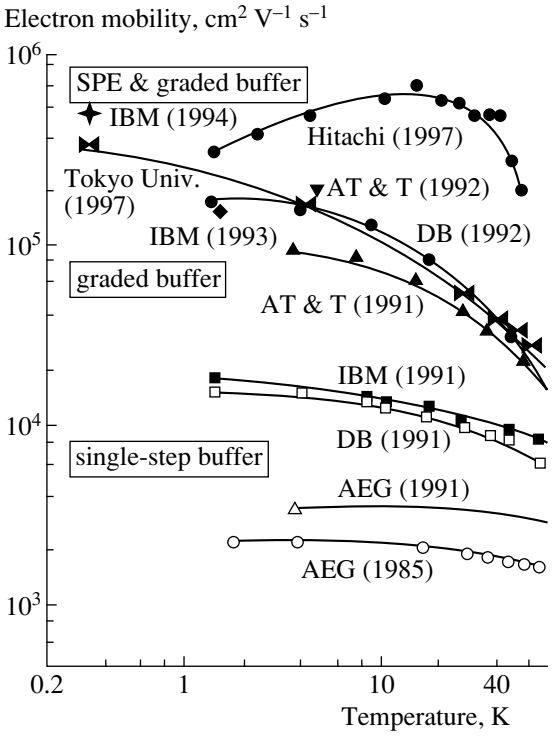

Fig. 21. Chronologically arranged collection of data on the temperature dependence of the Hall mobility for two-dimensional electron gas in pseudomorphic Si films grown on artificial GeSi substrates [135, 136].

Ismail *et al.* [136] drew attention to the fact that misfit dislocations (in addition to threading dislocations) could be found at the interface between the SiGe buffer layer and Si channel if the thickness of the channel layer exceeded the critical thickness. Using Ge_xSi_{1-x} buffer layers with a varying final composition (x = 0.34, 0.3, and 0.25) and growing Si films with subcritical and supercritical thicknesses, Ismail *et al.* [136] used transmission electron microscopy to ascertain that MDs were indeed formed at the SiGe/Si interface in accordance with the Matthews–Blakeslee model [7, 14]. The MD generation was accompanied by a decrease in electron mobility in the channel; this effect can be related to the strain field which is generated by 60° MDs and penetrates into the channel.

Ismail *et al.* [136] managed to obtain mobilities in 2DEG at a level of (300–400) × 10^3 cm^2 V^{-1} s^{-1} in structures with a pseudomorphic channel at T = 0.4–1.4 K; if the substrate was used as a back gate, the mobility was even higher (526000 cm^2 V^{-1} s^{-1} at T = 0.4 K). This result remained unsurpassed for a long time until Sugii *et al.* [137] reported an electron mobility of 800000 cm^2 V^{-1} s^{-1} at T = 15 K. The latter mobility is the highest ever achieved. In Fig. 21, we summarize the data [138, 139] on the temperature dependence of electron mobility in modulation-doped pseudomorphic Si channels on artificial GeSi substrates.

The low-temperature mobility of charge carriers is generally of no practical interest but serves as a sensitive indicator of the quality of SiGe/Si heterostructures. The charge-carrier mobility at room temperature or higher (to be more specific, from –60°C to 100°C) is important for practical applications. At these temperatures, the pattern changes significantly and scattering of electrons at the deformation potential of acoustical phonons becomes the main limitation of mobility. Corresponding calculations were carried out by Basu and Paul [140] for a specific structure (a $Si_{0.5}Ge_{0.5}/Si/Si_{0.5}Ge_{0.5}$ QW with an Si layer thickness of 6 and 9 nm on an $Si_{0.75}Ge_{0.25}$ relaxed buffer layer on Si(001) substrate). The calculations showed that the mechanism of intervalley scattering, which is dominant in bulk unstrained silicon, was found to be virtually suppressed in a stretched pseudomorphic Si film; in addition, the conductance of the channel [140] was shown to be governed by electrons with a low longitudinal effective mass (m^* = 0.19m_0). The combination of these factors in such a film makes it possible to attain an electron mobility which exceeds the mobility in bulk Si by a factor of 1.5–2 (even if the 2DEG density is equal to 1 × 10^{12} cm^{-2}). The predicted effect has been repeatedly

substantiated experimentally; an electron mobility exceeding 2000 $cm^2\ V^{-1}\ s^{-1}$ in modulation-doped pseudomorphic Si channels at room temperature is not something extraordinary (keeping in mind that electron mobility in intrinsic Si at 300 K is 1450 $cm^2\ V^{-1}\ s^{-1}$). The mobility equal to 2830 $cm^2\ V^{-1}\ s^{-1}$ reported in [141] is unprecedentedly high. In one of the recent studies in this field [142], mobility in the channel exceeded that in the bulk material also by a factor of 1.8.

4.2. Holes

The complex anisotropic three-subband structure of the valence-band top in silicon and germanium makes the problem of calculating the kinetic effects in *p*-Si and *p*-Ge extremely difficult even if strains are disregarded [143–145]. Elastic nonuniform strains (at a level of 1%) bring about a radical reconfiguration of constant-energy surfaces of the valence band. By way of example, Fig. 22 shows the constant-energy sections (E = 40 meV) of a heavy-hole band in Si subjected to uniaxial deformation in the [001] direction (panel *a*: 0.7% compressive strain; panel *b*: undeformed state; and *c*: 0.7% tensile strain). Taking into account that there are three types of holes (heavy, light, and those related to spin–orbit coupling), we find that the Hall factor (r_H) in *p*-Si can vary from 3 to 0.1 when the strain along the [001] direction varies from –1 to +1% [146]. Therefore, it is clear that calculation of the hole concentration based on the assumption that $r_H = 1$ may lead to unacceptably large errors. Theoretical approaches to calculating the hole and electron mobilities and the energy-band structure in pseudomorphic [grown on Si(100)] and unstrained Ge_xSi_{1-x} solid-solution films are outlined elsewhere (see papers [147–152] and book [153]).

Pseudomorphic SiGe films are used in device structures as materials for modulation-doped QWs with top and bottom layers composed of pure silicon or a solid solution with an increased content of germanium (Fig. 23). In this case, scattering by remote acceptors and at rough heterointerfaces is added to the mechanisms of scattering in bulk SiGe. It has been shown convincingly in a number of publications that scattering at the surface roughness is dominant at low (liquid-helium) temperatures [154]. As of 1995, the highest low-temperature mobility of holes in 2DHG has been 19820 $cm^2\ V^{-1}\ s^{-1}$ at T = 7 K in a modulation-doped "normal" (Fig. 23a) $Si/Si_{0.93}Ge_{0.07}/Si$ heterostructure (in this case, the sheet concentration of holes is $3.9 \times 10^{10}\ cm^{-2}$) [155].

The charge-carrier mobilities of 1300 $cm^2\ V^{-1}\ s^{-1}$ at 300 K and 14000 $cm^2\ V^{-1}\ s^{-1}$ at 77 K were reported [156] for 12.5-nm-thick Ge channels grown on relaxed buffer layers with a thickness of 3–5 μm and modulation-doped with Ga to a sheet hole concentration of $1 \times 10^{12}\ cm^{-2}$; the structure had a 1.2-μm-long gate and $Si_{0.4}Ge_{0.6}$ top and bottom layers. This made it possible to fabricate field-effect transistors (FETs) with the slope of the current–voltage characteristic (g_m) equal to 125 and 290 mS/mm at 300 and 77 K, respectively. It is worth noting that FETs with a graded-gap $Si_{1-x}Ge_x$ channel (with a thickness of 4.5 nm and with x varying from 0.7 to 0.55) fabricated on artificial $Si_{0.7}Ge_{0.3}$ substrates by the IBM company [157] are almost as good as the FETs reported in [156] with respect to the slope of the current–voltage characteristic; specifically, the IBM FETs had g_m = 105 and 205 mS/mm at 300 and 77 K, respectively (the channel length was 0.7 μm).

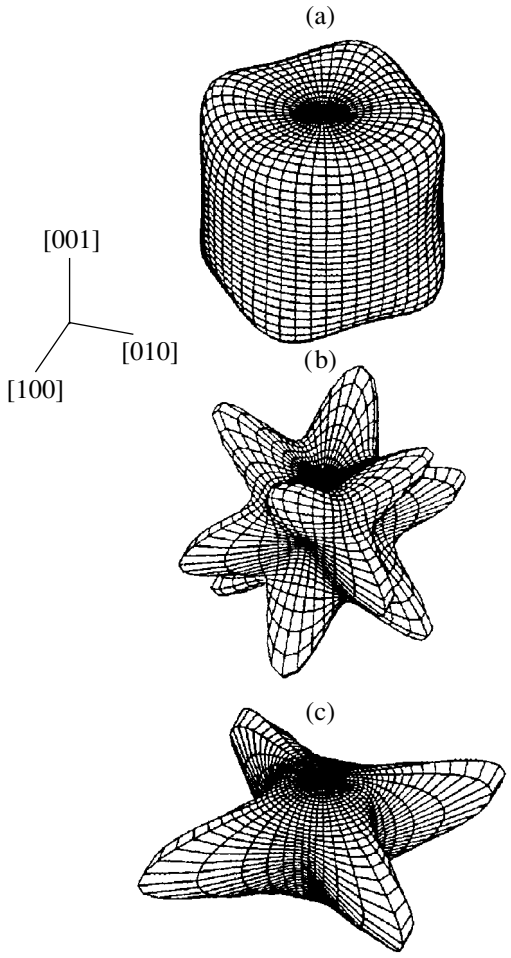

Fig. 22. Constant-energy surfaces (E = 40 meV) for the band of heavy holes in a silicon crystal: (a) a crystal stretched by 0.64% along the [001] direction; (b) an unstrained crystal; and (c) a crystal compressed by 0.64% along the [001] direction (reproduced with permission of the authors [143]).

Structures in which electrical parameters of 2DHG are measured include many layers in addition to the channel with 2DHG (see Fig. 23); these layers may affect the results of measurements. As a result, simple Hall effect measurements are inadequate to correctly determine the charge-carrier mobility. In this situation, the "mobility spectrum" method [158], which accounts for the conductivity of a parallel channel, yields more precise data on the mobility [159]. The Hall mobility

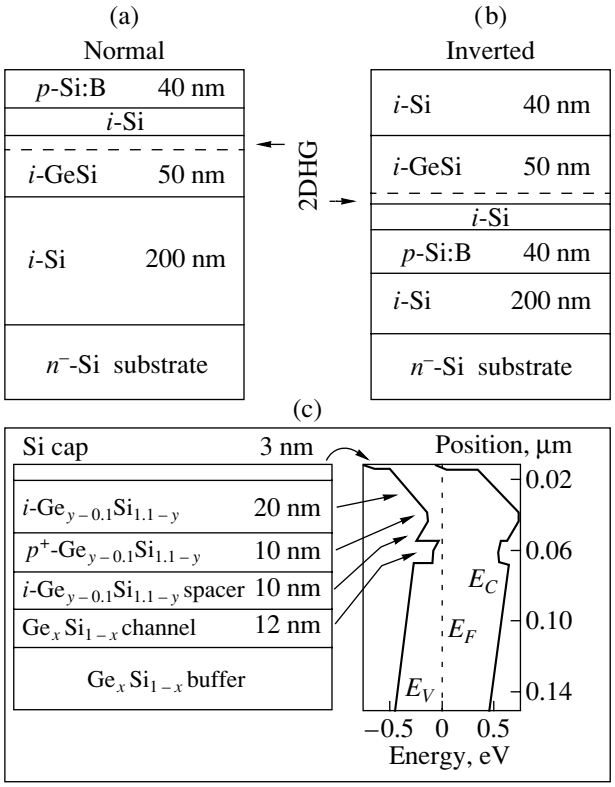

Fig. 23. Cross section of typical heterostructures used in measurements of the charge-carrier mobility in two-dimensional hole gas within pseudomorphic SiGe channels formed on Si substrates [(a) is a normal structure and (b) is an inverted structure)] and also (c) on artificial GeSi substrates [156].

can increase by 50% if parasitic *n*-type conductivities in *i*-type layers are taken into account [159].

As mentioned above, artificial SiGe substrates grown on a buffer layer with a varying composition have a number of serious drawbacks (see Subsection 2.2). One of these drawbacks is related to roughness, which tends to build up as thick (3–10 μm) buffer layers are grown: a typical amplitude of the profile can be as large as 10–15 nm. Over the last decade, numerous efforts have been made to reduce the thickness of the GeSi buffer layer, thus decreasing the roughness of its surface, while retaining an acceptable density of threading dislocations or even reducing it. The method suggested by Chen *et al.* [20] was found to be the most appropriate; this method is based on the use of Si and GeSi buffer layers grown at low temperatures. The electrical parameters of 2DHG in an SiGe/Si heterosystem fabricated using this technology represent the state of the art in this field. In what follows, we consider the relevant results.

Irisawa *et al.* [160] grew $Si_{0.33}Ge_{0.67}$/Ge/$Si_{0.33}Ge_{0.67}$ structures with Ge QWs modulation-doped with B; an $Si_{0.73}Ge_{0.27}$ buffer layer grown at low temperatures was used. The amplitude of the LT-Si surface roughness did not exceed 5 nm. Irisawa *et al.* systematically varied the thickness of the Ge channel (the growth temperature was 350°C) and obtained hole mobilities of 1300 $cm^2 V^{-1} s^{-1}$ (20 K) and 1175 $cm^2 V^{-1} s^{-1}$ (300 K) at a Ge channel thickness of 7.5 nm. A decrease in the growth temperature to 300°C made it possible to obtain a hole mobility of 1320 $cm^2 V^{-1} s^{-1}$ at 300 K. It should be mentioned that the data on hole mobilities of about 1700 $cm^2 V^{-1} s^{-1}$ (300 K) reported previously by Ueno *et al.* [161, 162] were found to be erroneous [160] as a result of incorrect Hall measurements.

Until recently, the highest hole mobility in a pseudomorphic Ge channel (1700 $cm^2 V^{-1} s^{-1}$ at 300 K with $p_s = 7.9 \times 10^{11}$ cm^{-2}) was measured in a $Ge_{0.7}Si_{0.3}$/Ge/$Ge_{0.7}Si_{0.3}$ heterostructure (d_{Ge} = 15 nm) with etched off Si substrate [163]; this mobility is still lower than that in bulk Ge. At the same time, the theory [164] unambiguously predicts a significant increase in the hole mobility in Ge films compressed or stretched along the [001] direction; as a result, the mobility exceeds that in unstrained crystal. As recently as 2002, the mobility-spectrum method was used to ascertain that the hole mobility in elastically strained Ge films is indeed higher than the mobility in an unstressed bulk crystal [165]. Relaxed $Si_{0.33}Ge_{0.67}$ buffer layers were grown in two stages [165]. First, a 50-nm-thick Si layer was formed at 400°C on *n*-Si substrate with a resistivity of 5–10 Ω cm; a 500-nm-thick $Si_{0.73}Ge_{0.27}$ film was then grown on this layer at 600°C. Next, a 50-nm-thick layer with the same composition was grown at 300°C and overgrown at 500°C with a 500-nm-thick $Si_{0.33}Ge_{0.67}$ layer. Finally, a SiGe film doped with B to a concentration of $\sim 2 \times 10^{18}$ cm^{-3} was grown epitaxially on top of the above complex system of buffer layers; a 20-nm-thick Ge active layer was then grown on an undoped 20-nm-thick spacer. The hole mobility in the Ge layer at room temperature was 2940 $cm^2 V^{-1} s^{-1}$, with the sheet concentration of the charge carriers being equal to 5.11×10^{11} cm^{-2}. It is clear that the technology used is quite efficient, so that the correctly measured hole mobility in pseudomorphic Ge film exceeds the mobility in a bulk Ge crystal by 55% (the latter mobility is the highest among all semiconductors). A hole mobility of 2700 $cm^2 V^{-1} s^{-1}$ in a similar structure was also attained owing to doping of $Si_{0.3}Ge_{0.7}$ buffer layers with Sb [166]. Lastly, we note that a high hole mobility in an SiGe/Si heterosystem not only improves the high-frequency characteristics of transistors but also facilitates the solution of the so-called "short channel" problem [167, 168].

4.3. Summary

Thus, it is experimentally ascertained at present that the electrical parameters of 2DEG and 2DHG in pseudomorphic Si, SiGe, and Ge layers grown on artificial SiGe substrates, which are optimized with respect to the structure and surface morphology, excel the kinetic properties of electrons and holes in unstrained

crystals. Therefore, we may expect that these structures will be widely used in the near future in the electronics of superlarge-scale integration. At the same time, it is also clear that much effort is still needed in order to develop a commercial technology for the fabrication of complementary MOSs; research in this field is being actively pursued [169–171]. Leading researchers at IBM emphasized at the IEEE International Solid-Circuit Conference [172] that the crucial factor for the commercial success of SiGe/Si-based HBTs is the fact that, in their production, it is possible to use the same equipment and the same technological processes as those used in the production of Si integrated circuits. It is not inconceivable that the use of artificial SiGe substrates will make it possible to attain real success in the development of relevant FETs.

5. CONCLUSION

As a result of more than 20 years of studies of the structural characteristics of plastically relaxing constant-composition GeSi layers grown under conventional conditions, it became clear that the density of threading dislocations in these films is unacceptably high. In our opinion, this is caused by the virtually identical dependences of the density of generated misfit dislocations (MDs) and the velocities of propagation of their threading segments in GeSi heterostructures grown under conventional growth conditions on mismatch stresses. In order to reduce the MD generation rate and, at the same time, preserve an acceptable propagation velocity of the already existing threading dislocation segments, a method for growing graded buffer layers has been suggested; the first encouraging results have been obtained using this method. New methods for film growth, which were developed recently, made it possible to extend the separate effect on the generation and propagation (including annihilation) of MDs; as a result, the crystalline quality of the grown GeSi films improved.

Over the last decade, intensive studies of the growth processes of heterostructures were replaced by practical applications of these structures. As a result of this development, we have observed both unprecedentedly high room-temperature mobilities (exceeding those in bulk crystals) of electrons and holes in 2DEG and 2DHG in Si/GeSi heterojunctions and large-scale applications of these structures in the development of FET metal–insulator–semiconductor transistors.

With respect to the so-called "compliant" substrates, it can be considered proven that the mechanism of elastic relaxation in a stressed film due to the sliding of the film over a viscous substrate is effective only at small distances in the mesoscopic range when the film is of the island type. Relaxation of stresses in extended films occurs via the introduction of misfit dislocations and glide of their threading segments.

We still have some unresolved problems. These include

(i) the remaining ambiguity in choosing a specific method for growing the heterostructures with artificial substrates (some of these methods have still not been adequately tested);

(ii) a deficit in experimental data on the determination of specific mechanisms responsible for a decrease in the density of threading dislocations in such heterostructures; and

(iii) the lack of a widely acceptable technology for forming "compliant" substrate.

ACKNOWLEDGMENTS

This study was supported by the Russian Foundation for Basic Research (project nos. 00-02-17461 and 00-02-17638); the Program for Support of Leading Scientific Schools in the Russian Federation (grant no. 00-15-96806), the program "Promising Technologies and Devices for Microelectronics and Nanoelectronics"; and state contracts from the Ministry of Industry, Science, and Technologies of the Russian Federation (contract nos. 37.029.1.1.0032 and 37.039.1.1.0041). This study was also supported in part in the framework of the federal special program "Integration of Science and Higher Education in Russia for 2002–2006" through Novosibirsk State University and the Scientific Training Center "Technology and Physics of Semiconductor Nanostructures" (contract no. I0765).

REFERENCES

1. F. Schäffler, Semicond. Sci. Technol. **12**, 1515 (1997); Thin Solid Films **321**, 1 (1998).
2. D. J. Paul, Thin Solid Films **321**, 172 (1998).
3. Yu. B. Bolkhovityanov, O. P. Pchelyakov, and S. I. Chikichev, Usp. Fiz. Nauk **171**, 689 (2001) [Phys. Usp. **44**, 655 (2001)].
4. D. C. Houghton, J. Appl. Phys. **70**, 2136 (1991).
5. A. Fisher, Appl. Phys. Lett. **64**, 1218 (1994).
6. V. T. Gillard, W. D. Nix, and L. B. Freund, J. Appl. Phys. **76**, 7280 (1994).
7. J. W. Matthews and A. E. Blakeslee, J. Cryst. Growth **27**, 118 (1974).
8. E. A. Fitzgerald, Mater. Sci. Rep. **7**, 92 (1991).
9. H. Alexander, in *Dislocations in Solids*, Ed. by F. R. N. Nabarro (Elsevier, New York, 1986), Vol. 7, p. 113.
10. I. Yonenaga, Phys. Status Solidi A **171**, 41 (1999).
11. L. B. Freund, J. Appl. Phys. **68**, 2073 (1990).
12. S. M. Hu, J. Appl. Phys. **69**, 7901 (1991).
13. D. C. Houghton, C. J. Gibbings, C. G. Tuppen, *et al.*, Appl. Phys. Lett. **56**, 460 (1990).
14. J. W. Matthews, J. Vac. Sci. Technol. **12**, 126 (1975).
15. M. L. Green, B. E. Weir, D. Brasen, *et al.*, J. Appl. Phys. **69**, 745 (1991).

16. R. Hull, J. C. Bean, and C. Buescher, J. Appl. Phys. **66**, 5837 (1989).
17. E. P. Kvam, D. M. Maher, and C. J. Humphreys, J. Mater. Res. **5**, 1900 (1990).
18. V. I. Vdovin, Phys. Status Solidi A **171**, 239 (1999).
19. P. M. Mooney, F. K. LeGoues, J. Tersoff, and J. O. Chu, J. Appl. Phys. **75**, 3968 (1994).
20. H. Chen, L. W. Guo, Q. Cui, *et al.*, J. Appl. Phys. **79**, 1167 (1996).
21. K. K. Linder, F. C. Zhang, J.-S. Rieh, *et al.*, Appl. Phys. Lett. **70**, 3224 (1997).
22. J. H. Li, C. S. Peng, Y. Wu, *et al.*, Appl. Phys. Lett. **71**, 3132 (1997).
23. C. S. Peng, Z. Y. Zhao, H. Chen, *et al.*, Appl. Phys. Lett. **72**, 3160 (1998).
24. J. H. Li, C. S. Peng, Z. H. Mai, *et al.*, J. Appl. Phys. **86**, 1292 (1999).
25. P. I. Gaiduk, A. N. Larsen, and J. L. Hansen, Thin Solid Films **367**, 120 (2000).
26. Yu. B. Bolkhovityanov, A. K. Gutakovskii, V. I. Mashanov, *et al.*, Thin Solid Films **392**, 98 (2001).
27. Yu. B. Bolkhovityanov, A. K. Gutakovskii, V. I. Mashanov, *et al.*, J. Appl. Phys. **91**, 4710 (2002).
28. M. S. Abrahams, L. R. Weisberg, C. J. Buiocchi, and J. Blanc, J. Mater. Sci. **4**, 223 (1969).
29. J. W. Burd, Trans. Metall. Soc. AIME **245**, 571 (1969).
30. E. A. Fitzgerald, Y.-H. Xie, M. L. Green, *et al.*, Appl. Phys. Lett. **59**, 811 (1991).
31. S. B. Samavedam and E. A. Fitzgerald, J. Appl. Phys. **81**, 3108 (1997).
32. E. A. Fitzgerald, M. T. Currie, S. B. Samavedam, *et al.*, Phys. Status Solidi A **171**, 227 (1999).
33. J. Tersoff, Appl. Phys. Lett. **62**, 693 (1993).
34. S. Y. Shiryaev, J. L. Hansen, A. N. Larsen, *et al.*, Phys. Rev. B **52**, 15 881 (1995).
35. U. König, Phys. Scr. T **68**, 90 (1996).
36. M. T. Currie, S. B. Samavedam, T. A. Langdo, *et al.*, Appl. Phys. Lett. **72**, 1718 (1998).
37. E. Kasper, K. Lyutovich, V. Bauer, and M. Oemie, Thin Solid Films **336**, 319 (1998).
38. J. Kuchenbecker, H. Kibbewl, P. Muthsom, and U. König, Thin Solid Films **389**, 146 (2001).
39. S. I. Romanov, V. I. Mashanov, L. V. Sokolov, *et al.*, Appl. Phys. Lett. **75**, 4118 (1999).
40. B. Holländer, S. Mantl, R. Liedtke, *et al.*, Nucl. Instrum. Methods Phys. Res. B **148**, 200 (1999).
41. H. Trinkaus, B. Holländer, St. Rongen, *et al.*, Appl. Phys. Lett. **76**, 3552 (2000).
42. T. Y. Tan and U. Gösele, Appl. Phys. A **64**, 631 (1997).
43. D. D. Perovic, G. C. Weatherly, J.-M. Baribeau, and D. C. Houghton, Thin Solid Films **183**, 141 (1989).
44. Y. H. Luo, J. Wan, R. L. Forrest, *et al.*, J. Appl. Phys. **89**, 8279 (2001).
45. J. W. Matthews, A. E. Blakeslee, and S. Mader, Thin Solid Films **33**, 253 (1976).
46. S. M. Bedair, T. P. Humphreys, N. A. El-Masry, *et al.*, Appl. Phys. Lett. **49**, 942 (1986).
47. P. L. Gourley, T. J. Drummond, and B. L. Doyle, Appl. Phys. Lett. **49**, 1101 (1986).
48. I. J. Fritz, P. L. Gourley, L. R. Dawson, and J. E. Schirber, Appl. Phys. Lett. **53**, 1098 (1988).
49. T. Kawai, H. Yonezu, Y. Ogasawara, *et al.*, Appl. Phys. Lett. **63**, 2067 (1993).
50. N. El-Masry, J. C. L. Tarn, T. P. Humphreys, *et al.*, Appl. Phys. Lett. **51**, 1608 (1987).
51. M. Yamaguchi, M. Sugo, and Y. Itoh, Appl. Phys. Lett. **54**, 2568 (1989).
52. S. F. Fang, K. Adomi, S. Iyer, *et al.*, J. Appl. Phys. **68**, R31 (1990).
53. J. W. Matthews, Philos. Mag. **13**, 1207 (1966).
54. Y. Takano, M. Hisaka, N. Fujii, *et al.*, Appl. Phys. Lett. **73**, 2917 (1998).
55. A. Sakai, K. Sugimoto, T. Yamamoto, *et al.*, Appl. Phys. Lett. **79**, 3398 (2001).
56. G. L. Luo, P. Y. Chen, X. F. Lin, *et al.*, Appl. Phys. A **70**, 449 (2000).
57. H. J. Osten and E. Bugiel, Appl. Phys. Lett. **70**, 2813 (1997).
58. D. Li, C. Huang, B. Cheng, *et al.*, J. Cryst. Growth **213**, 308 (2000).
59. C. W. Leitz, M. T. Currie, A. Y. Kim, *et al.*, J. Appl. Phys. **90**, 2730 (2001).
60. J. L. Liu, C. D. Moore, G. D. U'Ren, *et al.*, Appl. Phys. Lett. **75**, 1586 (1999).
61. J. L. Liu, K. L. Wang, C. D. Moore, *et al.*, Thin Solid Films **369**, 121 (2000).
62. J. L. Liu, S. Tong, Y. H. Luo, *et al.*, Appl. Phys. Lett. **79**, 3431 (2001).
63. K. Samonji, H. Yonezu, Y. Takaji, *et al.*, Appl. Phys. Lett. **69**, 100 (1996).
64. T. Obata, K. Komeda, T. Nakao, *et al.*, J. Appl. Phys. **81**, 199 (1997).
65. M. M. Rahman, H. Matada, T. Tambo, and C. Tatsuyama, Appl. Surf. Sci. **175–176**, 6 (2001).
66. M. M. Rahman, H. Matada, T. Tambo, and C. Tatsuyama, J. Appl. Phys. **90**, 202 (2001).
67. A. Sakai, T. Tatsumi, and K. Aoyama, Appl. Phys. Lett. **71**, 3510 (1997).
68. H. Lafontaine, B. F. Mason, S. J. Rolfe, *et al.*, J. Vac. Sci. Technol. B **16**, 599 (1998).
69. D. Dentel, J. L. Bischoff, L. Kubler, *et al.*, J. Cryst. Growth **191**, 697 (1998).
70. S. Bozzo, J.-L. Lazzari, B. Holländer, *et al.*, Appl. Surf. Sci. **164**, 35 (2000).
71. W.-X. Ni, K. Lyutovich, J. Alami, *et al.*, J. Cryst. Growth **227–228**, 756 (2001).
72. G. Bai, M.-A. Nicolet, C. H. Chern, and K. L. Wang, J. Appl. Phys. **75**, 4475 (1994).
73. R. Beanland, J. Appl. Phys. **72**, 4031 (1992); J. Appl. Phys. **77**, 6217 (1995).
74. M. Bauer, K. Lyutovich, M. Oehme, and E. Kasper, Thin Solid Films **369**, 152 (2000).
75. P. Asoka-Kumar, H.-J. Gossmann, F. C. Unterwald, *et al.*, Phys. Rev. B **48**, 5345 (1993).
76. A. P. Knights, R. M. Gwilliam, B. J. Sealy, *et al.*, J. Appl. Phys. **89**, 76 (2001).
77. T. Ueno, T. Irisawa, and Y. Shiraki, J. Cryst. Growth **227**, 761 (2001).

78. R. Hall and J. C. Bean, J. Vac. Sci. Technol. A **7**, 2580 (1989).
79. L. Fedina, A. Gutakovskii, A. Aseev, *et al.*, Philos. Mag. A **77**, 423 (1998).
80. Y. Yamashita, F. Jyobe, Y. Kamiura, and K. Maeda, Phys. Status Solidi A **171**, 27 (1999).
81. J. P. Hirth and J. Lothe, *Theory of Dislocations*, 2nd ed. (Wiley, New York, 1982; Atomizdat, Moscow, 1972).
82. S. Öberg, P. K. Sitch, R. Jones, and M. I. Heggie, Phys. Rev. B **51**, 13138 (1995).
83. R. Hull, E. A. Stach, R. Tromp, *et al.*, Phys. Status Solidi A **171**, 133 (1999).
84. H. Gottschalk, N. Hiller, S. Sauerland, *et al.*, Phys. Status Solidi A **138**, 547 (1993).
85. M. Pasemann, D. Hoehl, A. L. Aseev, and O. P. Pchelyakov, Phys. Status Solidi A **80**, 135 (1983).
86. D. J. Eaglasham, P. A. Stolk, H.-J. Gossmann, and J. M. Poate, Appl. Phys. Lett. **65**, 2305 (1994).
87. J. Li and K. S. Jones, Appl. Phys. Lett. **73**, 3748 (1998).
88. L. Fedina, O. I. Lebedev, G. Van Tendello, *et al.*, Phys. Rev. B **61**, 10 336 (2000).
89. J. S. Speck, M. A. Brever, G. Beltz, *et al.*, J. Appl. Phys. **80**, 3808 (1996).
90. Yu. A. Tkhorik and L. S. Khazan, *Plastic Deformation and Misfit Dislocations in Heteroepitaxial Systems* (Naukova Dumka, Kiev, 1983), p. 135.
91. Y. H. Lo, Appl. Phys. Lett. **59**, 2311 (1991).
92. F. K. LeGoues, A. R. Powell, and S. S. Iyer, J. Appl. Phys. **75**, 7240 (1994).
93. C. Carter-Coman, R. Bicknell-Tassius, A. S. Brown, and Nan Marie Jokerst, Appl. Phys. Lett. **70**, 1754 (1997).
94. K. Brunner, H. Dobler, G. Abstreiter, *et al.*, Thin Solid Films **321**, 245 (1998).
95. Z. Yang, J. Alperin, W. I. Wang, *et al.*, J. Vac. Sci. Technol. B **16**, 1489 (1998).
96. D. M. Hansen, P. D. Moran, K. A. Dunn, *et al.*, J. Cryst. Growth **195**, 144 (1998).
97. P. D. Moran, D. M. Hansen, R. J. Matyi, *et al.*, Appl. Phys. Lett. **75**, 1559 (1999).
98. F. Y. Huang, M. A. Chu, M. O. Tanner, *et al.*, Appl. Phys. Lett. **76**, 2680 (2000).
99. Y. H. Luo, J. L. Liu, G. Jin, *et al.*, Appl. Phys. Lett. **78**, 1219 (2001).
100. G. Taraschi, T. A. Langdo, M. T. Currie, *et al.*, J. Vac. Sci. Technol. B **20**, 725 (2002).
101. F. E. Ejeckam, M. L. Seaford, Y. H. Lo, *et al.*, Appl. Phys. Lett. **71**, 776 (1997).
102. G. Patriarche, C. Meriadec, G. LeRoux, *et al.*, Appl. Surf. Sci. **164**, 15 (2000).
103. St. Senz, G. Kästner, U. Gösele, and V. Gottschalch, Appl. Phys. Lett. **76**, 703 (2000).
104. G. Patriarche and E. Le Bourhis, Appl. Surf. Sci. **178**, 134 (2001).
105. L. B. Freund and W. D. Nix, Appl. Phys. Lett. **69**, 173 (1996).
106. W. A. Jesser, J. H. van der Merwe, and P. M. Stoop, J. Appl. Phys. **85**, 2129 (1999).
107. T. Y. Zhang and Y. J. Su, Appl. Phys. Lett. **74**, 1689 (1999).
108. Y. Obayashi and K. Shintani, J. Appl. Phys. **88**, 105 (2000).
109. D. Zubia, S. D. Hersee, and T. Khraishi, Appl. Phys. Lett. **80**, 740 (2002).
110. A. S. Brown, J. Vac. Sci. Technol. B **16**, 2308 (1998).
111. G. Kästner, U. Gösele, and T. Y. Tan, Appl. Phys. A **66**, 13 (1998).
112. A. Bourret, Appl. Surf. Sci. **164**, 3 (2000).
113. G. Kästner and U. Gösele, J. Appl. Phys. **88**, 4048 (2000).
114. K. Vanhollebeke, I. Moerman, P. Van Daele, and P. Demeester, Prog. Cryst. Growth Charact. Mater. **41**, 1 (2000).
115. G. A. Antypas and J. Edgecumbe, Appl. Phys. Lett. **26**, 371 (1975).
116. Compd. Semicond. **7**, 47 (2001).
117. H. Yin, R. Huang, K. D. Hobart, *et al.*, J. Appl. Phys. **91**, 9716 (2002).
118. T. Tezuka, N. Sugiyama, S. Takagi, and T. Kawakubo, Appl. Phys. Lett. **80**, 3560 (2002).
119. P. L. Novikov, Yu. B. Bolkhovityanov, O. P. Pchelyakov, *et al.*, Semicond. Sci. Technol. **18**, 39 (2003).
120. D. Bellet, in *Properties of Porous Silicon*, Ed. by L. Canham (INSPEC, London, 1997), p. 127.
121. O. P. Pchelyakov, Yu. B. Bolkhovityanov, A. V. Dvurechenskiĭ, *et al.*, Fiz. Tekh. Poluprovodn. (St. Petersburg) **34**, 1281 (2000) [Semiconductors **34**, 1229 (2000)].
122. C. W. Pei, J. B. Héroux, J. Sweet, *et al.*, J. Vac. Sci. Technol. B **20**, 1196 (2002).
123. J. Berntgen, A. Shueppen, P. Maier, *et al.*, Mater. Sci. Eng. B **89**, 13 (2002).
124. B. Jagannathan, M. Khater, F. Pagette, *et al.*, IEEE Electron Device Lett. **23**, 258 (2002).
125. A. T. Vink, C. J. Werkhoeven, and C. van Opdorp, in *Proceedings of Topical Conference on Characterization Techniques for Semiconductor Materials and Science* (Electrochemical Society Spring Meeting, Seattle, 1978).
126. F. M. Ross, R. Hall, D. Bahnk, *et al.*, J. Vac. Sci. Technol. B **10**, 2008 (1992).
127. L. M. Giovane, H.-C. Luan, A. M. Agarwal, and L. C. Kimerling, Appl. Phys. Lett. **78**, 541 (2001).
128. Y.-J. Mii, Y.-H. Xie, E. A. Fitzgerald, *et al.*, Appl. Phys. Lett. **59**, 1611 (1991).
129. U. König, M. Glück, and G. Höck, J. Vac. Sci. Technol. B **16**, 2609 (1998).
130. T. E. Whall and E. H. C. Parker, Thin Solid Films **368**, 297 (2000).
131. H.-J. Herzog, T. Hackbarth, G. Höck, *et al.*, Thin Solid Films **380**, 36 (2000).
132. E. A. Fitzgerald, Y.-H. Xie, D. Monroe, *et al.*, J. Vac. Sci. Technol. B **10**, 1807 (1992).
133. D. Monroe, Y.-H. Xie, E. A. Fitzgerald, *et al.*, J. Vac. Sci. Technol. B **11**, 1731 (1993).
134. R. M. Feenstra, M. A. Lutz, F. Stern, *et al.*, J. Vac. Sci. Technol. B **13**, 1608 (1995).

135. A. Yutani and Y. Shiraki, J. Cryst. Growth **175–176**, 504 (1997).
136. K. Ismail, F. K. LeGoues, K. L. Saenger, *et al.*, Phys. Rev. Lett. **73**, 3447 (1994).
137. N. Sugii, K. Nakagawa, Y. Kimura, *et al.*, Semicond. Sci. Technol. A **13**, 140 (1998).
138. M. Miyao, K. Nakagawa, N. Sugii, and S. Yamaguchi, Microelectron. Eng. **47**, 221 (1999).
139. K. Ismail, F. K. LeGoues, K. L. Saenger, *et al.*, Phys. Rev. Lett. **73**, 3447 (1994).
140. P. K. Basu and S. K. Paul, J. Appl. Phys. **71**, 3617 (1992).
141. K. Ismail, S. F. Nelson, J. O. Chu, and B. S. Meyerson, Appl. Phys. Lett. **63**, 660 (1993).
142. M. T. Currie, C. W. Leitz, T. A. Langdo, *et al.*, J. Vac. Sci. Technol. B **19**, 2268 (2001).
143. F. L. Madarazs and F. Szmulowicz, Phys. Rev. B **24**, 4611 (1981).
144. F. Szmulowicz, Phys. Rev. B **28**, 5943 (1983).
145. F. Szmulowicz, Phys. Rev. B **34**, 4031 (1986).
146. J. E. Dijkstra and W. Th. Wenckebach, J. Appl. Phys. **85**, 1587 (1999).
147. J. M. Hinckley and J. Singh, Phys. Rev. B **41**, 2912 (1990).
148. T. Manku and A. Nathan, Phys. Rev. B **43**, 12634 (1991).
149. T. Manku and A. Nathan, IEEE Electron Device Lett. **12**, 704 (1991).
150. T. Manku and A. Nathan, IEEE Trans. Electron Devices **39**, 2082 (1992).
151. S. K. Chun and K. L. Wang, IEEE Trans. Electron Devices **39**, 2153 (1992).
152. Y. Fu, K. J. Grahn, and M. Willander, IEEE Trans. Electron Devices **41**, 26 (1994).
153. *Physical Models of Semiconductor Quantum Devices*, Ed. by Ying Fu and M. Willander (Kluwer Academic, Boston, 1999).
154. T. E. Whall, J. Cryst. Growth **157**, 353 (1995).
155. D. W. Smith, C. J. Emeleus, R. A. Kubiak, *et al.*, Appl. Phys. Lett. **61**, 1453 (1992).
156. U. König and F. Schäffler, IEEE Electron Device Lett. **14**, 205 (1993).
157. M. Arafa, P. Fay, K. Ismail, *et al.*, IEEE Electron Device Lett. **17**, 124 (1996).
158. W. A. Beck and J. R. Anderson, J. Appl. Phys. **62**, 541 (1987).
159. G. Höck, M. Glück, T. Hackbath, *et al.*, Thin Solid Films **336**, 141 (1998).
160. T. Irisawa, H. Miura, T. Ueno, and Y. Shiraki, Jpn. J. Appl. Phys. **40**, 2694 (2001).
161. T. Ueno, T. Irisawa, and Y. Shiraki, Physica E (Amsterdam) **7**, 790 (2000).
162. T. Ueno, T. Irisawa, Y. Shiraki, *et al.*, Thin Solid Films **369**, 320 (2000).
163. S. Madhavi, V. Venkataraman, and Y. H. Xie, J. Appl. Phys. **89**, 2497 (2001).
164. M. V. Fischetti and S. E. Laux, J. Appl. Phys. **80**, 2234 (1996).
165. M. Myronov, T. Irisawa, O. A. Mironov, *et al.*, Appl. Phys. Lett. **80**, 3117 (2002).
166. T. Irisawa, S. Tokumitsu, T. Hattori, *et al.*, Appl. Phys. Lett. **81**, 847 (2002).
167. P. W. Li and W. M. Liao, Solid-State Electron. **46**, 39 (2002).
168. P. W. Li and W. M. Liao, J. Vac. Sci. Technol. A **20**, 1030 (2002).
169. M. T. Currie, C. W. Leitz, T. A. Langdo, *et al.*, J. Vac. Sci. Technol. B **19**, 2268 (2001).
170. C. W. Leitz, M. T. Currie, M. L. Lee, *et al.*, Appl. Phys. Lett. **79**, 4246 (2001).
171. M. Myronov, P. J. Phillips, T. E. Whall, and E. H. C. Parker, Appl. Phys. Lett. **80**, 3557 (2002).
172. S. Subbanna, D. Ahlgren, D. Harame, and B. Meyerson, in *Proceedings of IEEE International Solid-State Circuits Conference* (1999), Paper MP 4.1.

Translated by A. Spitsyn

Semiconductors, Vol. 37, No. 5, 2003, pp. 519–522. Translated from Fizika i Tekhnika Poluprovodnikov, Vol. 37, No. 5, 2003, pp. 539–542.

ATOMIC STRUCTURE AND NONELECTRONIC PROPERTIES OF SEMICONDUCTORS

Propagation of Nonequilibrium Phonons in Single-Crystal ZnTe

T. I. Galkina, A. Yu. Klokov, A. I. Sharkov*, Yu. V. Korostelin, and V. V. Zaĭtsev

Lebedev Physical Institute, Russian Academy of Sciences, Leninskiĭ pr. 53, Moscow, 119991 Russia

**e-mail: shark@sci.lebedev.ru*

Submitted October 2, 2002; accepted for publication October 2, 2002

Abstract—Propagation of nonequilibrium acoustic phonons in ZnTe single crystals at helium temperature was studied with phonons being both optically generated and produced by a metal-film heater. Experiments with [110] ZnTe allowed for the detection of the arrival of longitudinal and transverse acoustic phonons, which are particularly well resolved when generated by a heated metal film. A bolometer also detected emission of ZnTe material with a time constant $\tau \sim 90$ ns, which can apparently be attributed to the luminescence of oxygen complexes, because the lifetimes of other complexes and bound excitons are substantially shorter.

1. INTRODUCTION

The II–VI compounds have aroused interest in connection with their application as film photodetectors in the visible region of the spectrum since the middle of the last century; this was followed by their wide application in acoustoelectronics, optoelectronics, and laser technology. Thin [110]-oriented ZnTe waters have recently found use as coherent electro-optical sensors with a detection band width of up to 40–50 THz [1, 2].

This situation calls for a comprehensive study of the thermal properties of ZnTe to achieve good heat dissipation, which, in turn, would permit one to reduce degradation of ZnTe-based devices and, hopefully, to improve their response times.

Data on nonequilibrium heat transport in ZnTe are lacking in the literature, except for [3]—a communication that gave preliminary results of the first investigation in this field. The goal of this study was to gain insight into the propagation pattern of nonequilibrium acoustic phonons generated by various means in ZnTe single crystals.

2. EXPERIMENTAL

The propagation of nonequilibrium phonons was studied in samples of single-crystal ZnTe ($\rho \sim 10$–$20\ \Omega$ cm) in the form of [110]-oriented wafers with a thickness of 970 μm and surface area of 6×6 mm^2 [4].

We additionally measured the photoluminescence (PL) of the sample whose thermal properties had been studied.

The PL spectra were measured at 2 K. The sample was optically pumped with an argon laser emitting 2.41-eV photons (514.5 nm). The spectrum was analyzed with a double-grating monochromator providing a resolution of 0.1 meV. The photomultiplier signals were fed to a narrow-band amplifier with a lock-in detector.

Figure 1 shows a PL spectrum of a ZnTe single crystal measured at $T = 2$ K. In addition to the intrinsic radiation due to the free exciton (*FE*, *FE*-LO), the PL spectrum includes lines which are due to recombination of excitons bound to neutral donors (D^0X) and four acceptors A^0X: Cu, Li, Ag, and *k* (an unidentified acceptor)

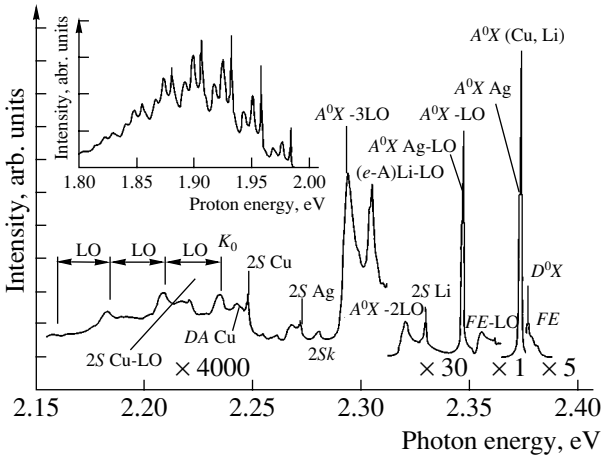

Fig. 1. Photoluminescence spectrum of ZnTe obtained at $T = 2$ K, argon laser ($\lambda = 514.5$ nm) excitation density 10 W/cm^2. Inset shows emission spectrum of the exciton bound to O_{Te}.

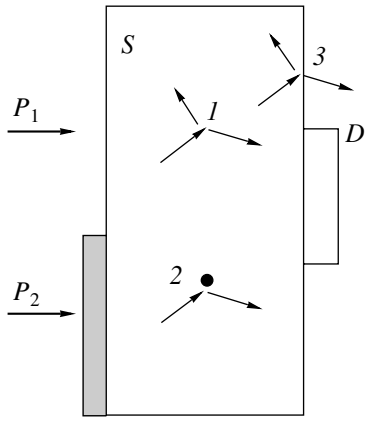

Fig. 2. Main processes involving the generated acoustic phonons: (*1*) spontaneous decay, (*2*) elastic scattering, and (*3*) sample boundary effects.

[5]. In the latter case, the spectrum also includes, in addition to the main A^0X lines (where A = Cu, Li, Ag), the so-called two-hole transitions denoted in Fig. 1 by $2S\,A$ (A = Cu, Li, Ag, k). The long-wavelength part of the spectrum contains a structure of four lines, in which a short-wavelength line (K_0) is caused by a zero-phonon transition and the three other lines represent LO-phonon replicas of K_0. According to [6], K_0 originates from the emission of a complex defect containing a Zn vacancy.

The inset in Fig. 1 presents a PL spectrum around 1.9 eV, which is due to the emission of excitons bound to the isoelectronic impurity O_{Te} (oxygen in the Te sublattice) [7]. The peak emission intensity is about 10^4 times lower than the intensity of the A^0X line. However, unlike the narrow A^0X line, the O_{Te} spectrum extends over a wide spectral range, which is caused by strong electron–phonon coupling (LO, LA, and TA phonons are emitted) [7]. This spectrum is typical of bulk ZnTe crystals (see, e.g., the cathodoluminescence spectrum of samples grown in an argon environment [4]).

The propagation of nonequilibrium phonons in ZnTe was studied by the heat pulse technique. The schematic of the experiment and the main processes occurring with nonequilibrium phonons are shown in Fig. 2. Nonequilibrium phonons are generated in sample S by pulsed excitation. In our experiments, the excitation was effected by light with a photon energy greater than the band gap of the material under study ($P1$); in this situation, phonons are generated directly in the sample as a result of both the cooling of hot carriers and nonradiative recombination, or via heating by a laser pulse of a metal film deposited on the sample ($P2$). In their propagation through the sample, the generated phonons undergo spontaneous anharmonic decay (*1*), elastic scattering by lattice defects (*2*), and so on. Upon being absorbed in detector D, they produce a signal. The specific processes occurring with the nonequilibrium phonons and the mode of their propagation are derived from the shape of the time-resolved signal.

We used photoexcitation of the sample surface by pulses of an LGI-21 nitrogen laser (λ = 337 nm, $\tau_{1/2}$ = 7.5 ns) and heating by these pulses of a 150-nm thick gold film deposited on the sample surface.

To detect the arrival of nonequilibrium phonons in transmission geometry, a superconducting bolometer based on fine-grained aluminum was deposited on the opposite surface of the sample [8]. The detection system included an RU3-33 broadband preamplifier and a computer-controlled stroboscopic V9-5 voltage converter. The time resolution of the detection system was about 5 ns.

2.1. Photoexcitation

The solid line in Fig. 2 shows typical bolometer response in the case of ZnTe surface photoexcitation. The response is seen to consist of several superimposed peaks.

The first peak, whose leading edge is not delayed in time, is due to a light pulse striking the bolometer. This cannot be the laser pulse passing through the crystal since the nitrogen laser photon energy ($\hbar\nu$ = 3.7 eV) is greater than the ZnTe band gap width (E_g = 2.4 eV); As a result, the absorption coefficient of light in ZnTe for this wavelength is equal to ~10^5 cm^{-1}, so that the light cannot pass through the 970-μm-thick crystal. At the same time, as already mentioned, illumination of ZnTe gives rise to luminescent emission in the red spectral region; this emission can traverse the crystal. Analysis shows that the first peak of the signal decays exponentially (~exp($-t/\tau$)), with a characteristic time τ = 90 ns (dashed line in Fig. 2); we believe that this signal can be related to emission from the oxygen complex [9], because the lifetimes of the other complexes and bound excitons are considerably shorter [7].

The phonon part of the response, which was derived by subtracting the exponential curve from the total signal, is shown in Fig. 3 by circles (a similar spectrum obtained at a different excitation level is given in [3]). Numbers in the phonon part of the response indicate the arrival of differently polarized phonons. Peak *1* starting at t = 235 ns corresponds to the arrival of longitudinal acoustic (LA) phonons with a propagation velocity of 3.88 μm/ns. The next peak *2* starting at t = 420 ns corresponds to the arrival of fast transverse acoustic (FTA) phonons propagating at 2.35 μm/ns. Interestingly, the amplitude of this peak is smaller than that of the peak corresponding to the arrival of the LA phonons, although the density of states of FTA phonons is four times that of the LA phonons. The next peak *3*, a fairly diffuse one, is due to the show transverse acoustical(STA) phonons, whose propagation velocity is 2.18 μm/ns.

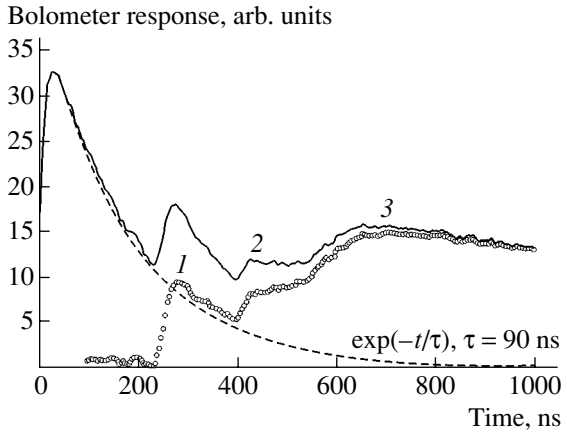

Fig. 3. Solid line: typical bolometer response to the photoexcitation of ZnTe surface by nitrogen laser pulses. Dashed line shows the exponential decay with characteristic time $\tau = 90$ ns. Circles identify the "phonon" response component. The numbers indicate the peaks of arrival of (*1*) LA phonons, (*2*) FTA phonons, and (*3*) STA phonons.

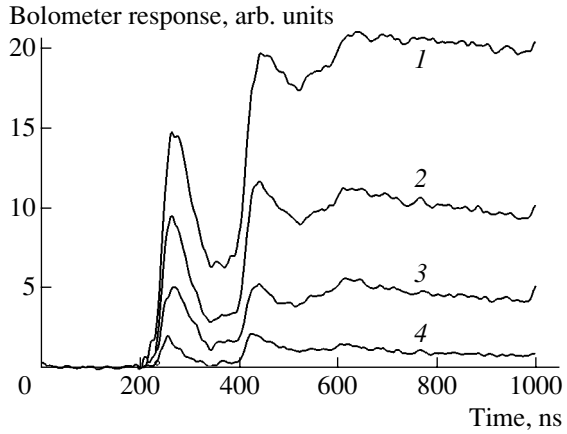

Fig. 4. Bolometer response to a gold film deposited on ZnTe surface and heated by nitrogen laser with pulse energies $E =$ (*1*) 1.0, (*2*) 0.5, (*3*) 0.25, and (*4*) 0.14 μJ.

2.2 Gold Film Heater

The solid lines in Fig. 4 represent the bolometer response signals obtained when a gold film deposited on the ZnTe surface and heated by laser pulses is used as the phonon generator. One can see differences when this is compared with the case of phonon generation by photoexcitation of the ZnTe surface. First, as would be expected, there is no peak due to the arrival of the luminescent emission. Next, the peaks associated with the LA and FTA phonons are substantially sharper. This circumstance should be attributed to the fact that the gold film heated by laser pulses generates phonons of a lower frequency ($\nu \sim 1.5$ THz) than in the case of photoexcitation ($\nu \sim 3.1$ THz). Since the phonon mean free path with respect to elastic scattering by point defects depends heavily on phonon frequency, $\tau = 1/(A_{scat}\nu^4)$, where ν is the phonon frequency and A_{scat} is the elastic scattering constant, these lower frequency phonons are scattered substantially less, and this brings about sharper responses. It should also be noted that the peaks become progressively sharper with increasing excitation energy. It would seem that this observation is in contradiction with the previous statement, because the film pumped at higher excitation energies is heated to higher temperatures and, accordingly, generates phonons of higher energies, which should be scattered more intensely. At the same time, this behavior of the response may be caused by the fact that phonons generated in the entire excitation energy range have mean free paths comparable to or exceeding the crystal thickness. In this case, the peak shape is governed by phonon generation during the film cooling rather than by phonon scattering. A hotter film, as shown in [10], cools at a higher rate, thus reducing the duration of the LA and FTA phonon peaks.

Interestingly, when a pulse-heated metal film is used as the phonon generator, the relative peak amplitude becomes dependent on excitation energy; indeed, as the latter increases, the amplitude of the peak corresponding to the FTA phonons, which was initially equal to that of the LA peak, becomes substantially larger. The amplitude of the third peak varies even more strongly. While at lower energies its amplitude is smaller than that of the LA and FTA peaks (curve *4* in Fig. 4), it first becomes equal in amplitude to the others as the energy increases and, after that, outgrows them. We believe that this may be due either to a decrease in the fraction of the LA phonons as a result of decay processes, whose intensity grows with increasing phonon frequency, or to the formation of a hot phonon spot [11, 12].

An analysis of the experimental response signals in which they are compared with Monte Carlo calculations [13], as was done, for instance, for CdTe [14], would require knowledge of phonon decay constants in ZnTe, and these are not available at present.

3. CONCLUSION

The heat pulse technique was employed to study the propagation of nonequilibrium acoustic phonons (both higher frequency ones produced by optical excitation and the comparatively low-frequency species generated by a heated metal film) in a ZnTe single crystal sample. The transmission of both longitudinal (LA) and transverse (FTA and STA) phonons was detected. The good resolution with phonons with different polarizations confirms the high quality of the ZnTe single crystal used in this study.

ACKNOWLEDGMENTS

We are indebted to V. P. Martovitskiĭ for X-ray characterization of the samples and to Yu.V. Klevkov for valuable comments.

This study was supported by the Russian Foundation for Basic Research (project no. 02-02-17392) and the RAS Commission for the Support of Young Scientists (6th Competition, grant no. 24).

REFERENCES

1. Q. Wu and X.-C. Zhang, Appl. Phys. Lett. **71**, 1285 (1997).
2. A. Leitenstorter, S. Hunshe, J. Shah, *et al.*, Appl. Phys. Lett. **74**, 1516 (1999).
3. T. I Galkina, A. Yu. Klokov, A. I. Sharkov, *et al.*, Physica B (Amsterdam) **316–317**, 243 (2002).
4. Yu. V. Korostelin, V. I. Kozlovsky, and P. V. Shapkin, J. Cryst. Growth **214–215**, 870 (2000).
5. H. Venghaus and P. J. Dean, Phys. Rev. B **21**, 1596 (1980).
6. B. A. Wilson, C. E. Bonner, R. D. Feldman, *et al.*, J. Appl. Phys. **64**, 3210 (1988).
7. P. Dean and D. C. Herbert, in *Excitons. Topics in Current Physics*, Ed. by K. Cho (Springer, Berlin, 1979), Vol. 14, p. 55.
8. A. Yu. Blinov, M. M. Bonch-Osmolovskiĭ, T. I. Galkina, *et al.*, Kratk. Soobshch. Fiz. **7**, 31 (1989).
9. Y. Burki, W. Czaja, V. Capozzi, and P. Schwendimann, J. Lumin. **60–61**, 4 (1994).
10. A. I. Sharkov, A. Yu. Klokov, and T. I. Galkina, Fiz. Tverd. Tela (St. Petersburg) **43**, 446 (2001) [Phys. Solid State **43**, 463 (2001)].
11. M. M. Bonch-Osmolovskii, T. I. Galkina, A. Yu. Klokov, *et al.*, Solid State Commun. **92**, 203 (1994).
12. D. V. Kazakovtsev and I. B. Levinson, Zh. Éksp. Teor. Fiz. **88**, 2228 (1985) [Sov. Phys. JETP **61**, 1318 (1985)].
13. M. M. Bonch-Osmolovskiĭ, T. I. Galkina, A. Yu. Klokov, *et al.*, Fiz. Tverd. Tela (St. Petersburg) **38**, 1051 (1996) [Phys. Solid State **38**, 582 (1996)].
14. A. I. Sharkov, T. I. Galkina, A. Yu. Klokov, and Yu. V. Klevkov, Fiz. Tverd. Tela (St. Petersburg) **45**, 159 (2003) [Phys. Solid State **45**, 163 (2003)].

Translated by G. Skrebtsov

Semiconductors, Vol. 37, No. 5, 2003, pp. 523–525. Translated from Fizika i Tekhnika Poluprovodnikov, Vol. 37, No. 5, 2003, pp. 543–545.

ELECTRONIC AND OPTICAL PROPERTIES OF SEMICONDUCTORS

Magnetooptical Oscillations in Bismuth at $T \geq 77$ K

O. V. Kondakov* and K. G. Ivanov**

** Elets State University, Elets, 399700 Russia*

*** St. Petersburg State University of Technology and Design, St. Petersburg, 191186 Russia*

Submitted July 18, 2002; accepted for publication September 5, 2002

Abstract—The oscillations caused by optical interband electron transitions at the point *L* of the Brillouin zone of bismuth are studied in the temperature range of 77–280 K and magnetic fields up to $B = 22$ T. It is shown that the method of simulation of the experimental line shape allows one not only to refine the band parameters of the material, but also to obtain detailed information about physical reasons for the specific features observed in the experimental magneto-optical spectra. © *2003 MAIK "Nauka/Interperiodica".*

In this paper, we report the results of studying the transmission of IR radiation by a strip line consisting of two translation-symmetrical halves of a bismuth single crystal separated by a gap on the order of the optical wavelength ($\lambda = 10.6$ μm) [1]. The measurements were performed in pulsed magnetic fields up to $B = 22$ T and in the temperature range $T = 77$–280 K. The direction of the magnetic field coincided with the binary axis of bismuth single crystal (**B** ∥ *c*).

The temperature was varied using a heater mounted on the wall of the sample holder and was controlled with an accuracy of 1.0 K. These conditions eliminated uncontrolled changes in temperature and its gradients in the course of experiments (see [2, 3]).

The use of a strip line provides the possibility of increasing the signal by a factor of 5–10 in comparison with the signal obtained by direct reflection from the crystal surface [4].

As can be seen from Fig. 1, with increasing temperature, the intensity *I* of the transmitted signal and the number of magnetooptical oscillations decrease, the half-width of the peaks increases, and the peaks shift to higher magnetic fields.

In order to account for all the features of the experimental spectrum in its simulation, it is not sufficient to consider the contribution of only interband and intraband transitions in the Landau levels [3, 4]. One should introduce a complex quantity which accounts for the contribution of electrons from other bands. This enables one to obtain good agreement between the experimental and calculated line shapes.

The complex permittivity ε_l was studied previously in [5, 6] but without taking magnetic quantization into account. Comparison of the experimental data on magnetoreflection obtained in [4–6] and also in our experiments with the results of calculations shows that the real part of the permittivity ε_l' considerably exceeds the imaginary part ε_l'' (Table 1).

Simulating the line shape in a magnetooptical experiment with due regard for the influence of the electrons in other bands on the dielectric-constant function yields more precise values of E_g/m_c^* (Table 2), in contrast with the data given in [3, 4].

The set of pronounced oscillations in magnetooptical experiments in a wide temperature range (Fig. 1) allows the temperature, orientation, field, and concentration dependences of the relaxation time to be studied.

In [3] it is shown that the relaxation time increases linearly with an increase in the inverse temperature at 110 K or higher due to the phonon origin of an increase in the rate of the charge-carrier collisions with scattering centers.

Analysis of the dynamics in changes of the relative intensity, the half-width at half-maximum, and the form of magnetooptical oscillations in our experimental spectra allows us conclude that the intensity of oscillations *I* grows stronger with increasing magnetic field

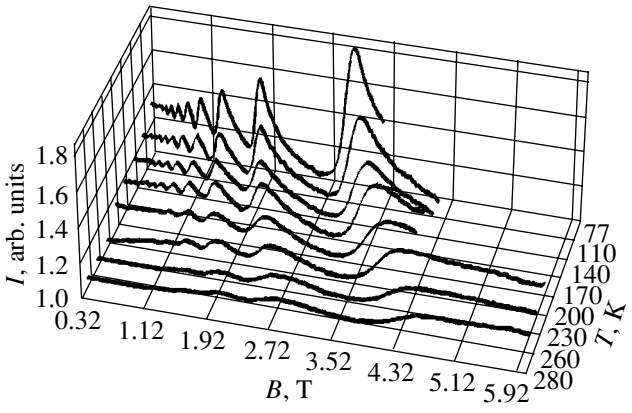

Fig. 1. Intensity of magnetooptical oscillations as a function of the magnetic field at various temperatures.

1063-7826/03/3705-0523$24.00

Table 1. The values of real ε_l' and imaginary ε_l'' parts of permittivity ε_l

T, K	ε_l'	ε_l''
77	60	60
110	60	50
140	63	50
170	63	32
200	63	32
230	63	1
260	63	1
280	63	1

Table 2. The values of parameters E_g/m_c^* for **B** ∥ c in bismuth at various temperature

T, K	E_g/m_c^*		
	Simulation of the line shape (this study)	Approximation by a polynomial [3]	Approximation by a polynomial [4]
77	6.13	6.56	6.68
110	5.83	6.22	6.37
140	5.46	5.90	6.03
170	5.27	5.57	5.65
200	4.97	5.23	5.23
230	4.88	4.88	4.76
260	4.60	4.52	4.24
280	4.38	4.28	3.87

Note: E_g is the band gap, eV; m_c^* is the effective cyclotron mass of electron in the units of m_0 (m_0 is the mass of a free electron).

than it could be expected from the theory on the assumption of constant relaxation time τ (Fig. 2).

Such discrepancy between theory and experiment can be alleviated by the introduction of a field-dependent relaxation time. Indeed, the scattering of charge carriers by phonons can occur only if there exist unfilled final states. The experiment is performed under the conditions of magnetic quantization when the unoccupied states in the conduction band are separated from the occupied states by an energy gap equal to the distance between neighboring Landau levels. The energy spacing between the Landau levels increases with increasing magnetic field; and for a certain magnitude of magnetic field determined by the value of the effective cyclotron mass of an electron m_c^*, this energy spacing initially becomes equal to the phonon energy and then exceeds it. This results in an abrupt decrease in the probability of electron–phonon scattering, which manifests itself as an increase in the effective intensity (and also as the decrease in the half-width at a half-height) of specific features in magnetotransmission interpreted as an increase in the relaxation time with increasing magnetic field. The relaxation time as a function of magnetic field when the vector of induction of the magnetic field is parallel to the binary axis of bismuth crystal is shown in Fig. 3. The curves shown in Fig. 3 can be associated with the features of the phonon spectrum in bismuth. Indeed, the existence of acoustic and optical modes that differ greatly in energy, and the possibility of two-phonon processes, should result in a

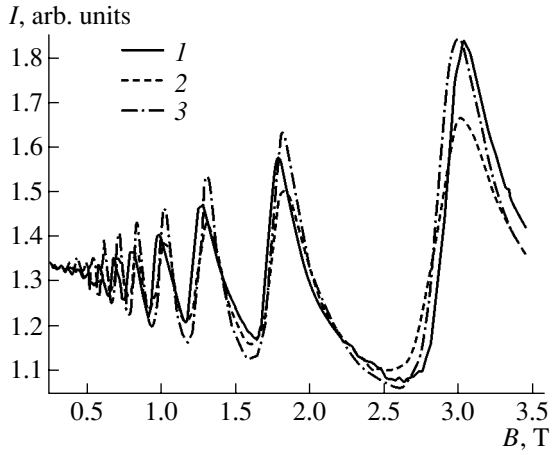

Fig. 2. Dependence of the intensity of magnetooptical oscillations on the magnitude of the magnetic field: (*1*) experiment; (*2*) calculation, $\tau = 2 \times 10^{-13}$ s; and (*3*) calculation, $\tau = 3 \times 10^{-13}$ s.

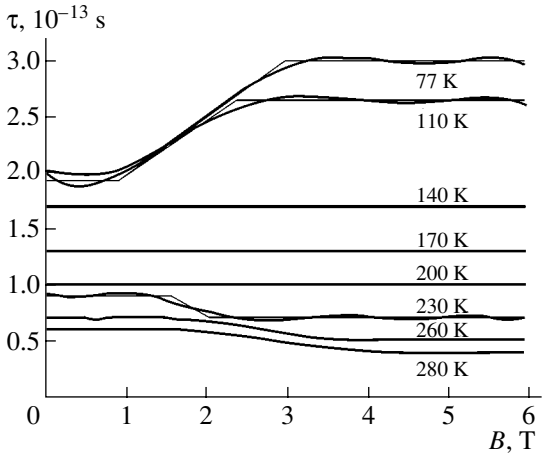

Fig. 3. Relaxation time as a function of magnetic field. The curves were used for simulating the line shape of the magnetooptical spectrum at various temperatures. Simulation by two values of relaxation times (for low and high magnetic fields) is shown by thin lines; simulation by a polynomial is shown by a thick line.

complex mechanism of interaction of charge carriers with the phonon subsystem.

According to the data reported in [7, 8], at $T = 77$ K, only acoustic phonons are effectively excited. Typical values of the energy of acoustic phonons fall in the range of 3.7–6.5 meV [7, 8]. In fields up to 1 T, the energy spacing between the neighboring Landau levels does not exceed 6.5 meV. In the fields $B > 1$ T, the optical transitions of charge carriers occur at the levels with the principal quantum numbers $j = 1, 2, 3, 4$, with the energy spacing between these levels being considerably larger than the energy of an acoustic phonon. This is the reason why the relaxation time increases. Under these conditions, the scattering is governed either by the two-phonon mechanism involving acoustic phonons or by the processes involving optical phonons with a characteristic temperature of 130 K. Both scattering processes are highly improbable at a temperature $T = 77$ K.

When the temperature increases to $T = 110$ K, the value of E_g/m_c^* changes (Table 1) and the peaks slightly shift to higher magnetic fields (Fig. 1). However, it is of importance that the processes of scattering by two acoustic phonons now become possible, and the contribution of optical phonons to scattering processes also considerably increases. This results in a noticeable decrease in the relaxation time in the fields $B > 2$ T.

At $T = 140$ K, where the Debye temperature is reached, the optical phonons with energies of 11–13 meV become involved in the scattering processes; the spectrum in this case is described by a single relaxation time in the entire range of magnetic fields. Such a situation is observed in the temperature range up to $T = 230$ K, where the contribution of two-phonon processes of scattering by optical phonons becomes essential. These processes occur in sufficiently strong magnetic fields, i.e., when the spacing between neighboring Landau levels becomes comparable with the doubled energy of an optical phonon. A further increase in temperature to $T = 280$ K preserves this situation; the spectra are again characterized by two relaxation times.

In the fields $B = 6$–22 T the relaxation time remains constant. The absence of a field dependence of relaxation time in the ultraquantum limit of magnetic fields confirms the suggested mechanism of the $\tau(B)$ dependence.

Thus, the value of the cyclotron mass of the electron, on which the energy spacing between neighboring Landau levels depends, and the existence of acoustic and optical phonons of various energy in bismuth govern the dependence of the relaxation time on the magnetic field.

The strip line experimental method makes it possible to observe all the special features of interaction of radiation with magnetized plasma in a solid in a wide temperature range. Simulation of the line shape allows one to explain the observed special features in the behavior of the parameters responsible for the basic properties of the material under study.

REFERENCES

1. K. G. Ivanov and O. V. Kondakov, Fiz. Tverd. Tela (Leningrad) **32**, 290 (1990) [Sov. Phys. Solid State **32**, 164 (1990)].
2. K. G. Ivanov, O. V. Kondakov, and V. M. Grabov, *Electrical Relaxation and Kinetic Effects in Solids* (Sochi, 1991), p. 3.
3. K. G. Ivanov, O. V. Kondakov, S. V. Brovko, and A. A. Zaĭtsev, Fiz. Tekh. Poluprovodn. (St. Petersburg) **30**, 1585 (1996) [Semiconductors **30**, 831 (1996)].
4. M. P. Vecchi, J. R. Pereira, and M. S. Dresselhaus, Phys. Rev. B **14**, 298 (1976).
5. V. G. Golubev, V. N. Evseev, K. G. Ivanov, and V. I. Ivanov-Omskiĭ, Zh. Tekh. Fiz. **50**, 1992 (1980) [Sov. Phys. Tech. Phys. **25**, 1159 (1980)].
6. S. Kanada, M. Nakayama, and M. Tsuji, J. Phys. Soc. Jpn. **41**, 1954 (1976).
7. A. A. Lopez, Phys. Rev. **175**, 823 (1968).
8. F. E. Macfarlane, J. Phys. Chem. Solids Suppl. **32** (1), 989 (1971).

Translated by A. Zalesskiĭ

Semiconductors, Vol. 37, No. 5, 2003, pp. 526–531. Translated from Fizika i Tekhnika Poluprovodnikov, Vol. 37, No. 5, 2003, pp. 546–551.

ELECTRONIC AND OPTICAL PROPERTIES OF SEMICONDUCTORS

A Local Specific Feature of Variation in the Spectrum of Picosecond Superluminescence upon Adding Excited Carriers to a Non-Fermi Electron–Hole Plasma in GaAs

N. N. Ageeva*, I. L. Bronevoi*^, A. N. Krivonosov*, S. E. Kumekov, and S. V. Stegantsov***

** Institute of Radio Engineering and Electronics, Russian Academy of Sciences, Mokhovaya ul. 11, Moscow, 101999 Russia*

^e-mail: bil@mail.cplire.ru

*** Almaty Technological University, Almaty, 480012 Kazakhstan*

Submitted June 10, 2002; accepted for publication September 9, 2002

Abstract—A dense hot electron–hole plasma and picosecond superluminescence appeared upon pumping of a GaAs layer by a picosecond (*ex*) optical pulse. The distribution of electrons over the conduction band was modulated with a period equal to the LO-phonon energy. The effect of additional pumping of GaAs (p_i) by an optical pulse with a photon energy of $\hbar\omega_p < \hbar\omega_{ex} - 0.1$ eV on the superluminescence was investigated. In the case of simultaneous pumping by *ex* and p_i pulses, a local maximum or minimum appeared in the spectrum of relative increase in the superluminescence energy at the photon energy, which corresponds to the peak in the superluminescence-energy spectrum of the active region of the GaAs layer. The local maximum appeared when the electrons that were excited by the p_1 pulse to the level with a depleted population emitted LO phonons (one phonon per each electron) and recombined. The local minimum appeared when electrons were excited by the p_2 pulse to the level with the Fermi population. The spectral width of the local maximum and minimum turned out to be narrower than the calculated width of the energy level from which the electrons recombine. © *2003 MAIK "Nauka/Interperiodica".*

1. INTRODUCTION

The purpose of this study is to clarify the influence of additional excitation of charge carriers by a pulse (p_i) with a photon energy of $\hbar\omega_p < \hbar\omega_{ex}$ on the intense picosecond superluminescence that occurs upon the pumping of GaAs by a powerful picosecond (*ex*) optical pulse. The electrons were excited by p_i pulses to the region near the bottom of the conduction band, where the electron-energy distribution was strongly modulated, i.e., differed from the Fermi distribution. The experiments were carried out at room temperature.

Let us initially describe the situation that occurs in the case of pumping of GaAs by the *ex* pulse with the photon energy $\hbar\omega_{ex} = 1.558$ eV and a duration of 14 ps. Upon the interband absorption of a powerful *ex* pulse in a thin (~1-μm) GaAs layer, a dense hot electron–hole plasma (EHP) arises and picosecond superluminescence occurs [1–4]. The latter is considered to mean induced radiative recombination in an active GaAs medium without a resonator with a characteristic relaxation time of ~10 ps. The superluminescence relaxation is interrelated with the relaxation of the temperature and concentration of the EHP [5, 6]. As estimations show, the superluminescence intensity integrated over the spectral range exceeds 10^8 W/cm^2.

Under these conditions, the energy distribution of electrons in the conduction band is modulated by oscillations with a period $\hbar\omega_{LO}$ ($\hbar\omega_{LO}$ is the energy of the longitudinal optical (LO) phonon) [7]. Periodically located regions arise in which the populations of energy levels are depleted in comparison with the population characteristic of the Fermi distribution of electrons. The following physical mechanism was suggested to explain the modulation of the electron-energy distribution [7].

The superluminescence intensity B_ω increases with an increase in the superluminescence-recombination rate of charge carriers: $(dn/dt)_R \propto \int \alpha_\omega B_\omega d\omega$. Here, ω is the frequency of superluminescence radiation and α_ω is the absorption coefficient in the light-amplification region; the integral is taken over the spectral amplification band. An increase in $|(dn/dt)_R|$ prevents $|\alpha_\omega|$ from increasing in the amplification region. For high superluminescence intensities, this causes depletion of the inverse population of the energy levels near the bottom of the conduction band, from which the electrons are induced to recombine, compared with the population in the case of the Fermi distribution of EHP. Such a depletion is represented by the difference between two absorption spectra for the amplification region, one of which is experimental and the other is calculated under the assumption of Fermi distribution for EHP (Fig. 1). Let us call this difference the dip in the amplification

range. The shape of the dip spectrum is similar to that of the part of the superluminescence-energy spectrum which is located above the energy W_s^t (the superluminescence energy at those two values of $\hbar\omega$ which determine the dip boundaries [8]) (Fig. 1).

The depletion of populations leads to non-compliance with the principle of detailed balancing. As a result, intense transitions of electrons to the levels with depleted inverse population occur; these transitions are accompanied by the emission of LO phonons. The transitions with the emission of LO phonons turn out to be so intense that they lead to the formation of another region of population depletion in the conduction band. The second depletion region is located above the first one; the energy spacing between these regions is equal to the energy of the LO phonon $\hbar\omega_{\mathrm{LO}}$. The second depletion region results in the formation of a shoulder in the experimental absorption spectrum at $\hbar\omega > 1.417$ eV (Fig. 1). The further extension of this process upward over the conduction band leads to the periodic modulation of the electron-energy distribution within the band.

We used the mechanism of modulation described in [7] to explain the effects we revealed:

(i) the modulation of the bleaching (increase in transparency) spectrum of the GaAs layer by *phonon* oscillations with a period

$$\Delta = \hbar\omega_{\mathrm{LO}}(1 + m_e/m_h),$$

where m_e and m_h are the effective masses of an electron and a heavy hole, respectively [7];

(ii) the energy transport of electrons which occurs via emission of LO phonons in the course of picosecond superluminescence in GaAs [9];

(iii) "LO-phonon" correlation between the picosecond-superluminescence spectrum and the specific features of the absorption spectrum of GaAs in the case of the non-Fermi distribution of carriers [8].

The effects reported in [7–9] allow one to assume that, under the above experimental conditions, the relaxation times $\tau_{e\text{-LO}}$ and $\tau_{c\text{-}c}$ become comparable. Here, $\tau_{e\text{-LO}}$ is the time of such relaxation of electrons to the bottom of the conduction band, under which the electrons, emitting LO phonons, undergo transitions to the level with depleted population [9]. The quantity $\tau_{c\text{-}c}$ is the time of intraband energy relaxation of electrons due to collisions between the carriers, leading to the Fermi distribution of electrons. The fact that the times $\tau_{e\text{-LO}}$ and $\tau_{c\text{-}c}$ become comparable has not been explained theoretically yet and continues to arouse interest. For comparison, according to the calculations [7–9], in the dense quasi-equilibrium EHP, $\nu_{e\text{-LO}}^{-1} \gg \tau_{c\text{-}c}$ ($\nu_{e\text{-LO}}$ is the rate of emission of LO phonons by an electron) for the electrons from the energy region in which the above effects were observed.

It is worth noting that the largest depth of the dip within the amplification region at the photon energy

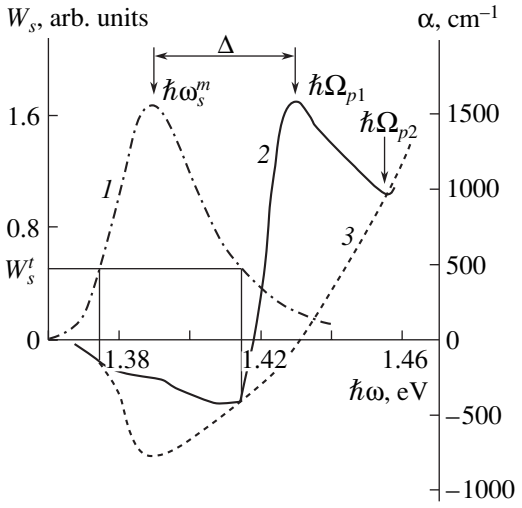

Fig. 1. (*1*) Spectrum of superluminescence radiation emerging from GaAs normally to the surface of the active region of the epilayer, (*2*) experimental light-absorption spectrum of photoexcited GaAs, and (*3*) calculated light-absorption spectrum for the case of Fermi distribution of the EHP in GaAs. The figure is taken from [8]. The arrows point to the photon energies $\hbar\Omega_{p_1}$ and $\hbar\Omega_{p_2}$ of the pulses p_1 and p_2, which were used in this study, as well as to the photon energy $\hbar\omega_s^m$.

$\hbar\omega_s^m$ is larger than the amplification factor α measured at $\hbar\omega_s^m$ by a factor of 2. Here, $\hbar\omega_s^m$ is the photon energy at which the superluminescence spectrum of the active region of GaAs is peaked (Fig. 1). It follows from this relation that the inverse frequency λ^{-1} of induced recombination transitions, which are accompanied by emission of photons with the energy $\hbar\omega_s^m$, is also comparable with the intraband relaxation time $\tau_{c\text{-}c}$.

In this study, in the spectrum of substantial relative increase in the energy of picosecond superluminescence, which is caused by the additional excitation of electrons by the p_i pulse, an abnormally narrow local minimum and maximum were detected. This phenomenon, observed in the case of simultaneous pumping of GaAs by picosecond *ex* and p_i pulses, is described and discussed in detail below.

2. EXPERIMENTAL

In this study, we analyzed a sample irradiated by an *ex* pulse. The thickness and composition of the epitaxial layers, as well as the pulse parameters, were identical to those used in [8]. Therefore, the results obtained in [8] (see Fig. 1) are completely applicable to this study.

The sample was an $Al_{0.22}Ga_{0.78}As$–GaAs–$Al_{0.4}Ga_{0.6}As$ heterostructure with layer thicknesses of 1.2, 1.6, and 1.2 μm, respectively. The heterostructure was grown by molecular-beam epitaxy on a GaAs(100) substrate.

Then, the heterostructure was separated from the substrate. This operation was not performed in [8]. The concentrations of donor and acceptor impurities in the heterostructure did not exceed 10^{15} cm^{-3}. The $Al_xGa_{1-x}As$ layers were designed to stabilize the surface recombination and mechanical strength. These layers are transparent to light of the frequency used in the experiment. An antireflection coating was deposited on the outer surfaces of the $Al_xGa_{1-x}As$ layers. As a result, the portion of light reflected normally to the layer surface was no more than 2%.

The heterostructure was irradiated by one (*ex*) or two ($ex + p_i$) pulses with an approximately Gaussian spatial distribution of intensity; the pulses were focused onto a single point. The duration of both p_i and *ex* pulses was equal to 14 ps. The diameters of the focal spots of the *ex* and p_i pulses were equal to 0.5 and 0.46 mm, respectively. In the case of pumping of GaAs by the p_i pulse only, the EHP concentration was just close to the threshold one, at which superluminescence appears.

The photoexcited active region of the GaAs layer, where superluminescence occurred upon pumping by the *ex* pulse and which was additionally enhanced upon pumping by the p_1 or p_2 pulses, was located at a distance of about 1.4 mm from the side face of the heterostructure. During the excitation pulse, this circumstance made it possible to exclude the following: (i) the effect of the positive feedback caused by the reflection of the superluminescence radiation from the side face of the heterostructure (the superluminescence radiation passed through the photoexcited region after the excitation pulse), and (ii) the effect of lattice defects near the side face of the heterostructure. The superluminescence radiation propagated mainly in the plane of the GaAs layer. After the emission from the side face of the heterostructure, the spectrum of the picosecond-superluminescence energy integrated over time, W_s, was measured in the solid angle of 4°.

Due to the absorption in the nonexcited region of the GaAs layer, the spectrum we measured differed from the superluminescence spectrum of the photoexcited active region of the GaAs layer. The superluminescence spectrum of the active region is shown in Fig. 1, which is taken from [8]. In [8], owing to the poor waveguiding properties of the sample, we measured the spectrum of radiation emerging from a similar sample normally to its surface. As was mentioned above, we used the *ex* pulse with the same parameters as those of the pumping pulse used in [8]. The thicknesses of the layers and the composition of the samples were also identical. Therefore, we can assume that Fig. 1 also shows the superluminescence spectrum measured in this study for the active region of the GaAs layer upon pumping by the *ex* pulse.

It is understandable that the shoulder at $\hbar\omega > 1.417$ eV in the light-absorption spectrum measured in this study, which is related to the depletion of the carrier population, also coincided with the shoulder in the spectrum measured in [8] and represented by curve *2* in Fig. 1.

Despite the partial absorption of superluminescence radiation in the passive region of the GaAs layer, we found some specific spectral features which allowed us to draw a number of substantial conclusions. In order to exclude, wherever possible, the effect of absorption of the superluminescence radiation in passive region of the GaAs layer, the spectrum of the relative increase in the superluminescence energy $W_s(ex + p_i)/W_s(ex) = f(\hbar\omega)$ was measured. This increase is due to the fact that the pumping by the p_1 pulse was added to the pumping of the sample by the *ex* pulse. Here, $W_s(ex + p_i)$ and $W_s(ex)$ are the energies of superluminescence for the cases of combined pumping by the *ex* and p_i pulses and pumping by the *ex* pulse solely, respectively.

In these experiments, p_i pulses with two values of the photon-energy, $\hbar\Omega_{p_1}$ and $\hbar\Omega_{p_2}$ (shown by arrows in Fig. 1), were used. The first value $\hbar\Omega_{p_1} = \hbar\omega_s^m + \Delta =$ 1.43 eV coincided with the frequency corresponding to the shoulder peak in the absorption spectrum. Upon the absorption of the p_1 pulse, the electrons were excited to the energy level of the conduction band, which had the largest depletion of population in the second depletion region. The energy of this level exceeded by $\hbar\omega_{LO}$ the energy of the level which was maximally depleted in the first depletion region and from which the electrons recombined, emitting photons with the energy $\hbar\omega_s^m$. The variation in the superluminescence was investigated in detail for the spectral region close to the photon energy $\hbar\omega_s^m$. Upon simultaneous irradiation of the heterostructure with *ex* and p_1 pulses, the picosecond-superluminescence energy increased substantially compared with the case of superluminescence upon pumping of GaAs by the *ex* pulse solely. In this case, a local maximum at $\hbar\omega = \hbar\omega_s^m$ appeared in the spectrum of the relative increase in the superluminescence energy $W_s(ex + p_i)/W_s(ex) = f(\hbar\omega)$ (Fig. 2). The base width of the local maximum was 1.9 meV.

No local maximum was observed in the spectral dependences $W_s(ex + p_1)/W_s(ex) = f(\hbar\omega)$ measured for $\tau_d = -20$ ps and $\tau_d = 20$ ps, where the *ex* and p_1 pulses were not overlapped in time. Here, τ_d is the delay time of the p_1 pulse with respect to the *ex* pulse (Fig. 3). Thus, the local maximum appeared specifically under the conditions of simultaneous pumping by the *ex* and p_1 pulses.

The second energy value of the p_i pulse $\hbar\Omega_{p_2} =$ 1.455 eV corresponds to the short-wavelength edge of the shoulder in the absorption spectrum (Fig. 1). Upon absorption of the p_2 pulse, the electrons were excited to that level in the conduction band, at which there was no population depletion. The energy of this level exceeds, by less than $\hbar\omega_{LO}$, the energy of the level to which elec-

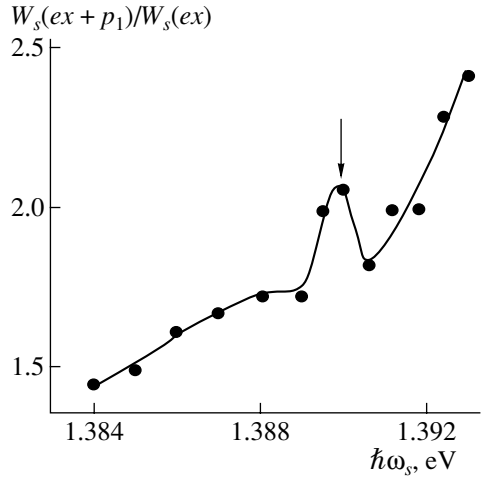

Fig. 2. Spectrum of relative increase in the superluminescence energy, caused by the addition of synchronous pumping of the sample by the p_1 pulse to pumping by the *ex* pulse. $\hbar\omega_{ex}$ = 1.558 eV, $\hbar\Omega_{p_1}$ = 1.43 eV. The arrow points to the photon energy $\hbar\omega_s \approx \hbar\omega_s^m \approx \hbar\Omega_{p_1} - \Delta$.

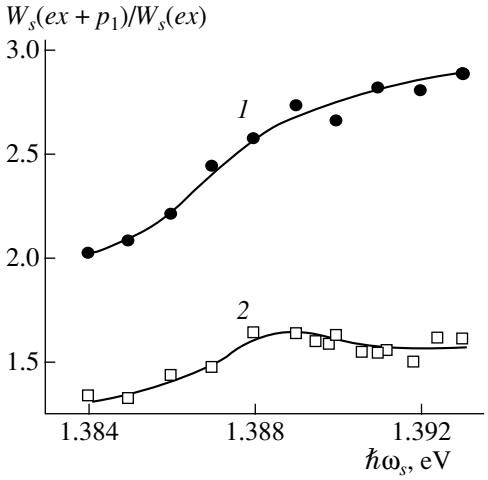

Fig. 3. Spectrum of relative increase in the superluminescence energy, caused by the addition of pumping of the sample by the p_1 pulse to the pumping by the *ex* pulse; the pulses were not overlapped in time. $\hbar\omega_{ex}$ = 1.558 eV, $\hbar\Omega_{p_1}$ = 1.43 eV; (*1*) τ_d = –20 ps, (*2*) τ_d = 20 ps (τ_d is the delay time of the p_1 pulse with respect to the *ex* pulse).

trons were excited due to the absorption of the p_1 pulse. Upon simultaneous pumping by the *ex* and p_2 pulses, a local minimum appeared in the spectrum of the relative increase in the superluminescence energy $W_s(ex + p_2)/W_s(ex) = f(\hbar\omega)$; however, this also occurred at the photon energy $\hbar\omega = \hbar\omega_s^m$ (Fig. 4). The base width of the local minimum was 1.7 meV.

3. RESULTS AND DISCUSSION

As was explained above, upon generation of EHP by the *ex* pulse, regions with a lowered population of the energy levels are formed in the conduction band, giving rise to corresponding depletion regions in the electron-energy distribution. These regions are located with the period $\hbar\omega_{\mathrm{LO}}$. The electrons were excited to the level with the largest depletion in the second depletion region in the conduction band by the p_1 pulse with the photon energy $\hbar\Omega_{p_1}$, which resulted in a local enhancement of radiation with the photon energy $\hbar\omega_s \approx \hbar\omega_s^m \approx \hbar\Omega_{p_1} - \Delta$ (Fig. 2). The base width of the local maximum in the experimental spectrum $W_s(ex + p_1)/W_s(ex) = f(\hbar\omega)$ was equal to 1.9 meV. The appearance of a local maximum in the $W_s(ex + p_1)/W_s(ex) = f(\hbar\omega)$ spectrum points to the following. After the excitation of electrons by the p_1 pulse, some of them emit LO phonons (one phonon per electron) and undergo transitions to the levels with the largest depletion in the first depletion region at the bottom of the conduction band. At these levels, the electrons, having experienced no energy relaxation due to the interactions with other electrons of the conduction band, are forced to recombine, thus enhancing the superluminescence at $\hbar\omega_s \approx \hbar\omega_s^m$. This confirms the fact that $\tau_{e\text{-LO}}$ and $\tau_{c\text{-}c}$ are comparable. Hence, the effective lifetime of an electron at such a level, $\tau_{SR} = \lambda^{-1}$, and the quantity $\tau_{c\text{-}c}$ are also comparable. Here, λ is the rate of forced recombination transitions at $\tau_d \approx 0$, during which photons with an energy $\hbar\omega_s^m$ are emitted. We should note that the same assumption, based on the value of the dip depth in the amplification region, was formulated in the Introduction.

The base width of the local maximum in the experimental spectrum $W_s(ex + p_1)/W_s(ex) = f(\hbar\omega)$, as was mentioned above, was equal to 1.9 meV. In this case, the width ΔE of the level from which an electron recombines emitting a photon with an energy $\hbar\omega_s^m$ should be equal to $\Delta E \le 1.9$ meV. According to the uncertainty principle, the effective lifetime of an electron at this level $\tau_{SR} \ge 3.5 \times 10^{-13}$ s and the rate $\lambda \le 2.9 \times 10^{12}$ s^{-1}. The evaluations by formulas (6.2.35) and (4.3.19) from [10] for quasi-equilibrium carrier distribution yield the following times (i) of relaxation of the perturbation of the Fermi gas at an energy of 25 meV due to the electron–electron scattering, $\tau_{e\text{-}e} = 4 \times 10^{-15}$ s, and (ii) of absorption of an LO phonon by an electron with an energy of 25 meV, $\tau_{e\text{-}ph} = 9 \times 10^{-14}$ s. For calculations, we used 5×10^{18} cm^{-3} as the value of the concentration of electron–hole pairs and T = 52 meV for the temperature. These values correspond to the calculated absorption spectrum with the Fermi distribution of the EHP, which is shown in Fig. 1. The times $\tau_{e\text{-}e}$ =

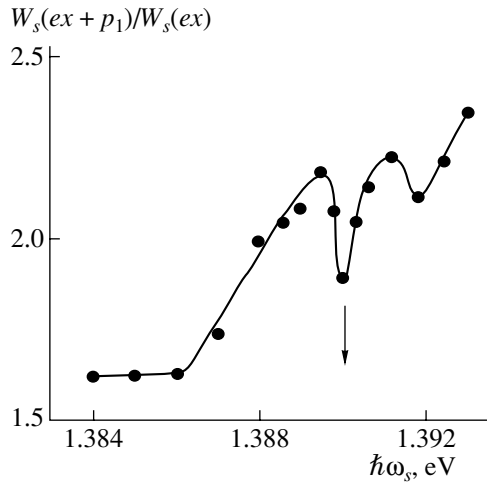

Fig. 4. Spectrum of relative increase in the superluminescence energy, caused by the addition of synchronous pumping of the sample by the p_2 pulse to the pumping by the *ex* pulse. $\hbar\omega_{ex} = 1.558$ eV, $\hbar\Omega_{p_2} = 1.455$ eV. The arrow point to the photon energy $\hbar\omega_s \approx \hbar\omega_s^m$.

4×10^{-15} s and $\tau_{e\text{-}ph} = 9 \times 10^{-14}$ s turned out to be substantially smaller than the time $\tau_{SR} \geq 3.5 \times 10^{-13}$ s. Therefore, doubt arises whether it is possible to use the estimates obtained under the assumption that the true modulated carrier distribution is the approximated Fermi distribution in the situation under investigation. Apparently, there are either some unknown reasons for increasing the times $\tau_{e\text{-}e}$ and $\tau_{e\text{-}ph}$ or some unknown specific features of the physical mechanism of formation of the local maximum in the spectrum of the relative increase in the picosecond superluminescence.

We should note that the picosecond superluminescence relaxes after the pumping with a characteristic time of ~10 ps. The superluminescence energy was measured, i.e., the superluminescence intensity integrated over time. It is demonstrated in this study that, in the spectrum $W_s(ex + p_1)/W_s(ex) = f(\hbar\omega)$, a local maximum appeared during the synchronous pumping of the sample by the *ex* and p_1 pulses with $\tau_d \approx 0$ (Fig. 2). When the intensity of light in the *ex* pulse approximately passes through the maximum, the depletion of the electron populations, which is distributed with a period $\hbar\omega_{LO}$ in the conduction band, is strongest [7, 11]. The strongest superluminescence recombination, which is necessary to create the depletion, should also occur under these conditions. The density of nonequilibrium LO phonons is also close to the largest value during photoexcitation [12]. After the *ex* pulse, the depletion of populations and superluminescence recombination are substantially weaker [5–7, 11] and the density of nonequilibrium LO phonons is lower too. When the excitation by a p_1 pulse was carried out after the *ex* pulse with the delay time $\tau_d = +20$ ps, no local maximum appeared in the spectrum of the relative increase in the superluminescence (Fig. 3). Consequently, the local maximum appears under conditions of strong depletion of populations, strong superluminescence recombination, and high density of nonequilibrium LO phonons.

The reason for the absence of a local maximum at $\tau_d = -20$ ps, when the sample was initially irradiated with a p_1 pulse and then with a *ex* pulse (Fig. 3), is evident, and we will not discuss it.

At the present time, it is difficult to conclusively establish the physical mechanism of formation of the local minimum in the spectrum of relative increase in the superluminescence energy $W_s(ex + p_2)/W_s(ex) = f(\hbar\omega)$ (Fig. 4).

We may assume that the spectrum of energy states is renormalized due to the coherent interaction of the superluminescence radiation with electrons and a gap arises in this spectrum [13]. The spectral position of the gap coincides with the maximum of the superluminescence spectra. The gap width $2\hbar\lambda$ should be equal to the base width of the local minimum (1.7 meV) in the spectrum of relative increase in the superluminescence energy (Fig. 4). In this case, the frequency of interband transitions $\lambda = 1.3 \times 10^{12}$ s^{-1}. For GaAs,

$$\hbar\lambda = 0.017 J^{1/2}(\text{eV}).$$

Here, J is the intensity of superluminescence radiation measured in GW/cm^2. The superluminescence radiation should be monochromatic and, consequently, occupy a very narrow region in the vicinity of the photon energy $\hbar\omega_s^m$ in the superluminescence spectrum. Accordingly, we obtain the evaluation of $J = 2.5 \times 10^6$ W/cm^2. The interaction of electrons with the electromagnetic field is coherent if the frequency of interband transitions λ exceeds the frequency of intraband electron scattering $1/\tau$, i.e., $\lambda\tau > 1$. In order to satisfy this relation, τ should exceed 7.7×10^{-13} s. In the above analysis we found that the effective lifetime of electrons at the isolated level $\tau_{SR} \geq 3.5 \times 10^{-13}$ s. The estimations of the lifetimes τ and τ_{SR} made by us do not exclude the explanation of the local minimum considered here; however, they are obviously insufficient to confirm it.

There is another question, specifically, why the spectral widths of the local minimum and maximum turn out to be approximately equal? A possible reason is that the energy levels that lie within these extrema should have approximately the same energy. The electrons excited by the p_1 pulse have the same energy, and these electrons, each emitting one LO phonon, should undergo transitions to approximately the same level. If we assume that the local minimum represents a gap in the spectrum of the energy states of electrons, it is worth noting that monochromatic radiation is required to form the gap. For the spectrum of picosecond superluminescence, monochromatic radiation, in the

extreme case, is the radiation caused by the recombination of electrons from the same level.

In our opinion, the issues analyzed in Section 3 are of interest for subsequent investigations both from a physical and practical points of view. The practical interest is due to the need to understand the physical processes that may occur in ultra-high-speed semiconductor optoelectronic devices, whose operation is based on the use of powerful ultrashort pulses of induced radiation and pumping (more than one pulse simultaneously).

ACKNOWLEDGMENTS

This study was supported by the Russian Foundation for Basic Research, project no. 01-02-16694.

We thank V.I. Perel', Yu.D. Kalifati, and G.N. Shkerdin for their helpful participation in discussions and useful advice.

REFERENCES

1. D. Hulin, M. Joffre, A. Migus, *et al.*, J. Phys. (Paris) **48**, 267 (1987).
2. N. N. Ageeva, I. L. Bronevoi, E. G. Dyadyushkin, and B. S. Yavich, Pis'ma Zh. Éksp. Teor. Fiz. **48**, 252 (1988) [JETP Lett. **48**, 276 (1988)].
3. N. N. Ageeva, I. L. Bronevoi, E. G. Dyadyushkin, *et al.*, Solid State Commun. **72**, 625 (1989).
4. I. L. Bronevoi and A. N. Krivonosov, Fiz. Tekh. Poluprovodn. (St. Petersburg) **32**, 537 (1998) [Semiconductors **32**, 479 (1998)].
5. Yu. D. Kalafati and V. A. Kokin, Zh. Éksp. Teor. Fiz. **99**, 1793 (1991) [Sov. Phys. JETP **72**, 1003 (1991)].
6. I. L. Bronevoi and A. N. Krivonosov, Fiz. Tekh. Poluprovodn. (St. Petersburg) **32**, 542 (1998) [Semiconductors **32**, 484 (1998)].
7. I. L. Bronevoi, A. N. Krivonosov, and V. I. Perel', Solid State Commun. **94**, 805 (1995).
8. N. N. Ageeva, I. L. Bronevoi, A. N. Krivonosov, *et al.*, Fiz. Tekh. Poluprovodn. (St. Petersburg) **36**, 144 (2002) [Semiconductors **36**, 136 (2002)].
9. I. L. Bronevoi and A. N. Krivonosov, Fiz. Tekh. Poluprovodn. (St. Petersburg) **33**, 13 (1999) [Semiconductors **33**, 10 (1999)].
10. V. F. Gantmakher and Y. B. Levinson, *Carrier Scattering in Metals and Semiconductors* (Nauka, Moscow, 1984; North-Holland, Amsterdam, 1987).
11. I. L. Bronevoi, A. N. Krivonosov, and T. A. Nalet, Solid State Commun. **98**, 903 (1996).
12. S. E. Kumekov and V. I. Perel', Zh. Éksp. Teor. Fiz. **94** (1), 346 (1988) [Sov. Phys. JETP **67**, 193 (1988)].
13. V. M. Galitskiĭ and V. F. Elesin, *Resonance Interaction of Electromagnetic Fields with Semiconductors* (Énergoatomizdat, Moscow, 1986), p. 192.

Translated by N. Korovin

Semiconductors, Vol. 37, No. 5, 2003, pp. 532–536. Translated from Fizika i Tekhnika Poluprovodnikov, Vol. 37, No. 5, 2003, pp. 552–556.

ELECTRONIC AND OPTICAL PROPERTIES OF SEMICONDUCTORS

Phonon-Assisted Exciton Luminescence in GaN Layers Grown by MBE and Chloride-Hydride VPE

M. G. Tkachman*^, T. V. Shubina*, V. N. Jmerik*, S. V. Ivanov*, P. S. Kop'ev*, T. Paskova, and B. Monemar****

** Ioffe Physicotechnical Institute, Russian Academy of Sciences, St. Petersburg, 194021 Russia*

*** Department of Physics and Measurement Technology, Linköping University, S-581 83 Linköping, Sweden*

^ e-mail: masha@beam.ioffe.rssi.ru

Submitted September 9, 2002; accepted for publication September 11, 2002

Abstract—Optical properties of GaN layers grown by the molecular-beam epitaxy (MBE) and chloride-hydride vapor-phase epitaxy (CHVPE) have been studied, and the quality of two types of samples has been compared. The photoluminescence spectra have an excitonic nature for both types of layers. To determine precisely the nature of exciton transitions, the reflectance spectra were studied. A key point was the investigation of phonon-assisted exciton luminescence, which provides information on the density distribution of the exciton states. Temperature dependences of the exciton transition energy and the ratio of intensities of one- and two-phonon replicas were studied. The high quality of both types of layers has been confirmed, though the concentration of acceptors in MBE-grown samples is higher than in CHVPE samples. *© 2003 MAIK "Nauka/Interperiodica".*

1. INTRODUCTION

Semiconducting nitrides of Group III elements are currently under intensive investigation. These compounds have a direct band structure with the energy gap ranging from 6.2 (AlN) to 1.9 eV (InN) or lower; thus, they are being applied in various optoelectronic devices (short-wavelength devices first and foremost).

As is known, the optical properties of semiconductors are strongly dependent on the behavior of excitons in a material, including their scattering on structural inhomogeneities (impurities, defects) and elementary excitations (phonons, etc.). Experiment and theory show that, for the case of polar semiconductors with direct transitions, excitons interact mainly with longitudinal optical (LO) phonons [1, 2]. Among the radiative processes related to the interaction of excitons with LO phonons, it is necessary to draw attention to free exciton luminescence with simultaneous emission of phonons. The principal specific feature of the spectral lines related to this process is the fact that their shape reflects the kinetic-energy distribution of free excitons, thus providing information on the density of exciton states in structures of varied quality [1, 3].

Phonon-assisted optical processes have been thoroughly studied in such polar semiconductors as CdS, CdSe, ZnO, and Cu_2O [1–3], whereas some specific features of exciton-phonon interaction in wide-gap nitrides deserve further study.

In the present study, we perform a comparative analysis of the quality of GaN layers grown by chloride-hydride vapor-phase epitaxy (CHVPE), which are promising substrates for nanostructures, and those obtained using molecular-beam epitaxy (MBE), as the basic methods for nanostructure growth. The photoluminescence (PL) and reflection spectra are studied, in particular, the shape and relative intensity of single-phonon and two-phonon (1LO and 2LO) replicas of the free A-exciton line.

2. SAMPLES AND EXPERIMENT

Two types of samples were studied. A thick (~25 μm) GaN layer was grown by CHVPE at a temperature of 1090°C on Al_2O_3(0001) substrate. The second sample, ~0.7 μm thick, was also grown on Al_2O_3(0001) substrate without a buffer by plasma-assisted MBE at 650°C [5]. Preliminary characterization of the structures was done using X-ray diffraction analysis (XRD), transmission electron microscopy (TEM), and scanning electron microscopy (SEM).

The PL and reflection spectra were recorded in a closed-cycle He cryostat at a temperature of 15 K. The temperature dependences of the PL spectra were studied in the temperature range of 15–280 K. The luminescence was excited by an He–Cd laser (325 nm). A xenon lamp was used in the study of the reflection spectra.

3. RESULTS AND DISCUSSION

Preliminary characterization demonstrated a high quality of thick CHVPE-grown GaN. According to TEM data, the density of dislocations in the surface

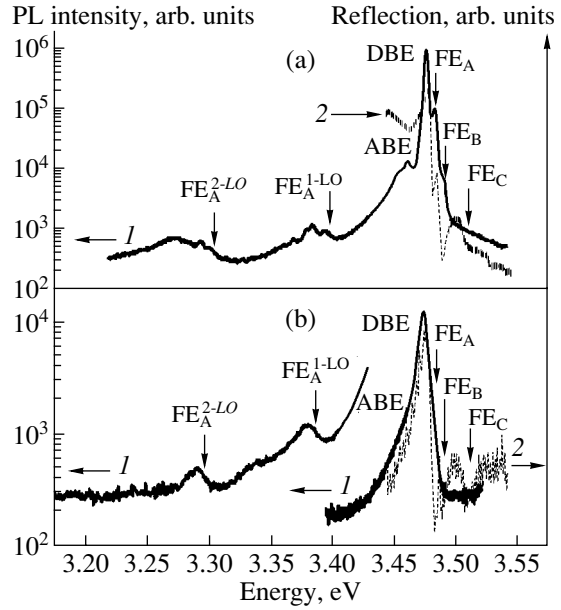

Fig. 1. (*1*) PL and (*2*) reflection spectra of GaN layers grown by (a) CHVPE and (b) MBE. T = 13 K.

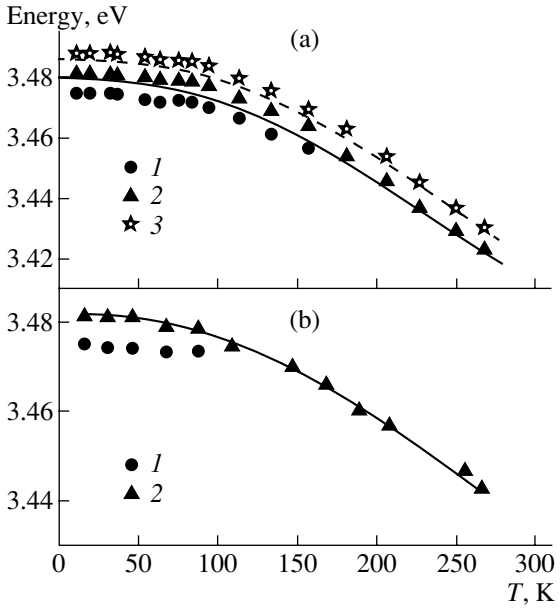

Fig. 2. The temperature dependences of the exciton transition energies for epitaxial GaN grown by (a) CHVPE and (b) MBE. Points: experimental dependence for the lines of (*1*) a donor-bound exciton (DBE), (*2*) a free A-exciton (FE$_A$), and (*3*) a free B-exciton (FE$_B$). Lines: fitting in terms of Pässler's model.

layer did not exceed 10^8 cm^{-2}. At room temperature, the layer experiences a biaxial compressive stress $\sigma \sim$ 0.2 GPa. According to XRD data, the structure has an unprecedentedly low deflection of columns from the growth axis **c** (the half-width of the ω-rocking curve in the Bragg configuration was ~62 seconds of arc). The structural characterization of thin MBE-grown GaN also showed a satisfactory quality of the layer. Average densities of vertical screw (10^8 cm^{-3}) and edge (10^{10} cm^{-3}) dislocations determined by XRD are close to the values in the thick layer.

Figure 1a shows the PL spectrum of a thick CHVPE-grown GaN layer recorded at T = 13 K. To unambiguously identify the PL lines, the surface reflection spectrum was recorded. The spectrum clearly shows excitonic features, and the energy spacings between them correlate with the known energies of free excitons in GaN [6]. The PL line of a donor-bound exciton (DBE) dominates at a low temperature. The low-energy shoulder of the DBE line is related to an acceptor-bound exciton (ABE). The emission lines of free A and B excitons (FE$_A$ and FE$_B$) are well resolved. The main DBE line also dominates in the spectrum of the thin MBE-grown GaN layer (Fig. 1b). A shoulder related to a free A-exciton is also seen. The observed resonance energies of the A-exciton emission are 3.4810 and 3.4820 eV for CHVPE- and MBE-grown samples, respectively, which indicates that the MBE-grown layer is more strained. However, the presence of excitonic features in the spectrum of MBE-grown GaN confirms the satisfactory quality of this sample.

For both samples, temperature dependences of the PL spectra were studied. According to earlier data [7, 8], at temperatures above 50 K, the free A-exciton line becomes dominant and the intensity of the main DBE line decreases. Temperature dependences of the exciton energies (Figs. 2a, 2b) were fitted using Pässler's analytical model [9], which describes fairly well the temperature behavior of energy levels in homoepitaxial GaN layers [10]:

$$E(T) = E(0) - \frac{\alpha_p \Theta_p}{2} \times \left[\frac{\rho}{2} \left(\sqrt[4]{1 + \frac{\pi^2}{6}\left(\frac{4T}{\Theta_p}\right)^2 + \left(\frac{4T}{Q_p}\right)^4} - 1 \right) + (1-\rho)\left(\coth\left(\frac{\Theta_p}{2T}\right) - 1 \right) \right], \quad (1)$$

where $E(0)$ is the energy of the main transition at T = 0 K; α_p is the slope of the high-temperature part of the $E(T)$ dependence; the parameter $\rho \geq 0$ determines the contribution of long-wavelength acoustic phonons, and $(1 - \rho)$, the interaction with optical and short-wavelength acoustic phonons; and Θ_p is defined in terms of the Debye temperature Θ_D as $\Theta_p \approx 2/3\Theta_D/(1 - 1/2\rho)$. The parameter ρ plays a key role in this model, as it specifies a change in the curvature of the fitting curve,

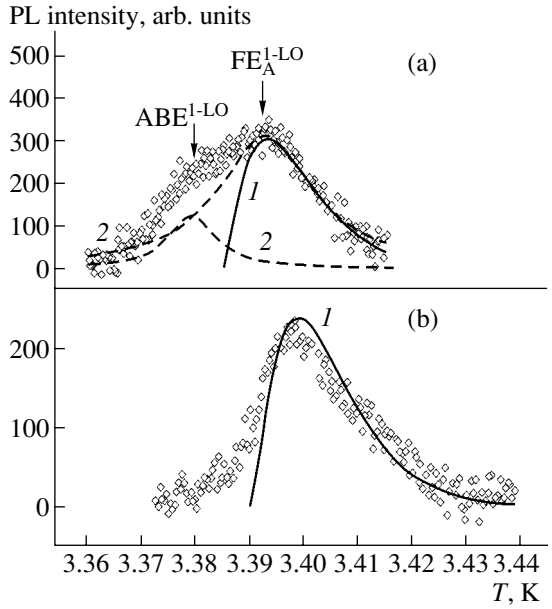

Fig. 3. PL spectra of a 1LO-replica of a free A-exciton for GaN layers grown by (a) CHVPE (recorded at $T = 64$ K) and (b) MBE ($T = 68$ K). Points: experimental data. Lines: (*1*) the dependence $I \sim E^{3/2}\exp(-E/kT)$, (*2*) the deconvolution of the experimental spectrum into two lines using the Lorentz profiles.

whereas the slope α and the point of intersection of the high- and low-temperature asymptotes are fixed.

A satisfactory approximation of the temperature dependences of the energy of the free A-exciton (FE_A) line for the samples under study was achieved at the same value of $\Theta_p = 420$ K and at different slopes α_p: 0.42 for CHVPE- and 0.29 for MBE-grown GaN. The values of the parameter ρ also differed: 0.3 for CHVPE-grown and 0.4 for MBE-grown GaN. This difference in the parameters describing the exciton–phonon interaction is indicative of different mechanisms of interaction with phonons in our samples, and it is this fact that stimulated us to investigate the phonon-assisted PL spectra.

The 1LO- and 2LO-phonon replicas of the free A-exciton line are well resolved in the PL spectra under study. Phonon replicas of ABE and DBE excitons are also observed (Fig. 1). The energy positions of the phonon replicas coincide with the known energy of an optical phonon in GaN (~92 meV). The 1LO-replica of ABE is well resolved in the PL spectra, and the intensity of single-phonon DBE luminescence is, by contrast, much smaller. The ratio of the intensities of the two-phonon replicas of these lines is quite the reverse. The two-phonon replica of DBE emerges, and the intensity of the 2LO-replica of ABE decreases. This effect was observed earlier [11, 12], where it was assigned to the difference in the radii of wave functions of excitons bound on a donor and an acceptor. Since there are "strict" momentum selection rules for the 1LO replica [3] (for more details, see below), the intensity of 1LO luminescence of a donor-bound exciton is low. With respect to two-phonon luminescence, since the process can proceed by various ways, the factor of a much higher density ($n \sim 10^{17}$ cm^{-3}) of intrinsic donors in the material becomes dominant and the two-phonon luminescence of a DBE exciton emerges.

The kinetic energy of excitons is directly manifested in the phonon-assisted radiative recombination of excitons. The shape of the phonon replica lines reflects the Maxwell distribution of excitons over kinetic energy. If thermal equilibrium exists in the exciton system, the line shape of the phonon-assisted exciton luminescence is well described by the Maxwell distribution [3]:

$$I_m^{LO} \sim (dN(k)/N)W_m(k) \sim E^{1/2}\exp(-E/k_BT)W_m(E), \quad (2)$$

where I_m^{LO} is the intensity of the respective phonon replica, m is the number of phonons involved in the process, E is the kinetic energy of an exciton, N is the density of exciton states, and $W_m(k, E)$ is the probability of phonon-assisted exciton emission of order m for an exciton with the kinetic energy E [1, 3]. The shapes of spectral lines for one- and two-phonon processes are essentially different, due to the difference in the quasi-momentum conservation rules for these processes. As shown in [3, 13], studying the shape of lines in the phonon luminescence spectra furnishes direct information on the real density of exciton states and on exciton scattering mechanisms (the presence and distribution of impurities, etc.). However, the dissimilarity in the momentum conservation rules for 1LO and 2LO processes results in significant differences in the line shapes for these processes. Indeed, in the case of 1LO luminescence involving an exciton with a momentum k_{ex}, the momentum of a generated phonon can only have a single value, $k_f \approx k_{ex}$, whereas for the two-phonon process the momentum conservation law looks like $k_{ex} = k_f' + k_f''$. This condition can be satisfied in multiple ways, with k_f' and k_f'' taking a number of values. As discussed in detail and confirmed experimentally [3], the line shape of two-phonon luminescence is well described by the Maxwell distribution $I \sim E^{1/2}\exp(-E/kT)$; i.e., the probability W_2 is independent of the exciton energy and is nearly the same for different excitons, with only the distribution of the kinetic energies of excitons manifested in the spectrum. The probability of the one-phonon process $W_1 \sim E$ (or k^2); thus, the line shape of one-phonon luminescence is described by the expression $I \sim E^{3/2}\exp(-E/kT)$. Therefore, it is the line shape of the one-phonon replica in the exciton luminescence spectra that contains information on the mechanisms of exciton scattering in a crystal. Previously, these results were obtained theoretically in [14,15].

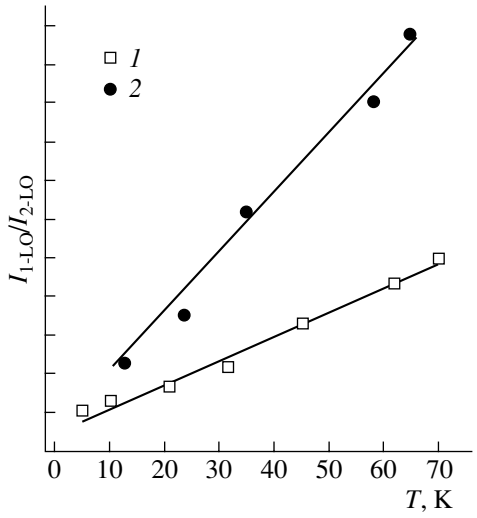

Fig. 4. The ratio of intensities of 1LO- and 2LO-replicas of the free A-exciton line vs. temperature. (*1*) CHVPE- and (*2*) MBE-grown samples. For clarity, the data for the MBE-grown sample are shifted along the ordinate axis.

We studied the shape of one-phonon replicas of free A-exciton luminescence lines for both types of GaN layers (Fig. 3). The shape of the 1LO spectral line of the thick CHVPE-grown layer is well described by the relation $I \sim E^{3/2}\exp(-E/kT)$ (Fig. 3b), whereas the spectrum of the thin MBE-grown sample (Fig. 3a) contains a clearly resolved additional component, which we identified as a 1LO replica of the emission line of an acceptor-bound exciton. This assignation is confirmed (as mentioned above) by the fact that the contribution of the acceptor-bound exciton is well pronounced in the one-phonon replica [12], whereas, in the two-phonon replica, the contribution of the donor-bound exciton is dominant, with the acceptor line virtually disappearing. Since the intensities of ABE^{1LO} and FX_A^{1LO} phonon replicas are comparable, we can assume that acceptor impurities are present in thin MBE-grown GaN layers. Carbon can act as an impurity of this kind, as confirmed by the SIMS spectra of MBE-grown GaN structures [16]. The different ways in which the momentum conservation laws are formulated for one- and two-phonon luminescence not only lead to a dissimilarity in the respective line shapes, but also cause a change in the relative intensities of these lines with temperature. As shown earlier [1, 14], the probability of the 1LO-process is proportional to the squared momentum of an exciton. With increasing temperature, the average thermal momentum of an exciton grows. Consequently, the overall probability of one-phonon recombination increases and the intensity of the 1LO-line becomes higher. Since the probability of the two-phonon process is, to a first approximation, independent of the magnitude of exciton momentum, we can calculate, with a knowledge of the relations describing the shape of one- and two-phonon emission lines, the ratio of their integral intensities as a function of temperature [3]:

$$S = I^{1LO}/I^{2LO} \sim T, \quad (3)$$

where I^{1LO} and I^{2LO} are the integrated intensities of the one- and two-phonon lines.

Figure 4 shows the intensity ratio of 1LO- and 2LO-lines as a function of temperature for CHVPE- and MBE-grown GaN samples. As can be seen, the intensity ratio of the phonon replicas linearly increases with temperature but the slope of the dependence is higher for the MBE-grown layer. As shown in [1, 13], this indicates that scattering on impurities and intrinsic defects, whose concentration is higher in the MBE-grown layer, makes a considerable contribution to the radiative recombination of excitons.

4. CONCLUSION

The study of zero-phonon and phonon-assisted PL has been used to compare the quality of CHVPE- and MBE-grown epitaxial GaN layers. Excitonic spectral features were observed for thin layers grown by MBE without a buffer at thicknesses about 25 times smaller than those of CHVPE-grown layers. This indicates that MBE is a promising technique for the fabrication of high-quality nanostructures.

The comparative study of the shape and the temperature dependence of 1LO- and 2LO-phonon replicas for thick CHVPE-grown GaN layers has shown that the phonon-assisted recombination of excitons in these layers is not affected by scattering on impurities and defects, which is observed in thin MBE-grown GaN layers. The comparison of the shapes of 1LO-phonon replicas for two types of samples indicates that the concentration of acceptor impurity (probably, carbon) is higher in MBE-grown layers compared with CHVPE-grown GaN samples.

REFERENCES

1. S. A. Permogorov, in *Excitons*, Ed. by E. I. Rashba and M. D. Sturge (North-Holland, Amsterdam, 1982; Nauka, Moscow, 1985).
2. R. S. Knox, *Theory of Excitons* (Academic, New York, 1963; Mir, Moscow, 1966).
3. E. F. Gross, S. A. Permogorov, and B. S. Razbirin, Usp. Fiz. Nauk **103**, 431 (1971) [Sov. Phys. Usp. **14**, 104 (1971)].
4. T. Paskova, S. Tungasmita, E. Valcheva, *et al.*, MRS Internet J. Nitride Semicond. Res. **5S1**, W3.14 (2000).
5. V. N. Jmerik, V. V. Mamutin, V. A. Vekshin, *et al.*, Mater. Sci. Eng. B **59**, 60 (1999).
6. B. Monemar, Mater. Sci. Eng. B **59**, 122 (1999).
7. B. Monemar, J. P. Bargman, T. Lundström, *et al.*, in *Proceedings of Topical Workshop on III–V Nitrides*,

Nagoya, Japan (1995); Solid State Electron. **41**, 181 (1997).

8. S. Chichibu, T. Azuhata, T. Sota, and S. Nakamura, J. Appl. Phys. **79**, 2784 (1996).
9. R. Pässler, J. Appl. Phys. **83**, 3356 (1998).
10. K. Thonke, K. Kornitzer, M. Grehl, *et al.*, IPAP Conf. Ser. 1: IWN2000, 587 (2000).
11. K. P. Korona, A. Wysmolek, J. M. Baranovski, *et al.*, Mater. Res. Soc. Symp. Proc. **482**, 501 (1998).
12. T. V. Shubina, T. Paskova, A. A. Toropov, *et al.*, Phys. Status Solidi B **228**, 481 (2001).
13. I. A. Buyanova, J. P. Bergman, B. Monemar, *et al.*, Solid State Commun. **8**, 497 (1998).
14. A. I. Ansel'm and Yu. A. Firsov, Zh. Éksp. Teor. Fiz. **30**, 719 (1956) [Sov. Phys. JETP **3**, 564 (1956)].
15. K. K. Rebane, V. G. Fedoseev, and V. V. Khizhnyakov, in *Proceedings of IX International Conference on Physics of Semiconductors* (Moscow, 1968).
16. E. Calleja, M. A. Sánchez-García, and F. J. Sánchez, Phys. Rev. B **62**, 16826 (2000).

Translated by D. Mashovets

Semiconductors, Vol. 37, No. 5, 2003, pp. 537–545. Translated from Fizika i Tekhnika Poluprovodnikov, Vol. 37, No. 5, 2003, pp. 557–564.

ELECTRONIC AND OPTICAL PROPERTIES OF SEMICONDUCTORS

Electronic Properties of Irradiated Semiconductors. A Model of the Fermi Level Pinning

V. N. Brudnyi*, S. N. Grinyaev*, and N. G. Kolin**

** Kuznetsov Physicotechnical Institute, pl. Revolyutsii 1, Tomsk, 634050 Russia*

e-mail: brudnyi@ic.tsu.ru

*** Karpov Institute of Physical Chemistry (Obninsk Branch), Obninsk, Kaluga oblast, 249033 Russia*

Submitted July 22, 2002; accepted for publication October 16, 2002

Abstract—A theoretical model of a defect state with highest localization in a semiconductor crystal is suggested. This model can be used to calculate the steady-state position of the Fermi level in radiation-modified semiconductors and to estimate the barrier height in metal–semiconductor contacts and the energy-band offsets in semiconductor heterojunctions. It is shown that the deepest level in the band gap of each semiconductor corresponds to the above state. This level plays a role similar to that of the level of electronic chemical potential in a bulk imperfect semiconductor and at the interphase boundary. Numerical calculations of the energy position of the level under consideration in the band gaps of Group IV and III–V compound semiconductors were performed. © *2003 MAIK "Nauka/Interperiodica".*

1. INTRODUCTION

It is well known that high-energy irradiation (bombardment with gamma-ray photons, electrons, ions, and fast neutrons) of semiconductors gives rise either to localized energy defect states of dangling bonds, in the case of irradiation with gamma-ray photons, electrons, or low-energy protons, or to local energy levels and tails of the gap states due to formation of point defects and macroscopic defect clusters, as a result of irradiation with heavy ions or fast neutrons. All these states radically affect the electrical properties of semiconductors. This is caused by the fact that, as a result of the buildup of radiation defects in the crystal lattice of semiconductors, the Fermi level position changes, which represents the main cause of modification of a material's electronic characteristics. The Fermi level position in an imperfect semiconductor and, correspondingly, the electronic properties of such a material are governed by a balance between radiation defects of donor and acceptor types. Since the types and properties of the majority of radiation defects, especially in compound semiconductors, are poorly known, the main problem in studying the properties of radiation-modified materials is related to the development of a model for an irradiated semiconductor; this model should be applicable to the calculation of electronic properties of this semiconductor, taking into account that there is a lack of information about the origin and parameters of radiation defects.

In this study, we develop a theoretical model that ensures a unified understanding of the processes occurring in the course of both radiation modification of electronic characteristics of semiconductors and the formation of interphase boundaries. This model is based on the well-known phenomenon of Fermi level pinning in the steady-state (limiting) position F_{sat}, which is characteristic of every semiconductor and is independent of irradiation conditions and the history of a material [1, 2]. Numerous studies show that similar Fermi level pinning occurs in covalent (and highly covalent) semiconductors at the metal–semiconductor interfaces (Schottky barriers) and semiconductor heterojunctions. Moreover, experimental data indicate that there is close agreement between the values of F_{sat} and F_{bS} (the latter stands for the Schottky barrier height) in studied materials [3, 4]. This observation indicates that there is a unified origin of the Fermi level pinning both in semiconductors with a high density of intrinsic structural defects and at the interphase boundaries; this circumstance makes it possible to consider the phenomenon of pinning using a unified approach.

2. BASIC CONCEPTS

Since the physics of interfaces in semiconductors has been developed to a much greater extent than that of radiation-modified semiconductors, we will start with a consideration of the problem of Fermi level pinning at interphase boundaries. Models of Fermi level pinning at interfaces are typically based on the concepts of the origin of defect-related (gap) states in the semiconductor band gap. In the defect-related models (the model of surface atomic disorder [5] and the model of unified defect [6]), it is assumed that a defect is a necessary component of an interphase boundary; it is also assumed that characteristics of this defect are more important in interphase-boundary formation than bulk

thermodynamic potentials (the work function, electron affinity, and so on). In the model of atomic disorder, the tails of the density of states appearing in the surface region of the semiconductor as a result of atomic disorder are considered as the aforementioned defects; in addition, the position of the chemical potential at the interface is identified with the minimum of the density of surface states. In the unified-defect model, it is assumed that the Fermi level pinning at the interface occurs in the vicinity of the defect which exceeds in concentration all other defects; the dominant defects of this type presumably include vacancies, antisite defects, and defect clusters formed during fabrication of the barrier. Insufficient information about the origin of possible defects and difficulties in obtaining reliable calculated energies of corresponding defect states responsible for interphase-boundary formation limit the applicability domain of defect-related models. Therefore, idealized models of interfaces have become widely accepted; these models are based on the concept of gap quantum-mechanical states of the tunneling type, which are introduced into the band gap of a semiconductor in the surface region [7]. Filling these states with electrons defines the position of the level of the charge (local) electroneutrality E_{LNL} for an interphase boundary and, thus, the properties of this boundary [8, 9]. A special feature of these studies [8, 9] consists in the fact that the Schottky barrier height and, correspondingly, the energy-band offsets in heterojunctions are completely defined by the parameters of the electronic energy-band spectrum of a bulk crystal and are independent of the interphase-boundary state. This circumstance makes it possible to use the calculated value of E_{LNL} for estimating the Fermi level position F_{sat} in bulk semiconductors subjected to high-energy radiation. The values of E_{LNL} calculated on the basis of the above models were found to be close to experimental data on both F_{sat} in irradiated semiconductors and F_{bS} for the Schottky barriers [2, 4, 9].

In this study, we used the results of previous experimental and theoretical investigations [1, 2, 4, 10] to develop a new approach to the problem of Fermi level pinning in an imperfect crystal and at the interphase boundary; in this approach, the level of local electroneutrality E_{LNL} is treated as a particular case of electronic-structure invariants, which are independent from the crystal matrix in a group of semiconductors with related types of chemical bonding. Such invariants that can be related to the observed physical quantities are the moments of the single-particle Green function. In particular, the first moment of the Green function characterizes the charge density; the highest localization of this density for a gap state defines the energy level, which is identical in related semiconductors. It is assumed in the model that there exist localized states which have almost the same energies in all similar semiconductive materials; we develop a model for determining the energy-level position for such localized states. We also consider the relation of this level to the limiting position of the Fermi level in a bulk semiconductor enriched with radiation defects and also with the height of the barrier at the interface and offsets of energy bands in semiconductor heterojunctions.

3. MODEL CALCULATIONS

Let W be the potential of a defect which introduces a deep localized state, and let H_0 be the Hamiltonian of an ideal crystal. The energy E and the wave function $\Phi(r)$ of the deep-level center are determined from the Schrödinger equation

$$(H_0 + W)\Phi(r) = E\Phi(r).$$

The wave function $\Phi(r)$ can either be represented in the form of an expansion in the ideal-crystal states $\psi_{nk}(r)$ as

$$\Phi(r) = \sum_{nk} C_{nk}\psi_{nk}(r), \qquad H_0\psi_{nk}(r) = E_{nk}\psi_{nk}(r) \tag{1}$$

or determined from the integral equation

$$\Phi(r) = \int G_0(r, r')W(r')\Phi(r')dV',$$

where $G_0(r, r')$ is the Green function for an ideal crystal, i.e.,

$$G_0(r, r') = \sum_{nk} \psi_{nk}(r)\psi^*_{nk}(r')/(E - E_{nk}). \tag{2}$$

Summation is performed over all bands n and wave vectors k within the first Brillouin zone. Using formulas (1) and (2), we can write the coefficients C_{nk} in the expansion as

$$C_{nk} = M_{nk}/(E - E_{nk}),$$
$$M_{nk} = \langle \psi_{nk}|W|\Phi\rangle.$$

For highly localized defect states, the matrix element M_{nk} depends only slightly on the wave vector; as a result, this dependence can be ignored in the first approximation. In addition, it follows from calculations of wave functions for point defects that the coefficients C_{nk} have pronounced peaks in the vicinity of the band extrema; these peaks are governed mainly by the energy denominator $E - E_{nk}$. This circumstance makes it possible to ignore the dependence of M_{nk} on the band number as well. As a result, we obtain the following approximate expression for the wave function of the defect:

$$\Phi_E(r) = M\sum_{nk} \psi_{nk}(r)/(E - E_{nk}). \tag{3}$$

The mean matrix element of the defect potential M is determined from the condition for the wave-function normalization

$$M = \left(-\frac{\partial G_0(E)}{\partial E}\right)^{-1/2},$$

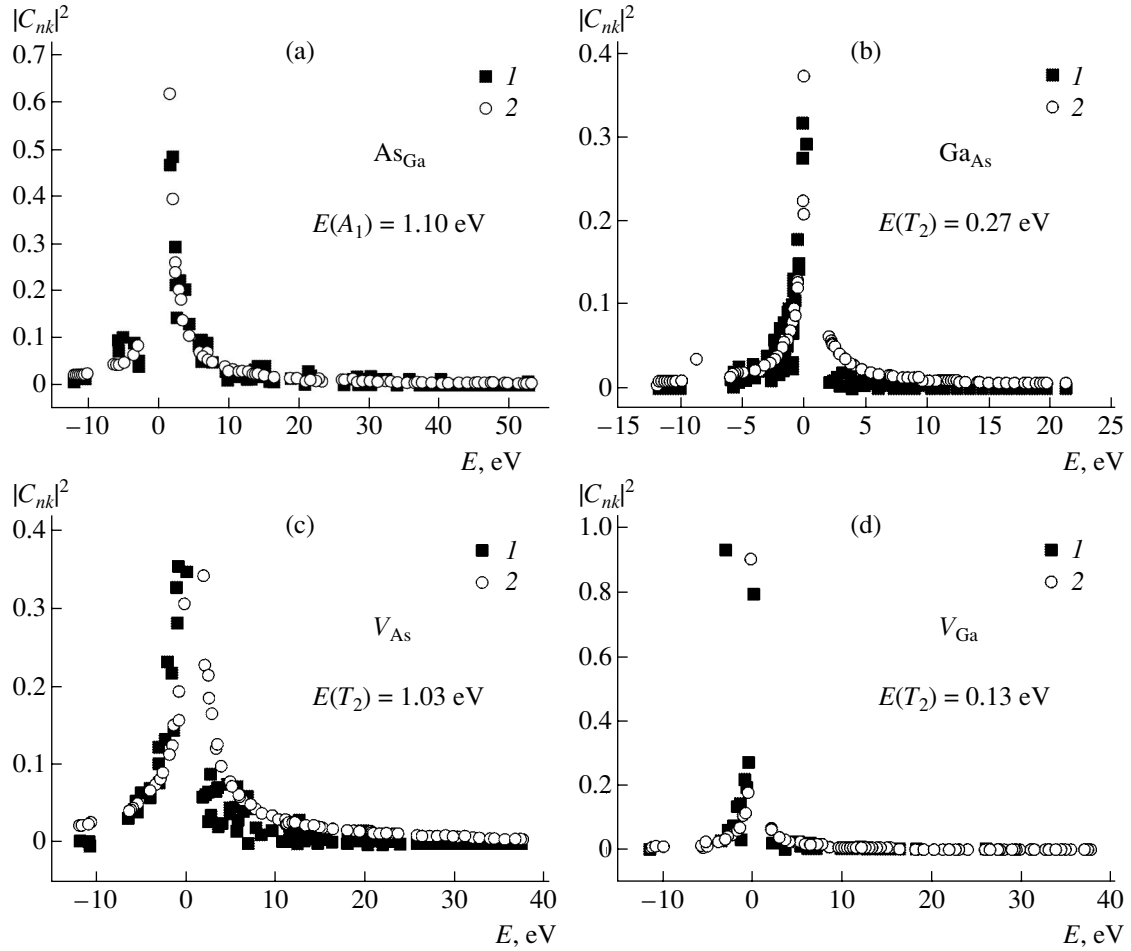

Fig. 1. Squared moduli of coefficients in the expansion (in symmetrized Bloch functions) of localized functions of intrinsic defects (a) As_{Ga}, (b) Ga_{As}, (c) V_{As}, and (d) V_{Ga} in GaAs: (*1*) the results of pseudopotential-based calculations and (*2*) the coefficients in model function (*3*). The energies are reckoned from the valence-band top.

where

$$G_0(E) = \sum_{nk} \frac{1}{(E - E_{nk})} = \int \frac{\rho(E')dE'}{(E - E')}$$

is the energy representation of the Green function $G_0(r, r')$ and $\rho(E)$ is the density of states in an ideal crystal. Function (3) depends only on the bulk energy-band spectrum and the Bloch wave functions of an ideal crystal. The energy corresponding to this function satisfies the equation $[-\partial G_0(E)/\partial E]^{1/2} = G_0(E)$ and depends only on the density of states.

Pantelides *et al.* [11] used the method of Green functions to show that the deep-level state of an unrelaxed vacancy in Si could be described using model wave function (3). We similarly studied the localized states generated by the intrinsic defects in GaAs, i.e., gallium vacancies V_{Ga}, arsenic vacancies V_{As}, and antisite defects Ga_{As} and As_{Ga}, which can be introduced into GaAs using high-energy irradiation. The deep levels of defects were calculated using the pseudopotential methods and an extended unit cell ($8 \times 8 \times 8$) in a basis of symmetrized combinations of Bloch functions for an ideal crystal (see [10, 12]).

In Fig. 1, we show the calculated squared moduli of coefficients C_{nk} for symmetrized functions at the points in the Brillouin zone which are equivalent to the point Γ in the superlattice; the corresponding coefficients in model function (3) calculated for the deep-level energies determined from the pseudopotential calculation are also shown. With allowance made for the correction of the spin–orbit splitting of the valence band, the energy-level positions coincide with those reported by Grinyaev and Chaldyshev [10, 12]. It follows from Fig. 1 that, for all states (as in the case of a vacancy in Si [11]), the wave functions of deep-level centers are mostly composed of the states in the vicinity of extrema of the valence and conduction bands; i.e., these functions are similar to those obtained in the effective-mass approximation. It can be seen from a comparison of the data shown in Fig. 1 that the coefficients of the model function yield an averaged (and satisfactory) description of the results of exact calculation. The charge den-

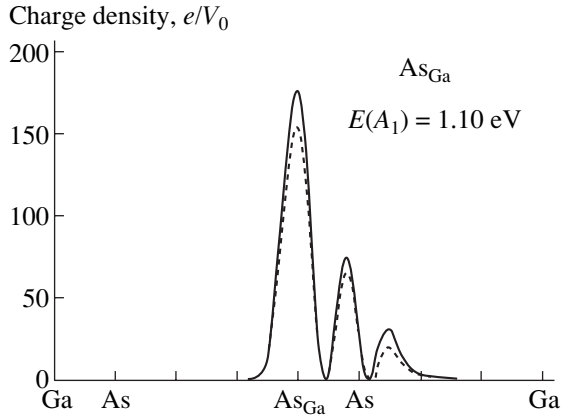

Fig. 2. The distribution of the charge density for the deep center A_1 of the antisite defect As_{Ga} in GaAs along the direction of the covalent bond [111]. V_0 is the volume of an extended unit cell. The solid line represents the results of the pseudopotential-based calculation, and the dashed line corresponds to the calculation based on model function (3).

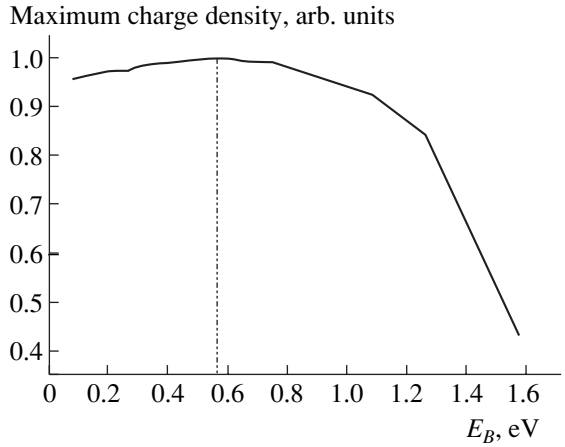

Fig. 3. The maximum of the charge density for a deep state with symmetry A_1 in the cation sublattice as a function of the energy position of this state (level E_B) in the GaAs band gap; the calculation was based on the model function defined by formula (3).

sities of the states under consideration are localized in the vicinity of defects within a sphere with a radius of about 2–3 Å. The functions of deep-level centers depend not only on the moduli but also on the phases of coefficients in expansion (1). If the phases in the model-function expansion (3) are set the same as those for the function calculated by the pseudopotential method, the distributions of corresponding charge densities will be almost identical in both cases (Fig. 2). Localization of the defect function depends on the deep-level position in the band gap. Such a dependence is shown in Fig. 3 for model function (3), which has symmetry A_1 and is localized at a cationic lattice site in GaAs (As_{Ga}). A maximum in the charge density of this defect state is attained at the energy of $E_B \approx E_V + 0.57$ eV.

The aforementioned properties of the model function $\Phi_E(r)$ make it possible to use it as a trial function, which depends on the energy E as a parameter, to determine the deep-level position for the known defect potential. Typically, the relaxation and distortion of the lattice result in a reduction of symmetry of the actual-defect potential. The symmetry of relaxed defect depends on its type. For example, the symmetry can be completely absent for the complex defects produced as a result of irradiation. Therefore, we will assume in what follows that the defect potential does not possess symmetry and that expansion (3) consists of nonsymmetrized Bloch functions $\psi_{nk}(r)$.

We now specify another crystal whose crystalline potential differs from the initial potential by ΔV. Generally, another deep-level energy $E + \Delta E$ and another wave function $\Phi + \Delta\Phi$ would correspond to the previous defect. Using expression (3), we obtain the following correction to the energy of the deep level in the initial crystal in the first order of perturbation in parameter ΔV in the initial crystal:

$$\Delta E = M^2 \sum_{nk,\, n'k'} \langle \psi_{nk}(r)|\Delta V|\psi_{n'k'}(r)\rangle/(E - E_{nk})(E - E_{n'k'}).$$

If the Bloch wave functions corresponding to the Hamiltonian functions H_0 and $H_0 + \Delta V$ are close to each other, the condition for minimization of ΔE with respect to the deep-level position E

$$\partial\Delta E/\partial E = 0$$

yields the equation

$$\left[\sum_{nk} 1/(E - E_{nk})^3\right]\left[\sum_{nk} 1/(E - E_{nk})^2\right]^{-1} \times \sum_{nk} \Delta E_{nk}/(E - E_{nk})^2 - \sum_{nk} \Delta E_{nk}/(E - E_{nk})^3 = 0, \quad (4)$$

where ΔE_{nk} is the difference between the energy-band spectra (the band offsets) for two crystals. The deep-level energy defined by Eq. (4) depends on the characteristics of two crystals (in terms of ΔE_{nk}) and, therefore, is not transitive. However, compounds with the same types of chemical bonding and crystal structure have generally similar energy-band spectra; as a result, ΔE_{nk} depend (on average) more weakly on the band number and wave vector compared with the quantity in the denominator in Eq. (4) if the deep level E_B is located within the band gap. The above is especially true for the second term in Eq. (4); this term includes the higher power of the energy difference, $(E - E_{nk})^3$. Therefore, it follows that Eq. (4) has an approximate solution defined by the relation

$$2\sum_{nk} 1/(E_B - E_{nk})^3 = \frac{\partial^2 G_0(E_B)}{\partial E^2} = 0, \quad (5)$$

Table 1. Calculated band-gap widths E_g, positions of the deep defect level E_B, and the levels of local electroneutrality E_{LNL}; experimental values of the steady-state Fermi level position in an irradiated semiconductor F_{sat} and the Schottky barrier heights F_{bS}; and the calculated position of the level E_B in reference to the vacuum level (E_B^{abs})

Crystal	E_g	E_B	E_{LNL}^*	E_{LNL} [16]	F_{sat} (experiment) [2, 4]	F_{bS} (experiment) [4, 16]	E_B^{abs}
Si	1.20	0.47	0.39	0.36	0.39	0.32–0.48	4.65
Ge	0.78	0.26	0.18	0.18	0.13	0.07–0.18	4.54
3*C*-SiC	2.42	1.53	1.40	–	–	1.0–1.05	–
BP	1.99	0.95	0.81	–	–	0.87	–
AlP	2.48	1.37	1.20	1.27	–	–	–
AlAs	2.24	1.07	0.88	1.05	–	0.94–1.04	4.93
AlSb	1.60	0.63	0.47	0.45	0.5	0.55–0.60	4.64
GaP	2.37	1.16	1.00	0.81	1.0 ± 0.2	0.94–1.27	4.89
GaAs	1.51	0.77	0.63	0.50	0.6	0.52–0.82	4.73
GaSb	0.87	0.24	0.14	0.07	0.02–0.05	0.07–0.10	4.61
InP	1.43	1.03	0.89	0.76	1.0	0.76–0.98	4.67
InAs	0.42	0.53*	0.51*	0.50	0.52	0.42–0.47	4.78
InSb	0.24	0.17*	0.12*	0.01	0.0	0.0–0.15	4.66

Note: Asterisks (*) indicate refined data obtained in this study with 913 special points taken into consideration; the values of E_{LNL}^* were calculated according to the model reported in [2]; the energies are expressed in eV; and the calculated values of E_B, E_{LNL}, and F_{sat} are given in reference to the valence-band top.

where the energy E_B depends on the energy-band spectrum of only one of the crystals and, thus, satisfies the condition for transitivity. It follows from the form of the wave function for the deep-level center (3) that Eq. (5) corresponds to the condition for maximization of both the relevant normalization factor and the mean defect potential M; accordingly, the condition for highest localization of the state near the defect is also satisfied. Thus, the deep-level center with the highest degree of localization of the wave function has an energy E_B; the latter depends the least on the crystal matrix, into which the center under consideration is introduced.

The energies E_B for various crystals were calculated using formula (5), the methods of singular points [13] and empirical nonlocal pseudopotential [14, 15], and taking into account the spin–orbit interaction. For the majority of compounds, the values of E_B can be determined within ~0.02 eV if ten special points and ~100 spin orbitals are taken into account. In the case of narrow-gap InSb and InAs compounds, the position of the E_B level depends more heavily on the states in the Γ valley of the lower conduction band, in which the effective electron mass is low. Therefore, we took into account 913 special points in the irreducible part of the Brillouin zone in order to improve the accuracy of calculating E_B; these points were determined by the method of extended unit cell ($32 \times 32 \times 32$). The graphical solution to Eq. (5) for GaAs is shown in Fig. 4. The calculated energy levels E_B in reference to the valence-band top are listed in Table 1. The positions of the electroneutrality levels E_{LNL} calculated previously [2, 16] for the semiconductors under consideration and the experimental values of the Schottky barrier height F_{bS} (mainly, for contacts with Au and Al [9, 16]) are also listed in Table 1.

It can be seen from the results listed in Table 1 that, despite approximations used in deriving Eq. (5), the obtained values of E_B are close to the limiting position of the Fermi level in the band gap of irradiated semiconductors F_{sat} and to the Schottky barrier heights F_{bS}; in addition, the dependence of E_B on the band gap in the sequence of materials under investigation is similar to the corresponding dependences of F_{bS} and F_{sat}. Such a correlation between calculated and experimental data show that, as in the case of E_B, the positions of E_{sat} and F_{bS} are governed mostly by averaged integrated characteristics of the crystal energy-band spectrum. Using calculated values of E_B and experimental data for the first ionization potentials I_p of the semiconductors under consideration [17], we can estimate the level position E_B on the absolute energy scale (in reference to the "vacuum" level). These values of $E_B^{\text{abs}} = I_p - E_B$ are listed in Table 1. According to estimations, the mean value of $E_B \langle E_B^{\text{abs}} \rangle$ for the materials under investigation is equal to about 4.71 eV. These data support the conclusion that E_B is a unified energy level in all related tetrahedral semiconductors.

Table 2. Energies of interband transitions E_g, $E_{\Gamma X}$, $E_{\Gamma L}$, E_1, and Δ_0; and the deep-center level E_B and the level of local electroneutrality E_{LNL} in model [2] for GaAs, InAs, and InSb at two temperatures T

Semiconductor	T, K	E_g	$E_{\Gamma X}$	$E_{\Gamma L}$	E_1	Δ_0	E_{LNL}	E_B
GaAs	10	1.52	1.94	1.82	3.12	0.34	0.61	0.76
	300	1.44	1.88	1.78	3.06	0.34	0.59	0.73
InAs	10	0.42	1.84	1.51	2.70	0.41	0.51	0.53
	300	0.35	1.76	1.43	2.62	0.41	0.49	0.49
InSb	10	0.24	1.03	0.71	2.00	0.86	0.12	0.17
	300	0.17	0.93	0.63	1.93	0.86	0.09	0.12

Note: Energies are expressed in eV.

Table 3. Magnitudes of the valence-band offsets ΔE_V at interfaces between semiconductors according to this study (ΔE_V^*) and according to calculations based on the models reported in [2, 16]

Heterostructure	$\lvert\Delta a\rvert$, Å	ΔE_V^*	ΔE_V [2]	ΔE_V [16]	ΔE_V, experiment [17, 19]
Ge/Si	0.22	0.21	0.21	0.18	0.17, 0.2, 0.4
GaP/Si	0.02	0.69	0.61	0.45	0.62, 0.80
GaAs/Si	0.22	0.30	0.24	0.14	0.05
Si/GaSb	0.66	0.23	0.25	0.29	0.05, 0.15
InAs/Si	0.62	0.06	0.11	0.14	0.15
InP/Si	0.43	0.56	0.50	0.40	0.56, 0.57
GaAs/Ge	0.01	0.51	0.45	0.32	0.35, 0.56, 0.65
AlAs/Ge	0.01	0.81	0.70	0.87	0.89, 0.92, 0.95
GaP/Ge	0.20	0.90	0.82	0.63	0.80, 0.88
InP/Ge	0.21	0.77	0.71	0.58	0.64
InAs/Ge	0.40	0.27	0.32	0.32	0.33
AlAs/GaAs	0.01	0.30	0.25	0.55	0.34, 0.45, 0.56
InAs/GaAs	0.40	0.24	0.12	0.0	0.05, 0.17
GaSb/InAs	0.04	0.29	0.36	0.43	0.40, 0.46, 0.51, 0.57
AlSb/GaSb	0.04	0.39	0.33	0.38	0.4, 0.45, 0.46
GaP/InP	0.41	0.13	0.11	0.05	0.27
InP/GaAs	0.21	0.26	0.26	0.26	0.36
GaP/GaAs	0.20	0.39	0.37	0.31	0.63

Note: $\lvert\Delta a\rvert$ is the difference between the lattice constants of the heterostructure components. Energies are expressed in eV.

We considered the temperature dependence of the E_B level for GaAs, InAs, and InSb. This dependence is related to changes in the energy-band structure, which are caused by thermal expansion of the lattice and vibrations of the lattice atoms. In order to take these vibrations into account, we renormalized the atomic pseudopotentials using the Debye–Waller factor and by accounting for standard deviations (see [18]). The results of calculations for two temperatures (10 and 300 K) are listed in Table 2. The data show that $\partial E_B/\partial T \approx (1/3)\partial E_g/\partial T$ in a wide-gap semiconductor (e.g., GaAs) and $\partial E_B/\partial T \approx (1/2)\partial E_g/\partial T$ in narrow-gap semiconductors (e.g., InSb and InAs). An increase in the temperature coefficient for the E_B level in narrow-gap semiconductors is related to the corresponding increase in the temperature dependence of energies of side valleys in the lower conduction band; these side valleys make the major contribution to the Green function and its derivatives with respect to energy.

Using the condition for the continuity of the E_B level at the heteroboundaries between related semiconductors and the relation

$$\Delta E_V = E_B(1) - E_B(2),$$

where $E_B(1)$ and $E_B(2)$ are the energy levels E_B in reference to the top of the valence bands in semiconductors 1 and 2, we can also estimate the valence-band offsets for various semiconductor heterostructures (Table 3). In the calculation under consideration (as in [2, 9]), the stresses, which appear in the layers and are caused by a mismatch in the lattice constants of components, were disregarded; as a result, the best agreement between theory and experiment is mainly observed for less stressed structures. For the known parameters of strains in the layers, corrections to the band offsets can be accounted for in the model under consideration in terms of corresponding changes in the energy-band spectra of semiconductors.

4. DISCUSSION

We note that, in this study, the model of a deep-level center is not directly related to any specific defect in the crystal. Rather, in this model, which constitutes a development of the unified-defect model [5], a single, albeit very important, attribute of the deep-level center is taken into account, specifically, the most pronounced localization of the wave function for this center compared to all other possible defects in the material. It is for the energy $E = E_B$ that the lowest sensitivity of this deep level to variations in the crystalline semiconductor matrix and to the type of metal at the interface is ensured. In this case, localized states with energies close to that of the level E_B are least sensitive to the type of crystal in the sequence of related semiconductors; the defects corresponding to these states [such as the well-known center *EL*2 in GaAs (the As_{Ga} antisite defect)] can accumulate in the course of irradiation, which is confirmed by experimental data on the spectra of electron spin resonance [20]. It is noteworthy that the specific type of radiation defects dominant in a semiconductor depends to a great extent on irradiation conditions (the sample temperature, the energy and mass of incident particles, and so on) and sometimes on the material's history; in the particular case of the energy region $E = E_B$, the density of defect states can be insignificant. For example, in the case of irradiation of GaAs with γ-ray photons or electrons (1–2 MeV) at temperatures $T \lesssim 295$ K, so-called electron (*E*) and hole (*H*) traps are accumulated; presumably, these traps are related to elementary defects in the As sublattice and have levels concentrated in the upper and lower halves of the band gap, respectively (i.e., away from the energy $E_B = E_V - 0.77$ eV for GaAs [21]). Such a system of radiation defects is found to be thermally unstable and anneals out at temperatures in the vicinity of 200°C. At the same time, irradiation of GaAs with electrons at elevated temperatures (>200°C) or with ions or fast neutrons at about 295 K leads to the preferential formation of so-called *P* centers whose energy levels are grouped around the energy E_B [21, 22]. Hypothetically, these centers correspond to more complex defects (e.g., clusters), since they remain stable even when the samples are heated to high temperatures (as high as 450–650°C). We may assume that, in the course of high-temperature irradiation (when elementary defects are mobile in the crystal lattice) or irradiation of the semiconductor with heavy ions or fast neutrons, which form collective defects (so-called displacement spikes), defects of the cluster type should be preferentially formed; these defects can pin the Fermi level in the vicinity of E_B, as was shown by the example of Ga clusters in GaAs [10]. However, when applied to irradiated semiconductors, this problem requires special consideration with allowance made for the nature and sizes of the defect clusters.

Since a deep-level defect with an energy E_B is formed from the Bloch states, which correspond to large regions of the Brillouin zone and to many energy bands, the properties of this defect depend only slightly on the special features of the energy-band structure in the energy interval close to the band gap E_g of the semiconductor and also on the specific type of material and orientation of the interphase boundary. As a result, the electronic properties of an irradiated semiconductor (e.g., the Hall coefficient and the Seebeck coefficient) are governed precisely by the special features of the energy-band spectrum of the semiconductor in the energy interval near E_B; i.e., the above properties depend on the positions of the levels Γ_{6C} in direct-gap semiconductors and the levels X_{6C} and L_{6C} in indirect-gap semiconductors and also on the position of the Γ_{8V} level in reference to the energy $E_B(\equiv F_{sat})$. For example, the high resistivity of irradiated GaAs (~10^8–10^9 Ω cm at 300 K [23, 24]) and the n^+-type electrical conductivity of irradiated InAs (~10^{-3} Ω cm at 300 K [25]) are caused by the fact the level F_{sat} is pinned near the middle of the narrowest band gap in GaAs and in the conduction band of InAs (Table 1). This circumstance is related to specific features of the energy-band spectrum in the semiconductors under consideration. In particular, the n^+-type conductivity in irradiated InAs is caused by the low position of the level Γ_{6C}, which is formed by the heavy In cation, in reference to the energy E_B. The special features of the electronic properties of other irradiated semiconductors can be considered similarly. For example, the $p(p^+)$-type conductivity of irradiated binary antimonides is caused by significant spin–orbit splitting of the valence band in these materials. Thus, the level position $F_{sat}(\equiv E_B)$ in the energy-band spectrum of a crystal controls the steady-state electron n_{sat} (and hole p_{sat}) concentrations and, correspondingly, the electronic properties of an irradiated semiconductor. Notably, the radiation-induced modification of a semiconductor's electrical characteristics can be considered as compensation of the electrical activity of doping chemical impurities due to the introduction of radiation defects; as a result of this compensation, the initial con-

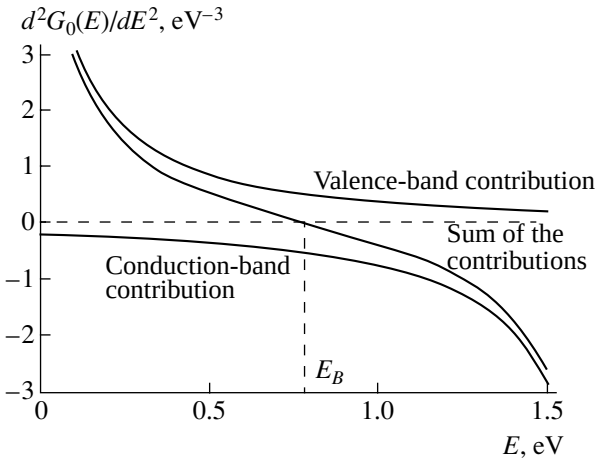

Fig. 4. Graphical solution to Eq. (5) for a GaAs crystal. The partial contributions of the valence and conduction bands and the sum of these contributions are shown.

centration of free electrons n_0 or holes p_0 varies according to the following expressions:

$$n_{\text{sat}} = n_0 \exp[(F_0 - F_{\text{sat}})/kT],$$
$$p_{\text{sat}} = p_0[-(F_0 - F_{\text{sat}})/kT].$$

Here, F_0 is the initial (before irradiation) Fermi level position in a semiconductor. By analogy with doping by introducing chemical impurities, high-energy irradiation can be considered as the doping of a semiconductor with radiation defects (see, e.g., [26]). However, it should be taken into account that, in the former case (doping with impurities), the material's properties (the conductivity type and the concentration of free charge carriers) are governed by the type and solubility of the chosen chemical impurity in the semiconductor under consideration. In contrast, in the latter case (doping with radiation defects), the "ultimate" electronic parameters of the irradiated material are inevitably strictly controlled by the corresponding universal value of F_{sat} ($\equiv E_B$) for each semiconductor; this value depends on the energy spectrum of an ideal crystal and is independent of both the conditions of high-energy irradiation and the history (the growth method and impurity types) of a material.

5. CONCLUSION

The results of experimental studies and calculations reported in this paper show that pinning of the Fermi level both in a bulk imperfect crystal irradiated with high-energy particles and at the interface (at a Schottky barrier or a heterojunction) occurs in the vicinity of the deepest defect state of the crystal within the band gap of a semiconductor. This defect state is formed from the gap states with the highest localization, which is confirmed by experimental studies of irradiated semiconductors under conditions of uniform compression [27]. As a result, the level E_B of the defect state under consideration corresponds to the direction-averaged position of the branching point in the complex energy-band structure of a semiconductor and is consistent with the results of calculations in terms of models [2, 9] based on the above concept. Indeed, as follows from the data shown in Fig. 4, the solution (5) to Eq. (4), used to determine the position of E_B, and the corresponding solutions for calculating the position of the local-electroneutrality level E_{LNL} in the models reported in [2, 9] correspond to the inflection point for the Green function. This circumstance accounts for the correlation between calculated data listed in Table 1 for various theoretical approaches to the problem of the pinning of the Fermi level in semiconductors. The level E_B is a universal energy level in all related semiconductors and represents a basic crystal parameter; it characterizes both the properties of a bulk imperfect semiconductor and the characteristics of the interface in the semiconductor. Since this level is insensitive to the type of radiation defects in the crystal lattice, the models of the Fermi level pinning, which are based on the concepts of a gap (the tails in the density of states) and local defect states in the crystal, should yield virtually the same quantitative results. This ensures unification of electronic characteristics (the position of the level F_{sat}) in a semiconductor containing point structural defects (after irradiation with γ-ray photons, electrons, or low-energy protons) or in a material with defect clusters (after irradiation with fast neutrons or heavy ions).

ACKNOWLEDGMENTS

This study was supported by project no. 1630, "High-Stability Radiation-Resistant Semiconductors," of the International Science & Technology Center.

REFERENCES

1. V. N. Brudnyĭ, Izv. Vyssh. Uchebn. Zaved., Fiz. **29** (8), 84 (1986).
2. V. N. Brudnyi, S. N. Grinyaev, and V. E. Stepanov, Physica B (Amsterdam) **212**, 429 (1995).
3. W. Walukiewicz, J. Vac. Sci. Technol. B **5**, 1062 (1987).
4. V. N. Brudnyĭ and S. N. Grinyaev, Fiz. Tekh. Poluprovodn. (St. Petersburg) **32**, 315 (1998) [Semiconductors **32**, 284 (1998)].
5. H. Hasegawa and Hideo Ohno, J. Vac. Sci. Technol. B **4**, 1130 (1986).
6. W. E. Spicer, P. W. Chye, P. R. Skeatch, *et al.*, J. Vac. Sci. Technol. **16**, 1422 (1979).
7. V. Heine, Phys. Rev. A **138**, 1689 (1965).
8. F. Flores and C. Tejedor, J. Phys. C **20**, 145 (1987).
9. J. Tersoff, Phys. Rev. B **30**, 4874 (1984).
10. S. N. Grinyaev and V. A. Chaldyshev, Fiz. Tekh. Poluprovodn. (St. Petersburg) **35**, 84 (2001) [Semiconductors **35**, 86 (2001)].
11. S. T. Pantelides, N. O. Lipari, and J. Bernholc, Solid State Commun. **33**, 1045 (1980).

12. S. N. Grinyaev and V. A. Chaldyshev, Fiz. Tekh. Poluprovodn. (St. Petersburg) **30**, 2195 (1996) [Semiconductors **30**, 1144 (1996)]; Fiz. Tekh. Poluprovodn. (St. Petersburg) **32**, 1094 (1998) [Semiconductors **32**, 980 (1998)].
13. D. J. Chadi and M. L. Cohen, Phys. Rev. **8**, 5747 (1973).
14. V. A. Chaldyshev and S. N. Grinyaev, Izv. Vyssh. Uchebn. Zaved., Fiz. **26** (3), 38 (1983).
15. S. N Grinyaev and S. G. Kataev, Physica B (Amsterdam) **191**, 317 (1993).
16. J. Tersoff, J. Vac. Sci. Technol. B **4**, 1066 (1986).
17. Ying-Chao Ruan and W. Y. Ching, J. Appl. Phys. **62**, 2885 (1987).
18. V. T. Bublik, Phys. Status Solidi A **45**, 543 (1978).
19. G. Margaritondo, Phys. Rev. B **31**, 2526 (1985).
20. H. J. Bardeleben and J. C. Bourgoin, Phys. Rev. B **33**, 2890 (1986).
21. D. Pons and J. C. Bourgoin, J. Phys. C **18**, 3839 (1985).
22. V. N. Brudnyi and V. V. Peshev, Phys. Status Solidi A **105**, K57 (1988).
23. V. N. Brudnyi and V. M. Diamond, Solid State Commun. **54**, 355 (1985).
24. N. G. Kolin, L. V. Kulikova, and V. B. Osvenskiĭ, Fiz. Tekh. Poluprovodn. (Leningrad) **22**, 1025 (1988) [Sov. Phys. Semicond. **22**, 646 (1988)].
25. N. G. Kolin, V. B. Osvenskiĭ, N. S. Rytova, and U. S. Yugova, Fiz. Tekh. Poluprovodn. (Leningrad) **21**, 521 (1987) [Sov. Phys. Semicond. **21**, 320 (1987)].
26. V. V. Kozlovskiĭ, V. A. Kozlov, and V. N. Lomasov, Fiz. Tekh. Poluprovodn. (St. Petersburg) **34**, 129 (2000) [Semiconductors **34**, 123 (2000)].
27. V. N. Brudnyĭ, Fiz. Tekh. Poluprovodn. (St. Petersburg) **33**, 1290 (1999) [Semiconductors **33**, 1166 (1999)].

Translated by A. Spitsyn

Semiconductors, Vol. 37, No. 5, 2003, pp. 546–550. Translated from Fizika i Tekhnika Poluprovodnikov, Vol. 37, No. 5, 2003, pp. 565–569.

ELECTRONIC AND OPTICAL PROPERTIES OF SEMICONDUCTORS

Relaxation of a Defect Subsystem in Silicon Irradiated with High-Energy Heavy Ions

S. A. Smagulova*, I. V. Antonova, E. P. Neustroev*, and V. A. Skuratov*****

** Yakutian State University, Yakutsk, 677891 Russia*

*** Institute of Semiconductor Physics, Siberian Division, Russian Academy of Sciences, pr. Akademika Lavrent'eva 13, Novosibirsk, 630090 Russia*

**** Joint Institute for Nuclear Research, ul. Zholio-Kyuri 6, Dubna, Moscow oblast, 141980 Russia*

Submitted October 14, 2002; accepted for publication October 28, 2002

Abstract—The relaxation of a silicon defect subsystem modified by the implantation of high-energy heavy ions was studied by varying the electrical properties of irradiated Si crystal annealed at a temperature of 450°C. It is shown that quenched-in acceptors are introduced into Si crystals as a result of irradiation with comparatively low doses of Bi ions and subsequent relatively short annealing (no longer than 5 h); the distribution of these quenched-in acceptors has two peaks located at a depth of about 10 μm and at a depth corresponding approximately to the ions' projected range (43.5 μm). The peaks in the distribution of quenched-in acceptors correspond to the regions enriched with vacancy-containing defects. As the heat-treatment duration increases, the acceptor centers are transformed into donor centers with the centers' spatial distribution remaining intact. Simultaneously, an almost uniform introduction of quenched-in donors occurs in the entire crystal beyond the depth corresponding to the projected range of ions. © *2003 MAIK "Nauka/Interperiodica".*

1. INTRODUCTION

Irradiation of a crystalline material with high-energy (higher than 1 MeV/amu) ions transforms the defect–impurity structure of this material in a relatively large volume, i.e., to a depth of several tens of micrometers. In this case, in contrast to implantation of medium-energy ions, not only do the ions penetrate to a greater depth but also the role of the surface as a sink for introduced defects as the surface becomes much diminished. In addition, the formation of regions with a prevalence of vacancy-containing point defects (from the surface to a depth of about $(1/2)R_p$, where R_p is the projected range of ions), of large vacancy clusters (at a depth of about R_p), and of interstitial defects (at a depth greater than $(1/2)R_p$ and greater than R_p) is observed [1, 2]. The phenomena of gettering of metals and oxygen, not only at a depth corresponding approximately to R_p but also at a depth of about $(1/2)R_p$ [3, 4], result from the above separation of defects. Furthermore, the depth of $(1/2)R_p$ is to a great extent conditional; a specific depth corresponding to the appearance of a peak (e.g., in the distribution of gettered impurity) is typically shifted somewhat in reference to the exact value of $(1/2)R_p$. The relaxation of a damaged crystal lattice occurs even at relatively moderate temperatures of heat treatment and is accompanied with variations in the electrical properties of a material. These variations can be deduced, e.g., from changes in the number of quenched-in donors (oxygen-containing defects), which are electrically active defects in silicon [5]. These centers are formed in silicon at temperatures T from 350 to 550°C, with the formation rate attaining a maximum at 450°C. At low oxygen concentrations and (or) heavy damage to the crystal lattice, quenched-in acceptors that formed in the regions enriched with vacancy-containing defects may compete with quenched-in donors in silicon in the aforementioned temperature range [6]. The aim of this study is to gain insight into the relaxation of the defect subsystem in silicon irradiated with high-energy heavy ions, using crystal annealed at a temperature of 450°C after irradiation as an example.

2. EXPERIMENTAL

As the starting material, we used silicon crystals with a thickness of 350–380 [mu]m; these crystals were grown by the Czochralski method (Cz-Si) and contained oxygen at a concentration of 1×10^{18} cm^{-3}. The oxygen concentration was determined from an infrared-absorption band at 1107 cm^{-1} using the calibration coefficient of 3.14×10^{17} cm^{-2}. The Cz-Si crystals were doped with boron to a concentration of $(0.8–1.0) \times 10^{15}$ cm^{-3}. The crystals were irradiated with Kr and Bi ions using a U-400 cyclotron at the Nuclear-Reaction Laboratory at the Joint Institute for Nuclear Research. The parameters of irradiation, the projected ranges of ions, and the concentrations of doping impurity in as-grown crystals are listed in Table 1. The temperature of the samples during irradiation did not exceed 50°C. The samples were subjected to postirradiation annealing at T = 450°C in atmospheric air. The concentration and

Table 1. Parameters of irradiation, projected ranges of ions R_p, and concentrations of doping impurity in the as-grown crystals

Ions	Doping level, 10^{15} cm^{-3}	Conductivity type	Ion energy, MeV	Dose F, cm^{-2}	R_p, μm
Bi^+	1	*p*	710	7×10^{12}	43.5
Kr^+	1	*p*	305	1×10^{14}	37
Kr^+	1	*p*	246	3×10^{14}	32

depth distribution of charge carriers were determined from the measurements of capacitance–voltage (*C–V*) characteristics and the Hall effect coefficient. In order to obtain the concentration profiles of electrically active centers, we used layer-by-layer etching of Si crystals in an HF : HNO_3 (1 : 100) solution. Error in determining the thickness of the removed layer could accumulate as a result of multiple etching events; this error did not exceed ±4 μm at relatively great depths (close to R_p).

3. RESULTS

3.1. The Effects Observed at Depths no Greater than R_p

According to the results of measurements of *C–V* characteristics, the entire implanted layer was compensated before the heat treatment of silicon crystals irradiated with high-energy ions. Annealing (for 5 h at 450°C) of a *p*-type CZ-Si crystal implanted with Bi^+ ions brings about a recovery of the *p*-type conductivity at a depth extending to the projected range R_p of ions. In the hole-concentration profile, we can recognize a peak at a depth of about 10 μm (see Figs. 1a, 1b) and a peak at a depth corresponding approximately to R_p after annealing the samples for 5 h. An increase in the annealing duration to $t \geq 7$ h brought about the inversion of the conductivity type (to the *n*-type) in the entire volume of the implanted layer, both in the vicinity of R_p and at greater depths. Notably, the shape of the electron concentration profile in the region between the surface and R_p (Figs. 1c, 1d) did not change significantly in comparison with the hole concentration profile (Figs. 1a, 1b): the same peaks in the depth distribution of free charge carriers are observed. Thus, relatively small changes in the hole-concentration distribution as a result of annealing for 2–5 h are followed by a drastic change in the conductivity type as a result of 7-h annealing, with the concentration of electrons and their distribution retained after further increase in the heat-treatment duration.

A somewhat different situation took place after implanting Kr^+ ions with energies of 246 and 305 MeV (see Table 1). In this case, the formation of donor centers was observed even after annealing for 2 h at 450°C; a layer with *n*-type conductivity was detected in the surface region (Fig. 2). A compensated region was observed at depths ranging from the *n*-type layer position to R_p. The electron concentration in the *n*-type layer increased with increasing heat-treatment duration; the depth of this layer also increased and became as great as R_p after annealing for 10 h (Fig. 2). It is noteworthy that a peak at a depth of 6–7 μm can be seen in the electron-concentration profile after annealing for 10 h.

3.2. The Effects Observed at Depths Greater than R_p

Variations in the average charge-carrier concentration at depths greater than R_p (averaging was performed over the entire thickness of the sample ignoring the layer near R_p) in relation to the heat-treatment duration for samples irradiated with different ions are shown in Fig. 3. As was mentioned above, the *p*-type conductivity converts to *n*-type in the Si samples irradiated with Bi^+ ions and then annealed for 5 and 7 h. The donor concentration required to attain the observed electron concentration is equal to 2×10^{15} cm^{-3}. A further increase in the heat-treatment duration to 10 h no longer affects the electron concentration. In the case of irradiation with Kr^+ ions, the most intense formation of donor centers is observed when the heat-treatment duration does not exceed $t = 2$ h; if this duration is $t > 2$ h, the concentration of donor centers increases more gradually with increasing *t*. However, the conductivity-type conversion is not observed in the entire range of *t* under consideration. Moreover, the hole concentration increases when the depth corresponding to R_p is reached from the substrate side; i.e., an increase in the concentration of shallow acceptor centers is observed. A decrease in the hole concentration in the as-grown unirradiated crystal due to introduction of quenched-in donors is also shown in Fig. 3.

4. DISCUSSION

4.1. The Effects Observed at Depths no Greater than R_p

It is well known that irradiation of high-resistivity silicon crystals with electrons or neutrons leads to the formation of shallow-level acceptor centers [6]. The structure of these centers remains to be clarified; nevertheless, they are believed [6] to be comparatively simple complexes of vacancies with background impurities. The involvement of vacancies in the formation of quenched-in acceptors is confirmed by the results obtained in this study. The introduction of quenched-in acceptors is observed only if Bi^+ ions are implanted; the interaction of these ions with Si crystals is character-

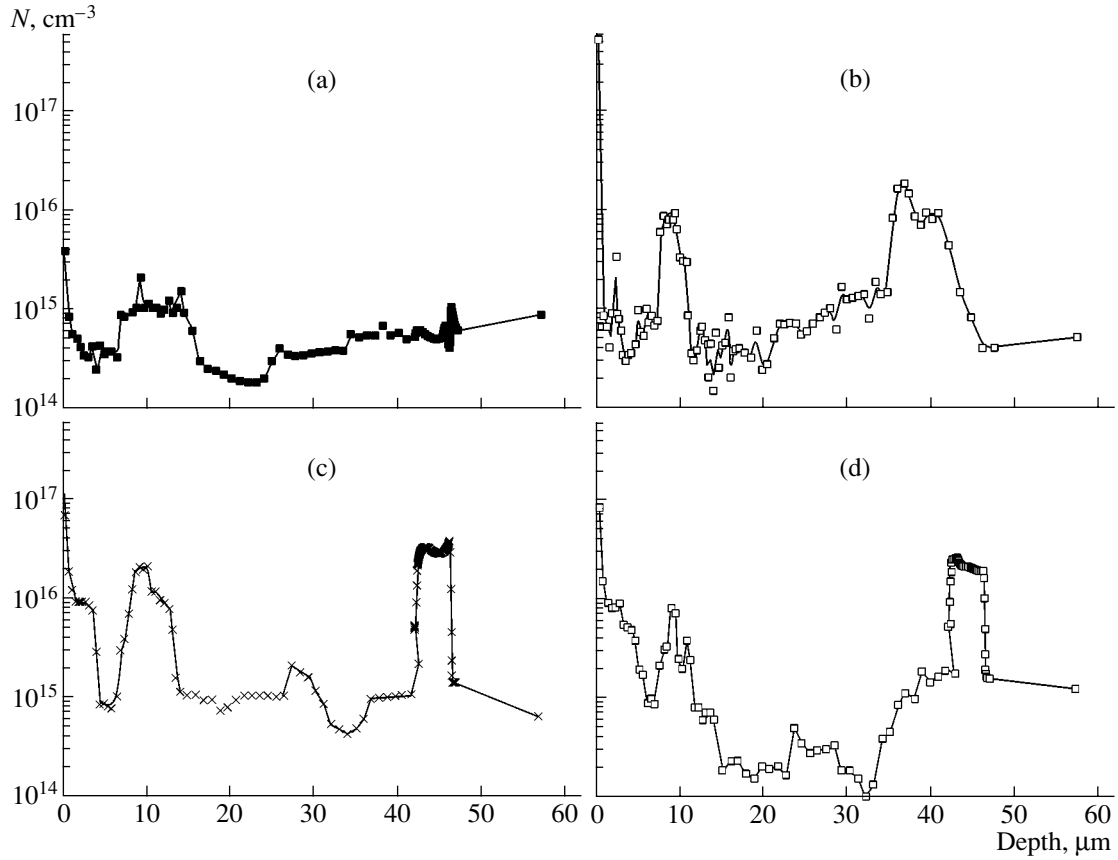

Fig. 1. The concentration (N) distributions for (a, b) holes and (c, d) electrons over the depth in Cz-Si crystals irradiated with 710-MeV Bi at a dose of 7×10^{12} cm^{-2} and then subjected to annealing for (a) 2, (b) 5, (c) 7, and (d) 10 h at 450°C.

ized by the highest specific energy losses through ionization and elastic scattering. For the sake of comparison, Table 2 lists the results of computations of both the highest ionization losses $(dE/dx)_{\text{ion}}$ in the region of the ion track for each ion and the number of vacancies (N_V) at the peak of elastic losses; the computations were realized using the TRIM-95 software package. The threshold energy for displacement was set at 15 eV. The number of displacements integrated over the range for each ion is also listed in Table 2. A higher local density of vacancies in the central region of the ion track during irradiation with Bi^+ ions can be the cause of formation of both a greater number and larger clusters of vacancy-type defects along the ion path (especially at a depth corresponding to the highest elastic losses) compared with what is observed for Kr^+ ion implantation. In addition, we cannot exclude specific phenomena related to the influence of a high ionization density on the silicon structure, notwithstanding the fact that ionization does not constitute an independent source of radiation-defect production in the case of irradiation with high-energy ions with energy losses no higher than 30 keV/nm [7]. Such phenomena can include a decrease in the threshold energy for the displacement of atoms from lattice sites, which is observed in the case of irradiation of silicon with 5.68-GeV Xe ions [8]. At the same time, the integrated number of defects (see Table 2) produced by irradiation with Bi is almost an order of magnitude smaller than that in the case of irradiation with Kr ions; this is caused by the fact that the doses of Bi ions were much lower than those of Kr ions. Most likely, differ-

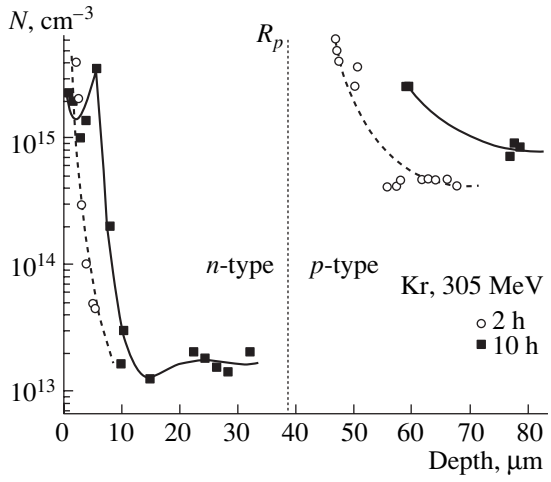

Fig. 2. Concentration (N) profiles of electrons in the p-type Cz-Si crystals irradiated with 305-MeV Kr^+ ions at a dose of 1×10^{14} cm^{-2} and then annealed for 2 and 10 h at 450°C.

Table 2. Characteristics of primary radiation defects produced in silicon as a result of irradiation with bismuth and krypton ions

Ion	$(dE/dx)_{ion}$, keV/nm	N_V, nm^{-1}	N_VF, 10^{21} cm^{-3}	N_{VI}, 10^{18} cm^{-2}
Bi^+	22.5	19.7	1.4	1.37
Kr^+ (305 MeV)	9.2	10.8	1.1	3.55

Note: $(dE/dx)_{ion}$ is the highest ionization loss per ion; N_V is the number of vacancies at the peak of elastic losses per ion; N_VF is the calculated concentration of vacancies at the peak of elastic losses for the ion dose under consideration; and N_{VI} is the number of vacancies integrated over the ion range for the given ion dose.

ences in the local density (concentration in the region of the ion track) and spectrum of defect clusters, i.e., formation of larger vacancy clusters upon irradiation with Bi ions, account for the fact that quenched-in acceptors are formed only in the case of irradiation with Bi, even at low doses.

The peak of the acceptor concentration at a depth of about 10 μm (Fig. 1) corresponds to the region where various impurities are efficiently gettered at vacancy-containing defects (the so-called $(1/2)R_p$ effect) [2–4]. The peak of the acceptor concentration at a depth corresponding approximately to R_p also coincides with a peak in the concentration of large vacancy-containing defects in silicon; at the same time, various impurities, in particular, oxygen, are efficiently gettered in this region [3]. This means that the role of vacancies in the formation of quenched-in acceptors can be indirect. For example, vacancies may simply play the role of nucleation centers for some complexes (clusters) composed of impurity atoms gettered at radiation defects.

Apparently, an abrupt change of the *p*-type conductivity in the samples annealed for 5 h to the *n*-type conductivity in the sample annealed for 7 h can be explained assuming that the addition of a certain defect (or some impurity atom, for example, oxygen) to a quenched-in acceptor center gives rise to predominant donor properties of this center. This inference is based not only on drastic changes in the electrical conductivity under a relatively small increase in the heat-treatment duration but also on complete agreement between spatial distributions of holes and electrons. In addition, the emergence of the peak in the electron concentration profile at a depth corresponding to R_p can be partially related to the activation of Bi impurity, which is a donor in silicon.

An alternative explanation for the close agreement between the spatial distributions of donors and acceptors can be based on the realization of the following mechanism. As was mentioned above, quenched-in acceptors [6] can be composite complexes of vacancies and background impurities; i.e., the quenched-in acceptors can be formed of large vacancy-containing clusters introduced by bismuth and decorated with impurities. In the course of heat treatment, large vacancy-containing clusters dissociate into smaller clusters; apparently, this dissociation takes several hours as the annealing temperature is relatively low (450°C). As long as vacancy-containing clusters are dissociated and point vacancy-related defects appear in the crystal, the latter defects manifest themselves as catalysts for the formation of oxygen-related quenched-in donors.

If particles with lower energies and masses (N^+ [9] and Kr^+) are used for ion implantation, in which case comparatively large vacancy-containing clusters are not formed, the introduction of acceptor centers is not observed. The annealing kinetics for shallower radiation defects is different; as a result of Kr^+ ion implantation, quenched-in donors are formed near the surface even after annealing for 2 h.

4.2. The Effects Observed at Depths Greater than R_p

As a rule, no changes were observed in the rates of introduction of quenched-in donors at depths greater than the projected range in the crystals annealed after ion implantation in comparison with annealed as-grown crystals (Fig. 3, Kr^+) [9]. The use of ions with a higher mass and energy (Bi^+) gave rise to another unusual effect, i.e., to the enhanced formation of quenched-in donors in the entire undamaged crystal layer at depths greater than R_p. Typically, similar effects

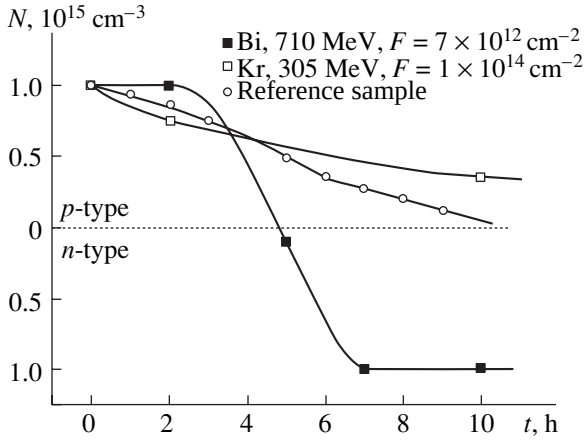

Fig. 3. Dependences of the average charge-carrier concentration N on the heat-treatment duration t at 450°C in the bulk of the Si samples (at depths greater than R_p) irradiated with Bi and Kr ions; the corresponding dependence for the reference (unirradiated) sample is also shown. The ion energies and doses are indicated in the panel.

are observed in the case of implantation of ions with medium energies [10, 11]. The enhanced introduction of donors at depths greater than R_p is usually observed in the temperature range of 380–520°C and only in Cz-Si (with higher oxygen concentration [10, 11]), which indicates that quenched-in donors are formed. The appearance of additional concentrations of self-interstitials [12] or vacancies [10, 11] is often considered a plausible mechanism foe the enhanced introduction of quenched-in donors. As is well known, enrichment of silicon with self-interstitials is invariably observed at depths greater than R_p in the case of high-energy ion implantation [1, 2, 4]. However, the effect of enhanced introduction of quenched-in donors is observed only in specific cases (possibly, when relatively low doses of ions are used). This fact suggests that diffusion of vacancies (stimulating the enhanced formation of quenched-in donors) to the silicon bulk from the relatively undamaged region in the vicinity of R_p occurs in the course of annealing of silicon implanted with bismuth ions. It is worth noting that a 7-h delay in the enhanced formation of quenched-in donors is observed both in the region of depths lower than R_p and in the undamaged part of the crystal. An increase in the ion dose and the corresponding accumulation of defects at a depth close to R_p (and possibly the onset of amorphization as well) suppresses the emission of free vacancies into the crystal bulk in the course of annealing at 450°C; this suppression is caused by the formation of another set of radiation defects that are annealed out at higher temperatures. As a result, the effect of enhanced formation of radiation defects is not observed at high ion doses.

5. CONCLUSION

The above experimental data indicate that quenched-in acceptors are formed in silicon as a result of irradiation with relatively low-doses of heavy Bi^+ ions and subsequent annealing at 450°C (the heat-treatment duration does not exceed 5 h); the concentration profile of these acceptors has two peaks (a peak at a depth of 10 μm and a peak at a depth corresponding approximately to R_p) and replicates the profile of vacancy-containing defects. As the heat-treatment duration is increased, acceptor centers are transformed into donor centers, with the concentration profile of the centers remaining intact. Simultaneously, quenched-in donors are formed almost uniformly with a concentration as high as 2×10^{15} cm^{-3} in the entire crystal bulk (at depths greater than R_p). A further increase in the heat-treatment duration to 10 h virtually does not affect either the concentration itself or the concentration profile of quenched-in donors. The observed phenomena are attributed to the effect of vacancies which enhance the formation of quenched-in donors.

REFERENCES

1. R. Kögler, A. Peeva, P. Werner, *et al.*, Nucl. Instrum. Methods Phys. Res. B **175–177**, 340 (2001).
2. R. Kalyanaraman, T. E. Haynes, M. Yoon, *et al.*, Nucl. Instrum. Methods Phys. Res. B **175–177**, 182 (2001).
3. A. Agarwal, K. Christensen, D. Venables, *et al.*, Appl. Phys. Lett. **69**, 3899 (1996).
4. R. A. Brown, O. Kononchuk, G. A. Rozgonyi, *et al.*, J. Appl. Phys. **84**, 2459 (1998).
5. A. Borgezi, B. Pivac, A. Sassella, and A. Stella, J. Appl. Phys. **77**, 4169 (1995).
6. V. F. Stas', I. V. Antonova, E. P. Neustroev, *et al.*, Fiz. Tekh. Poluprovodn. (St. Petersburg) **34**, 162 (2000) [Semiconductors **34**, 155 (2000)].
7. A. Dunlop, G. Jaskierowicz, and S. Della-Negra, Nucl. Instrum. Methods Phys. Res. B **146**, 302 (1998).
8. A. R. Chelyadinskiĭ, V. S. Varichenko, and A. M. Zaĭtsev, Fiz. Tverd. Tela (St. Petersburg) **40**, 1627 (1998) [Phys. Solid State **40**, 1478 (1998)].
9. E. P. Neustroev, I. V. Antonova, V. P. Popov, *et al.*, Nucl. Instrum. Methods Phys. Res. B **171**, 443 (2000).
10. I. V. Antonova, E. P. Neustroev, V. P. Popov, and V. F. Stas', Perspekt. Mater. **1**, 43 (2001).
11. I. V. Antonova, E. P. Neustroev, V. P. Popov, *et al.*, Physica B (Amsterdam) **270** (1–2), 1 (1999).
12. V. V. Voronkov, G. I. Voronkova, A. V. Batunina, *et al.*, Fiz. Tverd. Tela (St. Petersburg) **42**, 1969 (2000) [Phys. Solid State **42**, 2022 (2000)].

Translated by A. Spitsyn

Semiconductors, Vol. 37, No. 5, 2003, pp. 551–552. Translated from Fizika i Tekhnika Poluprovodnikov, Vol. 37, No. 5, 2003, pp. 570–571.

ELECTRONIC AND OPTICAL PROPERTIES OF SEMICONDUCTORS

Diffusion of Europium in Silicon

D. É. Nazyrov

Ulugbek National University of Uzbekistan, Tashkent, 700174 Uzbekistan

Submitted November 18, 2002; accepted for publication November 20, 2002

Abstract—The diffusion of europium in silicon has been studied for the first time in the temperature range 1100–1250°C by the direct radioactive-tracer method. The diffusion parameters of europium impurity in silicon have been established. © *2003 MAIK "Nauka/Interperiodica".*

A study of the diffusion of rare-earth elements (REE) in silicon is of interest in view of their application in improving the thermal stability and radiation hardness of silicon and in the context of specific features of the electronic structure of elements belonging to this group [1–3], as well as prospects for the application of REE-doped silicon in optoelectronics as a source of light [4].

However, studies of this kind have been few in number and their results are contradictory. Our experiments on diffusion of praseodymium [5], scandium [6], erbium and thulium [7], promethium [8], and yttrium, as well as the results obtained in studying the diffusion of samarium and gadolinium in silicon, indicate that, similarly to other Group III elements (B, Al, Ga, In), these impurities move in silicon via crystal lattice sites.

This communication reports the results obtained in studying the diffusion of an REE, i.e., europium, in silicon. Previously, the diffusion of this element was studied only indirectly [11, 12], whereas the present communication reports data obtained using the direct radioactive-tracer method.

A layer of europium chloride or a dopant containing a radioactive isotope in the form of an oxide, $^{152}Eu_2O_3$, was deposited, respectively, from solution or by vacuum evaporation onto the surface of *n*-type silicon samples ($\rho = 15\ \Omega$ cm, area ~1.5 cm^2, thickness ~380 μm). Diffusion annealing was performed in air or in evacuated (10^{-4} Torr) quartz cells in the temperature range 1100–1250°C in the course of 5–48 h. After the annealing, the samples were repeatedly washed with hydrofluoric acid and a mixture of H_2O_2 and HCl. The concentration profile of the diffusing substance was determined by the sectioning method. Thin layers were etched off in a 1 : 4 solution of HF and HNO_3, with the samples washed with a mixture of H_2O_2 and HCl, and the residual beta activity of a sample was measured on a UMF-1500M low-background installation with an SBT-11 counter. The thickness of the layers removed (0.05–0.5 μm) was determined by weighing the sample. The autoradiograms obtained before and after annealing, and also those measured in the course of sample sectioning, indicate that the europium impurity is uniformly distributed across the sample and there are no inclusions.

Assuming that Fick's law is observed and the surface concentration of the impurity is time-independent (diffusion from a constant source into a semi-infinite body), we determined the diffusion coefficient D of europium in silicon. For this purpose, the experimental curve of the residual amount of impurity was approximated, as was done in [5], with a theoretical curve for diffusion from a constant source

$$Q(x) = 2c_0\sqrt{Dt}i\mathrm{erf}(cx)/2\sqrt{Dt},$$

where c_0 is the surface concentration, x is the total thickness of layers removed in sectioning, and t is the time of diffusion.

As follows from the data obtained (see figure), the diffusion coefficient of europium in silicon grows with increasing temperature from $\sim 2 \times 10^{-12}$ to 10^{-11} cm^2/s. The temperature dependence of the diffusion coeffi-

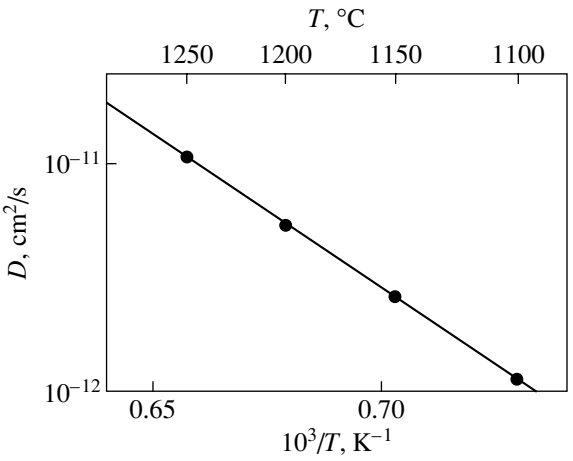

Temperature dependence of the diffusion coefficient of europium in silicon. Points, experiment; solid straight line, calculation.

1063-7826/03/3705-0551$24.00 © 2003 MAIK "Nauka/Interperiodica"

cient is of the Arrhenius type and can be described at 1100–1250°C by the relation

$$D_{Eu} = 2 \times 10^{-2} \exp(-2.8/kT)\ \text{cm}^2/\text{s}.$$

The depth to which europium penetrates into silicon, evaluated using $2\sqrt{Dt}$ in this study, did not exceed several micrometers, with the surface concentration of europium equal to ~10^{18} cm^{-3}.

Comparison of the results obtained in studying the diffusion of europium with earlier data on REE diffusion in silicon [5–12], obtained using radioactive tracers and other techniques, shows that the method by which a diffusing substance is deposited and the diffusion medium do not significantly affect the characteristics of REE diffusion in silicon. Based on the results obtained—diffusion coefficients and activation energies of europium diffusion—we can conclude that both europium, a Group IIIA impurity, and the already mentioned REE [5–10] diffuse in silicon similarly to other Group IIIB elements [13, 14] via crystal lattice sites.

REFERENCES

1. N. G. Bagraev, L. S. Vlasenko, V. M. Volle, *et al.*, Zh. Tekh. Fiz. **54**, 917 (1984) [Sov. Phys. Tech. Phys. **29**, 547 (1984)].
2. D. É. Nazyrov, A. R. Regel', and G. S. Kulikov, Priprint No. 1122, FTI AN SSSR (Physicotechnical Inst., USSR Academy of Sciences, Leningrad, 1987).
3. V. M. Glazov, A. Ya. Potemkin, G. G. Timoshina, and M. S. Mikhaĭlova, Fiz. Tekh. Poluprovodn. (St. Petersburg) **31**, 1025 (1997) [Semiconductors **31**, 875 (1997)].
4. N. A. Sobolev, Fiz. Tekh. Poluprovodn. (St. Petersburg) **29**, 1153 (1995) [Semiconductors **29**, 595 (1995)].
5. D. É. Nazyrov, V. P. Usacheva, G. S. Kulikov, and R. Sh. Malkovich, Pis'ma Zh. Tekh. Fiz. **14**, 1102 (1988) [Sov. Tech. Phys. Lett. **14**, 483 (1988)].
6. G. K. Azimov, S. Zaĭnabidinov, and D. É. Nazyrov, Fiz. Tekh. Poluprovodn. (Leningrad) **23**, 556 (1989) [Sov. Phys. Semicond. **23**, 347 (1989)].
7. D. É. Nazyrov, G. S. Kulikov, and R. Sh. Malkovich, Fiz. Tekh. Poluprovodn. (Leningrad) **25**, 1653 (1991) [Sov. Phys. Semicond. **25**, 997 (1991)].
8. D. É. Nazyrov, G. S. Kulikov, and R. Sh. Malkovich, Pis'ma Zh. Tekh. Fiz. **23** (1), 46 (1997) [Tech. Phys. Lett. **23**, 68 (1997)].
9. D. É. Nazyrov and A. A. Iminov, in *Proceedings of International Conference on Photo-, Tenzo- and Thermoelectrical Phenomena in Semiconductor Materials*, Fergana (1999), p. 56.
10. S. Zaĭnabidinov, K. Adambaev, A. A. Iminov, and D. É. Nazyrov, Uzb. J. Phys. **4** (1), 66 (2002).
11. V. V. Ageev, N. S. Aksenova, V. N. Kokovina, and E. P. Troshina, Izv. Leningr. Élektrotekh. Inst. **211**, 80 (1977).
12. A. I. Borisenko, Yu. M. Volokobinskiĭ, V. N. Kokovina, *et al.*, Dokl. Akad. Nauk SSSR **262** (6), 1409 (1982).
13. B. I. Boltaks, *Diffusion and Pointed Defects in Semiconductors* (Nauka, Leningrad, 1972).
14. W. Frank, U. Gosele, H. Mehrer, and A. Seeger, *Diffusion in Crystalline Solids*, Ed. by G. E. Murch and A. S. Nowick (Academic, Orlando, Fla, 1984), p. 76.

Translated by M. Tagirdzhanov

Semiconductors, Vol. 37, No. 5, 2003, pp. 553–558. Translated from Fizika i Tekhnika Poluprovodnikov, Vol. 37, No. 5, 2003, pp. 572–577.

SEMICONDUCTOR STRUCTURES, INTERFACES, AND SURFACES

Photosensitive Structures Based on $CdGa_2Se_4$ Single Crystals

A. A. Vaĭpolin*, Yu. A. Nikolaev*, I. K. Polushina*, V. Yu. Rud'^, Yu. V. Rud'*, E. I. Terukov*, and N. Fernelius*****

** Ioffe Physicotechnical Institute, Russian Academy of Sciences, St. Petersburg, 194021 Russia*

*** St. Petersburg State Polytechnic University, St. Petersburg, 195251 Russia*

^ e-mail: rudvas@spbgtu.ru

**** Wright Air Force Laboratory, Wright Patterson Air Force Base, OH, USA*

Submitted September 26, 2002; accepted for publication October 4, 2002

Abstract—Photosensitive structures based on $CdGa_2Se_4$ single crystals have been fabricated for the first time: $In/CdGa_2Se_4$ surface-barrier structures and $InSe/CdGa_2Se_4$ heterostructures. The current–voltage characteristics and the quantum efficiency spectra of these structures were studied. The polarization photosensitivity of $In/CdGa_2Se_4$ structures were found. The photosensitivity is discussed taking into account the photoactive absorption in $CdGa_2Se_4$ crystals in the impurity-related and intrinsic spectral ranges. A conclusion has been made that $CdGa_2Se_4$ single crystals are promising for commercial applications in photoelectric converters of unpolarized and linearly polarized light. © *2003 MAIK "Nauka/Interperiodica".*

Anisotropic semiconductors $A^{II}B_2^{III}C_4^{VI}$ (where II stands for Cd or Zn; III, for Ga, In; IV, for Se, S) with a wide (up to ~4 eV) band gap can significantly extend the capabilities of modern semiconductor electronics for the short-wavelength spectral range [1, 2]. However, the issues of single-crystal growth, fabrication of semiconductor structures, and the study of their physical properties remain virtually unexplored. The current study, which deals with a promising new branch of semiconductor electronics, presents results obtained in the design of the first photosensitive structures based on single crystals of cadmium selenogallate $CdGa_2Se_4$, a representative of a new class of ternary compounds. These data open up new opportunities for investigations of the photoelectric properties of these compounds in natural and linearly polarized radiation (LPR).

1. $CdGa_2Se_4$ single crystals were grown by directed crystallization from a nearly stoichiometric melt of this compound in evacuated quartz crucibles coated with a film of pyrolytic carbon to suppress the interaction between the melt and the quartz surface. The crystallization was performed with the temperature gradient $\Delta T \cong 10°C\ cm^{-1}$ at a velocity of the crystallization front motion ~0.5 mm h^{-1}. According to X-ray diffraction data, the single crystals obtained belong to the space group S_4^2 with lattice constants $a = 5.740 \pm 0.003$ and $c = 10.739 \pm 0.006$ Å, which is in satisfactory agreement with the data [1, 3]. The grown crystals are easily cleaved along {112} facets, forming mirror planes. In transmitted white light, ~1-mm-thick $CdGa_2Se_4$ wafers have a uniform light-orange color. The average size of the obtained $CdGa_2Se_4$ single crystals was $\sim 10 \times 5 \times mm^3$. Without intentional doping, all of the grown single-crystals had *n*-type conduction with a dark resistivity $\rho \approx 10^7$–$10^9\ \Omega$ cm at $T = 300$ K.

The first studies of the electrical properties of contacts between $CdGa_2Se_4$ and metals have shown that the deposition of thin layers of ($d \approx 0.1$ mm) pure indium metal onto the cleaved surface of this compound enables the fabrication of $In/CdGa_2Se_4$ structures with pronounced electrical rectification. Figure 1 shows typical current–voltage (*I–V*) characteristics of such a structure in the dark (curve *1*) and under illumination from the side of the thin layer of barrier metal (curve *2*). The forward bias in $In/CdGa_2Se_4$ structures, in the dark and under illumination, always corresponds to the positive voltage applied to $CdGa_2Se_4$ crystal. The rectification factor, defined as the ratio of the forward to reverse current at fixed bias, can be as high as $K \approx 400$–500 (at $U \approx 2$ V) under illumination. This value greatly exceeds the rectification factor in the dark, which can be attributed to a decrease in the resistivity of the semiconductor when the surface-barrier structure is illuminated. Under external bias, $U > U_0$, the forward *I–V* characteristics are well described, both in the dark and under illumination from the side of the barrier contacts, by

$$I = (U - U_0)/R_0, \quad (1)$$

where U_0 is the cutoff voltage, and R_0 is the residual resistance (see table) decreasing under illumination (Fig. 1, curves *1* and *2*). The dark cutoff voltage of the

Photoelectric properties of structures based on *n*-$CdGa_2Se_4$ single crystals (T = 300 K)

Structure type	R_0, Ω	U_0, V	S_U^m, V W^{-1}	$\hbar\omega$, eV	δ, eV
In/$CdGa_2Se_4$*	2×10^8	0.8	500	2.7–3.7	>1
InSe/$CdGa_2Se_4$	4×10^7	0.9	80	1.95	0.3

* Structure illuminated from the side of the barrier contact.

I–V characteristics of In/$CdGa_2Se_4$ structures remains virtually unchanged under illumination and can be correlated with the potential barrier in the contact between In and the semiconductor. The forward *I–V* characteristics of surface-barrier structures at $U < 0.5$ V follow the standard photodiode equation [4]. The diode coefficient of the obtained structures $n \approx 12$–14 in the dark and decreases to 6–7 under illumination. This reflects the influence of high structure resistance on the forward *I–V* characteristics, which still hinders the discussion on the mechanism of current transport in these structures. The reverse current in In/$CdGa_2Se_4$ structures follows the power law $i \propto U^\gamma$, and in the range $U \le 5$ V the value of γ increases from 1.1 to 1.4 under illumination (Fig. 2, curves *1*' and *2*'), with no evidence of breakdown observed. Usually, the dark reverse currents in the best In/$CdGa_2Se_4$ structures are not higher than 10^{-7}–10^{-8} A under an external bias of ~5 V and T = 300 K.

Under illumination of the In/$CdGa_2Se_4$ structures, the photovoltaic effect appears with a positive voltage to which $CdGa_2Se_4$ corresponds and which is independent of the photon energy and light beam position on the structure surface. Generally, the photovoltaic effect dominates when the structures are illuminated from the side of the barrier contact. For example, under illumination by integral unfocused light of an incandescent lamp ($P \approx 80$ W), the open-circuit voltage is ~20 mV and the short-circuit photocurrent is $\sim 2 \times 10^{-8}$ A at T = 300 K. The highest voltage responsivity of the best surface-barrier structures was $S_U^m \approx 500$ V W^{-1}.

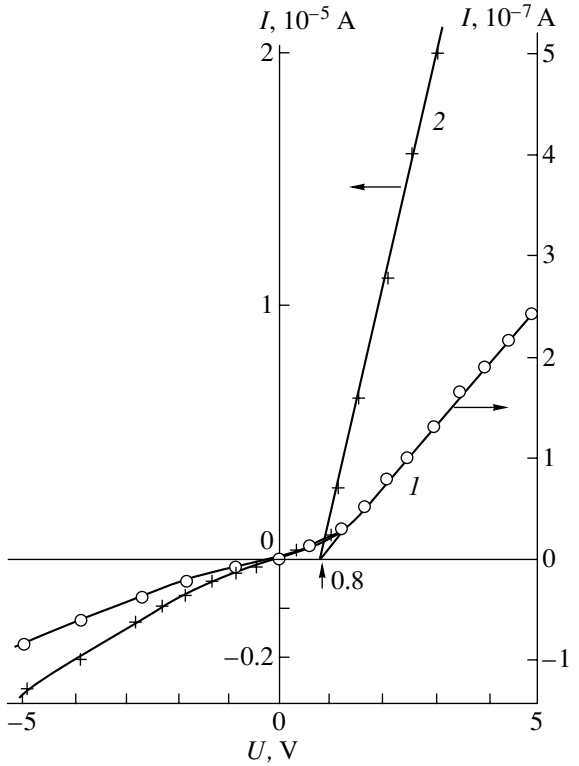

Fig. 1. *I–V* characteristics of a surface-barrier In/$CdGa_2Se_4$ structure at T = 300 K: (*1*) in the dark, (*2*) under exposure to integral light. Sample no. 6. The forward bias corresponds to a positive voltage applied to the $CdGa_2Se_4$ crystal.

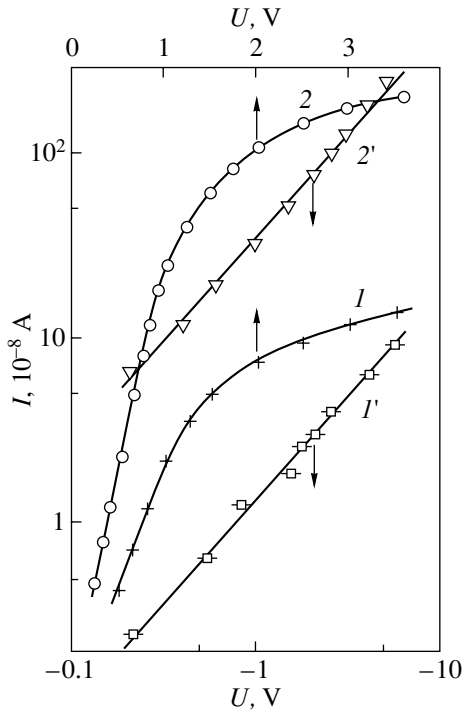

Fig. 2. (*1*, *2*) Forward and (*1*', *2*') reverse *I–V* characteristics of the In/$CdGa_2Se_4$ structure measured (*1*, *1*') in the dark and (*2*, *2*') under exposure to integral light at T = 300 K. Sample no 6.

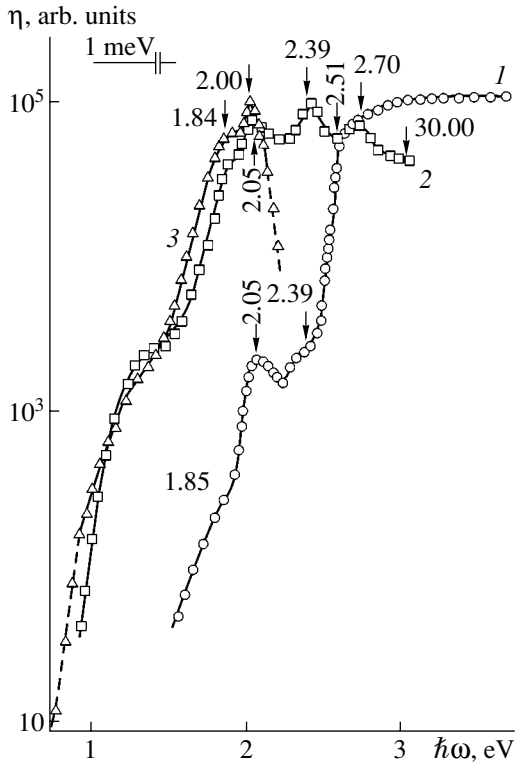

Fig. 3. Spectra of the relative quantum efficiency of photoconversion η of the $In/CdGa_2Se_4$ structure exposed to unpolarized light at $T = 300$ K. The structure is illuminated (*1, 2*) from the side of In and (*3*) from the $CdGa_2Se_4$ side. Samples: (*1* and *3*) no. 6, (*2*) no. 3.

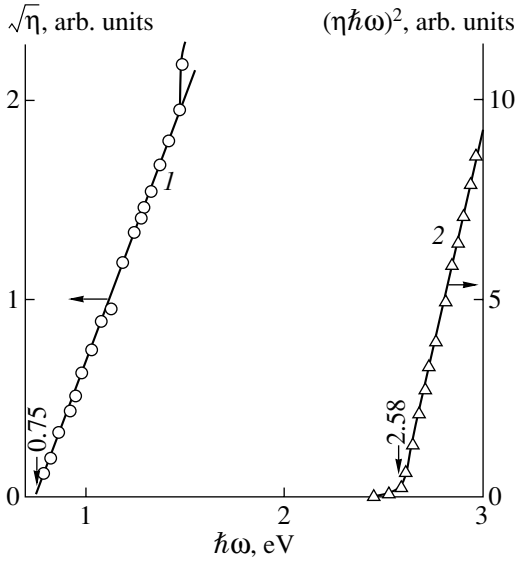

Fig. 4. Spectra of η in the coordinates (*1*) $\sqrt{\eta}$ – ħω and (*2*) $\sqrt{\eta}\,\hbar\omega$ – ħω. $In/CdGa_2Se_4$ structure, sample no. 6, $T = 300$ K.

Figure 3 shows typical spectra of the relative quantum efficiency of photoelectric conversion $\eta(\hbar\omega)$, calculated as the ratio of the short-circuit photocurrent to the number of incident photons, for two $In/CdGa_2Se_4$ structures exposed to unpolarized light. As follows from the figure, the surface-barrier $In/CdGa_2Se_4$ structures enable, in principle, photoelectric conversion in the rather wide spectral range from 0.6 to 3.6 eV. Under illumination from the barrier-contact side (Fig. 3, curves *1* and *2*), photosensitivity is mainly observed in the short-wavelength spectral range; by contrast, a sharp short-wavelength threshold at $\hbar\omega > 2$ eV always exists under illumination from the $CdGa_2Se_4$ substrate side (Fig. 3, curve *3*). This indicates that, in the case of high optical absorption, η decreases as the region of photogeneration of nonequilibrium carriers moves away from the active region of a structure. The long-wavelength part of the spectrum is nearly independent of the geometric characteristics of structure illumination, which is due to bulk photoexcitation at low optical absorption in $CdGa_2Se_4$ crystals. The photosensitivity spectrum of the Schottky barriers at $\hbar\omega < 1.4$ eV is well described by the Fowler law (Fig. 4, curve *1*) and, thus, can be attributed to the photoemission of nonequilibrium carriers. It is noteworthy that the extrapolation of the long-wavelength photosensitivity edge $\sqrt{\eta} \longrightarrow 0$ yields an energy barrier height $\xi_B \cong 0.75$ eV, which is in satisfactory agreement with U_0 found from the *I–V* characteristics of the same structures (Fig. 1).

Independently of the geometric characteristics of illumination, a fine structure in the form of three peaks at energies of 1.84, 2.0, and 2.05 eV is reproducibly manifested in the $\eta(\hbar\omega)$ spectra at photon energies above 1.5 eV. This structure can be attributed to photoactive absorption involving deep levels lying, respectively, at 0.74, 0.57 and 0.52 eV away from one of the unoccupied bands if account is taken of the $CdGa_2Se_4$ band gap $E_G = 2.57$ eV at $T = 300$ K, which was obtained from the optical absorption spectra [1, 5]. Detailed calculations of the band structure of $A^{II}B_2^{III}C_4^{VI}$ compounds have not be carried out yet, and, therefore, the nature of the fine structure of the $\eta(\hbar\omega)$ spectrum can also be attributed to the known weak pseudo-direct band-to-band transitions in $A^{II}B^{IV}C_2^{V}$ ternary semiconductors [6]. Evidently, further study is necessary to resolve this problem conclusively. Comparison of curves *1* and *2* in Fig. 3 shows that, if the $In/CdGa_2Se_4$ barriers are illuminated from the side of the In layer, the contribution of the long-wavelength structure to the photosensitivity of the barriers starts to vary significantly between different structures and ceases to be the principal one. For example, in some structures, photosensitivity is predominantly observed in the range of the fundamental absorption of $CdGa_2Se_4$ (Fig. 3, curve *1*). An exponential rise of photosensitiv-

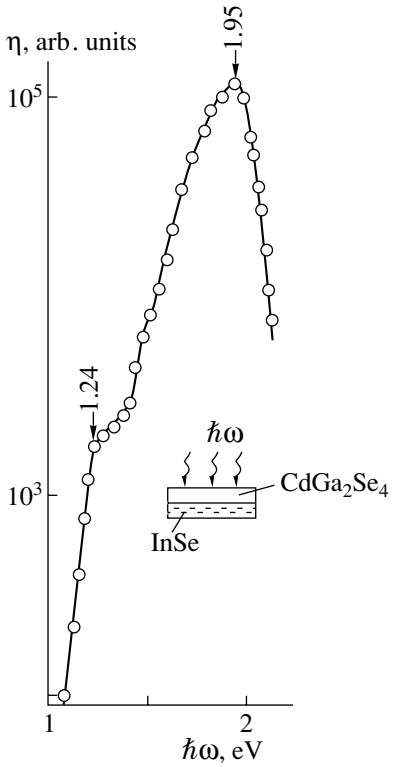

Fig. 5. The spectrum of the relative quantum efficiency of the photoelectric conversion η of InSe/$CdGa_2Se_4$ heterostructures exposed to unpolarized light at $T = 300$ K. Inset: schematic of the heterostructure and geometric characteristic of its illumination.

ity at $\hbar\omega > 2.4$ eV is characterized by a steep slope $S = \delta(\ln\eta)/\delta(\hbar\omega) \approx 20$ eV^{-1}, which, generally speaking, is typical of direct-gap semiconductors. As seen in Fig. 4 (curve *2*), the spectral dependence of quantum efficiency at $\hbar\omega > 2.6$ eV is linear in the coordinates $(\eta\hbar\omega)^2 - \hbar\omega$, which are typical of direct band-to-band transitions, and yields $E_G = 2.58$ eV upon the extrapolation $(\eta\hbar\omega)^2 \longrightarrow 0$, which is in good agreement with the data obtained from the analysis of the optical absorption in this crystal [5]. The increase in η at $\hbar\omega > E_G$ and the absence of a short-wavelength falloff in photosensitivity up to 3.6 eV, observed in the surface-barrier structures obtained, indicate a high efficiency of separation of photoexcited electron–hole pairs.

Along with the above-discussed example of the spectral dependence $\eta(\hbar\omega)$ achieved for the designed photoelectric converters, structures are also frequently obtained whose photosensitivity in the range $\hbar\omega < E_G$ is comparable with its value near E_G. A fine structure appears in the form of distinct peaks at $\hbar\omega \cong 1.84$, 2.0, 2.39, 2.70, and 3.0 eV in the η spectra of these structures. For the time being, there are no sufficient grounds for discussing the nature of these peaks. It is noteworthy, however, that the study of surface-barrier structures produced by standard technology reveals differences in their photosensitivity spectra. It seems natural to assign these differences to changes in the physical properties of $CdGa_2Se_4$ crystals, which, considering the data [1], can be presumably attributed to possible deviations from stoichiometry.

2. In the design of the first photosensitive structures based on *n*-$CdGa_2Se_4$ single crystals, we also used the method of bringing the cleaved (112) plane of these crystals into direct optical contact with the cleavage plane of lamellar *n*-InSe single crystals ($n \approx 10^{14}$ cm^{-3}, $U_n \approx 30$ cm^2 V^{-1} s^{-1}) at $T = 300$ K. The method used to fabricate these structures was similar to that employed in [7]. The heterostructure itself was produced after the deposition of current leads onto each of the semiconductor compounds. A single-crystal InSe wafer was mounted onto the surface of a microscope slide, and then a (112) mirror plane of $CdGa_2Se_4$ was pressed onto a freshly cleaved (001) mirror surface of InSe. Owing to the elasticity of *n*-InSe and the high surface quality of the contacting semiconductors, mild pressing and attrition of the adjoining surfaces provided a close optical contact of InSe and $CdGa_2Se_4$ [7, 8]. To fix the contact and ensure its long-term stability, $CdGa_2Se_4$ was pressed onto the (001) InSe surface with a spring. The heterostructure design is shown schematically in the insert in Fig. 5. As a rule, the heterostructures demonstrate rectification characterized by a factor $K \approx 2$–4 at the voltage $U \approx 50$ V, with the forward bias corresponding to the negative voltage applied to the *n*-InSe crystal. The linear approximation of the dark *I–V* characteristics has the form (1), with the U_0 and R_0 values close to those observed in surface-barrier structures based on the same crystals (see table). It is noteworthy that the parameters of the *I–V* characteristics in these structures are reproducible and show no degradation after InSe and $CdGa_2Se_4$ crystals are brought in contact. Figure 5 shows a typical spectral dependence of the relative quantum efficiency of photoelectric conversion in isotype *n*-InSe/*n*-$CdGa_2Se_4$ structures exposed to unpolarized light from the side of the wide-bandgap $CdGa_2Se_4$ component. These curves reproducibly demonstrate the known "window" effect with respect to the intensity of the optical radiation incident from the $CdGa_2Se_4$ side [4]. Indeed, the spectral position of the long-wavelength $\eta(\hbar\omega)$ edge corresponds to band-to-band transitions in the narrow-bandgap component of the heterostructure [3, 7], whereas the short-wavelength falloff of η at $\hbar\omega > 4.95$ eV (Fig. 5) is determined by the growing optical absorption in the $CdGa_2Se_4$ wafer, with a corresponding increase in the distance between the layer of photoexcited nonequilibrium carriers and the active region of the heterostructure. The predominance of heterostructure photosensitivity in the wide-bandgap component of the device results from the preferential localization of the active region in the bulk of $CdGa_2Se_4$, which is due to the difference in the doping level

between the heterostructure components. Special attention should also be given to the close similarity between the $\eta(\hbar\omega)$ spectra of heterostructures (Fig. 5) and the spectra of surface-barrier structures illuminated from the side of the $CdGa_2Se_4$ wafer (Fig. 3, curve *3*). The reason for this coincidence is that the $\eta(\hbar\omega)$ spectra in both types of structures are defined by the photoactive absorption in the crystal of the $CdGa_2Se_4$ ternary compound. Due to the radiation absorption in bulk $CdGa_2Se_4$, the peak of voltage responsivity is redshifted in heterostructures with respect to surface-barrier structures, and its magnitude appears to be lower than in $InSe/CdGa_2Se_4$ heterostructures (see table). For the same reason, the FWHM of $\eta(\hbar\omega)$ spectra in heterostructures is significantly narrower than in the surface-barrier structures fabricated on $CdGa_2Se_4$ of similar quality.

3. The photosensitivity to polarized radiation has been studied for the first time in surface-barrier structures oriented in the (112) plane. As seen in Fig. 6 (curves *1* and *2*), the photosensitivity of $In/CdGa_2Se_4$ surface-barrier structures exhibits a dependence of the quantum efficiency of photoelectric conversion, η, on the orientation of the electric field vector of the light wave $\boldsymbol{E}$ with respect to the tetragonal axis $\boldsymbol{c}$ of $CdGa_2Se_4$ single-crystal, which is typical of anisotropic crystals of ternary semiconductors [7, 9, 10]. Under illumination of the (112) plane and when the incident photon energy is fixed near the $CdGa_2Se_4$ band gap, the η polarization indicatrices follow Malus' law, so that in all cases $\eta^{\parallel} > \eta^{\perp}$, where the indices "$\parallel$" and "$\perp$" show the orientation of $\boldsymbol{E}$ with respect to $\boldsymbol{c}$. Figure 6 (curve *3*) shows a typical spectral dependence of the natural photopleochroism in $In/CdGa_2Se_4$ structures, calculated using the relation [9, 10]

$$P_N = (\eta^{\parallel} - \eta^{\perp})/(\eta^{\parallel} + \eta^{\perp}). \qquad (2)$$

The maximum coefficient of natural photopleochroism is observed near the energy of direct band-to-band *A*-transitions in $CdGa_2Se_4$ crystals, and its positive sign is in conformity with the selection rules for these transitions [11, 12]. It is necessary to emphasize that the maximum value $P_N^m \cong 12\%$ obtained in our study near the $CdGa_2Se_4$ E_G [1] can be raised by fabricating structures with a coplanar tetragonal axis on $CdGa_2Se_4$ wafers, because the orientation $\boldsymbol{E} \parallel \boldsymbol{c}$ is only partially accomplished in the structures on $CdGa_2Se_4$ wafers with (112) orientation. Special attention should be drawn to the fact that, in the range $\hbar\omega > E_G$, in which the allowed transitions from split-off subbands of the valence band come into play [1, 2], no P_N sign inversion is observed in the $In/CdGa_2Se_4$ structures under study, i.e., $\eta^{\parallel} > \eta^{\perp}$ (Fig. 6, curve *3*). This fact indicates that the influence of surface recombination is strongly suppressed in the best of the $In/CdGa_2Se_4$ structures obtained [9].

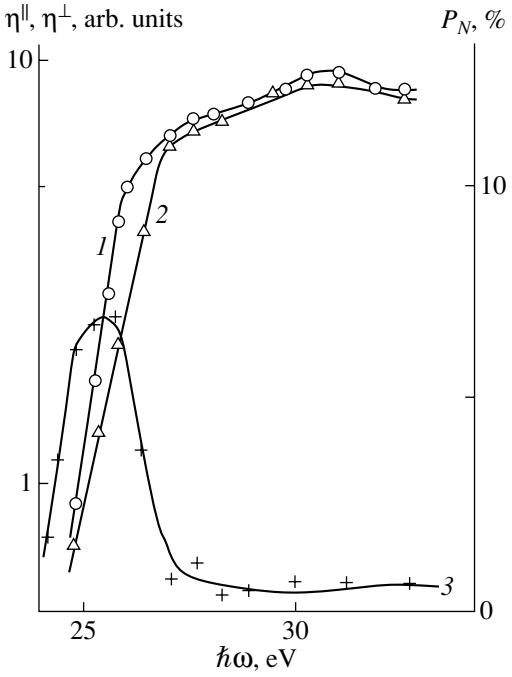

Fig. 6. Spectra of (*1*) $\boldsymbol{E} \parallel \boldsymbol{c}$, (*2*) $\boldsymbol{E} \perp \boldsymbol{c}$ photosensitivity, and (*3*) the coefficient P_N of natural photopleochroism of the $In/CdGa_2Se_4$ structure. T = 300 K, illuminated plane (112), sample no. 6.

Our study has demonstrated that $CdGa_2Se_4$ single crystals can find application in the design of photodetectors of unpolarized and linearly polarized radiation in a wide spectral range. The natural photopleochroism of structures based on $CdGa_2Se_4$ single crystals is selective and related to band-to-band *A*-transitions, similarly to the case of $A^{II}B^{IV}C^{V}$ and $A^{I}B^{III}C_2^{VI}$ ternary compounds [9, 10].

REFERENCES

1. A. N. Georgobiani, S. I. Radautsan, and I. M. Tiginyanu, Fiz. Tekh. Poluprovodn. (Leningrad) **19**, 193 (1985) [Sov. Phys. Semicond. **19**, 121 (1985)].
2. B. H. Bairamov, V. Yu. Rud', and Yu. V. Rud', MRS Bull. **23**, 41 (1998).
3. *Physicochemical Properties of Semiconductor Materials: Handbook*, Ed. by A. V. Novoselova and V. B. Lazarev (Nauka, Moscow, 1979).
4. A. Milnes and D. Feucht, *Heterojunctions and Metal–Semiconductor Junctions* (Academic, New York, 1972; Mir, Moscow, 1975).
5. R. Bacewicz, Phys. Lett. A **79A**, 121 (1979).

6. J. L. Shay and J. H. Wernick, *Ternary Chalcopyrite Semiconductors: Growth, Electronic Properties, and Applications* (Pergamon, New York, 1975).
7. I. V. Bodnar', V. Yu. Rud', and Yu. V. Rud', Fiz. Tekh. Poluprovodn. (St. Petersburg) **28**, 2137 (1994) [Semiconductors **28**, 1175 (1994)].
8. N. N. Konstantinova, M. A. Magomedov, V. Yu. Rud', and Yu. V. Rud', Fiz. Tekh. Poluprovodn. (St. Petersburg) **26**, 558 (1992) [Sov. Phys. Semicond. **26**, 317 (1992)].
9. Yu. V. Rud', Izv. Vyssh. Uchebn. Zaved., Fiz. **29** (8), 68 (1986).
10. F. P. Kesamanly, V. Yu. Rud', and Yu. V. Rud', Fiz. Tekh. Poluprovodn. (St. Petersburg) **33**, 513 (1999) [Semiconductors **33**, 483 (1999)].
11. F. M. Gashimzade and É. Sh. Kerimova, Preprint No. 21, IF AN AzSSR (Inst. of Physics, Academy of Sciences of Azerbaijan, Baku, 1980).
12. V. L. Panyugin, B. É. Ponedel'nikov, A. É. Rozenson, and V. I. Chizhikov, Izv. Vyssh. Uchebn. Zaved., Fiz. **22** (8), 57 (1979).

Translated by D. Mashovets

Semiconductors, Vol. 37, No. 5, 2003, pp. 559–563. Translated from Fizika i Tekhnika Poluprovodnikov, Vol. 37, No. 5, 2003, pp. 578–582.

LOW-DIMENSIONAL SYSTEMS

Structural and Optical Properties of InAs Quantum Dots in AlGaAs Matrix

D. S. Sizov, Yu. B. Samsonenko, G. E. Tsyrlin, N. K. Polyakov, V. A. Egorov, A. A. Tonkikh, A. E. Zhukov, S. S. Mikhrin, A. P. Vasil'ev, Yu. G. Musikhin, A. F. Tsatsul'nikov, V. M. Ustinov, and N. N. Ledentsov

Ioffe Physicotechnical Institute, Russian Academy of Sciences, St. Petersburg, 194021 Russia

Submitted June 25, 2002; accepted for publication June 28, 2002

Abstract—Structural and optical properties of InAs quantum dots (QDs) grown in a wide-bandgap $Al_{0.3}Ga_{0.7}As$ matrix is studied. It is shown that a high temperature stability of optical properties can be achieved owing to deep localization of carriers in a matrix whose band gap is wider than that in GaAs. Specific features of QD formation were studied for different amounts of deposited InAs. A steady red shift of the QD emission peak as far as ~1.18 μm with the effective thickness of InAs in $Al_{0.3}Ga_{0.7}As$ increasing was observed at room temperature. This made it possible to achieve a much higher energy of exciton localization than for QDs in a GaAs matrix. To obtain the maximum localization energy, the QD sheet was overgrown with an InGaAs layer. The possibility of reaching the emission wavelength of ~1.3 μm is demonstrated. © *2003 MAIK "Nauka/Interperiodica".*

1. INTRODUCTION

The investigations of self-organized quantum dots (QD) on GaAs substrates are motivated, among other factors, by the prospect of applying them in high-efficiency light-emitting devices [1]. Interest in heterostructures with self-organized QDs in the InAs/GaAs system is due to the possibility of expanding the spectral range of GaAs-based structures to wavelengths λ = 1.3–1.5 μm, which would open the way for the design of lasers with an emission wavelength longer than in InGaAs/GaAs QD lasers [2]. In particular, vertical-cavity surface-emitting lasers were designed [3], and 1.3-μm stripe lasers with a record-breaking low threshold current density and high internal differential efficiency have been fabricated [4, 5]. One of the most important parameters for lasing is the energy depth of carrier localization in QDs: the higher the confining barrier, the lower the threshold current density and the better the temperature stability of parameters [6].

We now consider the quantity

$$\Delta E = \Delta E_e + \Delta E_h = E_{pl}^{\mathrm{GaAs}} - E_{pl}^{\mathrm{QD}},$$

where ΔE_e is the energy spacing between the conduction band bottom and the electron ground state in a QD; ΔE_h is the spacing between the hole ground state in a QD and the valence band top; and E_{pl}^{GaAs} and E_{pl}^{QD} are the energies of electron–hole transitions for recombination in the matrix and QD, respectively. This quantity characterizes the energy of the electron localization in a QD with respect to a nonlocalized exciton in the matrix. An emission wavelength up to 1.4 μm has been achieved in In(Ga)As/GaAs QD structures [7], with ΔE_e not exceeding 0.55 eV. However, the use of a wide-bandgap AlGaAs matrix for QDs provides for a significant rise in ΔE.

As shown in [8], InAs QDs in $Al_{0.5}Ga_{0.5}As$ grow by the Stranski–Krastanow mechanism, with the transition to island growth after the deposition of 2.1 InAs monolayers (ML). This amount of deposited InAs is higher than in the case of growth on the GaAs surface, owing to a difference in the kinetics of indium deposition onto GaAs and AlGaAs surfaces [8]. In these structures, ΔE exceeded 0.6 eV. Temperature dependences of photoluminescence (PL) indicated a higher temperature stability of the optical properties of QDs in AlGaAs compared with QDs in a GaAs matrix, with the exciton localization energy in the latter case being smaller. The study of the effect of the $Al_xGa_{1-x}As$ matrix composition on QD optical properties revealed that the widening of the matrix band gap results in a smaller decrease in the PL intensity with rising temperature; this fact also indicates the strong effect of the exciton localization depth on the temperature stability of QD optical properties [9].

Here we present a detailed study of InAs QD formation in an $Al_{0.3}Ga_{0.7}As$ matrix. The effect of the amount of deposited InAs on the optical properties of QDs in the $Al_{0.3}Ga_{0.7}As$ matrix was also studied. It has been shown that the overgrowth of the QD layer with an InGaAs layer opens the way to obtain emission in the range up to ~1.3 μm.

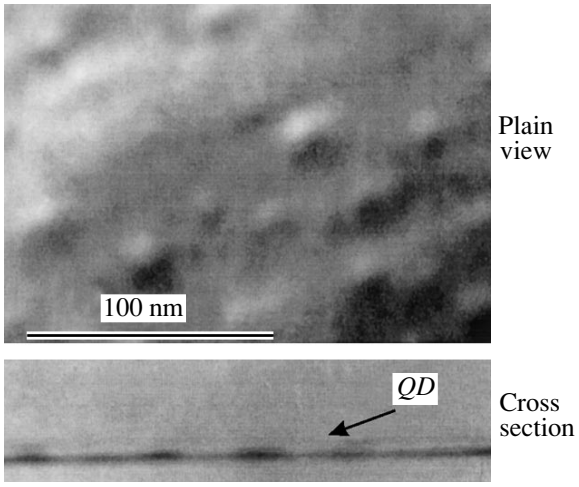

Fig. 1. TEM images of QDs in an $Al_{0.3}Ga_{0.7}As$ matrix.

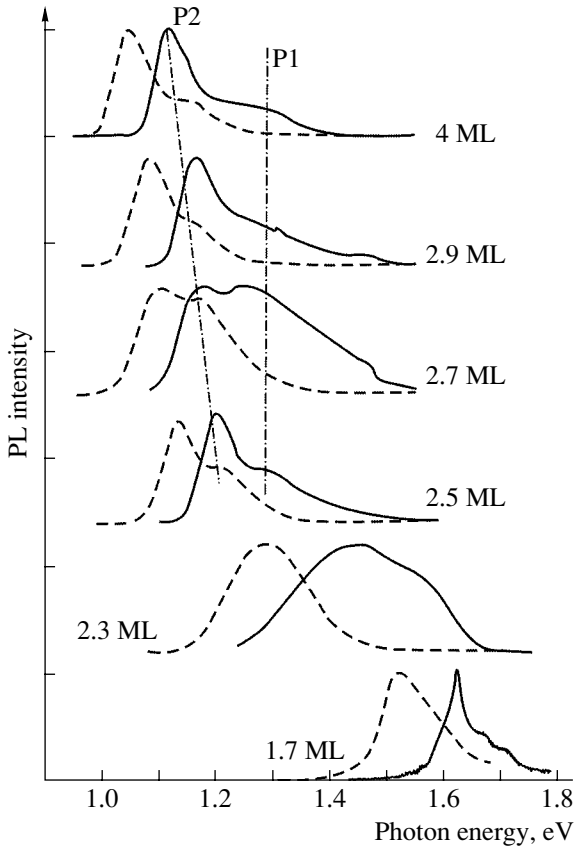

Fig. 2. PL spectra of QD structures with differing amounts of InAs deposited in the $Al_{0.3}Ga_{0.7}As$ matrix recorded at 77 K (solid lines) and 300 K (dashed lines).

2. EXPERIMENTAL

QD structures were grown by MBE. After the deposition of a GaAs buffer layer, a 0.1-μm-thick $Al_{0.3}Ga_{0.7}As$ layer was grown, with a sheet of InAs QDs deposited in the middle of this layer. To prevent carrier leakage to the surface and substrate, which is followed by nonradiative recombination, the $Al_{0.3}Ga_{0.7}As$ layer with QDs was confined by short-period superlattices (five AlGaAs/GaAs periods, 20/20 Å) on the sides of the substrate and surface. All layers, except the InAs QD sheet and the subsequent 5 nm of AlGaAs, were grown at the temperature of 600°C. QDs were formed by depositing a thin InAs layer at 485°C. The effective thickness of the InAs layer was varied between 1.7 and 4.5 ML, and the RHEED patterns recorded *in situ* demonstrated the formation of nanoislands after depositing more than 2 ML of InAs. The InAs growth rate was 0.1 ML s^{-1}. The sheet of InAs islands was then overgrown with a thin (5-nm) $Al_{0.3}Ga_{0.7}As$ layer at the temperature of InAs deposition to prevent the evaporation of InAs upon the subsequent rise in temperature [10]. In one of the samples, the sheet of InAs nanoislands was overgrown with an $In_{0.12}Ga_{0.88}As$ layer in an effort to increase the emission wavelength, and only then was the 5-nm $Al_{0.3}Ga_{0.7}As$ layer deposited. To compare optical properties, samples with InAs QDs in a GaAs matrix were also grown.

The PL was excited with an Ar-ion laser ($\lambda = 514.5$ nm, the excitation power density $P_{ex} = 500$ W cm^{-2}) and detected with a cooled Ge photodiode.

A TEM study was performed with a PHILIPS EM 420 electron microscope with a 100-kV accelerating voltage.

3. RESULTS AND DISCUSSION

Figure 1 shows the cross-sectional and plan-view TEM images of a structure containing QDs in an $Al_{0.3}Ga_{0.7}As$ matrix. The effective thickness of the InAs layer deposited in this structure was 2.5 ML. Three-dimensional (3D) InAs nanoislands and a thin two-dimensional (2D) InAs wetting layer [11] are seen in the images. According to TEM data, the lateral dimension and height of the nanoislands are ~18 and 5 nm, respectively, which corresponds to a typical QD size in a GaAs matrix [12]. Therefore, the use of $Al_{0.3}Ga_{0.7}As$ solid solution instead of pure GaAs as the matrix material causes no fundamental change in the QD formation mechanism.

Figure 2 shows the QD PL spectra for structures with differing amounts of InAs in the $Al_{0.3}Ga_{0.7}As$ matrix, recorded at temperatures $T = 77$ and 300 K. The spectrum of the sample with an effective InAs thickness of 1.7 ML contains a relatively narrow peak with a broadened short-wavelength wing. This type of spectrum shape indicates that the 2D InAs layer is retained and its thickness is lower than the critical value for QD formation. With the InAs thickness increasing to 2.3 ML, the PL peak is considerably broadened (to 240 meV) and red-shifted. A large line broadening indicates the beginning of 3D-island formation [13]. This result is consistent with the RHEED data showing that the QD formation in an $Al_{0.3}Ga_{0.7}As$ matrix begins at an effec-

tive InAs thickness of ~2 ML. A further increase in the InAs layer thickness red-shifts the PL peak to 1.18 μm at T = 300 K. In addition to a P2 peak related to the ground state, a short-wavelength shoulder P1 is observed; it can be related to recombination via smaller QDs or excited states.

Figure 3 shows the PL peak positions for QDs in $Al_{0.3}Ga_{0.7}As$ and GaAs matrices as functions of the InAs layer thickness. The calculated energy of the transition between electron and heavy hole states in an $InAs/Al_{0.3}Ga_{0.7}As$ quantum well (QW) with a thickness of 1 ML [14] is also shown. The PL peak of a QD in the $Al_{0.3}Ga_{0.7}As$ matrix exhibits a strictly monotonic red shift as the amount of InAs increases. The rate of shifting is higher when the effective thickness of the InAs layer is between 1.7 and 2.5 ML. This thickness corresponds to the onset of QD formation. In the GaAs matrix, the QD PL line position depends on the InAs layer thickness in a somewhat different manner: the peak position is virtually independent of the amount of deposited InAs at a thickness above 2.3 ML. Different behaviors of the QD PL peak positions in $Al_{0.3}Ga_{0.7}As$ and GaAs matrices can originate from different conditions of QD formation during the growth process. We believe that, in this case, we are dealing with differences in the kinetics of the surface processes during InAs deposition onto $Al_{0.3}Ga_{0.7}As$ and GaAs surfaces [8], including those differences related to the morphology of the $Al_{0.3}Ga_{0.7}As$ surface.

Because of the nearly complete termination of the shift of the PL line for QDs in the GaAs matrix, ΔE does not exceed ~0.42 eV. At the same time, ΔE is ~0.76 eV for QDs grown in the $Al_{0.3}Ga_{0.7}As$ matrix in the same mode. These results are indicative of deeper exciton localization in the $Al_{0.3}Ga_{0.7}As$ matrix. In our opinion, the reason for such a high ΔE is, in addition to the structural properties of the QDs themselves, the great height of the confining $Al_{0.3}Ga_{0.7}As$ barrier.

Figure 4 shows the temperature dependence of PL for a sample with QDs formed by deposition of 4 ML InAs in the $Al_{0.3}Ga_{0.7}As$ matrix. Two peaks, P_1 and P_2, 150 meV apart are well resolved at low temperatures. The relative intensity of the short-wavelength peak decreases with rising temperature. This temperature dependence of the intensity of these peaks indicates that they are related to recombination in QDs with different sizes. In this situation, the decrease in the short-wavelength peak intensity is due to carrier excitation into the matrix and the recapture of carriers by deeper QDs. The formation of two QD types can be related to specific features of the surface morphology of $Al_{0.3}Ga_{0.7}As$ [7], as well as to the kinetics of processes occurring during deposition in the $InAs/Al_{0.3}Ga_{0.7}As$ system.

The insert in Fig. 4 shows temperature dependences of the integral intensity, energy E_m, and FWHM of the PL peak for structures with 2.3 and 4 ML of InAs. The

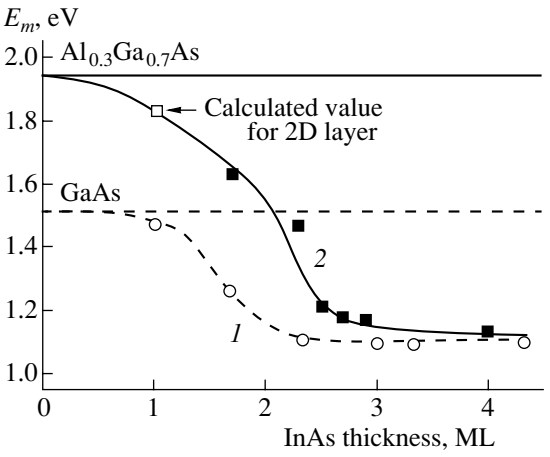

Fig. 3. The PL peak spectral position E_m vs. the amount of deposited InAs: (*1*) in a GaAs matrix, (*2*) in an $Al_{0.3}Ga_{0.7}As$ matrix.

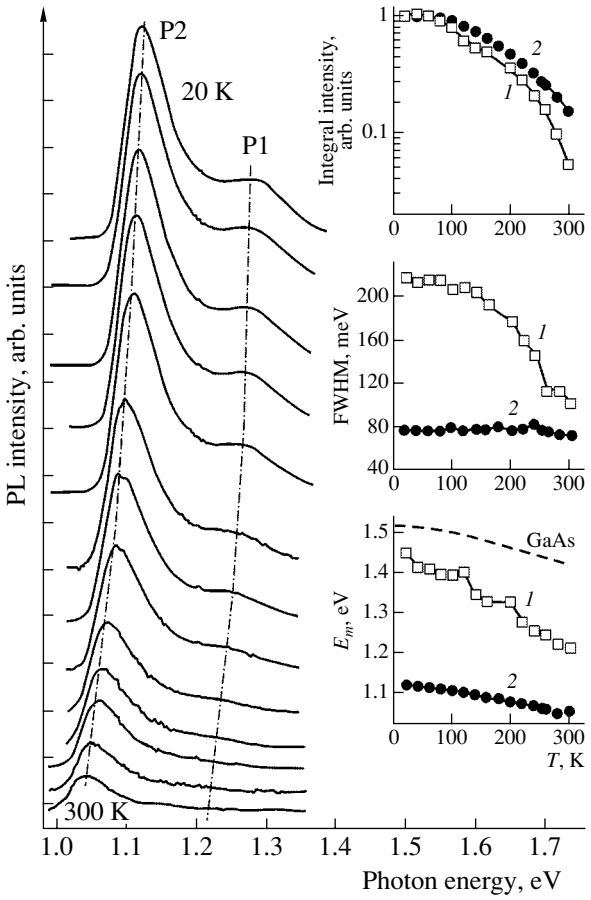

Fig. 4. The PL spectra at different temperatures for QDs in an $Al_{0.3}Ga_{0.7}As$ matrix. The effective thickness of the InAs layer was 4 ML. The spectra (top-down) correspond to the temperature variation from 20 to 300 K. Insert: temperature dependences of the integral intensity, full width at half-maximum (FWHM), and peak energy for structures with an InAs layer effective thickness of (*1*) 2.3 and (*2*) 4 ML.

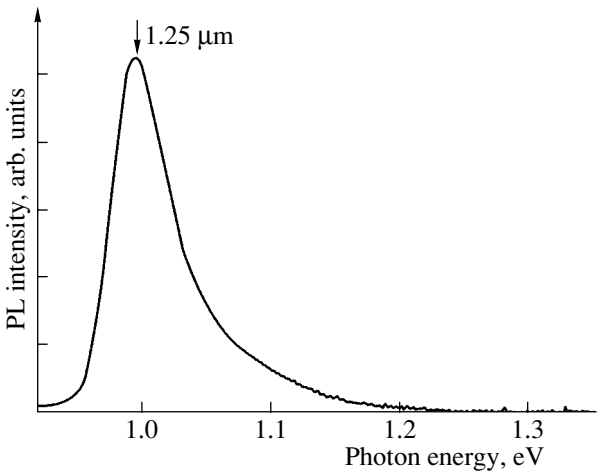

Fig. 5. The room-temperature PL spectrum of InAs QDs overgrown with an $In_{0.12}Ga_{0.88}As$ layer in an $Al_{0.3}Ga_{0.7}As$ matrix.

dependences are normalized to the integral intensity at the lowest temperature. The decrease in the PL integral intensity for a structure with 2.3 ML of InAs is three times that of a structure with 4 ML of InAs. The temperature-induced decrease in the PL integral intensity is due to nonradiative recombination of carriers thermally excited into the matrix. Since the average energy of the exciton localization in QDs formed by the deposition of 2.3 ML of InAs is less than that for 4 ML InAs, carrier excitation at low temperatures is more probable in the former case. This results in a stronger decrease in the emission intensity for the 2.3-ML InAs structure. Further, the thermal excitation of carriers is more probable for the least localized QD states responsible for the short-wavelength portion of the spectrum. This accounts for the considerable decrease in the linewidth for QDs formed by 2.3-ML InAs deposition. The temperature shift of the PL peak, in this case, is stronger than that for the 4-ML InAs structure, because it is caused not only by the temperature-related decrease in the band gap, but also by the redistribution of carriers between isolated QDs differing in their exciton localization energy. An insignificant temperature-induced decrease in the QD PL intensity for the 4-ML InAs structure is indicative of not only deep exciton localization, but also a low defect density in these samples.

Figure 5 shows the PL spectrum of the structure with an $Al_{0.3}Ga_{0.7}As$ matrix and QDs overgrown with an InGaAs layer. After deposition of an InAs layer with an effective thickness of 2.5 ML, an $In_{0.12}Ga_{0.88}As$ layer was deposited. A similar technique for QD growth in a GaAs matrix makes the QD emission wavelength much longer, 1.3 μm [15], and yields high-efficiency lasers for this spectral range. The increase in the wavelength may originate from several causes: the increase in the QD effective size owing to stimulated phase separation in InGaAs, the decrease in the elastic stress fields in QDs, and the quantum-mechanical effect associated with placing a QD in an InGaAs QW [15]. We have obtained room-temperature emission at a wavelength $\lambda = 1.25$ μm from such QDs grown in an $Al_{0.3}Ga_{0.7}As$ matrix (Fig. 5). Owing to a high potential barrier, the ΔE value in these structures is 0.86 eV. Therefore, the exciton localization energy for QDs in AlGaAs is considerably higher than that in a GaAs matrix.

4. CONCLUSION

The structural and optical properties of QDs in an $Al_{0.3}Ga_{0.7}As$ matrix have been studied. QDs in $Al_{0.3}Ga_{0.7}As$ are formed by the Stranski–Krastanow mechanism, which is the same way they are formed in a GaAs matrix. However, the critical thickness for the transition to island growth for QDs in $Al_{0.3}Ga_{0.7}As$ is slightly higher (~2 ML) than in a GaAs matrix.

In the case of an $Al_{0.3}Ga_{0.7}As$ matrix, the red shift of the QD PL spectral line is observed as the average InAs thickness increases up to 4 ML. By contrast, the red shift almost terminates at ~2.3 ML for QDs grown in a GaAs matrix. The overgrowing of QDs in the $Al_{0.3}Ga_{0.7}As$ matrix with an InGaAs layer allowed us to raise the emission wavelength to 1.25 μm, and to obtain an energy of exciton localization in a QD that was considerably higher than that for a GaAs matrix at the same emission wavelength.

The high temperature stability of the optical properties of QDs in a wide-gap $Al_{0.3}Ga_{0.7}As$ matrix offers promise for the design of light-emitting devices with improved thermal characteristics.

ACKNOWLEDGMENTS

This study was supported by INTAS, the Russian Foundation for Basic Research, and the Ministry of Industry and Science of the Russian Federation program “Physics of Solid-State Nanostructures”.

REFERENCES

1. Y. Arakawa and H. Sakaki, Appl. Phys. Lett. **40**, 939 (1982).
2. V. M. Ustinov and A. E. Zhukov, Semicond. Sci. Technol. **15**, R41 (2000).
3. J. A. Lott, N. N. Ledentsov, V. M. Ustinov, *et al.*, Electron. Lett. **36**, 1384 (2000).
4. S. S. Mikhrin, A. E. Zhukov, A. R. Kovsh, *et al.*, Fiz. Tekh. Poluprovodn. (St. Petersburg) **36**, 1400 (2002) [Semiconductors **36**, 1315 (2002)].
5. M. V. Maximov, L. V. Asryan, Yu. M. Shernyakov, *et al.*, IEEE J. Quantum Electron. **37**, 676 (2001).
6. B. V. Volovik, D. S. Sizov, A. F. Tsatsul’nikov, *et al.*, Fiz. Tekh. Poluprovodn. (St. Petersburg) **34**, 1368 (2000) [Semiconductors **34**, 1316 (2000)].

7. K. Kokie, H. Ohkawa, and M. Yano, Jpn. J. Appl. Phys. **38**, L417 (1999).
8. Y. S. Kim, U. H. Lee, D. Lee, *et al.*, J. Appl. Phys. **87**, 241 (2000).
9. M. V. Maximov, A. F. Tsatsul'nikov, B. V. Volovik, *et al.*, Phys. Rev. B **62**, 16671 (2000).
10. D. S. Sizov, M. V. Maksimov, A. F. Tsatsul'nikov, *et al.*, Fiz. Tekh. Poluprovodn. (St. Petersburg) **36**, 1097 (2002) [Semiconductors **36**, 1020 (2002)].
11. V. A. Shchukin, N. N. Ledentsov, P. S. Kop'ev, and D. Bimberg, Phys. Rev. Lett. **75**, 2968 (1995).
12. A. F. Tsatsul'nikov, A. R. Kovsh, A. E. Zhukov, *et al.*, J. Appl. Phys. **88**, 6272 (2000).
13. J. M. Moison, F. Houzay, F. Barthe, *et al.*, Appl. Phys. Lett. **64**, 196 (1994).
14. R. Heitz, T. R. Ramachandran, A. Kalburge, *et al.*, Phys. Rev. Lett. **78**, 4071 (1997).
15. M. Krjin, Semicond. Sci. Technol. **6**, 27 (1991).

Translated by D. Mashovets

Semiconductors, Vol. 37, No. 5, 2003, pp. 564–568. Translated from Fizika i Tekhnika Poluprovodnikov, Vol. 37, No. 5, 2003, pp. 583–587.

LOW-DIMENSIONAL SYSTEMS

Model of Multi-Island Single-Electron Arrays Based on the Monte Carlo Method

I. I. Abramov*, S. A. Ignatenko, and E. G. Novik

Belarussian State University of Information Science, Radio Engineering, and Electronics, ul. Brovki 6, Minsk, 220027 Belarus

** e-mail: nanodev@bsuir.edu.by*

Submitted July 11, 2002; accepted for publication October 16, 2002

Abstract—A two-dimensional model of multi-island single-electron arrays, based on a numerical solution to the Poisson equation and the Monte Carlo method, is suggested. The adequacy of the model is shown by comparing the *I–V* characteristics calculated for two different five-island structures with experimental data. This model was used to assess quantitatively a number of geometrical parameters of a single-electron device structure, which are difficult to determine experimentally. © *2003 MAIK "Nauka/Interperiodica".*

1. INTRODUCTION

The Monte Carlo method has become one of the principal approaches to constructing completely adequate models for describing the physical processes in a variety of device structures [1, 2]. For example, it will suffice to mention the theoretical studies [3, 4] of MOS (metal–oxide–semiconductor) transistors based on a number of semiconductors that are significant for microelectronics. It turned out that none of the semiconductor materials which have been studied offers significant advantages over silicon when transistor channels are shorter than 100 nm. Only indium phosphide is an exception. Unfortunately, a completely adequate and much needed model [3, 4] is difficult to develop and cannot be widely used. In particular, the calculation of a single point of the *I–V* characteristic of a MOS transistor using the DAMOCLES code requires from 10 to 100 h (or more!) using the high-efficiency IBM 3090S computing system. Therefore, great efforts are now being made to develop various efficient procedures for the models under consideration on the basis of physical approaches, approximations, and a fuller account of problem specific features [5].

The overall situation seams to be even more complicated for nanoelectronic device structures. Fortunately, the situation is somewhat less serious in the theoretical study of structures whose description using the semiclassical approach remains correct. Specifically such structures are single-electron devices [6, 7]. As is known, the Monte Carlo method is presently one of a few more or less efficient approaches for the theoretical analysis of multi-island single-electron one-dimensional arrays [6, 8, 9]. A popular code for Monte Carlo simulation is MOSES [9] in the case under consideration.

Nevertheless, the conventional models of multi-island single-electron one-dimensional arrays, based on the Monte Carlo method, have a significant limitation. These models rely on tunnel junction resistances and capacitances as required parameters for matching with experimental data. As a result, the relation between the model and the device design and material parameters is lost. Hence, applying the model in the course of theoretical studies and development of single-electron device structures is complicated.

This study is aimed at the development of a model of multi-island single-electron one-dimensional arrays on the basis the Monte Carlo method, devoid of the abovementioned drawback, as well as the confirmation of its adequacy by comparing it with experimental data. It is significant that the model suggested may be realized using a Pentium III computer; i.e., the model may be widely used.

2. MODEL

In [10–12], a two-dimensional numerical model of a single-electron transistor with a single island was suggested. In this model, the Poisson and master equations are solved. In [13], this approach was extended to the case of two-island single-electron one-dimensional arrays. The model described in [13] is characterized by an acceptable adequacy and high efficiency; unfortunately, the solution of the master equation becomes significantly more complicated as the number of tunnel junctions increases. Therefore, we apply this approach to single-electron structures with a large number of islands in combination with the Monte Carlo method.

Let us consider the essence of the model suggested. According to the classification [7], the device being analyzed was chosen to correspond to the principal block diagram of multi-island single-electron one-dimensional arrays (see Fig. 1). The initial parameters are the structure sizes, material properties, background

1063-7826/03/3705-0564$24.00 © 2003 MAIK "Nauka/Interperiodica"

charges at islands, and the controls: source, drain and gate voltages, and temperature *T*.

The Poisson equation in the form given in [10–12] is numerically solved in the region *ABCD* (Fig. 1). The influence of background charges at islands is taken into account using the approximation suggested in [13]. The Dirichlet boundary conditions at contacts and the Neuman conditions at free *ABCD* boundaries are chosen as boundary conditions. The numerical methods of the finite-difference approximation of the Poisson equation and the solutions of sets of linear algebraic equations are described in [10] in detail. The numerical solution of the Poisson equation yields a potential distribution in the device in relation to the geometrical and electrical parameters of the structure and control effects.

The resistances of the tunnel junctions and the probabilities of carrier transport through them are calculated by the known formulas, whose form when taking into account the role of the electrostatic potential for one-island structures is given in [10]. These formulas are easily extended to the case of multi-island structures.

The current passing through the tunnel junction is calculated by the formula (see [6, 13])

$$I = \frac{V_{\text{eff}}}{R}\left[1 - \exp\left(-\frac{eV_{\text{eff}}}{k_{\text{B}}T}\right)\right]; \quad (1)$$

$$V_{\text{eff}} = \frac{V_i + V_f}{2}, \quad (2)$$

where V_i and V_f are the voltages before and after electron tunneling, respectively; and k_{B} is the Boltzmann constant.

We now consider the procedure for calculating the *I–V* characteristic by the model suggested. The flowchart of this procedure in the case of one-point calculation is shown in Fig. 2. As an example, we explain it for the case of a five-island structure, i.e., $N = 5$.

First, the Poisson equation is solved for an initial (with the index $i = 0$) combination of excess carriers in islands, $\{n_i\} \equiv (n_1 = 0, n_2 = 0, n_3 = 0, n_4 = 0, n_5 = 0)$, and partial currents through all of the tunnel junctions are calculated by formulas (1) and (2). To save computer time, the values obtained are stored when the next combination $\{n_0\}$ arises. We note at once that the most time-consuming process is solving the Poisson equation. Therefore, this time-saving method in this model is expedient and shortens the computer time by three orders of magnitude, or even more in specific cases. Then the number *K* of tunnel events was selected. The larger the value of *K*, the more accurate the result; unfortunately, the computation time also increases. Then, according to the Monte Carlo method, the first random number $r_i \in [0, 1]$ is generated and the time t_i to the next tunnel event is determined,

$$t_i = -\frac{e\ln r_i}{\Sigma I}, \quad (3)$$

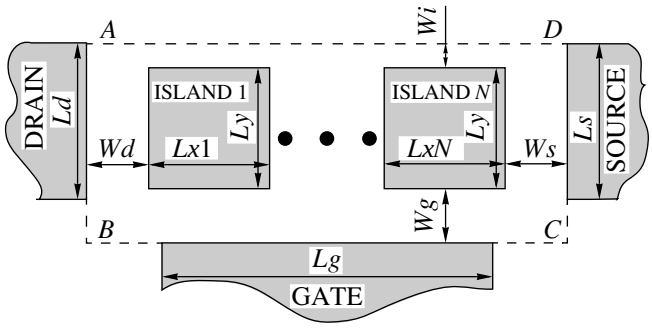

Fig. 1. Structure of the multi-island single-electron one-dimensional array.

where ΣI is the sum of partial currents for all the probable independent events, corresponding to tunneling of a carrier in two directions through either junction.

Then the next random number r_i is generated. The interval [0, 1] is partitioned into segments proportional to partial currents corresponding to tunneling of a carrier in two directions through either junction. A segment within which a given random number r_i occurs is advantageous. As a result, a new combination $\{n_i\}$ is determined. It is then checked whether this combination was found previously or not. If it was, partial currents are extracted from the computer memory; if not, the Poisson equation is solved and partial currents through all of the tunnel junctions are calculated and stored. It is then checked whether all the probable tunnel events (number *K*) were enumerated or not.

The total current *j* passing through an isolated tunnel junction is given by

$$I_j = \frac{n_j e}{t_\Sigma}, \quad (4)$$

where n_j is the number of carriers that passed through a given junction for the entire period, *e* is the elementary charge, and t_Σ is the total time of tunneling events. The validation criterion of the calculation is the equality of the currents I_j through all of the tunnel junctions within a certain accuracy.

The most significant differences between the model suggested and the models of [6, 8, 9], which are also based on the Monte Carlo method, are as follows: (i) the Poisson equation is solved in the form given in [10–12] with the aim of calculating the voltages at the tunnel junctions and (ii) the partial currents through the tunnel junctions calculated by formulas (1) and (2) are used instead of the tunneling rates. We note a number of advantages of the model suggested in comparison with the model of [13], in which the master equation is solved: (I) complex single-electron one-dimensional arrays with $N > 2$ can be calculated; (II) the procedure under consideration is based on a microscopic model of tunnel events, which more closely reflects the actual behavior of carriers in the single-electron

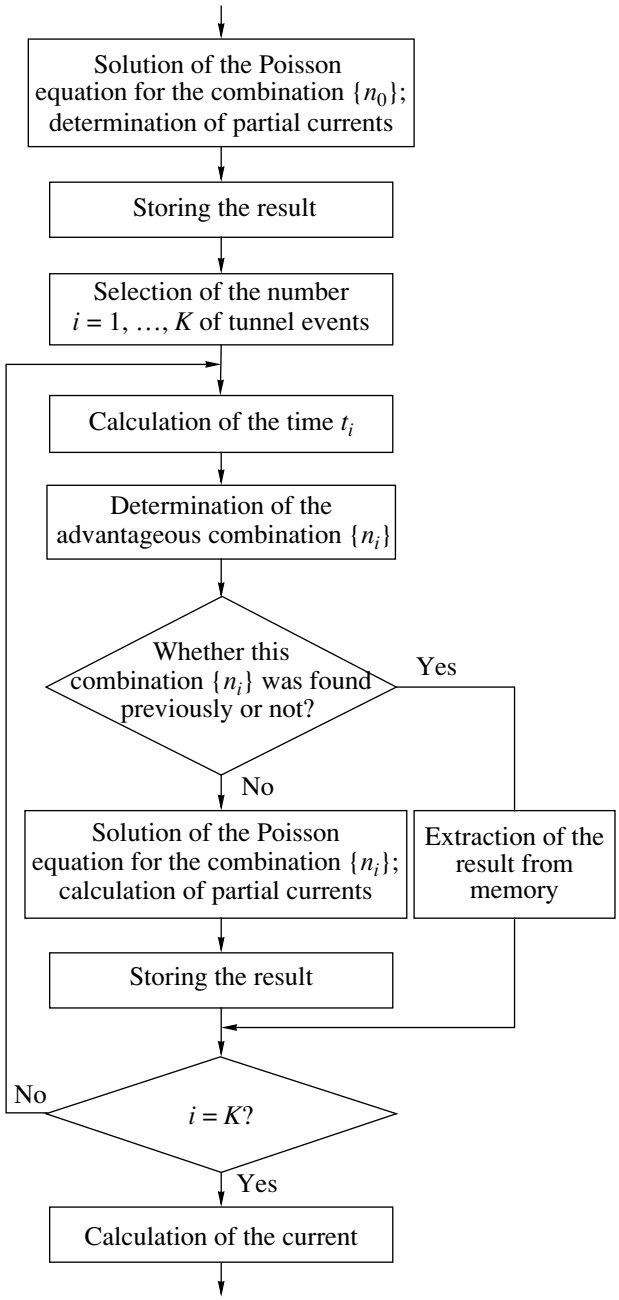

Fig. 2. Flowchart of the calculation procedure for a point of the *I–V* characteristic of single-electron one-dimensional arrays according to the model suggested.

structure; and (III) there is high stability of the computing process. The disadvantage of the model is much longer times for calculating the *I–V* characteristic at $N = 2$ in comparison with the model of [13]. Nevertheless, this time, e.g., for five-island one-dimensional arrays, is, in general, no longer than 10 h (which is acceptable) for the Pentium III computer.

The model suggested was realized in FORTRAN and incorporated in the MTJ-SET-NANODEV package for calculating multi-island single-electron one-dimensional arrays in the NANODEV software for simulating nanoelectronic devices [10]. All the results considered in Section 4 were obtained using a Pentium III computer.

3. RESULTS

As the object to be simulated, we took a single-electron transistor with five islands, i.e., $N = 5$. This choice is explained as follows. First, this number of islands allows manifestation of all the basic features of multi-island array operation, e.g., the temporal and spatial correlation of tunneling events. Second, in the case of a larger number of islands, the total resistance is high (the passing current is very small); hence, production of such structures is complicated. Therefore, data on structures with $N > 5$ are scarce in the literature. Third, the time of calculating the *I–V* characteristic unfortunately becomes longer as the number of islands increases further.

We now consider the simulation results confirming the adequacy of the model suggested. They were obtained at $K = 20000$, proceeding from the attainable equality of the currents through all the tunnel junctions within an error no larger than 0.1%.

In [14], the fabrication of a single-electron transistor with five islands is described, as are experimental data and results calculated by the MOSES code. We note that the structure is produced artificially and controlled using the SECO (step-edge cutoff) method. Titanium and *p*-type silicon are used as the island and tunnel junction materials, respectively. Figure 3 shows the experimental characteristic for the drain current I_d versus the drain voltage V_d (curve *1*), as well as the results calculated by the MOSES code (curve *2*) and the model suggested (curve *3*). One can see that both models satisfactorily fit the experimental data.

The model developed also fits well the experimental data on single-electron multi-island one-dimensional arrays based on other materials at various operating temperatures. Furthermore, the model suggested allows reconstruction of the basic sizes of the structures under study. To illustrate this, we now consider a very complex case.

In [15], a multi-island one-dimensional array is described in which AuPd nanoparticles are used as islands. The structure is rather complex (see Fig. 5 in [15]). As the author of [15] reports, it was possible to determine only the following initial parameters of the structure: (i) the number of tunnel junctions along the shortest drain–source distance was found to be six; (ii) the island sizes were from 2 to 3 nm; (iii) the source–drain distance was 20–30 nm. Thus, the available information is very ambiguous.

Figures 4a and 4b display the experimental data and the results calculated by the suggested model, respectively. One can see that, in general, the experiment and model agree satisfactorily at $T = 300$ and 77 K. The data

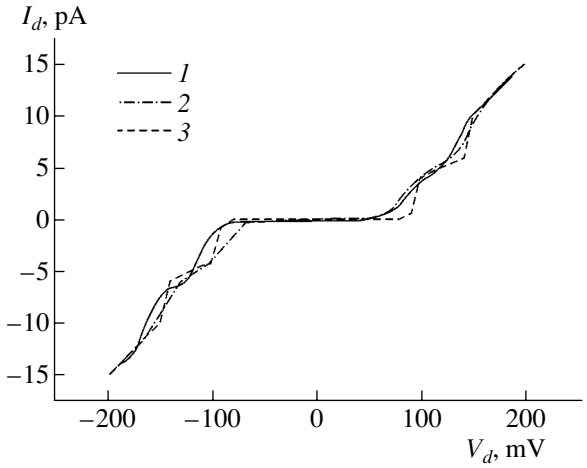

Fig. 3. *I–V* characteristics of the single-electron transistor with five islands: (*1*) experimental data, (*2*) calculation by the MOSES code, and (*3*) calculation by the model developed.

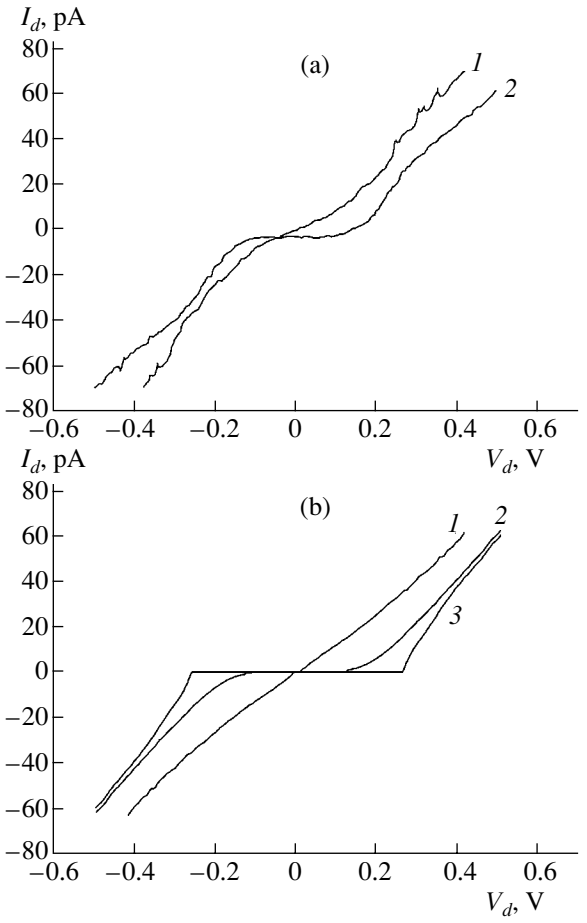

Fig. 4. *I–V* characteristics of the multi-island structure: (a) experimental data and the (b) the results of simulation according to the model developed; T = 300 (*1*), 77 (*2*), and 0.01 K (*3*).

in Fig. 4b were obtained with the following basic initial parameters of the structure: $N = 5$; the distance between islands is 1.5 nm; and the islands are of the same size (2.5×2.5 nm^2). Thus, the source–drain distance was taken as 21.5 nm ($6 \times 1.5 + 5 \times 2.5$). It is significant that all of these reconstructed initial parameters lie within the numerical range indicated by the author of [15] (see above). The results shown in Fig. 4b allow determination of the Coulomb blockade region in this structure at a very low temperature (T = 0.01 K), in particular [–0.25 V, +0.25 V]. Comparing curves *1–3* in Fig. 4b, one can ascertain that the Coulomb blockade effect is "destroyed" as the temperature increases to 300 K in the structure under study, which is fully confirmed by the experimental data in Fig. 4a.

The results obtained, in addition to confirming the conclusion on the adequacy of the model, also allow the following comments. First, the model suggested can be applied to reconstruct some of the initial parameters of multi-island single-electron one-dimensional arrays, e.g., their sizes. This seems to be of crucial importance in view of the likely problems in determining them experimentally, as in the case under consideration. Second, notwithstanding the seemingly high complexity of the single-electron structure being analyzed, it is possible to simulate it using the flowchart shown in Fig. 1. Thus, the basic physical principles of the operation of multi-island single-electron one-dimensional arrays are adequately described within the model suggested, which is based on a rather simple flowchart (Fig. 1). We note that this is also important, since the use of a practical structure configuration, in many cases, will cause significant additional problems in the numerical simulation of this type of single-electron structures. As a result, it would, in fact, become impossible to study theoretically the influence of the design and material parameters on electrical characteristics of these structures.

4. CONCLUSION

A two-dimensional model of multi-island single-electron one-dimensional arrays was developed on the basis of a numerical solution of the Poisson equation in combination with the Monte Carlo method. This model was shown to be reasonably adequate and efficient. The model may also be used to reconstruct some initial parameters that are difficult to determine from experimental data.

ACKNOWLEDGMENTS

We thank A.N. Korotkov for his helpful comments concerning the model described in this paper.

This study was supported in part by the Belarussian programs "Electronics", "Nanoelectronics", and by a grant from the Ministry of Education, Belarus.

REFERENCES

1. R. Hockney and J. Eastwood, *Computer Simulation Using Particles* (McGraw-Hill, New York, 1984; Mir, Moscow, 1987).
2. Yu. K. Pozhela, *Physics of High-Speed Transistors* (Mokslas, Vilnius, 1989).
3. M. V. Fishetti and S. E. Laux, Phys. Rev. B **38**, 9721 (1988).
4. M. V. Fishetti and S. E. Laux, IEEE Trans. Electron Devices **38**, 650 (1991).
5. H. Kosina, M. Nedjalkov, and S. Selberherr, IEEE Trans. Electron Devices **47**, 1898 (2000).
6. *Single Charge Tunneling: Coulomb Blockade Phenomena in Nanostructures*, Ed. by H. Grabert and M. H. Devoret (Plenum, New York, 1992); NATO ASI Ser., Ser. B **294** (1992).
7. I. I. Abramov and E. G. Novik, Fiz. Tekh. Poluprovodn. (St. Petersburg) **33**, 1388 (1999) [Semiconductors **33**, 1254 (1999)].
8. N. S. Bakhvalov, G. S. Kazacha, K. K. Likharev, and S. I. Serdyukova, Zh. Éksp. Teor. Fiz. **95**, 1010 (1989) [Sov. Phys. JETP **68**, 581 (1989)].
9. R. H. Chen, A. N. Korotkov, and K. K. Likharev, Appl. Phys. Lett. **68**, 1954 (1996).
10. I. I. Abramov and E. G. Novik, *Numerical Simulation of Metallic Single-Electron Transistors* (Bestprint, Minsk, 2000).
11. I. I. Abramov and E. G. Novik, Fiz. Tekh. Poluprovodn. (St. Petersburg) **34**, 1014 (2000) [Semiconductors **34**, 975 (2000)].
12. I. I. Abramov and E. G. Novik, Fiz. Tekh. Poluprovodn. (St. Petersburg) **35**, 489 (2001) [Semiconductors **35**, 474 (2001)].
13. I. I. Abramov, S. A. Ignatenko, and E. G. Novik, Fiz. Tekh. Poluprovodn. (St. Petersburg) **36**, 1272 (2002) [Semiconductors **36**, 1192 (2002)].
14. S. Altmeyer, A. Hamidi, B. Spangenberg, and H. Kurz, J. Appl. Phys. **81**, 8118 (1997).
15. H. Ahmed, J. Vac. Sci. Technol. B **15**, 2101 (1997).

Translated by A. Kazantsev

Semiconductors, Vol. 37, No. 5, 2003, pp. 569–572. Translated from Fizika i Tekhnika Poluprovodnikov, Vol. 37, No. 5, 2003, pp. 588–591.

LOW-DIMENSIONAL SYSTEMS

Dispersion of the Relaxation Time of Quasi-Two-Dimensional Electrons under Conditions of Ionized-Impurity Scattering in a Superlattice with Doped Quantum Wells

S. I. Borisenko

Kuznetsov Siberian Physicotechnical Institute, pl. Revolyutsii 1, Tomsk, 634050 Russia
e-mail: sib@elefot.tsu.ru

Submitted July 24, 2002; accepted for publication October 16, 2002

Abstract—Ionized-impurity scattering of quasi-two-dimensional electrons in GaAs/$Al_{0.36}Ga_{0.64}As$ superlattices (SLs) with doped quantum wells is considered. The scattering probability is calculated assuming that the electron wave function is represented by the ground-state eigenfunction of the lowest SL miniband. Analytical expressions describing dispersion of the longitudinal and transverse relaxation times with respect to the longitudinal wave vector are derived and numeric calculations are carried out. The dependence of the components of the relaxation-time tensor on the SL period and the temperature in the region around $T = 77$ K is analyzed.

1. INTRODUCTION

The theoretical treatment of electron scattering by ionized impurities in heterostructures with quantum wells (QWs) has been carried out in a number of studies [1–3]. In these studies, the relaxation time and the mobility characterizing the charge-carrier transport in the QW plane were calculated in the two-dimensional (2D) electron gas approximation. When a number of QWs are arranged to compose a superlattice (SL), transport in the SL miniband in the direction normal to the layers can take place in addition to the lateral transport; there are almost no publications where the impurity scattering-limited mobility of the charge carriers is calculated for this case. The solution of this problem was considered in [4], where the Boltzmann equation was used to derive formulas for the relaxation time and to analyze longitudinal and transverse mobility of quasi-2D electrons in GaAs/$Al_xGa_{1-x}As$ SLs. However, the calculation of the scattering probability was performed with a simplified electron wave function, taken as a Bloch-type sum of the wave functions of isolated, infinitely deep QWs. To this approximation, the transverse and longitudinal relaxation times appear to depend only on the transverse wave vector—in other words, on the energy of the motion perpendicular to the SL axis—and are independent of the longitudinal wave vector.

In this study, we analyze the scattering of quasi-2D electrons by ionized impurities in GaAs/$Al_{0.36}Ga_{0.64}As$ SLs with doped QWs. The scattering probability is calculated with the electron wave functions substituted by the eigenfunction of the ground state in the lowest SL miniband; this calculation yields the dependence of the electron relaxation time on the longitudinal wave vector. We derive analytical expressions describing the dispersion of the longitudinal and transverse relaxation times with respect to the longitudinal wave vector and carry out numerical calculations. The dependence of the components of the relaxation-time tensor on the SL period and on the temperature in the region around $T = 77$ K is also considered.

2. BASIC FORMULAS

Calculating the probability of intraminiband scattering of electrons in a SL by ionized impurities, we rely on the same approximation for the wave functions of the lowest miniband as that used in [5], i.e.,

$$\psi_{\boldsymbol{k}}(\boldsymbol{r}) = \frac{\exp(i\boldsymbol{k}\boldsymbol{r})}{\sqrt{V}}u_0(z), \tag{1}$$

where $\boldsymbol{k} = (k_\perp, k_z)$ is the electron wave vector (here, the z axis of the coordinate system is oriented along the SL axis) and $u_0(z)$ is the periodic part of the envelope Bloch function for $k_z = 0$. Then, in an SL with doped QWs, the probability of electron scattering from the state with the wave vector k to the state with the wave vector $\boldsymbol{k}'$ is given by

$$w(\boldsymbol{k}, \boldsymbol{k}') = \frac{2\pi e^4 Z^2 a N_I^{CW}}{\hbar\varepsilon_0^2\varepsilon^2 V d}\sum_{n, n' = -N_z/2}^{N_z/2} S_n^* S_{n'} W(\boldsymbol{q}_n) W(\boldsymbol{q}_{n'}) \times \left[1 - \frac{\sin\left[\pi\frac{a}{d}(n-n')\right]}{\pi\frac{a}{d}(n-n')}\right]\delta(E(\boldsymbol{k}') - E(\boldsymbol{k})), \tag{2}$$

where

$$S_n = \frac{1}{d}\int_{-d/2}^{d/2} \exp\left(i\frac{2\pi n}{d}z\right)|u_0(z)|^2 dz,$$
$$W(\boldsymbol{q}) = \frac{1}{\boldsymbol{q}^2 + \alpha^2}, \tag{3}$$

$$E(\boldsymbol{k}) = E = E_\perp + \frac{\Delta}{2}[1 - \cos(k_z d)],$$
$$E_\perp = \frac{\hbar^2 k_\perp^2}{2m_\perp}, \quad \boldsymbol{q}_n = \boldsymbol{k}' - \boldsymbol{k} + \frac{2\pi n}{d}\boldsymbol{e}_z, \quad -\frac{N_z}{2} < n < \frac{N_z}{2}, \tag{4}$$

N_z is the number of SL periods (which is assumed to be infinite), Δ is the width of the lowest miniband, a is the QW width, d is the SL period, $\boldsymbol{e}_z$ is a unit vector along the SL axis, $\boldsymbol{e}Z$ and N_I^{CW} are the charge and concentration of ionized impurities in the QWs, α is the screening coefficient, and ε is the static permittivity. Formula (2) is derived in the random-phase approximation for the case of uniform distribution of impurity over the QWs. In addition, uniformity of the dielectric function over the SL is presumed and the k_z dependence of $u_{k_z}(z)$ is assumed to be weak.

The nonequilibrium contribution to the electron distribution function was calculated in the form

$$g(\boldsymbol{k}) = e\frac{\partial f_0}{\partial \varepsilon}\sum_i \tau_i(\boldsymbol{k})\boldsymbol{E}_i v_i(\boldsymbol{k}), \tag{5}$$

where $\boldsymbol{E}_i$ are the components of the electric field strength, $\boldsymbol{v}(\boldsymbol{k}) = \nabla_{\boldsymbol{k}}E/\hbar$ is the electron velocity, and $f_0(\varepsilon)$ is the equilibrium Fermi–Dirac distribution function. The functions $\tau_i(\boldsymbol{k})$ represent the components of the relaxation-time tensor, which depend on the components of the wave vector. Calculation of these functions relies on the linearized Boltzmann's equation used to derive the following integral equations:

$$\tau_\perp(\boldsymbol{k}) = \tau_0(\mathbf{k})\left\{\sum_{\boldsymbol{k}'} \boldsymbol{w}(\boldsymbol{k}, \boldsymbol{k}')\tau_\perp(\boldsymbol{k}')\frac{\boldsymbol{k}_\perp \boldsymbol{k}'_\perp}{k_\perp^2} + 1\right\}, \tag{6}$$

$$\tau_\parallel(\boldsymbol{k}) = \tau_0(\mathbf{k})\left\{\sum_{\boldsymbol{k}'} \boldsymbol{w}(\boldsymbol{k}, \boldsymbol{k}')\tau_\parallel(\boldsymbol{k}')\frac{\sin(k'_z d)}{\sin(k_z d)} + 1\right\}. \tag{7}$$

Here,

$$\tau_0^{-1}(\boldsymbol{k}) = \sum_{\boldsymbol{k}'} \boldsymbol{w}(\boldsymbol{k}, \boldsymbol{k}') \tag{8}$$

is the total probability per unit time of electron scattering from the state with the wave vector $\boldsymbol{k}$. Let us consider the approximation of a quasi-2D electron gas ($\Delta = 0$ if $\Delta \ll k_0 T$). Using expression (2) for the scattering probability (where only the leading term with $n = n' = 0$ is taken into account), we can rewrite Eqs. (6) and (7) as

$$\frac{\tau_\perp(E_\perp, \vartheta)}{\tau_0(E_\perp, \vartheta)} = C_I \times \int_{-\pi}^{+\pi} \frac{2E_\perp \tau_\perp(E_\perp, \vartheta')d\vartheta'}{[t^2(\vartheta' - \vartheta)^2 + \gamma^2]^{3/2}[4E_\perp + t^2(\vartheta' - \vartheta)^2 + \gamma^2]^{3/2}} + 1, \tag{9}$$

$$\frac{\chi_\parallel(E_\perp, \vartheta)}{\tau_0(E_\perp, \vartheta)} = C_I \times \int_{-\pi}^{+\pi} \frac{[2E_\perp + t^2(\vartheta' - \vartheta)^2 + \gamma^2]\chi_\parallel(E_\perp, \vartheta')d\vartheta'}{[t^2(\vartheta' - \vartheta)^2 + \gamma^2]^{3/2}[4E_\perp + t^2(\vartheta' - \vartheta)^2 + \gamma^2]^{3/2}} + \sin(\vartheta), \tag{10}$$

where

$$\frac{1}{\tau_0(E_\perp, \vartheta)} = C_I \times \int_{-\pi}^{+\pi} \frac{[2E_\perp + t^2(\vartheta' - \vartheta)^2 + \gamma^2]d\vartheta'}{[t^2(\vartheta' - \vartheta)^2 + \gamma^2]^{3/2}[4E_\perp + t^2(\vartheta' - \vartheta)^2 + \gamma^2]^{3/2}}; \tag{11}$$

$$\chi_\parallel(E_\perp, \vartheta) = \tau_\parallel(E_\perp, \vartheta)\sin(\vartheta); \tag{12}$$

$$C_I = 2\left(\frac{e^2 Z}{4\pi\varepsilon_0\varepsilon}\right)^2 \frac{\hbar a N_I^{CW}}{m_\perp d^2};$$

and

$$t^2 = \frac{\hbar^2}{2m_\perp d^2}, \quad \gamma^2 = \frac{\hbar^2\alpha^2}{2m_\perp}, \quad \vartheta = k_z d.$$

It should be noted that, unlike in the case of acoustic-phonon scattering [5], the only parameter characterizing the SL in Eqs. (9)–(11) is the period d. Other parameters, such as the QW width and the barrier height and thickness, have little influence in the case of uniform distribution of impurity. The reason for this is that the contribution of terms with $n, n' \neq 0$ in the sum (2) is small in comparison with the zero-indexed term, which is related to the behavior of the Fourier component of the screened Coulomb potential at small values of the longitudinal wave vector.

The electron mobility was calculated as

$$\mu_{xx} = \mu_{yy} = \mu_\perp = e\langle\tau_\perp\rangle/m_\perp,$$
$$\mu_{zz} = \mu_\parallel = e\langle\tau_\parallel\rangle/\langle m_\parallel\rangle, \tag{13}$$

where

$$\langle\tau_\perp\rangle = \int_0^\infty [-f_0'(E_\perp)]\tau_\perp(E_\perp)E_\perp dE_\perp / \int_0^\infty f_0(E_\perp)dE_\perp, \tag{14}$$

$$\langle\tau_\parallel\rangle = \int_0^\infty [-f_0'(E_\perp)]\tau_\parallel(E_\perp)dE_\perp / \int_0^\infty [-f_0'(E_\perp)]dE_\perp, \tag{15}$$

$$\tau_\perp(E_\perp) = \frac{1}{\pi}\int_0^\pi \tau_\perp(E_\perp, \vartheta)d\vartheta,$$
$$\tau_\parallel(E_\perp) = \frac{2}{\pi}\int_0^\pi \tau_\parallel(E_\perp, \vartheta)\sin^2(\vartheta)d\vartheta, \quad (16)$$

$$\frac{1}{\langle m_\parallel\rangle} = \frac{1}{2}\left(\frac{\Delta d}{2\hbar}\right)^2\int_0^\infty [-f_0'(E_\perp)]dE_\perp / \int_0^\infty f_0(E_\perp)dE_\perp \quad (17)$$

is the energy-averaged value of the inverse longitudinal effective mass of electrons.

3. NUMERICAL ANALYSIS

The relaxation time and mobility of electrons under conditions of ionized-impurity scattering were calculated numerically for a GaAs/$Al_{0.36}Ga_{0.64}As$ compositional SL with doped QWs. We used the following material parameters for GaAs and $Al_xGa_{1-x}As$ [6]: $m_\perp = m^* = 0.066m_0$ and $\varepsilon = 13.18$. Nonlinear integral equations (9) and (10) were solved numerically by the difference method [7].

Dependences of the relaxation time on the energy of the transverse motion and on the longitudinal wave vector were calculated for an SL with $a = 5$ nm, $b = 8$ nm, and $\Delta = 0.10$ meV, where b is the barrier width. Calculation of the miniband width was carried out using the method described in [8]. The relaxation time was calculated under the condition $aN_I^{CW} = nd$ for nondegenerate electron gas with a density $n = 10^{16}$ cm^{-3} at $T = 77$ K. With these parameters, the energy-averaged relaxation times calculated by formulas (14) and (15) are $\langle\tau_\perp\rangle = 2.1$ ps and $\langle\tau_\parallel\rangle = 1.1$ ps. This is close to the value of $\langle\tau\rangle = 1.6$ ps for the relaxation time in uniformly doped GaAs calculated for the same parameters by the Brooks–Herring formula and to the value of $\langle\tau_\perp\rangle = \langle\tau_\parallel\rangle = 1.8$ ps for the acoustic-phonon-limited relaxation time of electrons calculated for the same SL [5]. The mobilities calculated by formulas (13) with $\langle m_\parallel\rangle = 25m_0$ are $\mu_\perp = 5.6$ m^2 V^{-1} s^{-1} and $\mu_\parallel = 7.9 \times 10^{-3}$ m^2 V^{-1} s^{-1}; this can be compared with the mobility in bulk GaAs: $\mu = 4.3$ m^2 V^{-1} s^{-1}.

The dependences of the transverse and longitudinal relaxation times on $\vartheta = k_z d$ for a constant transverse-motion energy $E_\perp = k_0T$ are plotted in Fig. 1 (curves *1* and *2*, respectively). One can see that both $\tau_\perp$ and $\tau_\parallel$ grow with increasing k_z. However, the transverse relaxation time exhibits only a moderate increase with k_z, whereas the longitudinal relaxation time tends to infinity as k_z approaches π/d.

The dependences of the transverse and longitudinal relaxation times averaged over the longitudinal wave vector on the energy of the transverse motion were calculated from (16) and are shown in Fig. 2 (curves *1* and *2*, respectively). Their behavior is close to the power law with the exponent being greater than unity for $\tau_\perp(E_\perp)$ and smaller than unity for $\tau_\parallel(E_\perp)$. One can see that the transverse relaxation time always exceeds the relaxation time in bulk GaAs (curve *3*), while, for the longitudinal relaxation time, this is the case only at $E_\perp < 3k_0T$. An approximate calculation carried out with the electron wave function taken as a Bloch-type sum of the wave functions of isolated, infinitely deep QWs [4] yields lower values of both $\tau_\perp(E_\perp)$ (curve *1*') and $\tau_\parallel(E_\perp)$(curve *2*'). In contrast to the transverse relaxation time, this discrepancy is considerable for the longitudinal relaxation time. This leads to a reduced anisotropy

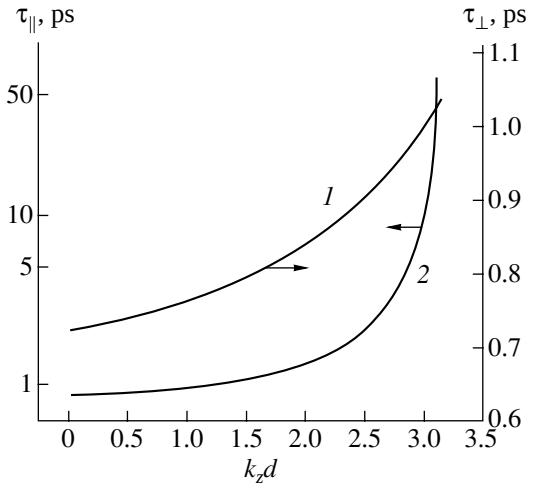

Fig. 1. Dispersion of the transverse and longitudinal relaxation times with respect to the longitudinal wave vector; $T = 77$ K, the transverse-motion energy $E_\perp = k_0T$.

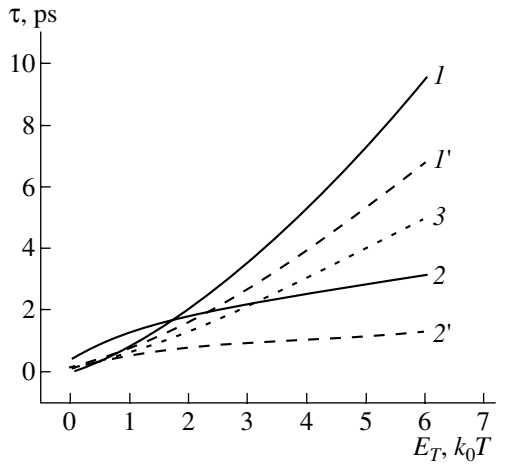

Fig. 2. Dispersion of the transverse and longitudinal relaxation times (averaged over the longitudinal wave vector) with respect to the transverse-motion energy: (*1*) $\tau_\perp(E_\perp)$, (*2*) $\tau_\parallel(E_\perp)$, (*1*') $\tau_\perp(E_\perp)$*, (*2*') $\tau_\parallel(E_\perp)$*, and (*3*) $\tau(E)$ for bulk GaAs; * marks the results obtained with the approximate wave function [4].

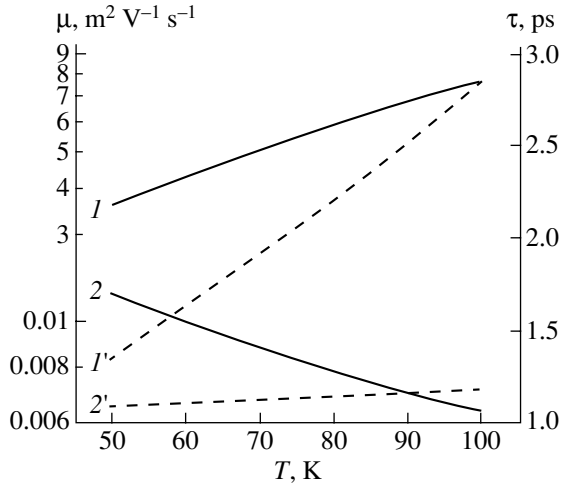

Fig. 3. Temperature dependences of the mobilities and the energy-averaged components of the relaxation-time tensor: (*1*) $\mu_\perp$, (*2*) $\mu_\parallel$, (*1'*) $\langle\tau_\perp\rangle$, and (*2'*) $\langle\tau_\parallel\rangle$.

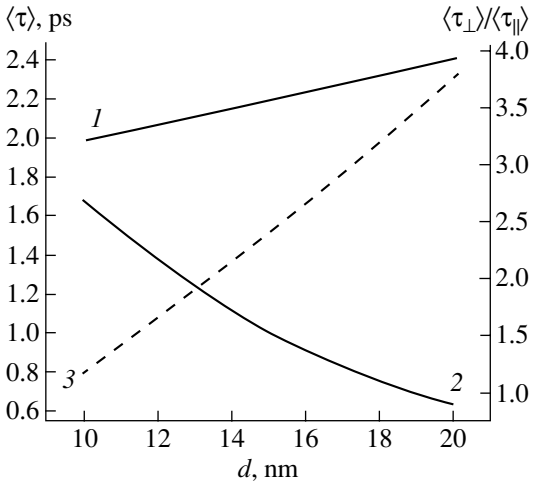

Fig. 4. Dependences of the energy-averaged components of the relaxation-time tensor on the SL period under constant electron density: (*1*) $\langle\tau_\perp\rangle$, (*2*) $\langle\tau_\parallel\rangle$, and (*3*) $\langle\tau_\perp\rangle/\langle\tau_\parallel\rangle$.

of the energy-averaged relaxation time calculated in this paper ($\langle\tau_\perp\rangle/\langle\tau_\parallel\rangle = 1.9$) in comparison with that obtained from the approximate calculation ($\langle\tau_\perp\rangle/\langle\tau_\parallel\rangle = 3.4$).

Differences in the variation of longitudinal and transverse relaxation times with the transverse-motion energy lead to different temperature dependences of the energy-averaged relaxation times and mobilities (Fig. 3). One can see that, with increasing temperature, $\langle\tau_\perp\rangle$ (curve *2'*) grows considerably weaker than $\langle\tau_\parallel\rangle$ (curve *1'*); as a consequence, the longitudinal mobility $\mu_\parallel$ (curve *2*) decreases with increasing temperature, while the transverse mobility $\mu_\perp$ (curve *1*) increases—a behavior similar to the mobility in bulk GaAs.

Dependences of the energy-averaged components of the relaxation-time tensor $\langle\tau_\perp\rangle$ and $\langle\tau_\parallel\rangle$ on the SL period under a constant electron density $n = 10^{16}$ cm^{-3} are shown in Fig. 4. One can see that an increase in the SL period leads to an increase in the transverse relaxation time (curve *1*) and a decrease in the longitudinal relaxation time (curve *2*). Due to this different behavior, the anisotropy of the relaxation time $\langle\tau_\perp\rangle/\langle\tau_\parallel\rangle$ increases nearly by a factor of four upon a twofold increase in the SL period (see curve *3*).

4. CONCLUSION

Thus, the following conclusions can be made from the numerical analysis of the electron scattering by ionized impurities in SLs with doped QWs, carried out using the electron wave function given by expression (1): (i) there is a pronounced dependence of the longitudinal relaxation time on the longitudinal wave vector; (ii) the longitudinal and transverse relaxation times show different dependences on the transverse-motion energy, which results in different temperature dependences of the longitudinal and transverse mobilities; and (iii) the anisotropy of the relaxation time increases with an increase in the SL period.

It should be noted that the results of the numerical analysis were obtained in an approximation assuming a quasi-2D nature of the electron gas. This imposes substantial limitations on the SL parameters (such as the width of the QWs and the height and thickness of the potential barriers) and the relationships between them, which ensure that the condition $\Delta \ll k_0 T$ remains valid. In order to extend the present treatment to the SLs where the electron gas no longer exhibits quasi-2D behavior, one needs to take into account the energy of longitudinal motion in the equation expressing total-energy conservation when an electron is scattered by an ionized impurity.

REFERENCES

1. J. Lee, H. N. Spector, and V. K. Arora, J. Appl. Phys. **54**, 6995 (1983).
2. A. Gold, Phys. Rev. B **35**, 723 (1987).
3. J. L. Thobel and L. Baudry, J. Appl. Phys. **73**, 233 (1993).
4. S. I. Borisenko, Fiz. Tekh. Poluprovodn. (St. Petersburg) **36**, 861 (2002) [Semiconductors **36**, 808 (2002)].
5. S. I. Borisenko, Fiz. Tekh. Poluprovodn. (St. Petersburg) **36**, 1237 (2002) [Semiconductors **36**, 1360 (2002)].
6. H. Landolt and R. Börnstein, in *Numerical Date and Functional Relationships in Science and Technology,* Ed. by O. Madelung (Springer, Berlin, 1987); New Ser. Group III, Vol. 22a, p. 451.
7. N. N. Kalitkin, *Numerical Methods* (Nauka, Moscow, 1978), Chap. 14, p. 455.
8. S. I. Borisenko and G. F. Karavaev, Fiz. Tekh. Poluprovodn. (St. Petersburg) **32**, 607 (1998) [Semiconductors **32**, 544 (1998)].

Translated by M. Skorikov

Semiconductors, Vol. 37, No. 5, 2003, pp. 573–580. Translated from Fizika i Tekhnika Poluprovodnikov, Vol. 37, No. 5, 2003, pp. 592–598.

LOW-DIMENSIONAL SYSTEMS

Electronic and Optical Properties of $AlAs/Al_xGa_{1-x}As(110)$ Superlattices

G. F. Karavaev, V. N. Chernyshov, and R. M. Egunov

Kuznetsov Physicotechnical Institute, Tomsk State University, pl. Revolyutsii 1, Tomsk, 634050 Russia

e-mail: karavaev@elefot.tsu.ru

Submitted July 29, 2002; accepted for publication October 16, 2002

Abstract—Electronic states in the conduction band of $(AlAs)_M(Al_xGa_{1-x}As)_N(110)$ superlattices are investigated for various M and N. It is shown that electronic properties of these structures are mainly determined by electrons of two pairs of valleys, namely, either Γ–X^Z or X^X–X^Y. Calculations based on the developed model of joining the envelope functions were carried out. Miniband spectra, symmetry, and localization of wave functions, as well as probabilities of miniband-to-miniband infrared absorption, are determined and analyzed. It is shown that, in the case of the X^X–X^Y pair of valleys, the absorption probabilities are high not only for polarization of light along the growth axis of the superlattice but also for the normal incidence of an optical wave on the structure surface. © *2003 MAIK "Nauka/Interperiodica".*

1. INTRODUCTION

When investigating electronic and optical properties of III–V-based nanostructures, most attention is given to structures for which the states in the center of the Brillouin zone (Γ point) play a leading role. Considerably fewer studies are devoted to the structures whose electronic properties are caused by the states at the edge of the Brillouin zone (X point). Previously, we considered similar structures with the [111] growth axis [1, 2]. This study is devoted to the theoretical investigation of the electronic and optical properties of $(AlAs)_M(Al_xGa_{1-x}As)_N$ superlattices (SL) with (110) interfaces. Here, M and N are the number of monolayers for the AlAs layer and a solid solution layer, respectively. To date, there is a lack of theoretical knowledge about these systems, in contrast with the structures with (001) and (111) interfaces. The symmetry of defect states for an SL with (001), (110), and (111) layers was investigated in [3]. The electronic states in GaAs(110) quantum wells were investigated in [4, 5]. The optical properties of GaAs/AlAs(110) SLs were investigated in [6]. To our knowledge, the SLs with a [110] growth axis and a rather large period, for which the role of the X electrons is decisive, have not been investigated.

Let us discuss the symmetry of an $(AlAs)_M(Al_xGa_{1-x}As)_N(110)$ SL. By virtue of the closeness of the lattice constants a for the AlAs and $Al_xGa_{1-x}As$ crystals, we will consider them to be equal and ignore the strains emerging in the SL which are caused by their actual distinction. Each atomic plane normal to the growth axis contains anions and cations. The distance between neighboring atomic planes equals $a/2\sqrt{2}$. Increasing numbers can be assigned to atomic planes as the distance from a certain plane (considered as the origin) increases. In this case, planes with even and odd numbers will emerge. The atomic arrangement for even (or odd) planes is identical. The atomic arrangement for odd planes differs by a certain vector in the (110) plane relative to even planes. Therefore, the SL symmetry depends on the M and N numbers. Let us first consider the translational symmetry. All possible SLs belong to an orthorhombic crystal system. For an even $M + N$ sum, it is convenient to select the SL unit cell in the form of a rectangular parallelepiped, which is based on the vectors $A_1 = (a/2)(1, -1, 0)$, $A_2 = (M + N)(a/2)(1, 1, 0)$, and $A_3 = a(0, 0, 1)$. Such a lattice is simple; it is denoted by a Γ_0 symbol. For an odd sum $M + N$, the A_1 and A_3 vectors are retained, whereas the A_2 vector can be selected in the form $A_2 = (M + N - 1)(a/2)(1, 1, 0) + (a/2)(1, 0, 1)$. The corresponding lattice is body-centered; it is denoted by a Γ_0^v symbol. The Brillouin zone for the Γ_0 lattice is rather simple and constitutes a rectangular parallelepiped. The Brillouin zone for the Γ_0^v lattice is shown in Fig. 1. Let us further consider the SL point symmetry. If there is a layer in which the ML number is odd, i.e., one or both numbers, M and N, are odd, the origin of coordinates can be placed at one of the atoms in the middle atomic plane of such a layer. In this case, the SL is symmetric relative to a rotation by 180° around the [001] axis and relative to reflections in the (110) and $(1\bar{1}0)$ planes. Corresponding space groups of symmetry are symmorphic (C_{2v}^1 for odd M and N, and C_{2v}^{20} for odd $M(N)$ and even $N(M)$). If the ML number is even for both layers, it is convenient to select the origin at the middle of one of

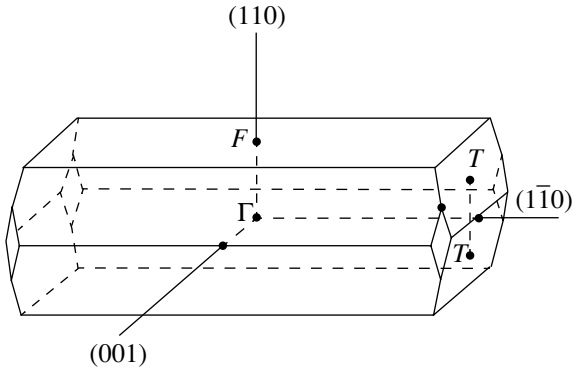

Fig. 1. Brillouin zone of the $(AlAs)_M(Al_xGa_{1-x}As)_N(110)$ superlattice; $(M + N)$ is an odd number.

the layers between two atomic planes. In this case, the SL is symmetric relative to the reflection in the $(1\bar{1}0)$ plane. However, the rotation by 180° and the reflection in the (110) plane should be accompanied by fractional translations; the SL should superpose itself due to this operation. The corresponding space group is non-symmorphic; it is symbolized as C_{2v}^7 [7].

2. MODELS OF ELECTRON SCATTERING AT THE HETEROINTERFACE

We investigated the electronic states for the SL in the approximation of an interface-discontinuous potential. In contrast with structures with (001) and (111) orientations [1, 2], we selected heterointerfaces in the middle of spacings between atomic layers. The calculation was carried out by the scattering-matrix method, and a complex band structure was determined by the empirical pseudopotential method. The calculation is described in detail elsewhere [1, 2]. To describe the electronic states in these structures, we developed corresponding approximate models in the framework of an approximation of envelope functions. They are briefly discussed below. A more detailed substantiation of the models suggested will be given in a separate report.

2.1. X^X–X^Y Model

Depending on the value of the component $k_\parallel$ of the wave vector, which is parallel to heterointerfaces, electronic minibands are formed from various valleys of starting components.

In the case $k_\parallel = (2\pi/a)(1/2, -1/2, 0)$, two X valleys exist, whose wave-vector components are normal to the heterointerface: $k_\perp^X = (2\pi/a)(1/2, 1/2, 0)$ ($\mathbf{k} = (2\pi/a)(100)$, X^X valley), and $k_\perp^Y = (2\pi/a)(-1/2, -1/2, 0$ ($\mathbf{k} = (2\pi/a)(0\bar{1}0)$, X^Y valley). For an even ML number, $M + N$, the X^X and X^Y points find themselves at the same point at the boundary of the Brillouin zone. For an odd ML number, they are found at various points on the T star (see Fig. 1). For this $k_\parallel$, two X wells (X^X and X^Y) exist in the AlAs layer and two X barriers exist in the $Al_xGa_{1-x}As$ layer; as a result, the X^X–X^Y mixing of states is possible.

Our investigations showed that, for the case $k_\parallel = (2\pi/a)(1/2, -1/2, 0)$, we can restrict ourselves to a four-valley model in which the wave function for each medium can be represented as

$$\Psi = F_{X1}^X|X_1^X\rangle + F_{X3}^X|X_3^X\rangle + F_{X1}^Y|X_1^Y\rangle + F_{X3}^Y|X_3^Y\rangle + \chi, \quad (1)$$

where $|X_1^X\rangle$, $|X_1^Y\rangle$, $|X_3^X\rangle$, and $|X_3^Y\rangle$ are the real wave functions of the X_1 and X_3 levels at the points X^X and X^Y; and F are the envelope functions for corresponding states. Joining conditions at the heterointerfaces are found for precisely these functions and their normal derivatives. For joining conditions of a desired wave function, allowance is made for contributions which are related to four valleys. However, this does not mean that only four summands should be represented in expansion (1). Even more than four terms can be involved in expansion (1); however, only four envelope functions can be considered as independent. Other contributions, which are described by the χ function in expansion (1), should be taken into account to determine the energy spectrum and wave functions more exactly.

It was found that the envelope functions F and their normal derivatives F' at the heterointerfaces satisfy the following joining conditions:

$$\tilde{\mathbf{F}}^A = \tilde{\mathbf{T}}\tilde{\mathbf{F}}^B. \quad (2)$$

Here, index A corresponds to the AlAs layer; index B corresponds to the solid solution layer; $\tilde{\mathbf{F}}^A$ and $\tilde{\mathbf{F}}^B$ are the column vectors with eight components: F_{X1}^X, F_{X3}^X, F_{X1}^Y, F_{X3}^Y, $(F_{X1}^X)'$, $(F_{X3}^X)'$, $(F_{X1}^Y)'$, and $(F_{X3}^Y)'$; and $\tilde{\mathbf{T}}$ is the (8×8) joining matrix. By virtue of the symmetry of the problem, the system of eight equations (2) could be reduced to two uncoupled systems of four equations. To this end, let us form symmetric and antisymmetric linear combinations of envelope functions and their derivatives, and write joining conditions for these functions. As a result, Eq. (2) transforms to the form

$$\mathbf{F}^A = \mathbf{T}\mathbf{F}^B, \quad (3)$$

where $\mathbf{F}^A$ and $\mathbf{F}^B$ are the column vectors,

$$\mathbf{F} = \frac{1}{\sqrt{2}}(F_{X1}^X + F_{X1}^Y, F_{X3}^X + F_{X3}^Y, (F_{X1}^X + F_{X1}^Y)', (F_{X3}^X + F_{X3}^Y)', F_{X1}^X - F_{X1}^Y, F_{X3}^X - F_{X3}^Y, (F_{X1}^X - F_{X1}^Y)', (F_{X3}^X - F_{X3}^Y)'); \quad (4)$$

$$\mathbf{T} = \mathbf{T}_1 \oplus \mathbf{T}_2. \quad (5)$$

The (4×4) matrices $\mathbf{T}_1$ and $\mathbf{T}_2$ take the form

$$\mathbf{T}_{1(2)} = x\mathbf{E} + (1-x)\mathbf{B}_{1(2)}, \quad (6)$$

where x characterizes the composition of the solid solution, $\mathbf{E}$ is a (4×4) unit matrix, and $\mathbf{B}_{1(2)}$ are the matrices determined according to the procedure [1, 2] and are equal to

$$\mathbf{B}_{1(2)} = \begin{pmatrix} 0.9715 & \mp 0.0109 & \mp 0.0073 & 0.0033 \\ \mp 0.0447 & 1.0236 & -0.0045 & \mp 0.0059 \\ \pm 0.1268 & -0.0679 & 1.0579 & \mp 0.0486 \\ -0.1761 & \pm 0.2938 & \mp 0.0039 & 1.0630 \end{pmatrix}. \quad (7)$$

The upper signs in matrix (7) are related to the $\mathbf{B}_1$ matrix, and the lower signs are related to the $\mathbf{B}_2$ matrix. Note that matrix elements which couple the envelope functions to their derivatives are not dimensionless. Numerical values in matrix (7) are given with the proviso that the length unit is the lattice parameter of the bulk material. The basis Bloch functions for bulk materials are determined with the proviso that the origin of coordinates is at the As atom; these functions are selected as real functions. As a result, the elements of matrices $\mathbf{B}_{1(2)}$ are also found to be real. Matrices $\mathbf{T}_1$ and $\mathbf{T}_2$ determined at the selected nth interface do not change in passing to the mth interface if the number K of monolayers between them is even, and matrix $\mathbf{T}_1$ transforms to matrix $\mathbf{T}_2$ and vice versa if K is odd. This variation in joining matrices can be formally described by the relationship $\mathbf{T}(m) = \mathbf{U}^{-1}(K)\mathbf{T}(n)\mathbf{U}(K)$, where

$$\mathbf{U}(K) = \begin{pmatrix} 0 & -\mathbf{E} \\ -\mathbf{E} & 0 \end{pmatrix}^K, \quad (8)$$

and $\mathbf{E}$ is a unit four-by-four matrix.

To carry out the numerical calculations, the joining conditions for envelope functions should be complemented by a model for determining the energy spectrum and wave functions for bulk materials. When solving the Schrödinger equation, the states associated with the X^X and X^Y points may be considered separately for each layer. In the neighborhood of the $X^{X(Y)}$ point, we find the wave function in a form of expansion in the wave functions of the $X_1^{X(Y)}$ and $X_3^{X(Y)}$ states of the conduction band and in two functions of the $X_5^{X(Y)}$ states of the valence band. Upon substituting these expansion into the Schrödinger equation for the $X^{X(Y)}$ valleys, we derive a system of linear equations for coefficients D of this expansion:

$$\begin{pmatrix} E_{X1} + E_0 w^2 - E & -iE_0 R_1^X w & iE_0 R_2^X w & 0 \\ iE_0 R_1^X w & E_{X3} + E_0 w^2 - E & 0 & iE_0 R_3^X w \\ -iE_0 R_2^X w & 0 & E_{X5} + E_0 w^2 - E & 0 \\ 0 & -iE_0 R_3^X w & 0 & E_{X5} + E_0 w^2 - E \end{pmatrix} \begin{pmatrix} D_1 \\ D_3 \\ D_{5y(x)} \\ D_{5z} \end{pmatrix} = 0. \quad (9)$$

Here, $w = (k_\perp - k_\perp^{X(Y)})a$; $E_0 = \hbar^2/2m_0a^2$; $\hbar$ is Planck's constant; m_0 is the rest mass of a free electron; and

$$R_1^X = i\langle X_1|P_X|X_3\rangle a\sqrt{2}/\hbar,$$
$$R_2^X = -i\langle X_1|P_Y|X_{5Y}\rangle a\sqrt{2}/\hbar,$$
$$R_3^X = -i\langle X_3|P_Z|X_{5Z}\rangle a\sqrt{2}/\hbar.$$

The energies of the X_1, X_3, and X_5 states, as well as the matrix elements $\langle X_i|P_\alpha|X_j\rangle$ of the momentum operator for the $Al_xGa_{1-x}As$ layer at various x, which are necessary for the calculation, are determined by the pseudopotential method and are given in [2]. Note that the set of equations (9) is identical for the X^X and X^Y valleys, since we are considering the case for a fixed $k_\parallel = (2\pi/a)(1/2, -1/2, 0)$.

From the conditions of solvability for the system of algebraic equations (9), the roots $w_j(E)$ are derived. In this case, not all roots derived are taken into account, but only those which satisfy the conditions for the applicability of Eqs. (9). There are four such roots for each system of equations. Thus selected, the $w_j(E)$ roots turn out to be very close to those found upon investigating the complex band structure by the pseudopotential method. The envelope functions of the X^X and X^Y wave functions take the form of linear combination of partial solutions $D_i^{X(Y)}(j)\exp(iw_jy'/a\sqrt{2})$, where $y' = (x+y)/\sqrt{2}$. The wave functions w_j for both valleys are identical. As a result, for each layer, general solution (1) depends on eight arbitrary coefficients.

2.2. Γ–X^Z Model

For $k_\parallel = 0$, the Γ state with $k_\perp = 0$ and a state with $k_\perp^Z = (2\pi/a)(110)$ exist. It is clear that the latter state is equivalent to the X^Z state to within the reciprocal lattice vector $\mathbf{b} = (2\pi/a)(\bar{1}\bar{1}1)$. For this $k_\parallel$ value, X wells and Γ barriers exist in the AlAs layer, and Γ wells and X barriers exist in the $Al_XGa_{1-X}As$ layer; the Γ–X mixing of

states is possible at the heterointerfaces. For an even ML number in the SL period, the Γ and X^Z points of the Brillouin zone of sphalerite convolve at the center of the Brillouin zone of the SL; and in the case of an odd ML number, the X^Z point finds itself at the Brillouin zone boundary (F point).

To describe electron states for $k_\parallel = 0$, a three-valley model is a good approximation. In this model, the wave function for each medium is written in the form

$$\Psi = F_1^\Gamma|\Gamma_1\rangle + F_{X1}^Z|X_1^Z\rangle + F_{X3}^Z|X_3^Z\rangle + \chi, \qquad (10)$$

where $|\Gamma_1\rangle$, $|X_1^Z\rangle$, and $|X_3^Z\rangle$ are the wave functions for the Γ_1, X_1, and X_3 states; F are the envelope functions for corresponding states; and the χ function

$$\chi = F_{5x}^Z|X_{5z}^Z\rangle + F_{5y}^Z|X_{5y}^Z\rangle + F_{15}^\Gamma|\Gamma_{15}^V\rangle + F_{15c}^\Gamma|\Gamma_{15}^C\rangle \qquad (11)$$

describes the contribution of X_5 states of the valence band and the nearest Γ_{15} states (the latter imply the combinations $|\Gamma_{15}\rangle = (1/\sqrt{2})(|\Gamma_{15x}\rangle + |\Gamma_{15y}\rangle)$).

As before, the envelope functions F and their normal derivatives F' at the heterointerfaces satisfy joining conditions of form (3); in this case, **F** are the six-component column vectors:

$$\mathbf{F} = (F_{X1}^Z, F_{X3}^Z, (F_{\Gamma1}^Z)', (F_{X1}^Z)', (F_{X3}^Z)', F_{\Gamma1}). \qquad (12)$$

The joining matrix T has a six-by-six order and, similarly to the previous case, can be represented in the form

$$\mathbf{T} = x\mathbf{E} + (1-x)\mathbf{B}. \qquad (13)$$

The **B** matrix, which is also determined according to the procedure [1, 2], has the form (for the same system of units)

$$\mathbf{B} = \begin{pmatrix} 0.9637 & 0.0064 & 0.0373 & 0 & 0 & 0 \\ 0.0005 & 0.9900 & 0.0299 & 0 & 0 & 0 \\ 0.0372 & -0.0594 & 0.9348 & 0 & 0 & 0 \\ 0 & 0 & 0 & 1.14477 & 0.1454 & 0.8011 \\ 0 & 0 & 0 & -0.0585 & 0.9524 & -0.8218 \\ 0 & 0 & 0 & 0.0252 & 0.0251 & 0.8020 \end{pmatrix}. \qquad (14)$$

In the **T** matrix, the elements describing the Γ–X^Z interaction change sign when the interface spaced at an odd number of monolayers is reached.

To find the envelope functions in the Γ and X^Z valleys, the systems of equations of type (9) should be used. A system of equations for the X^Z valley evidently differs from system (9):

$$\begin{pmatrix} E_{X1} + E_0w^2 - E & 0 & iE_0R_2^Xw & iE_0R_2^Xw \\ 0 & iE_{X3} + E_0w^2 - E & iE_0R_3^Xw & iE_0R_3^Xw \\ -iE_0R_2^Xw & -iE_0R_3^Xw & E_{X5} + E_0w^2 - E & 0 \\ -iE_0R_2^Xw & -iE_0R_3^Xw & 0 & E_{X5} + E_0w^2 - E \end{pmatrix} \begin{pmatrix} D_{X_1} \\ D_{X_3} \\ D_{X_{5x}} \\ D_{X_{5y}} \end{pmatrix} = 0. \qquad (15)$$

Here, $w = (k_\perp - k_\perp^Z)a$, and the other designations are similar to system (9).

For the Γ valley, we used a system of equations which permits one to adequately describe the nonparabolicity of the energy spectrum. We took into account the direct interaction of the Γ_1 level in the conduction band with the nearest Γ_{15} levels in the valence and conduction bands. As a result, we derived a system of three equations:

$$\begin{pmatrix} E_{\Gamma_1} + E_0w^2 - E & iE_0R_1^\Gamma w & -iE_0R_2^\Gamma w \\ -iE_0R_1^\Gamma w & E_{\Gamma_{15}^V} + E_0\lambda_V w^2 - E & 0 \\ iE_0R_2^\Gamma w & 0 & E_{\Gamma_{15}^C} + E_0\lambda_C w^2 - E \end{pmatrix} \begin{pmatrix} D_{\Gamma_1} \\ D_{\Gamma_{15}^V} \\ D_{\Gamma_{15}^C} \end{pmatrix} = 0. \qquad (16)$$

Here, $w = k_\perp a$;

$$\lambda_V = 1 + \frac{4E_0|R_3^\Gamma|^2}{E_{\Gamma_{15}^V} - E}, \quad \lambda_C = 1 + \frac{4E_0|R_3^\Gamma|^2}{E_{\Gamma_{15}^C} - E}$$

account for the direct interaction $\Gamma_{15}^C - \Gamma_{15}^V$ in effective masses; and

$$R_1^\Gamma = -i\langle\Gamma_1|P_X|\Gamma_{15}^V\rangle a\sqrt{2}/\hbar,$$
$$R_2^\Gamma = i\langle\Gamma_1|P_X|\Gamma_{15}^C\rangle a\sqrt{2}/\hbar,$$
$$R_3^\Gamma = -i\langle\Gamma_{15}^C|P_X|\Gamma_{15}^V\rangle a\sqrt{2}/\hbar.$$

Matrix elements of the momentum operator, similarly to the E_{Γ_1}, $E_{\Gamma_{15}}^V$, and $E_{\Gamma_{15}}^C$ energies, are determined by the pseudopotential method. From the conditions for the solvability of the sets of algebraic equations (15) and (16), the roots $w_j(E)$ that satisfy the conditions for the applicability of Eqs. (15) and (16) are found. It turns out that there are four such roots, if we consider the envelope functions of X functions, and two roots in the case of Γ functions. Thus-chosen roots are used to construct the general solution for envelope functions in the form of a linear combination of partial solutions $D_i^{\Gamma(Z)}(j)\exp(iw_j y'/a\sqrt{2})$. It is clear that, in this case the wave numbers w_j are different for the Γ and X^Z valleys.

Thus, the models presented in this section allow one to investigate various quantum properties of AlAs/Al_xGa_{1-x}As-based nanostructures. Note that our calculations with the use of the pseudopotential method and calculations based on the above models give practically identical results.

3. ANALYSIS OF ELECTRONIC PROPERTIES OF SUPERLATTICES

We investigated the situation where the resonance energies of the Γ states for the $Al_xGa_{1-x}As$ layer are higher than the energies of the X valleys for the AlAs layer. This condition is realized by the choice of x and N quantities, and allows one to exclude the influence of Γ electrons on the photoelectric properties. The properties of such superlattices are mainly governed by X electrons.

In this study, we report the results of calculations for the $(AlAs)_M(Al_xGa_{1-x}As)_N(110)$ structures, which are further denoted as (M, N), where M = 13 or 16 and N = 13 or 16 with x = 0.3. Let d_1 be the thickness of the AlAs layer, and d_2, the thickness of the solid solution layer. In this case, the SL period along the growth direction is $d = d_1 + d_2$. According to the Bloch theorem, with a shift by an integer SL vector (mainly along the growth axis by the period $d = d_1 + d_2$), the solution should be changed by a phase factor. Let us write this condition in the form

$$\mathbf{F}^{A(B)}(y') = e^{-iQd}\mathbf{U}(M+N)\mathbf{F}^{A(B)}(y'+d), \qquad (17)$$

where Q is the component of the wave vector of the SL along the [110] direction. If $k_\parallel = (2\pi/a)(1/2, -1/2, 0)$, Q is counted from the T point, into which the X^Y point convolves, the $\mathbf{F}$ vector is defined by formula (4), and the matrix $\mathbf{U}$ is defined by formula (8). If $k_\parallel = 0$, Q is counted from the Γ point, $\mathbf{F}$ takes form (12), and $\mathbf{U}$ is a diagonal six-by-six matrix, which differs from the unit matrix by four terms in the main diagonal (elements 1, 2, 4, 5), which are equal to $(-1)^{M+N}$.

Let us first consider the case $k_\parallel = (2\pi/a)(1/2, -1/2, 0)$. As was already noted above, the general solution for each layer depends on eight arbitrary coefficients. Since condition (17) is valid for each y', eight linear equations follow from this relationship, which link 16 unknown coefficients. Just as many equations for the same coefficients can be derived using the scattering matrix, which couples the states at opposite boundaries of the SL unit cell along the [110] direction. From the condition for solvability of these sets of equations, the spectrum of admissible energies is determined. Then, the envelope functions are constructed for each layer and the general solution of the problem is found in form (1). We described this procedure in detail previously [1].

The energy spectra for four lower states in relation to the wave vector Q of the SL for the SLs (13,13), (16,13), and (16,16) are shown in Fig. 2. Note that the energy position of minibands correlates well with the levels of corresponding quantum wells. Attention should be drawn to the radically different run of dispersion curves for the three cases under consideration. For the SL (13,13), the space group is C_{2v}^1 and all small corepresentations for the points at the Brillouin zone boundary along the line $(2\pi/a)(0.5 + \kappa, -0.5 + \kappa, 0)$, where $|\kappa| \le 0.5(N + M)^{-1}$, are one-dimensional [7]. Therefore, each miniband in Fig. 2a is nondegenerate. For the SL (16,16), the space group is C_{2v}^7 and its small corepresentations along this line are two-dimensional. Accordingly, the minibands are doubly degenerate (Fig. 2c). Finally, for the SL (16,13), all small corepresentations for the points along the same line, which now passes through the Brillouin zone and connects two nonequivalent points of the T star (see Fig. 1), are one-dimensional (the SL space group is C_{2v}^{20}) and the minibands are nondegenerate. It can be seen that the splitting of minibands is small, specifically, about 0.01–0.02 eV both for the first and second pair of minibands.

The total electron density for the structure (16,13) at Q = 0 for the first and third lower levels, which is averaged over the unit cell of a bulk crystal, is shown in Fig. 3. The dependences of the electron density for the second and fourth levels have a similar form. It can be seen that the electron density is concentrated mainly in

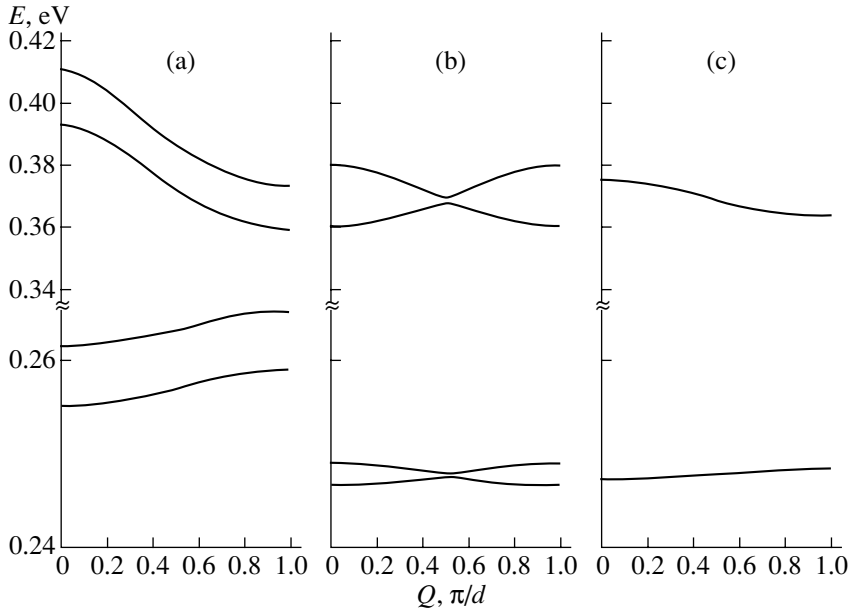

Fig. 2. Miniband spectrum for the $(AlAs)_M(Al_{0.3}Ga_{0.7}As)_M(110)$ superlattices—dependences of energy E on the wave vector Q for $k_{||} = (2\pi/a)(1/2, -1/2, 0)$. Numbers (M, N): (a) (13,13), (b) (16,13), and (c) (16,16). Miniband energies E are reckoned from the conduction band bottom of GaAs.

the AlAs layer. Similar behavior is also observed for most of the other structures investigated. A small discontinuity of the average electron density is observed at the heterointerface, which is associated with the difference between Bloch wave functions for the AlAs and $Al_xGa_{1-x}As$ layers. For all above-listed SLs, the Σ quantities, which characterize the SL ability to absorb infrared radiation, were calculated:

$$\Sigma = |\mathbf{e} \cdot \mathbf{P}_{12}|^2.$$

Here, $\mathbf{P}_{12} = \langle \Psi_1(\mathbf{r})|P|\Psi_2(\mathbf{r})\rangle$ is the matrix element of momentum between the wave functions of the first and second pair of minibands; and **e** is the polarization vector of the optical wave, which is chosen so that the value of Σ is largest. The calculation showed that the $(AlAs)_M(Al_xGa_{1-x}As)_N(110)$ structures can absorb normally incident radiation rather efficiently (see table). In the table, the indexes, which are given in the second column, numerate the functions of minibands as the energy increases. For the degenerate case (16,16), s (a) denotes the function which is symmetric (antisymmetric) relative to the reflection in the $(1\bar{1}0)$ plane, while the number indicates the miniband number. Note that zero values of the Σ quantity for the structures with an even ML number (13,13) and (16,16) are caused by the symmetry of wave functions. For these structures, similarly for both normal and lateral incidence of light, the Σ quantity decreases monotonically with increasing Q. For the structures (13,16) and (16,13), the Q dependence of Σ is different for dissimilar transitions. Furthermore, the values $\Sigma = 0$ for these functions, which are given in the table, simply mean that $\Sigma < 10^{-3}$. It can be seen from the results obtained that, in general, the Σ quantity for normal incidence is smaller than this quantity for lateral incidence of light on the structure by a factor of 3–4. The results obtained are quite acceptable, since the normal incidence of light can involve an area

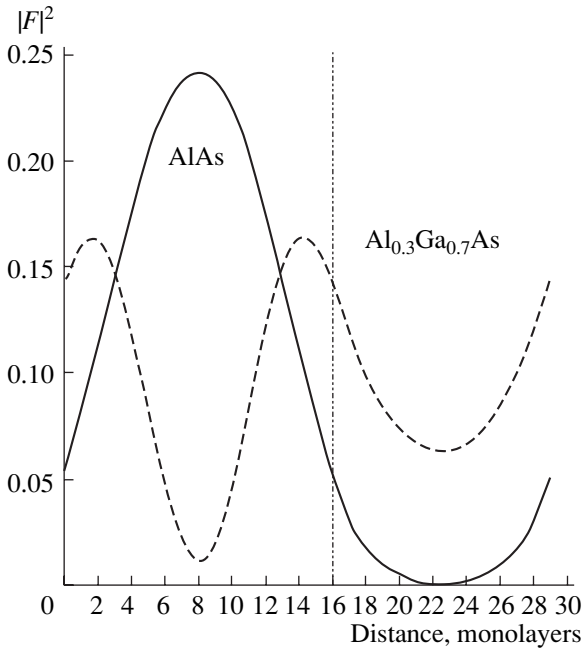

Fig. 3. Distribution of the total electron density $|F|^2$ over the period of the $(AlAs)_{16}(Al_{0.3}Ga_{0.7}As)_{13}(110)$ superlattice. The solid line corresponds to the first miniband, and the dashed line corresponds to the third miniband.

Optical parameter Σ for various directions of incidence of the optical wave

(*M*, *N*)	Transition	$Q = 0$		$Q = \pi/2d$		$Q = \pi/d$	
		Normal	Lateral	Normal	Lateral	Normal	Lateral
(13, 13)	1–3	0	0.348	0	0.436	0	0.573
	1–4	0.114	0	0.126	0	0.158	0
	2–3	0.129	0	0.14	0	0.169	0
	2–4	0	0.388	0	0.457	0	0.589
(13, 16)	1–3	0.021	0.314	0	0.451	0.021	0.314
	1–4	0.111	0.137	0.126	0	0.111	0.137
	2–3	0.131	0.207	0.142	0	0.131	0.206
	2–4	0.019	0.291	0	0.457	0.019	0.291
(16, 13)	1–3	0	0	0.113	0.002	0	0
	1–4	0.107	0.332	0.001	0.385	0.107	0.332
	2–3	0.137	0.478	0.004	0.401	0.137	0.478
	2–4	0	0	0.124	0.014	0	0
(16, 16)	s1–s2	0	0.372	0	0.406	0	0.447
	s1–a2	0.117	0	0.122	0	0.130	0
	a1–s2	0.117	0	0.122	0	0.130	0
	a1–a2	0	0.372	0	0.406	0	0.447

which is larger than that for lateral incidence by a factor of several orders of magnitude.

Let us briefly consider the results for $k_{\|} = 0$. In contrast with the previous case, the choice of *M* and *N* values basically does not affect the energy spectrum. As an example, the spectrum of the SL with $M = 16$, $N = 13$, and $x = 0.3$ is shown in Fig. 4. In this case, the *Q* component of the wave vector of the SL along the [110] direction is reckoned from the Γ point. Note that, in this case, the energy position of corresponding minibands is approximately 0.01 eV higher than that for $k_{\|} = (2\pi/a)(1/2, -1/2, 0)$. This correlates with the difference in effective masses for the $X^{X(Y)}$ and X^{Z} valleys along the [110] direction. The calculation demonstrated that the electron density is concentrated mainly in the AlAs layers. It is found that the Σ quantity for transitions from the first miniband to the second miniband for the normal incidence of light for all *Q* is considerably smaller compared with this quantity for the lateral incidence of light on the structure.

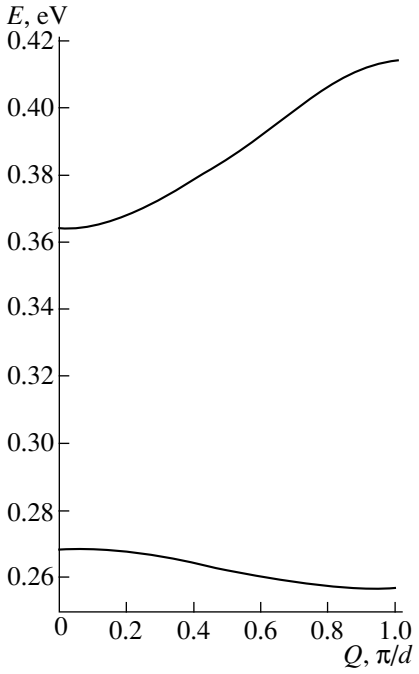

Fig. 4. Miniband spectrum for the $(AlAs)_{16}(Al_{0.3}Ga_{0.7}As)_{13}(110)$ superlattices as a function of the wave vector *Q* for $k_{\|} = 0$. Miniband energies *E* are reckoned from the conduction band bottom of GaAs.

4. CONCLUSION

In this study, the energy spectrum of electrons in an $(AlAs)_M(Al_xGa_{1-x}As)_N$ SL with (110) interfaces and solid solution composition $x = 0.3$ was investigated. In this case, the electrons of the *X* valleys play the main role, since the Γ states are higher in energy. In the general case, these *X* valleys are located at various points of the Brillouin zone of the SL. The energies of lower minibands were found, and the origin of corresponding states was analyzed. It was shown that the electron density in lower minibands is concentrated mainly in the AlAs layers. The squares of corresponding optical matrix elements were determined; it was shown that, similarly to an analogous SL with (111) interfaces, the

SLs investigated can absorb rather efficiently the radiation that is incident normally on the surface. It turns out that such behavior is characteristic of the states that are related to the $X^{X(Y)}$ valleys. However, for the states related to the X^Z valley, the absorption of radiation that is incident normally on the SL surface is actually forbidden. It was noted that the minibands that are related to the $X^{X(Y)}$ valleys are actually lower than the minibands related to the Γ–X^Z valleys in energy. Therefore, the former minibands will manifest themselves more clearly. Thus, the $(AlAs)_M(Al_xGa_{1-x}As)_N$ SLs grown in the [110] direction, similarly to the SL grown in the [111] direction [1, 2], may be of interest as structures for infrared photodetectors.

ACKNOWLEDGMENTS

This study was supported by the Russian Foundation for Basic Research, project no. 02-02-17848.

REFERENCES

1. G. F. Karavaev, V. N. Chernyshov, and R. M. Egunov, Fiz. Tekh. Poluprovodn. (St. Petersburg) **36**, 558 (2002) [Semiconductors **36**, 527 (2002)].
2. G. F. Karavaev, V. N. Chernyshov, and R. M. Egunov, Fiz. Tekh. Poluprovodn. (St. Petersburg) **36**, 709 (2002) [Semiconductors **36**, 670 (2002)].
3. P. Tronc, Yu. E. Kitaev, A. G. Panfilov, *et al.*, Phys. Rev. B **61**, 1999 (2000).
4. M. Yoshita, N. Kondo, H. Sakaki, *et al.*, Phys. Rev. B **63**, 075305 (2001).
5. S. Nojima, Phys. Rev. B **47**, 13535 (1993).
6. U. Schmid, N. E. Christensen, M. Cardona, *et al.*, Phys. Rev. B **45**, 3546 (1992).
7. O. V. Kovalev, *Representations of the Crystallographic Space Groups: Irreducible Representations, Induced Representations, and Corepresentations* (Nauka, Moscow, 1986; Gordon and Breach, Yverdon, Switzerland, 1993).

Translated by N. Korovin

Semiconductors, Vol. 37, No. 5, 2003, pp. 581–585. Translated from Fizika i Tekhnika Poluprovodnikov, Vol. 37, No. 5, 2003, pp. 599–603.

LOW-DIMENSIONAL SYSTEMS

Photoluminescence Study of AlGaAs/GaAs/AlGaAs Double Quantum Wells Separated by a Thin AlAs Layer

G. B. Galiev, M. V. Karachevtseva, V. G. Mokerov, V. A. Strakhov, G. N. Shkerdin, and N. G. Yaremenko*

Institute of Radio Engineering and Electronics, Russian Academy of Sciences, Moscow, 103907 Russia

** e-mail: tg275@ms.ire.rssi.ru; spike@fryazino.net*

Submitted May 22, 2002; accepted for publication October 28, 2002

Abstract—Photoluminescence (PL) spectra of $Al_{0.21}Ga_{0.79}As/GaAs/Al_{0.21}Ga_{0.79}As$ double quantum wells (DQWs) separated by a thin AlAs barrier have been studied in the temperature range 77–300 K. The well width was varied from 65 to 175 Å, and the thickness of the AlAs barrier was 5, 10, or 20 Å. In the case of a sufficiently thin (5, 10 Å) AlAs barrier, the energy spectrum of QW states is considerably modified by coupling between the QWs. This effect shifts the main spectral peak of PL, and specific features associated with the splitting of the ground state into symmetric and asymmetric states are observed in the spectra at higher temperatures. The DQW structure with a 20-Å-thick AlAs barrier is a system of two uncoupled asymmetric $Al_{0.21}Ga_{0.79}As/GaAs/AlAs$ QWs. The energy levels in double coupled QWs were calculated as functions of the well width and AlAs barrier thickness, and good correlation with the experimentally observed energies of optical transitions was obtained. *© 2003 MAIK "Nauka/Interperiodica".*

1. INTRODUCTION

Double quantum wells (DQWs), which constitute a system of two QWs separated by a thin (several monolayers) layer of another material, have been investigated experimentally and theoretically over the last three decades. Initially, these studies were closely associated with the problem of the fabrication and application of semiconductor superlattices, since a system of two coupled wells can be regarded as a unit cell of a superlattice.

Recently, new interest in these systems was inspired by studies which predicted new effects in DQWs and discussed their possible applications in micro- and optoelectronic devices. These effects include (i) an increase in mobility due to a decrease in the rate of electron-phonon scattering and (ii) population inversion for electron quantum subbands and the related stimulated emission [1, 2].

It is necessary to note that the majority of studies were performed with AlGaAs/GaAs/AlGaAs DQWs with a thin AlGaAs barrier having the same composition as the main barriers. The electrical and optical properties of this system have been thoroughly investigated. In particular, the photoluminescence (PL) spectra have been studied in relation to the thickness of the AlGaAs barrier and it was shown that the coupling of electron wave functions in the wells strongly modifies the energy spectrum of localized states in DQW for an AlGaAs barrier thickness up to 40 Å [3].

Much less studied is the AlGaAs/GaAs/AlGaAs DQW system with a thin AlAs layer as the separating barrier, impenetrable to phonons. A considerable decrease in the electron–phonon scattering and an improvement in the transport characteristics was predicted for this system [4]. In this case, it is necessary to ensure that, being a "phonon-wall," the AlAs barrier remains tunnel-transparent for electrons. Therefore, an important step in the engineering of AlGaAs/GaAs/AlGaAs DQWs with an AlAs barrier is the study of electron states as functions of the main parameters of a structure: the AlAs-layer thickness, width of wells, and height of the main $Al_xGa_{1-x}As$ barriers. One of the most informative methods for studying specific features in the energy spectrum of carriers in semiconductors is PL spectroscopy. Investigations of PL spectra enable the high-accuracy determination of the ground state energy in a QW at low temperatures and the energies of excited states at higher temperatures.

The goal of the present study is to investigate the temperature behavior of PL spectra of $Al_{0.21}Ga_{0.79}As/GaAs/Al_{0.21}Ga_{0.79}As$ DQWs with an AlAs barrier of varied thickness depending on the QW width and to correlate the data obtained with calculated energies of localized states in this system. The PL in similar structures has been studied in [5, 6]. However, in these studies, there was considerable discrepancy between the experiment and calculations. We believe that this incongruence resulted from several assumptions made by the authors to simplify the calculation of quantum levels, such as the equality of effective masses in all layers [5], or an infinitely high AlAs barrier [6]. In the present study, we have made an attempt to perform more stringent calculations tak-

1063-7826/03/3705-0581$24.00

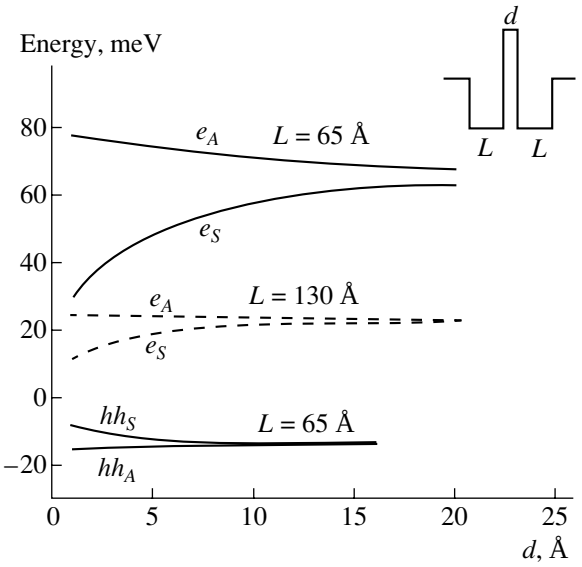

Fig. 1. Calculated energies of (e_S, e_A) electron and (hh_S, hh_A) hole levels relative to GaAs energy gap edges vs. the AlAs-barrier thickness d in an $Al_{0.21}Ga_{0.79}As/GaAs/Al_{0.21}Ga_{0.79}As$ DQW with the QW widths (solid lines) L = 65 Å and (dashed lines) L = 130 Å. Insert: a profile of the conduction band bottom.

ing into account the real parameters of all the layers in a DQW.

2. EXPERIMENTAL

A standard technique was applied in the study of PL spectra $I(h\nu)$. The PL was excited using a CW Ar-ion laser (488 nm) with the excitation density varied in the range 10–10^3 W cm^{-2}. A sample was placed in an optical cryostat, and its temperature was varied from liquid-nitrogen to room temperature. An FEU-62 photomultiplier was used as the photodetector.

Parameters of structures and peak energies $h\nu_{max}$ in PL spectra

Structure	L, Å	d, Å	$h\nu_{max}$, eV
SQW 61	65		1.552
DQW 55	65	20	1.565
DQW 62	65	5	1.552
SQW 54	130		1.523
DQW 46	130	20	1.528
DQW 50	130	10	1.524
DQW 56	130	5	1.520
SQW 45	260		1.510
DQW 52	90	20	1.546
SQW 51	180		1.514
DQW 59	175	20	1.516
SQW 58	350		1.507

The structures for study were grown by MBE on (100)GaAs substrates by successive deposition of the following undoped layers: a GaAs buffer layer (0.5 μm thick); an $Al_{0.21}Ga_{0.79}As$ lower barrier layer (310 Å); a GaAs layer serving as the QW material; an $Al_{0.21}Ga_{0.79}As$ top barrier (310 Å); and a GaAs (80 Å) capping layer. The growth temperature was 600°C for GaAs and AlAs, and 640°C for $Al_{0.21}Ga_{0.79}As$ layers; the ratio of As and Ga flow rates in the growth region was 30. Along with symmetric AlGaAs/GaAs/AlGaAs single QWs (SQW), DQWs were grown, which differed by the presence of a thin AlAs layer in the middle of the GaAs well, which was thus separated into two asymmetric AlGaAs/GaAs/AlAs wells of equal width. The insert in Fig. 1 shows a schematic profile of the conduction band bottom in a DQW. Structures with different QW widths L = 65–350 Å and thicknesses of the AlAs separating layer d = 5, 10, and 20 Å have been studied. The parameters of samples with double and single quantum wells (DQW and SQW) are listed in the table.

3. RESULTS OF CALCULATIONS

The energies of electron and hole levels in SQWs and DQWs with parameters corresponding to those in the structures under study have been calculated.

The energy levels in wells were obtained by solving the Schrödinger equations (three for SQW and five for DQW) taking into account the continuity of wave functions and their first derivatives at heterointerfaces. The calculations were performed using an approximation of the isotropic parabolic dependences of the electron and hole energies on the wave vector; the ratio between the offsets of the conduction and valence bands, $\Delta E_c/\Delta E_v$, was assumed to be 0.6/0.4.

The electron and hole energy levels E_n in SQWs with asymmetric barriers were found by numerically solving the equation

$$\frac{(ik-\gamma_1 k_1)(ik-\gamma_2 k_2)}{(ik+\gamma_1 k_1)(ik+\gamma_2 k_2)} - \exp(2ikL) = 0,$$

where i is an imaginary unit; $k = \sqrt{2mE_n}/\hbar$; $k_1 = \sqrt{2m_1(V_1 - E_n)}/\hbar$; $k_2 = \sqrt{2m_2(V_2 - E_n)}/\hbar$; V_1 and V_2 are the height of AlGaAs and AlAs barriers, respectively; m, m_1, and m_2 are the effective masses in the GaAs well and in the AlGaAs and AlAs barriers, respectively; L is the QW width; $\gamma_1 = m/m_1$; and $\gamma_2 = m/m_2$.

For a symmetric SQW, $k_2 = k_1$.

For a DQW, the equation for the calculation of levels can be simplified to the form

$$\left[\left(\beta + \frac{ik}{\gamma_2 k_2}\right)\Big/\left(\beta - \frac{ik}{\gamma_2 k_2}\right)\right]^2 - \exp(-2k_2 d) = 0,$$

where

$$\beta = \frac{\alpha\exp(-ikd/2) + \exp(ikd/2)}{\alpha\exp(-ikd/2) - \exp(ikd/2)},$$

$$\alpha = \frac{ik + \gamma_1 k_1}{ik - \gamma_1 k_1}\exp[ik(2L + d)],$$

L is the width of each of the asymmetric wells constituting the DQW, and d is the AlAs-barrier thickness.

Figure 1 shows the calculated results for DQWs with well widths L = 65 and 130 Å. At large enough d, when coupling between the wells in a DQW is absent, the calculation yields the energy of the ground level in an isolated SQW of the width L with asymmetric AlGaAs/GaAs/AlAs barriers. When the separating barrier becomes thinner, the coupling between the wells is enhanced, and the levels are split into symmetric (e_S, hh_S) and antisymmetric (e_A, hh_A) states. In the limit d = 0, the DQW turns into a single symmetric AlGaAs/GaAs/AlGaAs well of width 2L, and the split states turn into 1e and 2e (1hh and 2hh) levels in this well. Between the two limiting cases, the calculated dependences describe the electron spectrum of a system of two bound asymmetric wells, each of width L. It is seen that the coupling of electron wave functions is manifested to a greater extent in DQWs with narrower wells. The levels e_A and e_S merge in the DQW system with the well width L = 130 Å; i.e., the wells are no longer coupled at the AlAs-barrier thickness $d \gtrsim 15$ Å. A slight (~5 meV) splitting of electron levels still remains in QWs of the width L = 65 Å with d = 20 Å. Calculations show that the hole level is split to a much lesser extent than the electron level; at L = 130 Å, splitting is virtually absent, so the curves are not shown in the picture.

Figure 2 shows the calculated energies of the PL peak ($h\nu_{max}$) related to the transition 1e–1hh as functions of the well width for SQWs with symmetric and asymmetric barriers, AlGaAs/GaAs/AlGaAs and AlGaAs/GaAs/AlAs. The energy deficit with respect to the GaAs energy gap (E_{GaAs}) $E_{def} = h\nu_{max} - E_{GaAs}$, is plotted along the ordinate axis, which is commonly done in studies of the energy spectrum of localized states in quantum-confined semiconductor systems. This representation allows for a more accurate comparison of the experimental and calculated data than that in the case of absolute values. Furthermore, it excludes the temperature dependence of the GaAs energy gap and allows comparison of spectra recorded at different temperatures.

As seen in Fig. 2, the energy of the 1e–1hh transition is higher in asymmetric wells than in symmetric wells. The difference decreases as the width of the well increase, and it becomes negligible at d > 150 Å.

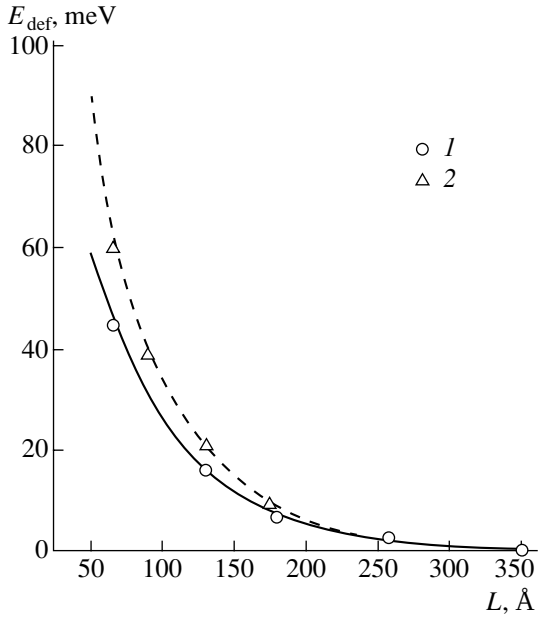

Fig. 2. Calculated dependences of $E_{def} = h\nu_{max} - E_{GaAs}$ on the QW width for SQWs: (solid line) symmetric AlGaAs/GaAs/AlGaAs SQW, (dashed line) asymmetric AlGaAs/GaAs/AlAs SQWs. Points: (*1*) experimental E_{def} values for symmetric SQWs, and (*2*) a DQW with a 20-Å-thick AlAs barrier.

4. DISCUSSION

Figures 3a and 3b show the experimental PL spectra $I(h\nu)$ recorded at T = 77 K. Each figure compares the spectra of two DQWs of the same width L which differ in the AlAs barrier thickness (5 and 20 Å) and the spectrum of a symmetrical SQW of the width 2L. The spectra of all the studied structures with double and single wells show a high-intensity band related to the transition between the ground states: this band corresponds to the 1e–1hh transition in an SQW and the e_S–hh_S transition in a DQW (the experimental values of the peak energy $h\nu_{max}$ of the main band are listed in the table). The shape of this band is nearly symmetric, its half-width being typical of undoped QWs (13–15 meV). It is noteworthy that the DQW spectra do not differ in their shape and half-width from the SQW spectra and that they contain no additional features, which confirms the high quality of the grown structures: the abruptness of heterointerfaces and the equality of widths of QWs constituting a DQW.

In the majority of structures, the spectra recorded at T = 77 K at a high excitation level contained, along with the main band, very weak bands in the high-energy part of the spectrum that were shifted from the main band by 90–100 meV. Judging from their energy position, these bands can be assigned only to transitions involving virtually bound carriers, i.e., electrons and holes in the continuum, with their energy close to the height of the main barriers ΔE_c and ΔE_v, respectively. The possibility of luminescence caused by a resonance increase in the

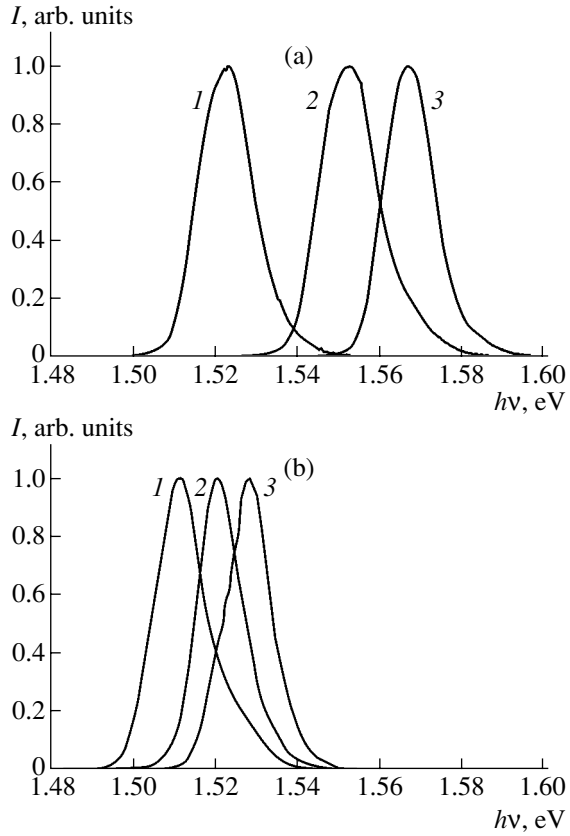

Fig. 3. PL spectra of different structures at T = 77 K. (a): (*1*) L = 130 Å (SQW 54); (*2*) L = 65 Å, d = 5 Å (DQW 62); (*3*) L = 65 Å, d = 20 Å (DQW 55). (b): (*1*) L = 260 Å (SQW 45); (*2*) L = 130 Å, d = 5 Å (DQW 56); (*3*) L = 130 Å, d = 20 Å (DQW 46).

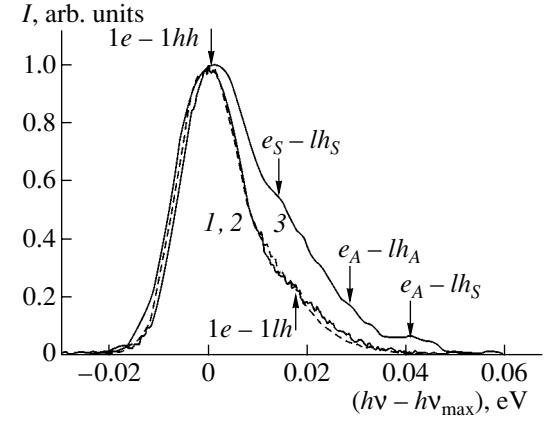

Fig. 4. PL spectra at T =180 K with band peak positions brought into coincidence for structures with a QW width L = 65 Å: (*1*) (dashed line) SQW 61; (*2*) (solid line) DQW 55, d = 20 Å; (*3*) DQW 62, d = 5 Å.

probability of capture by these levels was discussed in [7, 8]. In structures with L = 65 Å, the energy of these weak bands 1.660 ± 0.003 eV corresponds to the transition between electrons in a virtually bound state and holes at the 1*hh* level; in structures with L = 130 Å, these bands were observed at (1.610 ± 0.003) eV, which corresponds to the transition between the virtually bound holes and electrons at the 1*e* level. These bands were not observed at elevated temperatures due to the strong temperature quenching of luminescence.

For SQWs, the experimental data on the peak energies $h\nu_{max}$ of bands in the PL spectra correlate with the calculation for an SQW with symmetric barriers (solid curve in Fig. 2). For all DQWs with an AlAs barrier of thickness d = 20 Å, the energies $h\nu_{max}$ fall on the curve calculated for asymmetric SQWs (dashed curve). Even for the DQW with the thinnest wells L = 65 Å, for which, according to calculations, a small splitting of electron levels remains, the transition energy differs by no more than 1–2 meV from the value calculated for an asymmetric SQW of the same size. Therefore, at the AlAs layer thickness d = 20 Å and in the studied range of well widths 65–175 Å, any DQW may be regarded as a system of two isolated asymmetric wells.

As the AlAs barrier becomes thinner (d = 10 and 5 Å), its tunneling transparency increases, and the changes caused by enhanced coupling between the electron wave functions in a DQW are observed in the PL spectra. The spectral peaks are shifted to lower energies with respect to those for the DQW with d = 20 Å. Spectral features related to the splitting of the lowest electron and hole levels appear at high temperatures. According to calculations, the PL spectra of narrower wells are more strongly affected by coupling: at d = 5 Å, the spectral peak is shifted by 15 and 8 meV for the wells of 65 and 130 Å width, respectively (Figs. 3a and 3b). These data are in good agreement with the calculated dependence of the energy of the first electron level on the thickness of the AlAs barrier in coupled wells (Fig. 1).

With rising temperature, the peak of the main PL band of all of the structures shifts in accordance with the temperature dependence of the GaAs band gap and the short-wavelength shoulders related to filling of higher subband levels appear. The number and the energy positions of these transitions depend on the well width and also on the tunneling transparency of the separating AlAs barrier in the case of a DQW.

In narrow wells, in which the energy spacing between the first and second electron levels is large, high-energy transitions can be related only to the filling of higher hole states. Figure 4 shows spectra of structures with the same QW width L = 65 Å: an SQW and two DQWs differing in the AsAs-barrier thickness, with peak positions of the spectra brought into coincidence. The spectra of the DQW with d = 20 Å and the SQW spectrum show one and the same transition 1*e*–1*lh* at a distance of 18–19 meV from the main band, which coincides with the results of calculations for isolated wells. In the spectrum of coupled DQWs with an AlAs-barrier thickness d = 5 Å, in which the energy spacing between the symmetric and antisymmetric

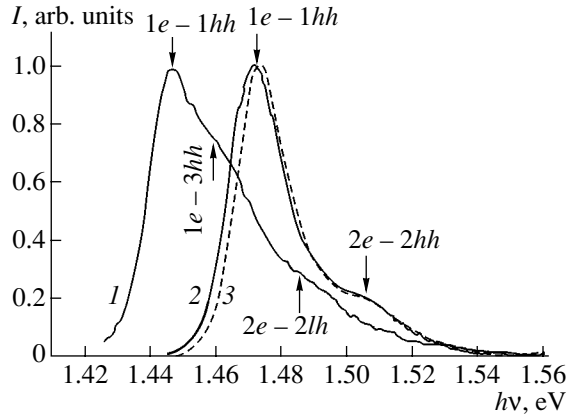

Fig. 5. PL spectra: (*1*) SQW 45, L = 260 Å, T = 250 K; (*2*) SQW 51, L = 180 Å, T = 210 K; (*3*) DQW 59, L = 175 Å, d = 20 Å, T = 210 K.

states arising from the splitting of the first electron level is 26 meV, the transitions involving these states were revealed on raising the temperature. The calculated energies of these transitions are indicated by arrows in the figure. The transition between the antisymmetric electron and symmetric hole levels, e_A–lh_S, which is forbidden in an ideally rectangular well, is rather clearly manifested in the spectrum. The appearance of this transition can be accounted for by the presence of a built-in field, which lifts the selection rules. This field exists even in undoped structures owing to a background impurity [9].

Thermal filling of the second electron level becomes possible in wide wells. The transitions from this level are revealed in high-temperature PL spectra of structures with well widths of 175 and 260 Å (Fig. 5).

5. CONCLUSION

Our study has shown that if a sufficiently thin (5, 10 Å) AlAs barrier is introduced into the middle of a $Al_{0.21}Ga_{0.79}As/GaAs/Al_{0.21}Ga_{0.79}As$ QW, the electron coupling between the wells in a DQW exerts a considerable influence on the energy spectrum of quantum states, which leads to a shift of the main PL band, and in high-temperature spectra, to the appearance of spectral features related to the splitting of levels into symmetric and antisymmetric states. At an AlAs-barrier thickness of 20 Å, a DQW is a system of two isolated wells with asymmetric AlGaAs/GaAs/AlAs barriers in the entire range of studied well widths. The lack of coupling between the wells is confirmed by coincidence of the PL spectra with the spectra of single wells of the same size. Good correlation between the experimentally observed and calculated energies of the optical transitions has been obtained.

REFERENCES

1. J. Pozela, V. Juciene, and K. Pozela, Semicond. Sci. Technol. **10**, 1076 (1995).
2. Z. Moussa, P. Boucaud, F. H. Julien, *et al.*, Electron. Lett. **31**, 912 (1995).
3. H. Kawai, J. Kaneko, and N. Watanabe, J. Appl. Phys. **58**, 1263 (1985).
4. K. Pozela, J. Pozela, and V. Juciene, in *Proceedings of 9th International Symposium on Nanostructures: Physics and Technology*, St. Petersburg, Russia (2001), p. 18.
5. J. Leburton, T. Schmiedel, B. D. McCombe, *et al.*, J. Appl. Phys. **72**, 4753 (1992).
6. M. Bayer, V. B. Timofeev, F. Faller, *et al.*, Phys. Rev. B **54**, 8799 (1996).
7. G. Bastard, U. O. Ziemelis, C. Delalande, *et al.*, Solid State Commun. **49**, 671 (1984).
8. S. V. Kozyrev and A. Ya. Shik, Fiz. Tekh. Poluprovodn. (Leningrad) **19**, 1667 (1985) [Sov. Phys. Semicond. **19**, 1024 (1985)].
9. A. V. Guk, V. É. Kaminskiĭ, V. G. Mokerov, *et al.*, Fiz. Tekh. Poluprovodn. (St. Petersburg) **31**, 1367 (1997) [Semiconductors **31**, 1178 (1997)].

Translated by D. Mashovets

Semiconductors, Vol. 37, No. 5, 2003, pp. 586–593. Translated from Fizika i Tekhnika Poluprovodnikov, Vol. 37, No. 5, 2003, pp. 604–611.

LOW-DIMENSIONAL SYSTEMS

Electron Heating by a Strong Longitudinal Electric Field in Quantum Wells

L. E. Vorob'ev, S. N. Danilov, V. L. Zerova*, and D. A. Firsov

St. Petersburg State Technical University, ul. Politekhnicheskaya 29, St. Petersburg, 195251 Russia

**e-mail: VZerova@rphf.spbstu.ru*

Submitted October 22, 2002; accepted for publication November 11, 2002

Abstract—The electron heating by a strong longitudinal electric field and the energy losses due to the scattering of nonequilibrium electrons by polar optical phonons in rectangular GaAs/AlGaAs quantum wells are studied. A simple model is suggested to calculate the rate of energy losses due to the scattering of electrons by nonequilibrium optical phonons. Some of the experimental results on the heating of charge carriers in quantum wells are discussed, and it is shown that taking nonequilibrium optical phonons into account significantly improves the agreement between the theoretical and experimental data. *© 2003 MAIK "Nauka/Interperiodica".*

1. INTRODUCTION

The intraband transitions of electrons in quantum wells (QWs) have been intensively studied in recent years. The reason is that some new types of optoelectronic devices can be developed on the basis of QWs. However, the heating of charge carriers in a QW by a longitudinal electric field (lying in the QW-layer plane) was analyzed only in a few studies. In most cases, electron heating during optical pumping was investigated [1]. There are also a number of theoretical and experimental studies where electron transport in superlattices in a transverse electric field was analyzed [2–5].

In this study, the electron heating by a strong longitudinal electric field and the energy losses of nonequilibrium charge carriers in QWs are analyzed. The energy losses due to the scattering of charge carriers by optical and acoustic phonons, both in bulk semiconductors [1, 6–8] and in QWs (see, for example, [9, 10]), have been investigated in a number of studies (including those where phonon accumulation was taken into account). In particular, it was found that phonon accumulation leads to a decrease in the rate of energy loss [11] and also affects the dynamic properties of nonequilibrium charge carriers. The models for simulating electron–phonon interaction are in agreement with the experimental data. The majority of theoretical models take into account scattering by optical and acoustic phonons, quantization of the phonon spectrum, phonon accumulation, and screening.

The purpose of this study is to consider the results of some experiments in which charge carriers in QWs were heated and to investigate the effect of nonequilibrium optical phonons on the energy-loss rate of carriers. A simple model for calculating the rate of energy losses of electrons due to their scattering by nonequilibrium optical phonons is suggested. It is shown that taking nonequilibrium optical phonons into account considerably improves the agreement between the theoretical and experimental data.

2. CALCULATION OF THE RELAXATION TIME AND THE RATE OF ENERGY LOSSES DUE TO SCATTERING BY POLAR OPTICAL PHONONS, WITH AND WITHOUT CONSIDERATION OF PHONON ACCUMULATION

Let us calculate the energy-loss rate of hot electrons in a QW. In polar semiconductors, hot charge carriers transfer their energy to the crystal lattice, mainly due to the scattering by long-wavelength polar optical (PO) phonons [12]. In this case, the rate of energy loss of one electron with a wave vector $\mathbf{k}$ lying in the QW plane is governed by the difference in the probabilities of phonon absorption and emission [12], i.e.,

$$d\mathcal{E}(\mathbf{k})/dt = \hbar\omega_0[w_a(\mathbf{k}) - w_e(\mathbf{k})], \qquad (1)$$

where ω_0 is the frequency of an optical phonon and $w_a(\mathbf{k})$ and $w_e(\mathbf{k})$ are the probabilities of phonon absorption and emission in the course of intrasubband transitions of an electron from the state with the wave vector $\mathbf{k}$. We assume that energy losses occur predominantly within the lower subband of an infinitely deep QW. This is a good approximation, since, in all of the experiments discussed below, the energy spacing between the subbands is large; therefore, the QWs can be considered as infinitely deep.

The smooth envelope of the wave function of an electron in the lower subband, $\Psi(x, y, z)$, represents the product of a plane wave and the wave function $\psi(z)$ that

1063-7826/03/3705-0586$24.00

describes the motion of the electron in the transverse direction (along the structure-growth axis *Oz*):

$$\Psi(x, y, z) = \frac{1}{\sqrt{S}}\exp(i\mathbf{k}\mathbf{r}_\perp)\psi(z),\quad \psi(z) = \sqrt{\frac{2}{L}}\sin\left(\frac{\pi z}{L}\right), \tag{2}$$
$$\mathbf{r}_\perp = (x, y),\quad \mathbf{k} = (k_x, k_y).$$

Here, S is the area of the quantum-confinement layer, L is the QW width, and $\mathbf{r}_\perp$ is the radius vector of an electron in the plane of the QW.

When emitting or absorbing phonons with all possible values of q, the electrons with the initial wave vector $\mathbf{k}_i$ undergo transitions to the final state $\mathbf{k}_j = \mathbf{k}_i \mp \mathbf{q}_\perp$, where the upper and lower signs correspond to the emission and absorption of a phonon, respectively. The expressions for the probabilities of emission and absorption upon such a transition, $w_e^{i\to j}(\mathbf{k}_i)$ and $w_a^{i\to j}(\mathbf{k}_i)$, respectively, can be written as

$$w_{a,e}^{i\to j}(\mathbf{k}_i) = \frac{2\pi}{\hbar}\sum_{\mathbf{k}_j}\left|H_{a,e}^{LO}\right|^2 f(\mathbf{k}_i)\{1 - f(\mathbf{k}_j)\} \times \delta[\mathscr{E}(\mathbf{k}_j) - \mathscr{E}(\mathbf{k}_i) \pm \hbar\omega_0]. \tag{3}$$

Here, $H_{a,e}^{LO}$ is the matrix element of the electron–phonon interaction and $f(\mathbf{k}_{i,j})$ is the value of the distribution function in the state $\mathbf{k}_{i,j}$. Expression (3) accounts for the possibility of partial occupation of the final states of the electron after scattering.

Some models for calculating the processes of electron–phonon interaction take into account the quantization of the phonon spectrum [13–15]. However, it was found that the quantization of the phonon-energy spectrum in heterostructures based on GaAs only slightly changes the energy-loss rate of electrons [16]. Therefore, when simulating the scattering processes, we disregarded phonon quantization.

Let us assume that the phonon spectrum of a heterostructure is the same as that of a bulk semiconductor. The matrix element describing the scattering of electrons within the lower subband of a two-dimensional (2D) system by the potential formed by three-dimensional (3D) long-wavelength PO phonons is constructed on the basis of the wave functions (2) and has the form [17]

$$H_{a,e}^{LO} = -i\frac{\sqrt{2\pi}e\sqrt{\hbar\omega_0}(\varepsilon_\infty^{-1} - \varepsilon_0^{-1})^{1/2}}{\sqrt{V}\sqrt{q_\perp^2 + q_z^2}}G_{ij}(q_z) \times \sqrt{N_q + \frac{1}{2} \mp \frac{1}{2}}\delta_{\mathbf{k}_j, \mathbf{k}_i \pm \mathbf{q}_\perp}. \tag{4}$$

Here, the upper and lower signs refer to the absorption and emission of a phonon, respectively; e is the elementary charge; V is the volume of the crystal; and ε_∞ and ε_0 are the high- and low-frequency permittivities of the polar semiconductor, respectively. The integral $G_{ij}(q_z)$ includes the overlapping of the wave functions of the initial and final electronic states ($\psi_i(z)$ and $\psi_j(z)$, respectively):

$$G_{ij}(q_z) = \frac{2}{L}\int_0^L\left[\sin\left(\frac{\pi}{L}z\right)\right]^2 e^{\pm iq_z z}dz. \tag{5}$$

There are a number of approximate methods for calculating integral (5). For example, in the momentum-conservation approximation (MCA) [18], integral (5) is approximated by the delta function. However, this approximation is not always accurate.

In order to eliminate error in the calculation of the intrasubband scattering in narrow QWs by the MCA method, we will use the calculation method suggested in [17]. Let us change the summation over $\mathbf{k}_j$ with the summation over $\mathbf{q}$ in expressions (3) in accordance with the law of conservation of momentum. Furthermore, in order to calculate the probabilities of scattering (3), we will change the summation over $\mathbf{q}$ with double integration; i.e., over $\mathbf{q}_\perp$ in the plane of the QW layer and over $\mathbf{q}_z$ along the transverse direction:

$$\sum_{\mathbf{q}} F(\mathbf{q}) \longrightarrow \int_{q_z=-\infty}^{q_z=+\infty}\frac{dq_z L}{2\pi}\int_{q_{\perp\min}}^{q_{\perp\max}}\int_{\theta=0}^{\pi} F(\mathbf{q}_\perp)\frac{2q_\perp dq_\perp d\theta S}{(2\pi)^2}. \tag{6}$$

Here, θ is the angle between the vectors $\mathbf{k}_i$ and $\mathbf{q}_\perp$. The limits of integration over $q_\perp$ for emission ($q_{\perp\min,\max}^e$) and absorption ($q_{\perp\min,\max}^a$) of phonons are determined from the law of conservation of energy:

$$q_{\perp\min,\max}^e = k_i \mp \sqrt{k_i^2 - 2m\omega_0/\hbar};$$
$$q_{\perp\min,\max}^a = \sqrt{k_i^2 + 2m\omega_0/\hbar} \mp k_i. \tag{7}$$

Here, m is the effective electron mass. The limits of integration over q_z are determined by the Brillouin zone boundaries; i.e., integration is performed from $-\pi/a$ to $+\pi/a$, where a is the lattice constant. Since $a \ll L$, these limits can be considered as infinite; i.e., from $-\infty$ to $+\infty$. The wave vector of the electron along the z direction is determined accurate to π/L; therefore, the wave vector of the phonon along the z direction is determined with the same accuracy.

Using expressions (4)–(7) to calculate the probabilities (3), we find that the probabilities of electron–phonon scattering are determined by the multiple integral, in which the integration variables (z, q_z, $q_\perp$, k_i and θ) are not separable. Let us denote the integral over q_z as $I_{ij}(q_\perp)$:

$$I_{ij}(q_\perp) = \int_{-\infty}^{+\infty}\frac{dq_z}{q_\perp^2 + q_z^2}|G_{ij}(q_z)|^2 = \int_{-\infty}^{+\infty}\frac{dq_z}{q_\perp^2 + q_z^2}\left|\frac{2}{L}\int_0^L\left[\sin\left(\frac{\pi z}{L}\right)\right]^2 e^{\mp iq_z z}dz\right|^2. \tag{8}$$

In the case of a rectangular, infinitely deep QW, the integral $I_{ij}(q_\perp)$ can be calculated analytically:

$$I_{ij}(q_\perp) = \pi L\left\{\frac{2}{(q_\perp L)^2} + \frac{1}{(q_\perp L)^2 + 4\pi^2} - \frac{32\pi^4[1-\exp(-q_\perp L)]}{(q_\perp L)^3[(q_\perp L)^3 + 4\pi^2]^2}\right\}. \quad (9)$$

Integration over the angle θ can also be performed analytically using the delta function. The functions $f(\mathbf{k}_i)$ and $f(\mathbf{k}_i \pm \mathbf{q}_\perp)$ can be regarded as the symmetric parts of the distribution function of electrons; in this case, $f(\mathbf{k}_i) = f(\mathscr{E}_{\mathbf{k}_i})$, $f(\mathbf{k}_i \pm \mathbf{q}_\perp) = f(\mathscr{E}_{\mathbf{k}_i} \pm \hbar\omega_0)$, and the distribution functions are independent of the angle θ. When integrating over θ, it is convenient to use the transformation $d\theta \longrightarrow d\cos\theta/\sin\theta = d\cos\theta/\sqrt{1-\cos^2\theta}$. Then, integration over cosθ yields the expression

$$\int_0^{2\pi} d\theta\,\delta\left(\frac{\hbar^2 q_\perp^2}{2m} \mp \frac{\hbar^2 k_i q_\perp}{m}\cos\theta \pm \hbar\omega_0\right)$$

$$= 2\int_{-1}^{1}\frac{d(\cos\theta)}{\sqrt{1-\cos^2\theta}}\,\delta\left(\frac{\hbar^2 q_\perp^2}{2m} \mp \frac{\hbar^2 k_i q_\perp}{m}\cos\theta \pm \hbar\omega_0\right) \quad (10)$$

$$= \frac{2m}{\hbar^2 k_i q_\perp}\frac{1}{\sqrt{1-(m\omega_0/\hbar k_i q_\perp \pm q_\perp/2k_i)^2}},$$

where the upper and lower signs refer to the processes of phonon emission and absorption, respectively.

It is convenient to go from integration over the wave vectors to integration over the corresponding energies $\mathscr{E}_{k_i} = \hbar^2 k_i^2/2m$ and $\mathscr{E}_{q\perp} = \hbar^2 q_\perp^2/2m$. Then, taking into account expressions (9) and (10), we obtain the following expressions for the probabilities of phonon emission and absorption by an electron with the energy $\mathscr{E}_{k_i}$:

$$w_e^{i\to j}(\mathscr{E}_{k_i}) = \frac{e^2\omega_0 m(\varepsilon_\infty^{-1} - \varepsilon_0^{-1})}{2\pi\hbar^2 k_i} \times \int_{q_{\perp\min}^e}^{q_{\perp\max}^e} dq_\perp I_{ij}(q_\perp)\left[1-\left(\frac{m\omega_0}{\hbar k_i q_\perp} + \frac{q_\perp}{2k_i}\right)^2\right]^{-1/2} \times f(\mathscr{E}_{k_i})[1-f(\mathscr{E}_{k_i} - \hbar\omega_0)](N_q+1);$$

$$w_a^{i\to j}(\mathscr{E}_{k_i}) = \frac{e^2\omega_0 m(\varepsilon_\infty^{-1} - \varepsilon_0^{-1})}{2\pi\hbar^2 k_i} \times \int_{q_{\perp\min}^a}^{q_{\perp\max}^a} dq_\perp I_{ij}(q_\perp)\left[1-\left(\frac{m\omega_0}{\hbar k_i q_\perp} - \frac{q_\perp}{2k_i}\right)^2\right]^{-1/2} \times f(\mathscr{E}_{k_i})[1-f(\mathscr{E}_{k_i} + \hbar\omega_0)]N_q. \quad (11)$$

The total probability of scattering by equilibrium polar optical phonons can be obtained by performing numerical integration of expressions (11) over k_i using the equilibrium distribution function of phonons $N_q = N_{q0}$, where

$$N_{q0} = \left[\exp\left(\frac{\hbar\omega_0}{k_B T}\right) - 1\right]^{-1}, \quad (12)$$

k_B is the Boltzmann constant, and T is the lattice temperature. The quantity that is inverse to the obtained total scattering probability determines the relaxation time.

The energy-loss rate of an electron with the wave vector **k** is determined by expressions (1) and (11). To obtain the average energy-loss rate, it is sufficient to average the difference of the probabilities (11) over the ensemble of electrons as follows:

$$\left\langle\frac{d\mathscr{E}}{dt}\right\rangle = \frac{\int(d\mathscr{E}/dt)k_i dk_i}{\int f(k_i)k_i dk_i}. \quad (13)$$

In order to take into account the effect of phonon accumulation, we introduce the nonzero lifetime of optical phonons τ_q. Let us assume that this lifetime is independent of the phonon wave vector. In this case, the nonequilibrium distribution function of phonons can be written as

$$N_q = N_{q0} + N_{qN} \approx N_{q0} + \frac{dN_q}{dt}\tau_q, \quad (14)$$

where N_{qN} is the nonequilibrium part of the distribution function of phonons and dN_q/dt is the rate of variation in the number of phonons with the wave vector **q**:

$$\frac{dN_q}{dt} = \frac{2\pi}{\hbar}\sum_{\mathbf{k}_i}\left|H_e^{LO}\right|^2 f(\mathbf{k}_i + \mathbf{q}_\perp)[1-f(\mathbf{k}_i)] \times \delta[\mathscr{E}(\mathbf{k}_i + \mathbf{q}_\perp) - \mathscr{E}(\mathbf{k}_i) - \hbar\omega_0] - \frac{2\pi}{\hbar}\sum_{\mathbf{k}_i}\left|H_a^{LO}\right|^2 f(\mathbf{k}_i)[1-f(\mathbf{k}_i + \mathbf{q}_\perp)] \times \delta[\mathscr{E}(\mathbf{k}_i) - \mathscr{E}(\mathbf{k}_i + \mathbf{q}_\perp) + \hbar\omega_0]. \quad (15)$$

The matrix elements H_e^{LO} and H_a^{LO}, which appear in (15), contain the nonequilibrium distribution function of phonons N_q. Let us use relation (14) for this function. This means that the quantity dN_q/dt appears on both sides of expression (15); i.e., expression (15) is

the equation for determining dN_q/dt. Let us denote the factors in (15) that are independent of dN_q/dt as $F_a(q_\perp)$ and $F_e(q_\perp)$ for the processes of absorption and emission, respectively. Then, the equation for dN_q/dt can be written as

$$\frac{dN_q(q_\perp)}{dt} = F_e(q_\perp)\left(N_{q0} + \frac{dN_q(q_\perp)}{dt}\tau_q + 1\right) - F_a(q_\perp)\left(N_{q0} + \frac{dN_q(q_\perp)}{dt}\tau_q\right). \quad (16)$$

The solution to this equation has the form

$$\frac{dN_q(q_\perp)}{dt} = \frac{F_e(q_\perp)(N_{q0}+1) - F_a(q_\perp)(N_{q0})}{1 - \tau_q[F_e(q_\perp) - F_a(q_\perp)]}. \quad (17)$$

The functions $F_a(q_\perp)$ and $F_e(q_\perp)$ contain all integration operations, as well as the dependence on the phonon wave vector we are interested in. In order to calculate these functions, we will replace the summation over $\mathbf{k}_i$ with integration, and then pass from the wave vectors $\mathbf{k}_j$ and $\mathbf{q}_\perp$ to the energies. After integrating over q_z and z in the same way as in (9), and over the angle θ using the delta function, the functions $F_a(q_\perp)$ and $F_e(q_\perp)$ will have the form

$$F_e(q_\perp) = \frac{\sqrt{2}e^2\omega_0 m^{3/2} L(\varepsilon_\infty^{-1} - \varepsilon_0^{-1}) I_{ij}(q_\perp)}{\hbar^3} \times \int\limits_{(\hbar\omega_0 + \mathscr{E}_{q_\perp})^2/4\mathscr{E}_{q_\perp}}^{\infty} \frac{f(\mathscr{E}_k - \hbar\omega_0)[1 - f(\mathscr{E}_{k_i})]}{\sqrt{\mathscr{E}_{k_i} - \frac{1}{4}(\hbar\omega_0/\sqrt{\mathscr{E}_{q_\perp}} + \sqrt{\mathscr{E}_{q_\perp}})^2}} d\mathscr{E}_{k_i};$$

$$F_a(q_\perp) = \frac{\sqrt{2}e^2\omega_0 m^{3/2} L(\varepsilon_\infty^{-1} - \varepsilon_0^{-1}) I_{ij}(q_\perp)}{\hbar^3} \times \int\limits_{(\hbar\omega_0 - \mathscr{E}_{q_\perp})^2/4\mathscr{E}_{q_\perp}}^{\infty} \frac{f(\mathscr{E}_k)[1 - f(\mathscr{E}_{k_i} + \hbar\omega_0)]}{\sqrt{\mathscr{E}_{k_i} - \frac{1}{4}(\hbar\omega_0/\sqrt{\mathscr{E}_{q_\perp}} - \sqrt{\mathscr{E}_{q_\perp}})^2}} d\mathscr{E}_{k_i}. \quad (18)$$

After determining $dN_q(q_\perp)/dt$ from (17) and (18), we can find the averaged energy-loss rate per electron, taking into account the nonequilibrium phonons:

$$\left\langle \frac{d\mathscr{E}}{dt} \right\rangle = \frac{\hbar\omega_0}{n_s} \int\limits_{q_\perp = 0}^{\infty} \int\limits_{\theta = 0}^{2\pi} \frac{q_\perp dq_\perp d\theta}{(2\pi)^2} \frac{dN_q(q_\perp)}{dt}. \quad (19)$$

Here, n_s is the surface electron concentration.

Let us evaluate the possible decrease in the obtained energy-loss rate due to the screening of phonons by a 2D electron gas. In order to do this, it is sufficient to multiply the induced potential by the factor $\varepsilon_\infty/(\varepsilon_\infty + q_d/q_\perp)$, where q_d is the inverse screening length [19]. This factor contains the ratio $q_d/q_\perp$ to the first power, in contrast to the case of a bulk semiconductor where the screening effect is governed by the square of this ratio. This fact indicates that 2D electron gas screens the phonons more weakly than 3D electron gas. For a GaAs QW with a thickness of 5–10 nm and a surface concentration n_s ranging from 1×10^{11}–5×10^{11} cm^{-2} at temperatures T = 100–300 K, the factor that accounts for screening ranges from 0.8 to 0.95; i.e., it is close to unity. Thus, in a QW with such parameters, the effect of screening on the energy-loss rate is insignificant.

3. RESULTS AND DISCUSSION

Let us consider a heterostructure with a GaAs/AlGaAs QW with a width L = 6 nm and doped to a concentration of 5×10^{17} cm^{-2}. Under these conditions, due to strong electron–electron scattering, the distribution function of electrons can be regarded as the Fermi distribution function. Thus, in order to describe the behavior of the electron gas during its heating by an electric field, we can introduce the hot-electron temperature T_e as a parameter into the Fermi distribution function

$$f(\mathbf{k}_i) = \left[\exp\left(\frac{\mathscr{E}_{k_i} - \mathscr{E}_F}{k_B T_e}\right) + 1\right]^{-1}. \quad (20)$$

Here, $\mathscr{E}_F$ is the chemical-potential level.

The lifetime of nonequilibrium optical phonons in GaAs, τ_q, which was determined from a comparison of the experimental data with the results of theoretical calculations of the energy-loss rate for a bulk semiconductor, is equal to 7×10^{-12} s [20].

The results of the calculations of the energy-loss rate in terms of the model suggested above are shown in Fig. 1 for two values of the lattice temperature. The dashed curves represent the case of scattering by equilibrium PO phonons; the solid lines correspond to the case where phonon accumulation is taken into account at $\tau_q = 7 \times 10^{-12}$ s. In the absence of an electric field, when the electron temperature T_e is equal to the lattice temperature T, electrons absorb and emit equal numbers of phonons and $\langle d\mathscr{E}/dt\rangle = 0$. When an electric field is applied, the average electron energy increases; accordingly, under steady-state conditions, the energy-loss rate gradually increases as well. The run of the dependences $\langle d\mathscr{E}/dt\rangle$ on T_e in 2D systems is similar to that for a bulk semiconductor (shown by the dash-and-dot lines in Fig. 1).

The effect of phonon accumulation results in decreasing $\langle d\mathscr{E}/dt\rangle$ due to the abrupt increase in the absorption rate of the accumulated nonequilibrium phonons. The inset in Fig. 1 shows the dependence of the nonequilibrium part of the phonon-distribution function $N_{qN} = (dN_q/dt)\tau_q$ on the reduced phonon wave vector, calculated according to (17) at the lattice temperature T = 77 K for two values of the electron temperature T_e. The maximum value of this function approximately corresponds to the magnitude of the phonon

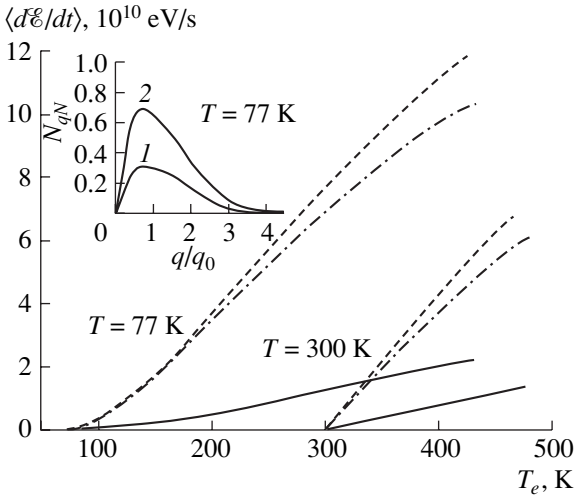

Fig. 1. Energy-loss rate of two-dimensional electrons upon their interaction with polar optical phonons in a GaAs/AlGaAs QW (the width $L = 6$ nm and the surface concentration $n_s = 3 \times 10^{11}$ cm^{-2}) per electron, disregarding phonon accumulation (dashed lines) and with consideration of this phenomenon at $\tau_q = 7 \times 10^{-12}$ s (solid lines), for two values of the lattice temperature. The dash-and-dot lines represent the results of the calculations of $\langle d\mathscr{E}/dt\rangle$ for bulk GaAs, disregarding the effect of nonequilibrium phonons. The nonequilibrium part of the distribution function of polar optical phonons for the same QW at $T = 77$ K is shown in the inset in relation to the reduced wave vector (the parameter $q_0 = \sqrt{2m\hbar\omega_0}/\hbar$; the electron temperature T_e = 300 (*1*) and 500 (*2*) K).

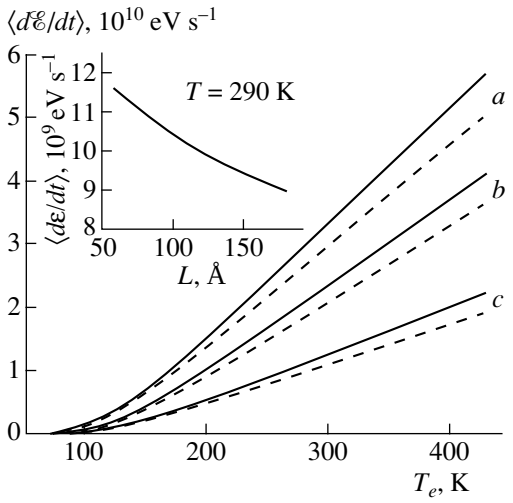

Fig. 2. Energy-loss rate of two-dimensional electrons (per electron) in GaAs/AlGaAs QWs with a surface concentration n_s = (*a*) 0.5×10^{11}, (*b*) 1×10^{11}, and (*c*) 3×10^{11} cm^{-2} calculated with consideration of the accumulation of polar optical phonons (phonon lifetime $\tau_q = 7 \times 10^{-12}$ s). The solid and dashed lines represent the data for QWs with a width $L = 6$ and 10 nm, respectively; $T = 77$ K. The dependence of the energy-loss rate on the QW width at $T = 77$ K, $T_e = 290$ K, and $n_s = 3 \times 10^{11}$ cm^{-2} is shown in the inset.

wave vector q_0, which is equal in magnitude to the wave vector of an electron whose energy is close to $\hbar\omega_0$: $q_0 = \sqrt{2m\hbar\omega_0}/\hbar$. As can be seen from Fig. 1, the number of nonequilibrium phonons abruptly increases with an increase in the electron temperature. In magnitude, the nonequilibrium part of the phonon-distribution function is close to unity at high electron temperatures. Therefore, the effect of the nonequilibrium phonons on the energy losses of electrons heated in a strong electric field turns out to be significant. For the phonon lifetime $\tau_q = 7 \times 10^{-12}$ s, the value of the energy-loss rate is smaller by a factor of 5–6 in comparison with the case where the nonequilibrium phonons are disregarded.

The effect of the doping level and the QW width on the average energy-loss rate, with consideration of the accumulation of polar optical phonons, is illustrated in Fig. 2. An increase in the electron concentration leads to a decrease in the energy losses per electron at a fixed value of the electric field. In addition, increasing the electron concentration results in a higher occupancy of the final states for the processes of phonon emission. Due to this circumstance, the value of $\langle d\mathscr{E}/dt\rangle$ decreases. The dependence of $\langle d\mathscr{E}/dt\rangle$ on the QW width, which follows from expression (9) in [17], is weak.

If we know the dependence of the energy-loss rate on the electron temperature, we can determine the electron temperature corresponding to a specified value of the longitudinal electric field. In order to determine the dependence of the electron temperature on the longitudinal electric field, we solved [21] the power-balance equation:

$$e\mu_e E^2 = \langle d\mathscr{E}/dt\rangle. \qquad (21)$$

Here, μ_e is the electron mobility and E is the applied electric field. The mobility of electrons in a longitudinal electric field was experimentally studied in [22] for a structure with rectangular GaAs/$Al_{0.22}Ga_{0.78}As$ QWs with a width $L = 6$ nm and a surface concentration of free electrons $n_s = 3 \times 10^{11}$ cm^{-2}. The attained value of the electron mobility only slightly depended on both the electric field and the temperature. Therefore, for the structure with similar parameters analyzed in the presence study, we used the average value of the mobility $\mu_e = 3400$ cm^2 V^{-1} s^{-1} determined in [22], which is independent of the longitudinal electric field. Figure 3 shows the dependences of the electron temperature on the electric field obtained by solving Eq. (21), both with and without allowance made for the accumulation of PO phonons (solid and dashed lines, respectively). It can be seen that phonon accumulation leads to a significant increase in T_e.

4. CONSIDERATION OF SOME EXPERIMENTAL RESULTS IN TERMS OF THE SUGGESTED CALCULATION MODEL

The results of calculating the energy-loss rate in terms of the model suggested here are in good agreement with the experimental data obtained in various studies. Let us consider some of these experimental results.

(i) In [11], the dependence of the energy-loss rate on the hot-electron temperature was obtained from photoluminescence spectra (see experimental dots in Fig. 4a). The experiment was carried out with a sample containing GaAs/AlGaAs QWs with a width $L = 6.5$ nm and a surface electron concentration $n_s = 1.42 \times 10^{12}$ cm^2 at $T = 4.2$ K. The calculations performed in terms of the model suggested in the present study showed that consideration of nonequilibrium phonons considerably improves the agreement between the theoretical and experimental data.

(ii) The experimental data obtained in [23] for wider GaAs/AlGaAs QWs by direct measurement of the energy-loss rate are shown in Fig. 4b. These measurements were performed using a combination of optical and electrical methods. The luminescence spectra, from which the temperature of carriers was determined, and the current–voltage characteristics, from which the power per carrier was independently obtained, were recorded simultaneously. The thickness of the QW layer in the structure studied in [23] was equal to $L = 25.8$ nm, the surface electron concentration $n_s = 3.9 \times 10^{11}$ cm^2, and the temperature $T = 1.8$ K. For this case, the calculation performed here with consideration of nonequilibrium phonons also adequately describes the experimental results.

(iii) Let us analyze the role played by the consideration of the nonequilibrium phonons in explaining the modulation of the intersubband absorption of far-infrared radiation in a strong longitudinal electric field. The modulation of the absorption coefficient α was experimentally studied in [22] in a structure with GaAs/$Al_{1-x}Ga_xAs$ QWs, in which the barrier regions were selectively doped. The parameters of the QWs were chosen in such a way as to make it possible to study the modulation at the short-wavelength edge of the peak related to the intersubband absorption of the radiation of a CO_2 laser. Electron heating by a longitudinal electric field leads to an increase in the energy spacing between two QW levels. As a result, the intersubband-absorption peak shifts to shorter wavelengths in comparison with the case when the field is absent and the absorption coefficient at the wavelength of the CO_2-laser radiation increases.

The reason as to why the energy-level spacing changes is as follows. The space charge that arises due to the selective doping of the intermediate barrier regions of the structure distorts the form of the potential and leads to the formation of a shallow QW in the barrier region. In a strong longitudinal electric field, elec-

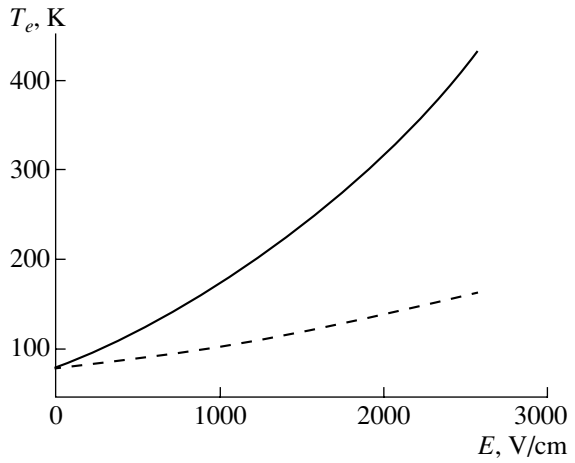

Fig. 3. Dependence of the electron temperature on the electric-field strength with consideration of the nonequilibrium polar optical phonons (solid line) and disregarding their effect (dashed line). The lattice temperature $T = 77$ K, the width of the GaAs/$Al_{0.24}Ga_{0.76}As$ QW $L = 6$ nm, and the surface concentration $n_s = 3 \times 10^{11}$ cm^{-2}.

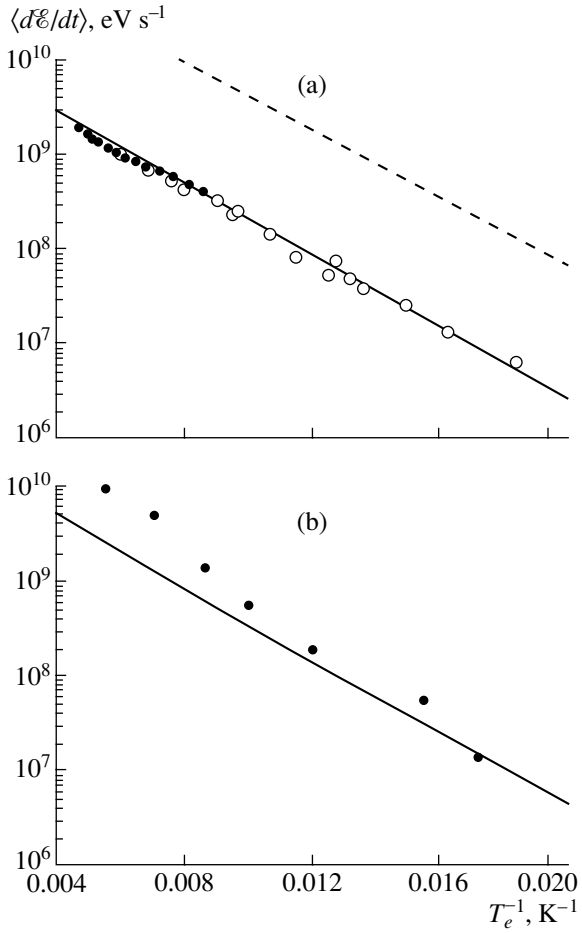

Fig. 4. Energy-loss rate for hot electrons in quantum wells. Dots represent the experimental data (a) from [11] and (b) from [23]. The solid and dashed lines represent the results of calculations in terms of the model suggested in the present study with and without consideration of the nonequilibrium phonons, respectively.

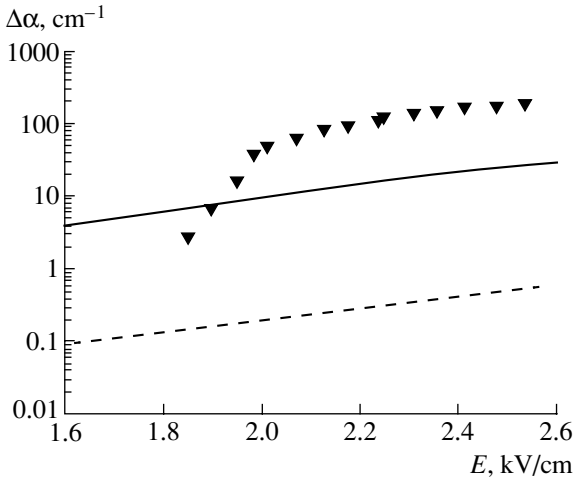

Fig. 5. Variation in the intersubband-absorption coefficient at the wavelength $\lambda = 10.6$ μm as a function of the longitudinal electric-field strength at $T = 77$ K. The dots represent the experimental data [22]; the solid and dashed lines represent the results of calculations in terms of the model suggested here with and without consideration of the nonequilibrium phonons, respectively.

trons are heated, undergo transitions from the lower to the upper subband, and become redistributed in the space between the main deep GaAs/AlGaAs QW and the shallow QW in the barrier region. The electrons that find themselves in the barrier region compensate the dopant charge. As a result, the depth of the QW in the barrier region decreases; accordingly, the upper-level energy increases.

In this study, the changes in the potential profile and in the energy-band spectrum of the sample under investigation depend on the applied electric field and are determined by finding a self-consistent solution to the Schrödinger and Poisson equations. The electron temperature corresponding to each value of the electric field is determined by solving the power-balance equation (21). In this case, the calculation of the energy-loss rate is performed with consideration of nonequilibrium PO phonons. The obtained value of the electron temperature as a parameter in the distribution function of electrons made it possible to determine the fraction of electrons that compensate the dopant charge in the barrier region. The Poisson equation allowed us to relate the change in the dopant charge with the change in the QW depth in the barrier region. The energy levels corresponding to the new shape of the potential were determined from the Schrödinger equation. Thus, the shift of the upper level, and, accordingly, of the intersubband-absorption peak was determined as a function of the applied electric field. The shift of the absorption peak, to the frequency of the CO_2-laser indicates that the absorptance at this frequency increases.

The experimental and theoretical dependences of the variation in the absorption coefficient of light $\Delta\alpha$ on the applied electric field E are shown in Fig. 5. For comparison, the results of calculations for the cases of scattering of electrons by equilibrium and nonequilibrium PO phonons are also shown. It can be seen that the calculation of the shift of the absorption peak with consideration of the nonequilibrium phonons yields better agreement between the calculated and experimental curves.

5. CONCLUSIONS

In this study, the effect of accumulation of polar optical phonons on the energy-loss rate of hot electrons in quantum wells was investigated. The simple model we suggested for calculating the energy-loss rate with consideration of nonequilibrium phonons describes fairly well the experimental data obtained in various studies. It is ascertained that the allowance made for nonequilibrium optical phonons in the theoretical calculations considerably improves the agreement between the results of the theoretical and experimental studies of the energy-loss rate and makes it possible the determine the electron temperature with higher accuracy.

ACKNOWLEDGMENTS

This study was supported by grants from the Ministry of Industry, Science and Technology of the Russian Federation; the Ministry of Education of the Russian Federation; and INTAS.

REFERENCES

1. J. Shah, in *Spectroscopy of Nonequilibrium Electrons and Phonons*, Ed. by C. V. Shank and B. P. Zakharchenya (North-Holland, Amsterdam, 1992); Ser. *Modern Problems in Condensed Matter Sciences*, Ed. by V. M. Agranovich and A. A. Maradudin, Vol. 35, p. 57.
2. H. T. Grahn, J. Kastrup, K. Ploog, *et al.*, Jpn. J. Appl. Phys. **34**, 4526 (1995).
3. J. Kastrup, R. Klann, H. T. Grahn, *et al.*, Phys. Rev. B **52**, 13761 (1995).
4. L. L. Bonilla, in *Nonlinear Dynamics and Pattern Formation in Semiconductors*, Ed. by F.-J. Niedernostheide (Springer, Berlin, 1995), Chap. 1.
5. E. Shomburg, A. A. Ignatov, J. Grenzer, *et al.*, Appl. Phys. Lett. **68**, 1096 (1996).
6. L. E. Vorobjev, V. I. Stafeev, and A. V. Shturbin, Phys. Status Solidi B **53**, 47 (1972).
7. L. E. Vorob'ev, F. I. Osokin, V. I. Stafeev, and A. V. Shturbin, Fiz. Tekh. Poluprovodn. (Leningrad) **8**, 1281 (1974) [Sov. Phys. Semicond. **8**, 833 (1974)].
8. L. E. Vorob'ev, Fiz. Tekh. Poluprovodn. (Leningrad) **8**, 1291 (1974) [Sov. Phys. Semicond. **8**, 839 (1974)].
9. K. Hess and G. J. Iafrate, in *Hot-Electron Transport in Semiconductors*, Ed. by L. Reggiani (Springer, Berlin, 1985), Chap. 7.
10. B. K. Ridley, in *Hot Carriers in Semiconductor Nanostructures: Physics and Applications*, Ed. by J. Shah (Academic, Boston, 1992), Chap. 2.

11. R. Gupta, N. Balcan, and B. K. Ridley, Semicond. Sci. Technol. B **7**, 274 (1992).
12. L. E. Vorob'ev, S. N. Danilov, E. L. Ivchenko, M. E. Levinshteĭn, D. A. Firsov, and V. A. Shalygin, *Kinetic and Optical Phenomena in Strong Electric Fields in Semiconductors and Nanostructures* (Nauka, St. Petersburg, 2000).
13. B. K. Ridley, Semicond. Sci. Technol. **4**, 1142 (1989).
14. R. Fuchs and K. L. Kleiwer, Phys. Rev. [Sect. A] **140**, 2076 (1965).
15. K. Huang and B. Zhu, Phys. Rev. B **38**, 2183 (1988).
16. Yu. Pozhela, K. Pozhela, and V. Yutsene, Fiz. Tekh. Poluprovodn. (St. Petersburg) **34**, 1053 (2000) [Semiconductors **34**, 1011 (2000)].
17. V. L. Gurevich, D. A. Parshin, and K. É. Shtengel', Fiz. Tverd. Tela (Leningrad) **30**, 1466 (1988) [Sov. Phys. Solid State **30**, 845 (1988)].
18. B. K. Ridley, J. Phys. C: Solid State Phys. **15**, 5899 (1982).
19. V. V. Mitin, V. A. Kochelap, and M. A. Stroscio, *Quantum Heterostructures* (Cambridge Univ. Press, Cambridge, 1999), p. 242.
20. J. A. Kash, J. C. Tsang, and J. M. Hvam, Phys. Rev. Lett. **54**, 2151 (1985).
21. *Hot Electrons in Semiconductors and Nanostructures*, Ed. by L. E. Vorob'ev (Gos. Tekh. Univ., St. Petersburg, 1999), p. 5.
22. L. E. Vorob'ev, S. N. Danilov, E. A. Zibik, *et al.*, Fiz. Tekh. Poluprovodn. (St. Petersburg) **29**, 1136 (1995) [Semiconductors **29**, 588 (1995)].
23. J. Shah *et al.*, Phys. Rev. Lett. **54**, 2045 (1985).

Translated by Yu. Sin'kov

Semiconductors, Vol. 37, No. 5, 2003, pp. 594–597. Translated from Fizika i Tekhnika Poluprovodnikov, Vol. 37, No. 5, 2003, pp. 612–615.

AMORPHOUS, VITREOUS, AND POROUS SEMICONDUCTORS

Semi-Insulating Silicon Carbide Layers Obtained by Diffusion of Vanadium into Porous 4*H*-SiC

M. G. Mynbaeva*^, A. A. Lavrent'ev, N. I. Kuznetsov*, A. N. Kuznetsov*, K. D. Mynbaev*, and A. A. Lebedev***

** Ioffe Physicotechnical Institute, Russian Academy of Sciences, St. Petersburg, 194021 Russia*
*** Crystal Growth Research Center, Nonprofit Partnership, St. Petersburg, 193036 Russia*
^e-mail: mgm@mail.ioffe.ru

Submitted September 27, 2002; accepted for publication October 4, 2002

Abstract—Semi-insulating silicon carbide layers have been obtained by diffusion of vanadium into porous 4*H*-SiC. The diffusion was performed from a film deposited by cosputtering of silicon and vanadium, with the content of the latter equal to 20%. The diffusion profile of vanadium in porous silicon carbide has a complex structure with a fast diffusion coefficient of 7×10^{-15} cm^2/s. The activation energy of the resistivity of vanadium-diffusion-doped porous SiC layers is 1.45 eV. The resistivity of vanadium-doped semi-insulating layers is 5×10^{11} Ω cm at 500 K, which exceeds the resistivity of undoped porous SiC by two orders of magnitude. The results obtained indicate that porous SiC is a promising material for semi-insulating substrates in device structures based on wide-bandgap semiconductors. © *2003 MAIK "Nauka/Interperiodica".*

Semi-insulating silicon carbide is a promising material for high-integration devices of microwave electronics operating at high temperatures and frequencies in strong electric fields [1–3]. In particular, substrates made of semi-insulating silicon carbide are used to fabricate devices based on such wide-gap semiconductors as SiC, GaN, and AlN. Semi-insulating SiC can be obtained by doping with compensating impurities, among which vanadium is the most widely used. As is known, V impurity is amphoteric for SiC; i.e., it can produce both deep acceptor and donor levels [4]. It is preferable, especially for the 4*H* polytype, that a deep donor level be created near the midgap, since it is material of this kind that retains a high resistivity at high temperatures [5].

Vanadium is commonly introduced into SiC either in the stage of crystal growth [1, 2] or during postgrowth treatment, e.g., by ion implantation with subsequent activation of the impurity [6, 7]. Doping SiC with vanadium is, however, far from being a simple task, since the working range of dopant concentrations is rather narrow. For example, light doping does not change the electrical properties of the material, and the doping level is bounded from above by the solubility limit, which is as low as $\sim 3 \times 10^{17}$ cm^{-3} for SiC [1, 8]. Precision doping of semiconducting materials is frequently done using the diffusion method; however, carrying out diffusion in SiC is complicated by the very low diffusion coefficients for most impurities at technologically reasonable temperatures. It is known, however, that effective and fast diffusion can be achieved in porous semiconductors with a developed internal surface [9]. Porous silicon carbide has already been used as a material for substrates for high-quality epitaxial layers of both SiC [10–12] and GaN [13]. In this context, it is of interest to obtain semi-insulating porous SiC, which could be used in device structures based on wide-bandgap semiconductors both as a substrate for the further growth of active layers and as an insulating layer. It is noteworthy that the possibility of using the semi-insulating properties of porous SiC itself for the passivation of *p–n* silicon carbide junctions has already been reported [14].

This communication reports on the fabrication of semi-insulating silicon carbide layers on the basis of vanadium-diffusion-doped porous SiC. Wafers of silicon carbide of the 4*H* polytype served as the starting material. Porous SiC was obtained by surface anodization of the wafers in an aqueous solution of hydrofluoric acid by the procedure described in [15]. During anodization, part of a wafer was covered with a mask and served as a reference in further experiments. According to cross-sectional images obtained by scanning electron microscopy (SEM), the thickness of the porous layer was 6 μm. After anodization, an alloy composed of silicon and vanadium was deposited on part of the wafer. The use of the Si+V alloy was governed by the necessity of achieving the minimum surface concentration of vanadium in order to prevent the introduction of vanadium into SiC above the solubility

1063-7826/03/3705-0594$24.00

limit, in which case precipitation occurs and the properties of the material inevitably degrade. The alloy was obtained by plasma cosputtering of a vanadium foil and a silicon wafer. After depositing the alloy, the SiC wafers were annealed in an atmosphere of nitrogen at 1100°C for 10 h. After the composition of the alloy was determined, the latter was removed from the surface of the SiC wafers by chemical etching.

The composition of the alloy on the surface of an annealed silicon carbide wafer was studied by Auger spectroscopy. The data obtained are shown in Fig. 2. The results for the porous and unanodized (reference) parts of the wafer are the same. It can be seen from the figure that the thickness of the Si+V layer on the surface of the SiC wafer is 400 nm. The content of vanadium in the Si+V alloy is about 20%, with vanadium distributed uniformly across the deposited alloy layer. Carbon was present on the surface of the alloy only as adventitious layer.

The distribution of vanadium in the SiC wafer was analyzed by secondary-ion mass-spectrometry (SIMS). Preliminary measurements demonstrated that, at vanadium concentrations of less than 10^{17} cm^{-3}, analysis of a sample with oxygen ions is required. To lower the vanadium detection limit, an increased current density of the oxygen ion beam was used and the parameters of the electron diaphragm were modified. The current of secondary Si ions (30 amu) from silicon carbide amounted to 2×10^5 pulses per second, whereas the current of the vanadium (51 amu) signal from the starting "pure" SiC amounted to 2 pulses per second. The vanadium concentration calculated for this current (in accordance with the ionization potential of V in SiC) was 10^{13} cm^{-3}. This is the minimum recordable concentration of vanadium (and, correspondingly, its detection limit) in SiC in the experiments described.

According to the results of SIMS analysis, after carrying out the process, vanadium is present in the unanodized (reference) part of the wafer only at the background level, i.e., V diffusion into SiC does not occur to any significant depth. This is seen in Fig. 2 (curve *1*). At the same time, it follows from Fig. 2 (curve *2*) that V diffusion from the Si+V layer into porous SiC does occur. The vanadium concentration is ~10^{16} cm^{-3} in the surface layer and gradually decreases away from the surface to become 10^{13} cm^{-3} (background level) at a depth of 450 nm. It is also noteworthy that, according to SIMS data, the surface layer of the SiC wafer is not enriched with silicon from the Si+V alloy.

As seen from curve *2* in Fig. 2, the vanadium concentration profile in porous SiC has a rather complex shape. To a depth of ~100 nm, the profile does not correspond to the known solutions of a diffusion equation with a concentration-independent coefficient. At the same time, Fig. 1 does not indicate any significant interdiffusion of elements across the interface between

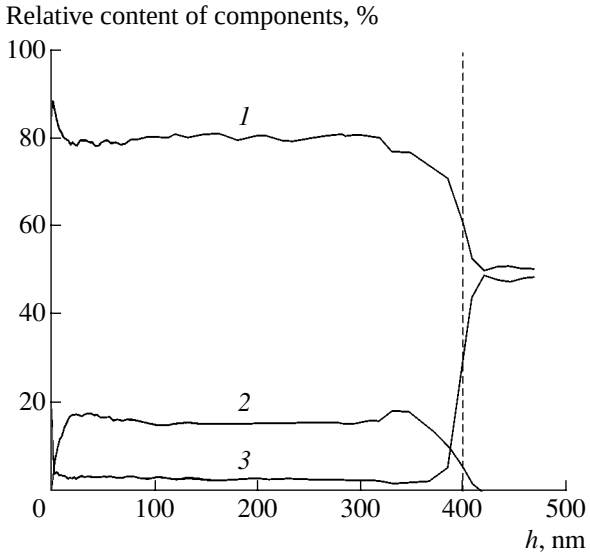

Fig. 1. Component distribution in a film of the Si+V alloy on the surface of a silicon carbide wafer after annealing, according to Auger spectroscopy: (*1*) for Si, (*2*) for V, and (*3*) for C. The dashed line shows the approximate position of the interface between the film and the SiC wafer.

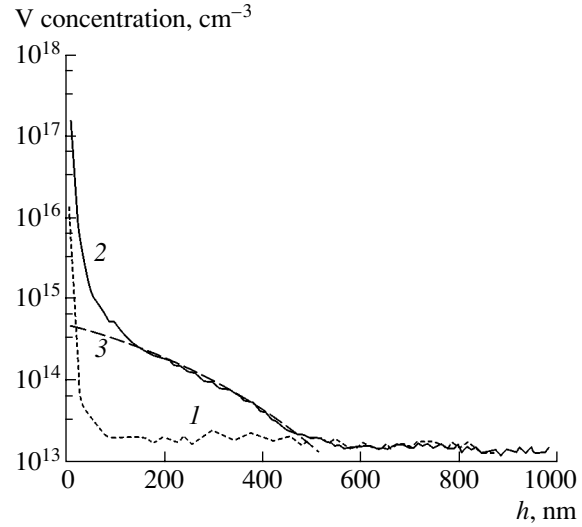

Fig. 2. Vanadium distribution in an SiC wafer after performing diffusion: (*1*) in unanodized part of the wafer, (*2*) in the porous part of the wafer, and (*3*) calculated diffusion profile.

Si+V and porous SiC. Presumably, this part of the profile reflects a complex interaction between V atoms and intrinsic defects at the interface during thermal treatment. It is also noteworthy that, according to SEM data, the structure of porous SiC obtained by anodization is, as a rule, nonuniform across the layer thickness [15], and, therefore, it would hardly be expected that a single classical diffusion profile could be obtained along the entire diffusion length. Nevertheless, part of curve *2* in Fig. 2, which begins at a depth of ~120 nm and can be

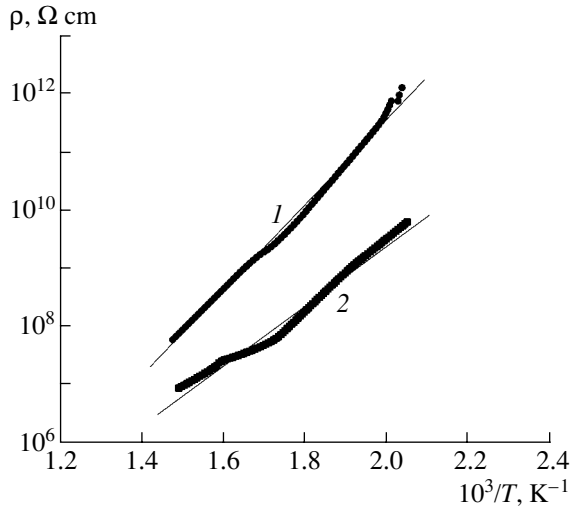

Fig. 3. Temperature dependences of the resistivity of porous silicon carbide: (*1*) for vanadium-diffusion-doped SiC, and (*2*) for SiC undoped and subjected to thermal annealing under the same conditions as those in V diffusion. Solid lines represent the results of linear fitting from which the activation energy was determined. The activation energy for undoped porous SiC is 1.09 ± 0.03 eV.

related to "fast" diffusion, is well described by a complementary error function, as seen from the calculated diffusion profile represented by curve *3*. The best fit is achieved with a V diffusion coefficient equal to 7.5×10^{-15} cm^2/s.

Since no V diffusion into the unanodized part of the wafer was observed, it seems impossible to evaluate the acceleration of diffusion in porous silicon carbide relative to the starting single-crystal SiC wafer (presently, no data on the diffusion coefficient of V in SiC can be found in the literature). Nevertheless, it is apparent that it is the porous structure of the anodized part of the wafer that enables vanadium diffusion from the Si+V alloy to a substantial depth. It is noteworthy that diffusion in SiC is, as a rule, performed at $T > 1600$°C, i.e., at much higher temperatures [16]. If the data of [16] are extrapolated to lower temperatures, then the coefficient of fast V diffusion in porous SiC will even exceed the diffusion coefficients of Be and B impurities, whose diffusion into SiC is the fastest.

To study the electrical properties of porous SiC with V introduced by diffusion, metal–semiconductor–metal structures were fabricated. An Ni contact pad 300 μm in diameter, deposited by vacuum evaporation, served as a contact to the vanadium-doped SiC layer. The contact to the rear side of the wafer was made of an alloy of In and Ga. The resistivity ρ of the layer of vanadium-doped porous SiC was determined by measuring the dc current across the structure at a bias of 30 V in the temperature range from 300 to 700 K. As shown by the measurements, the current across the structure was limited by the resistance of the vanadium-doped porous layer.

The temperature dependence of the resistivity of this layer is shown by curve *1* in Fig. 3. It can be seen that the dependence exhibits a region of exponential growth, with an activation energy of 1.45 ± 0.03 eV. Since it is known that vanadium gives rise to precisely this energy level in 4*H*-SiC [4], it seems reasonable to assume that the semi-insulating properties of the porous silicon carbide layer are determined in the case in question by the compensatory effect of vanadium.

It is noteworthy that the ρ value obtained for vanadium-diffusion-doped porous 4*H*-SiC is rather high: 5×10^{11} Ω cm at 500 K, which exceeds the ρ value measured for comparison on an undoped porous layer at the same temperature by two orders of magnitude (Fig. 3, curve *2*). The ρ value also exceeds the resistivity of semi-insulating SiC layers obtained by doping with vanadium during crystal growth [2, 17] and ion implantation [6, 7].

Thus, a porous structure of SiC subjected to anodization was successfully used to carry out diffusion of vanadium in order to obtain semi-insulating silicon carbide layers. The diffusion profile obtained at 1100°C has a complex structure with a fast diffusion coefficient of 7.5×10^{-15} cm^2/s. The activation energy of the resistivity of vanadium-diffusion-doped porous SiC layers is 1.45 eV. The resistivity of the semi-insulating layers is 5×10^{11} Ω cm at 500 K. The results obtained indicate that porous SiC is a promising material for semi-insulating substrates for device structures based on wide-gap semiconductors.

REFERENCES

1. H. McD. Hobgood, R. C. Glass, G. Augustine, *et al.*, Appl. Phys. Lett. **66**, 1364 (1995).
2. S. A. Reshanov, Diamond Relat. Mater. **9**, 480 (2000).
3. T. S. Sudarshan, G. Gradinaru, G. Korony, *et al.*, Diamond Relat. Mater. **6**, 1392 (1997).
4. A. A. Lebedev, Fiz. Tekh. Poluprovodn. (St. Petersburg) **33**, 129 (1999) [Semiconductors **33**, 107 (1999)].
5. S. A. Reshanov and V. P. Rastegaev, Diamond Relat. Mater. **10**, 2035 (2001).
6. T. Kimoto, T. Nakajima, H. Matsunami, *et al.*, Appl. Phys. Lett. **69**, 1113 (1996).
7. A. Edwards, D. N. Dwight, M. V. Rao, *et al.*, J. Appl. Phys. **82**, 4223 (1997).
8. M. Bickermann, B. M. Epelbaum, D. Hofmann, *et al.*, J. Cryst. Growth **223**, 211 (2001).
9. H. Yamanaka and M. Kamashiba, Jpn. J. Appl. Phys. **13**, 1661 (1974).

10. M. Mynbaeva, S. E. Saddow, G. Melnychuk, *et al.*, Appl. Phys. Lett. **78**, 117 (2001).
11. J. E. Spanier, G. T. Dunne, L. B. Rowland, and I. P. Hermann, Appl. Phys. Lett. **76**, 3879 (2000).
12. J. K. Jeong, M. Y. Um, H. J. Na, *et al.*, Mater. Sci. Forum **389–393**, 267 (2002).
13. M. Mynbaeva, A. Titkov, A. Kryzhanovski, *et al.*, MRS Internet J. Nitride Semicond. Res. **4**, 14 (1999).
14. A. O. Konstantinov, C. I. Harris, and E. Janzen, Appl. Phys. Lett. **65**, 2699 (1994).
15. S. E. Saddow, M. Mynbaeva, and M. McMillan, in *Silicon Carbide: Materials, Devices and Applications*, Ed. by Z. C. Feng and J. H. Zhao; Ser.: *Optoelectronic Properties of Semiconductors and Superlattices* (2003) (in press).
16. V. A. Dmitriev and M. G. Spencer, in *SiC Materials and Devices. Semiconductors and Semimetals* (Academic, New York, 1998), Vol. 52, p. 61.
17. A. Ellison, B. Magnusson, C. Hemmingson, *et al.*, Mater. Res. Soc. Symp. Proc. **640**, H1.2 (2001).

Translated by M. Tagirdzhanov

Semiconductors, Vol. 37, No. 5, 2003, pp. 598–603. Translated from Fizika i Tekhnika Poluprovodnikov, Vol. 37, No. 5, 2003, pp. 616–621.

AMORPHOUS, VITREOUS, AND POROUS SEMICONDUCTORS

Quantum-Chemical Simulation of the Influence of Defects on the Infrared Spectrum and the Electronic Structure of *a*-Se

A. S. Zyubin*, F. V. Grigor'ev, [1], and S. A. Dembovskiĭ**, [2]**

** Institute of Chemical Physics in Chernogolovka, Russian Academy of Sciences, Chernogolovka, Moscow oblast, 142432 Russia*

*** Kurnakov Institute of General and Inorganic Chemistry, Russian Academy of Sciences, Leninskiĭ pr. 31, Moscow, 119991 Russia*

[1] e-mail: fedgrigor@hotbox.ru

[2] e-mail: sergdemb@igic.ras.ru

Submitted November 12, 2002; accepted for publication November 18, 2002

Abstract—Quantum-chemical simulation of the influence of defects, such as hypervalent configurations and dipole valence-alteration pairs, on the IR-absorption spectrum and the electronic structure of *a*-Se has been carried out. It was shown that the formation of dipole valence-alteration pairs gives rise to an additional peak in the high-frequency region (337 cm^{-1}) and that the hypervalent configuration yields two additional peaks near the fundamental frequency of stretching vibrations. It was ascertained that the formation of hypervalent configurations causes significant shifts of the highest occupied and lowest unoccupied molecular orbitals, which should give rise to localized states in the band gap. These states can act as both electron traps and donors. In the X-ray-emission spectrum, only one of the defects considered here gives rise to an additional peak, which is spaced from the upper edge of the absorption band by 1.5 eV, which makes it possible to detect it experimentally. © *2003 MAIK "Nauka/Interperiodica".*

1. INTRODUCTION

As is known, neutral and diamagnetic defects in chalcogenide vitreous semiconductors (CVSs) govern many of their properties, including the absence of the dark signal of the electron spin resonance and the inability to form solid solutions with dopants [1]. Currently, there are several models of defect states in CVSs. The most widely used is the model of valence-alternation pairs (VAP) (or intimate valence-alternation pairs (IVAP)) [2], which assumes the existence of atomic pairs. Each pair consists of a positively charged overcoordinated atom and a negatively charged undercoordinated atom (in *a*-Se, C_3^+ and C_1^-, respectively, where the superscript stands for the charge and the subscript stands for the coordination). Within the model of hypervalent configurations (HVCs), atoms whose number of nearest neighbors Z_1 exceed that in the crystal of the same composition are assumed to be neutral and diamagnetic defects [3]. The model of soft atomic configurations (SACs) accounts for many properties of CVSs, under the assumption that defect configurations with abnormally small force constants exist in glasses [4].

Currently, the set of all experimental data does not allow one to ascertain reliably what type of defects is dominant in CVSs. Therefore, this problem may be solved, to some extent, by quantum-chemical simulation. The simulation results can make it possible to determine specific characteristics of defects, as well as explain experimentally the observed phenomena. It was ascertained by simulation that the defect-formation energy E_{def} in the VAP model exceeds the bonding energy E_b and the band gap E_g for almost all configurations, except for a dipole valence-alteration pair (VAP-*d*), in which a positively charged atom is immediately bound with a negatively charged one [5–8]. In our previous study [9], we showed that metastable HVCs may exist in amorphous Se. These configurations yield local minima of the potential surface, and their energy levels are significantly lower than that of the defect corresponding to the dangling bond. The content of such HVCs significantly exceeds the content of VAP defects. Furthermore, some of the atoms in HVCs are characterized by the bonds with nearest neighbors, which are weaker in comparison with an ordinary covalent bond. This means that such atoms are consistent with the SAC model.

The aim of this study is to analyze the influence of appreciable concentrations of HVC and VAP-*d* defects on the measurable characteristics of CVSs. With this purpose in mind, the infrared (IR) absorption spectra

Frequencies ν and relative intensities *I* of vibrations of the basic fragments of the *a*-Se CDN

Se_8 ring				Se_6 ring		Se_8H chain	
MP2		B3LYP		B3LYP		B3LYP	
ν, cm^{-1}	*I*, %	ν, cm^{-1}	*I*, %	ν, cm^{-1}	*I*, %	ν, cm^{-1}	*I*, %
277	0	257	0	263	0	265	100
277	0	256	0	254	100	265	9
272	100	256	0	254	100	253	15
272	100	255	100	243	0	249	24
271	0	255	100	243	0	246	7
267	0	255	0	202	0	238	24
267	0	234	0	151	12	224	0
260	0	219	0	127	0	128	1
121	0	118	0	97	0	131	2
121	0	118	0	97	0	105	1
119	27	114	10	78	8	105	1
106	0	104	0	78	8	76	1
93	47	91	49			43	0
93	47	91	49			38	0
74	0	70	0			26	0
74	0	70	0			16	0
33	0	35	0			13	0
33	0	35	0			12	0

are calculated for the metastable defects observed in [9], the influence of HVCs on the electronic structure of *a*-Se is considered, and the possible manifestation of these defects in the X-ray emission spectrum is discussed. Some suggestions are made concerning the relationship between peaks of the typical of *a*-Se in the IR spectrum (which are almost absent in the case of crystalline Se) and the defects studied.

2. SIMULATION METHOD

The model clusters were calculated by ab initio methods, taking into account the electron correlation both within the density-functional theory (B3LYP) and in terms of the second-order Möller–Plesset perturbation theory (conventional MP2 scheme). As a rule, the valence approximation was used, within which the influence of the core electrons of Se atoms was modeled by the LanL2 or Stevens–Basch–Krauss (SBK) pseudopotentials with corresponding valence-split bases with polarization atomic *d* orbitals added. The calculations are described in more detail in [9]. The calculations were carried out using GAMESS [10] and GAUSSIAN-94 [11] software at the Institute of Chemical Physics, Russian Academy of Sciences (RAS), and at the Institute of Organic Chemistry, RAS.

3. RESULTS AND DISCUSSION

3.1. Infrared Spectra of the Fragments of the a-Se Initial Network and of the Hypervalent Configurations in a-Se

First, we modeled the spectra of the Se_8 ring, the defect-free chain, and the Se_6 ring, which represent the basic elements forming the *a*-Se continuous disordered network (CDN). If the dangling bonds at the cluster boundaries are closed by hydrogen atoms, the coordinates of these bonds are not frozen, since the *a*-Se CDN is one-dimensional and the positions of its atoms are fixed much less rigidly than in three-dimensional CDNs, such as *g*-SiO_2. In this case, vibrations characterized by small effective masses, which are mostly related to the motion of hydrogen atoms, were removed from the calculated spectrum.

The data obtained are listed in the table. The Si_8 ring is characterized by three vibration groups, which are clearly pronounced in the IR spectrum. These group are related to changes in the lengths of the bonds, as well as in the valence and torsion angles. The first group is the most intense one. This fact is in agreement with the experimental data on the crystalline modifications constructed of Se_8 rings. Concerning the ratio of the intensities of the bands at 115 and 90 cm^{-1}, there is less agreement; specifically, the third band in the experi-

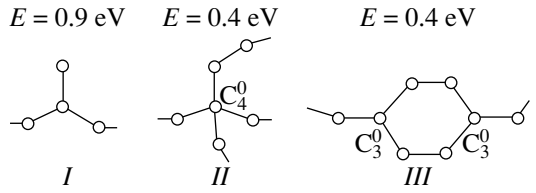

Fig. 1. Geometrical structure and relative stability of defects in *a*-Se: (*I*) VAP-*d*, (*II*) HVC C_4^0, and (*III*) HVC ring.

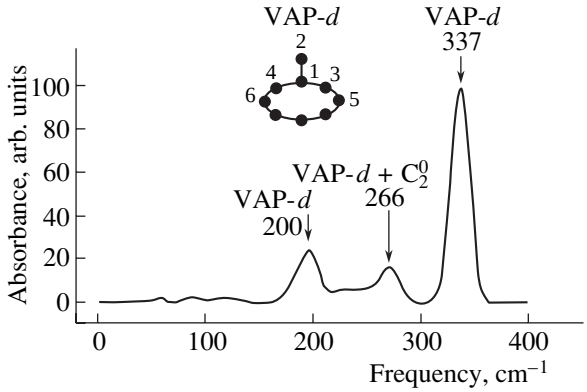

Fig. 2. IR absorption spectrum of the VAP-*d* defect.

mental IR spectrum has a lower intensity in comparison with the second one, while the calculation yields an inverse relation. In this case, the B3LYP scheme yields more significant distortions than the MP2 method. The frequencies corresponding to the bond stretching are overestimated by approximately 20 cm^{-1} within the MP2 method, whereas the B3LYP scheme shows better agreement with the experimental value of ν_{exptl} = 255 cm^{-1}. Concerning the bending vibrations, both approaches slightly (by 5–10 cm^{-1}) underestimate the frequencies (ν_{exptl} = 120 cm^{-1} [12]). When we pass to the strained Se_6 ring, the change in the vibrations related to the bond stretching is insignificant, whereas the frequencies of the second-group vibrations increase. In this case, the vibration intensities, in general, decrease and the relations between them change. As a result, two weak bands arise at 150 and 80 cm^{-1} in the IR spectrum of the Se_6 ring instead of bands at 120 and 95 cm^{-1} in the case of Se_8. The intensities of similar vibrations decrease even more strongly when passing to a chain. This is consistent with the IR-spectroscopy data on an Se trigonal crystalline modification constructed of infinite chains.

Thus, the methods we used quite satisfactorily reproduce the experimental IR spectra of crystalline Se modifications.

3.2. Spectra of Defect Configurations

The defect configurations we considered are shown in Fig. 1; their spectra are shown in Figs. 2–5. In order to minimize the influence of boundary hydrogen atoms that close the cluster on the IR spectrum, the VAP-*d* (*I*) defect was modeled at the eight-member ring and the HVC C_4^0 (*II*) defect was modeled at the intersection of two such rings. In the case of the VAP-*d* defect, the geometrical structure and relative stability were found to be the same as for the chain. The C_4^0 configuration is slightly strained: the relative energy *E* increases by 0.1 eV [9], and the geometrical parameters (interatomic distances) differ somewhat from those corresponding to the minimum in the case of chains: *r*(1–2) = 2.63 Å, *r*(1–3) = 2.75 Å, and *r*(1–4) = *r*(1–5) = 2.46 Å.

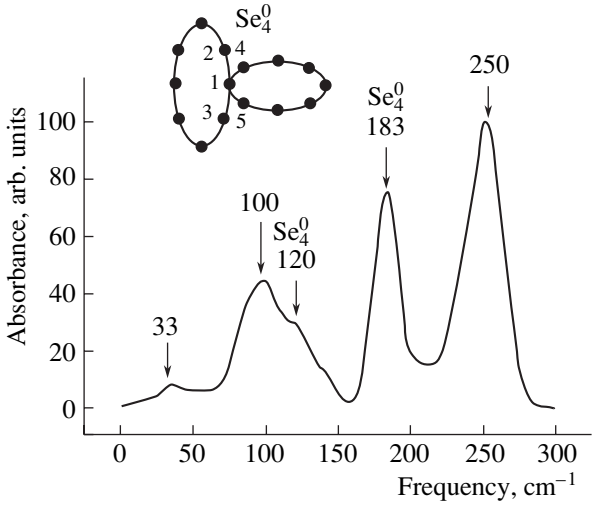

Fig. 3. IR absorption spectrum of the Se_4^0 center formed at the intersection of eight-member rings.

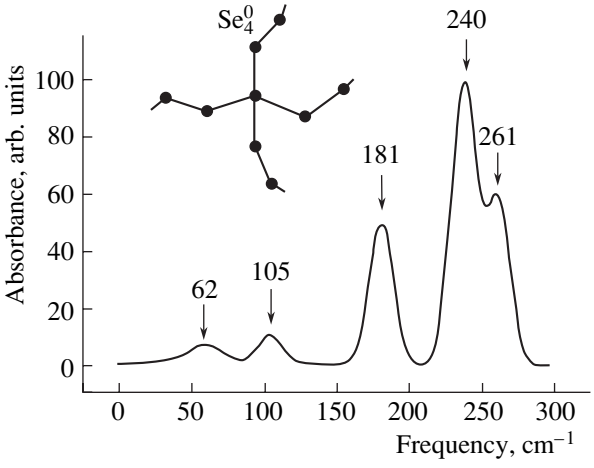

Fig. 4. IR absorption spectrum of the Se_4^0 center formed at the intersection of chains.

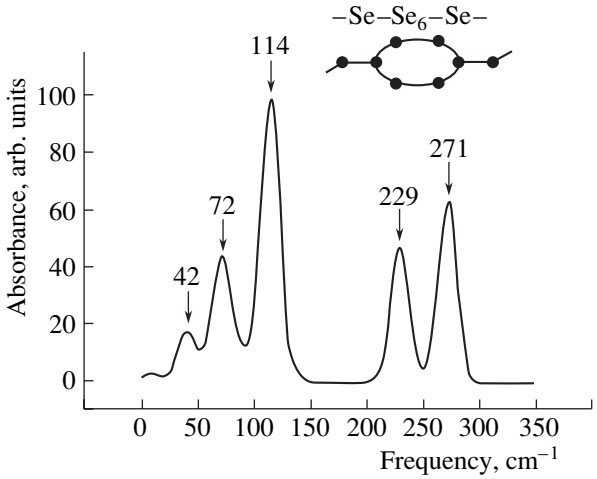

Fig. 5. IR absorption spectrum of the HVC six-member ring.

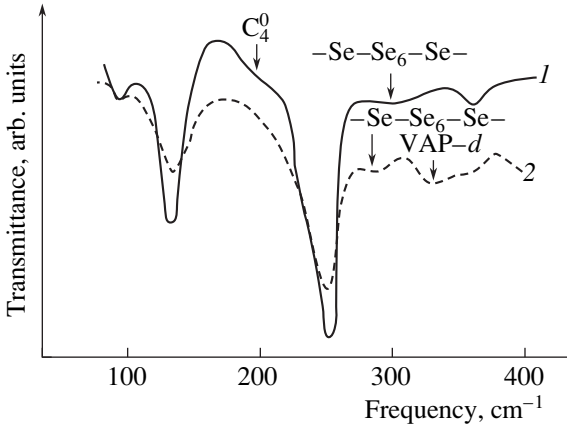

Fig. 6. Experimental IR transmission spectra of *a*-Se [12]: (*1*) red and (*2*) black amorphous selenium.

The model spectrum calculated within the cluster approach represents a discrete set of frequencies with corresponding intensities. In order to facilitate its comparison with the glass spectrum, represented as a continuous curve in the frequency–intensity coordinates, for the configurations modeling the defects, the calculated spectrum was transformed into the superposition of Gaussian curves: $I(f) = A_i\exp\{-[(f - a_i)/s]^2\}$, where f is the frequency, I is the relative intensity of the total spectrum, A_i is the relative intensity of an individual vibration, a_i is the frequency of an individual vibration, and s is the factor determining the Gaussian blurring (~10 cm^{-1}).

In the VAP-*d* defect, the bond 1–2 has a shorter length and is characterized by a larger force constant in comparison with the Se–Se bonds in defect-free configurations. This circumstance leads to a high value of the corresponding frequency of vibrations (337 cm^{-1}). The high intensity is caused by a large change in the dipole moment in the course of the motion of atoms 1 and 2 relative to each other, since they are oppositely charged. The peak at 266 cm^{-1} is caused by the vibrations along the bonds 4–6 and 3–5, which are also somewhat shorter than ordinary bonds due to the bond alternation that occurs in the defect. For the same reason, the bonds 4–1 and 3–1 are weaker than ordinary bonds and the frequency of corresponding vibrations is lower (~200 cm^{-1}). The vibrations related to the bending of valence and torsion angles are characterized by low relative intensities and are unlikely to be observed in the IR spectrum of *a*-Se.

Concerning the Se_4^0 defect, the spectra calculated for clusters consisting of rings and chains are shown in Figs. 3 and 4, respectively. Qualitatively, the spectra turn out to be similar. The basic differences are observed for the bending vibrations: their intensities are appreciably lower in the case of the cluster constructed of chains. In the frequency region corresponding to the stretching vibrations, two strong peaks (at ~250 and ~180 cm^{-1} in Fig. 3) are split off from the band corresponding to the vibrations of an ordinary Se–Se bond. The appearance of these peaks is caused by the fact that the Se_4^0 defect has two groups of weakened bonds; namely, bonds 1–4 and 1–5 (close to ordinary), and bonds 1–2 and 1–3, which are much less rigid. The peak at 261 cm^{-1} (see Fig. 4) is related to stronger bonds in the second coordination shell relative to Se_4^0.

The bond alternation in the ring HVC –Se–Se_6–Se– ($2C_3^0$) (Fig. 5) causes splitting of the peak at 256 cm^{-1} (corresponding to the frequency of the Se–Se vibrations in the defect-free CDN) into two peaks (at ~270 and ~230 cm^{-1}). Furthermore, a strong peak arises in the low-frequency region (~110 cm^{-1}), which is probably caused by a significant change in the electronic structure of this nonrigid configuration due to changes in its geometrical parameters (see [9]). Unfortunately, this peak is obscured because it appears in the region close to the central peak of the band related to the vibrations of the Se_8 ring.

We will now attempt to compare the differences between the experimental IR spectra of *a*-Se and *c*-Se with the results obtained here. One can see from Fig. 6 that additional weak minima, whose positions are consistent with the frequencies of strong vibrations in the HVCs, arise in the experimental transmission spectra when we pass to amorphous modifications. Arrows indicate features which, in our opinion, correspond to the vibrations in which the defects under study are involved. The low intensity of the additional absorption bands is caused by a low (few percent) content of defects.

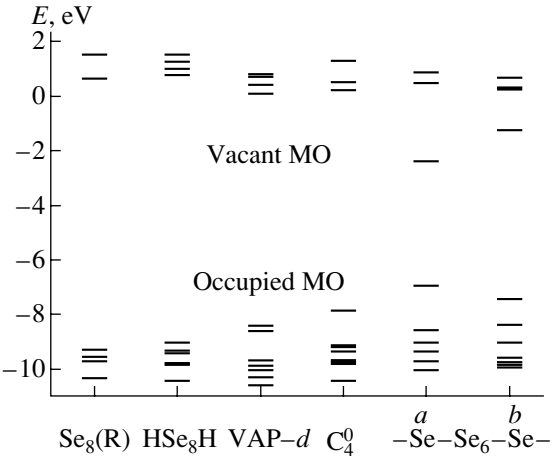

Fig. 7. Energies E of the highest occupied and lowest unoccupied molecular orbitals for the clusters simulating the fragments of the initial network and for the defects in amorphous selenium. For the Se–Se_6–Se configuration, the B3LYP (*a*) and MP2 (*b*) optimization methods were used. Se_8(R) denotes the Se_8 ring.

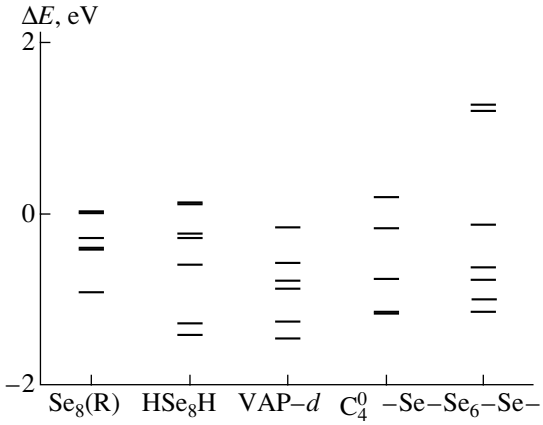

Fig. 8. Relative positions ΔE of the high-energy transitions in the X-ray emission spectrum of different configurations in *a*-Se. The reference point corresponds to the highest transition in the Se_8 ring (Se_8(R)).

3.3. Influence of Hypervalent Configurations on the Band Structure of Chalcogenide Vitreous Semiconductors

The formation of metastable HVCs results in significant changes in the structure of one-electron levels: the highest occupied molecular orbitals (HOMOs) and the lowest unoccupied molecular orbitals (LUMOs) are shifted upwards and downwards, respectively, in the energy scale; these shifts may be as high as 1–2 eV (see Fig. 7). Certainly, these data give only a rough idea of the changes in the CVS-band structure in the course of formation of HVC defects. A more consistent approach would be to compare the band gap with the energies of the electronic transitions between the boundary molecular orbitals (MOs); however, the direct calculation of MOs is a time-consuming problem. The spacings between the one-electron levels differ from the energies of corresponding transitions by the integrals of the Coulomb interaction between these MOs, as well as by the values of the relaxation and correlation corrections. Therefore, these spacings are significantly overestimated. Nevertheless, the changes in the structure of one-electron levels qualitatively illustrate the possibility of localized states (which can act as both electron traps and donors) appearing in the band gap.

According to this scheme, the energies of the one-electron levels of boundary MOs in the chain and Se_8 ring are close to one another. The appearance of the VAP-*d* defect causes a weak splitting-off of two levels from the edge of the valence band and a somewhat stronger splitting-off of two levels from the bottom of the conduction band. Another situation is observed in the case of C_4^0: changes in the LUMO position are insignificant, whereas the HOMO substantially shifts upward. Therefore, one might expect that the VAP-*d* defects should serve as low-efficient electron traps, while the C_4^0 defects may promote the appearance of electrons in the conduction band at lower excitation energies. In the case of HVC defects of the ring type ($2C_3^0$), the structure of both the HOMOs and LUMOs significantly changes. The configuration $2C_3^0$ is nonrigid, and its electronic structure substantially depends on geometrical parameters [9]. This dependence manifests itself not only in the electron-density distribution, but also in the behavior of boundary MOs: the geometrical parameters obtained within the B3LYP method result in more significant shifts than in the case where the structure is optimized within the MP2 method. Nevertheless, the qualitative picture remains the same. One might expect that such defects would facilitate the formation of localized excited states, which could then be involved in photostructural transformations. In our opinion, this problem is promising and interesting; however, it requires complex and time-consuming investigations.

3.4. X-ray Emission Spectra

The defect-caused splitting-off of individual levels from the edge of the valence band can shift the high-energy edge of the band in the X-ray emission spectrum (XES) when we pass from crystalline to amorphous modification. However, the value of the shift is ambiguously related to the behavior of the HOMOs, since defect formation also changes the positions of the core levels at which electrons are trapped. The possible influence of the defects considered above on the position of the edge of the band in the XES of Se was mod-

eled in this study on the basis of the spacings between the levels (calculated by the Hartree–Fock method) of several HOMOs and the levels of the 1*s* orbitals of the atoms, whose *p* orbitals make dominant contributions to the HOMOs under consideration. The corresponding diagram is shown in Fig. 8, where the position of the highest-energy transition in the eight-member ring is taken as a reference point. Unfortunately, in the clusters simulating the VAP-*d* and C_4^0 defects, the energies of the highest-energy transitions turned out to be almost the same as those in Se_8 or in the chain. Therefore, it is highly improbable that these defects could be detected using the XES technique. The HVC-ring (–Se–Se_6–Se–) defect shifts the edge of the XES band to a greater extent; however, one might expect the corresponding peak to be blurred due to the fact that this structure is nonrigid.

4. CONCLUSIONS

It was shown that hypervalent configurations give rise to additional peaks in the IR spectra both in the low- and high-frequency regions. The frequencies of strong high-frequency vibrations in clusters simulating HVC and VAP-*d* defects in selenium are in agreement with the positions of the additional peaks in the IR spectra, which arise when passing from crystalline Se to its amorphous modifications. The formation of HVCs results in the shifting of the LUMOs and HOMOs downwards and upwards, respectively, which should bring localized states (which split off from the edge of the valence band and the bottom of the conduction band) into existence in the band gap. It is probable that an additional peak, related to the HVC and spaced from the upper edge of the band by 1.0–1.5 eV, will arise in the X-ray emission spectra.

ACKNOWLEDGMENTS

This study was supported by the Russian Foundation for Basic Research (RFBR), project no. 00-03-32646. The calculations using GAUSSIAN-94 software were carried out at the Institute of Organic Chemistry, Russian Academy of Sciences, within the framework of RFBR project no. 98-07-90290.

REFERENCES

1. N. F. Mott and E. A. Davis, *Electronic Processes in Non-Crystalline Materials* (Clarendon Press, Oxford, 1979; Mir, Moscow, 1982).
2. M. Kastner, D. Adler, and H. Fritzsche, Phys. Rev. Lett. **37**, 1504 (1976).
3. S. A. Dembovskiĭ and E. A. Chechetkina, *Glass Formation* (Nauka, Moscow, 1999), p. 179.
4. M. I. Klinger and V. G. Karpov, Zh. Éksp. Teor. Fiz. **82**, 1687 (1982) [Sov. Phys. JETP **55**, 976 (1982)].
5. D. Vanderbilt and J. D. Joannopoulous, Phys. Rev. B **22**, 2927 (1980).
6. D. Vanderbilt and J. D. Joannopoulous, Phys. Rev. B **27**, 6311 (1983).
7. D. Hohl and R. O. Jones, Phys. Rev. B **43**, 3856 (1991).
8. S. A. Dembovskiĭ, A. S. Zyubin, and F. V. Grigor'ev, Fiz. Tekh. Poluprovodn. (St. Petersburg) **32**, 944 (1998) [Semiconductors **32**, 843 (1998)].
9. A. S. Zyubin, F. V. Grigor'ev, and S. A. Dembovskiĭ, Zh. Neorg. Khim. **48** (2003) (in press).
10. M. J. Frish, G. W. Trucks, and H. B. Schlegel, *Gaussian 94 (Revision D.1)* (Gaussian, Pittsburg, PA, 1995).
11. M. W. Schmidt, K. K. Baldridge, J. A. Boatz, *et al.*, J. Comput. Chem. **14**, 1347 (1993).
12. R. Zallen and G. Lucovsky, in *Selenium*, Ed. by. R. A. Zhigaro and N. C. Cooper (Van Nostrand–Reinhold, New York, 1974), p. 167.

Translated by A. Kazantsev

Semiconductors, Vol. 37, No. 5, 2003, pp. 604–610. Translated from Fizika i Tekhnika Poluprovodnikov, Vol. 37, No. 5, 2003, pp. 622–628.

AMORPHOUS, VITREOUS, AND POROUS SEMICONDUCTORS

Phase Transformations Initiated in Thin Layers of Amorphous Silicon by Nanosecond Excimer Laser Pulses

G. D. Ivlev and E. I. Gatskevich

Institute of Electronics, Belarussian Academy of Sciences, Belarus

e-mail: ivlev@inel.bas-net.by

Submitted June 25, 2002; accepted for publication November 6, 2002

Abstract—The reflection of a probing beam with a wavelength $\lambda = 0.63$ μm from a silicon surface layer (*a*-Si) amorphized by ion implantation was detected during its melting and solidification initiated by excimer ArF laser radiation. When the irradiation energy is below the epitaxial threshold, a single event of *a*-Si layer melting leads to the formation of single nanocrystals separated from one another in the amorphous matrix rather than to the appearance of polycrystalline material. The presence of nanocrystals makes possible the formation of polycrystalline Si from a melt under exposure to a second laser pulse and allows the intermediate crystallization of Si in a laser-induced sequence of phase transitions. The data obtained are compared to the results of studying the phase transitions initiated in similar experimental conditions in thin layers of hydrogenated *a*-Si layers on glass substrates. © *2003 MAIK "Nauka/Interperiodica".*

INTRODUCTION

As is known, Phase transformations initiated in the systems consisting of amorphous silicon on a crystal Si substrate *a*-Si/*c*-Si [1, 2] or on a quartz or glass substrate *a*-Si/glass [3–5] by single-shot nanosecond laser radiation with an energy density E above the melting threshold E_{ma} of a thin (~10^{-5} cm) *a*-Si layer may cause the formation [from the melt (l-Si)] of fine-grained (FG) and/or coarse-grained (CG) polycrystalline silicon (*pc*-Si) with an average grain size ranging from 5–10 nm to ~0.1 μm, respectively. When E exceeds the threshold E_{ec}, the laser heating of the *a*-Si/*c*-Si system causes the melting front to propagate into the single-crystal layer. If this is the case, the epitaxial process *l*-Si ⟶ *c*-Si is realized. Furthermore, phase transitions *a*-Si ⟶ *l*-Si ⟶ *a*-Si are possible [1] in amorphous Si layers subjected to short (with the half-maximum duration $\tau_p < 10$ ns) pulses of the second harmonic of YAG:Nd or ruby lasers, as well as in hydrogenated *a*-Si/glass layers under the ultraviolet (UV) pulsed radiation of excimer lasers [3–5]. Although a large body of data has been accumulated in this field, there are still some gaps in the knowledge concerning, primarily, the kinetics of fast phase transitions that take place in highly nonequilibrium conditions of pulsed irradiation. Moreover, some of the currently available data are contradictory. For example (see [1] and references therein), the phase transition *l*-Si ⟶ *a*-Si was not observed during the laser melting of pure *a*-Si; this fact was considered by the authors as indicative of a significant role played by impurity in this transformation process. However, this statement is inconsistent with the data of another experiment where such a phase transition took place in pure *a*-Si samples obtained by the amorphization of a single-crystal surface by Si^+ ions. Another issue yet to be clarified is to what extent the initial (a_1) and final (a_2) structural states, i. e., before and after the phase transitions a_1-Si ⟶ *l*-Si ⟶ a_2-Si, correspond to the amorphous phase of Si. The forgoing considerations have motivated this study, which is aimed at gaining insight into melting and solidification processes that take place in thin *a*-Si layers subjected to UV radiation of an excimer laser.

EXPERIMENTAL

The experiments were held under conditions similar to [5] with the use of an EMG-100 excimer laser with a wavelength $\lambda = 0.193$ μm and a pulse duration $\tau_p = 10$ ns. Implantation of 75-keV P+ ions into KDB-10 (*p*-Si:B, $\rho = 10$ Ω cm) (111) wafers at a dose of 2×10^{15} cm^{-2} resulted in the formation of a 0.1-μm-thick amorphous layer. We varied the energy density E by moving the focusing lens along the laser beam axis. The area to be irradiated was defined by a thin metal plate with an orifice 0.5 mm in diameter placed immediately ahead of the sample, which was spaced from the lens by more than the focal distance. A probing He–Ne laser beam ($\lambda = 0.63$ μm) polarized in the plane of incidence was focused onto a 0.05-mm-wide spot centered within the irradiated zone with the angle of incidence being 30°. After the probing beam reflected from the sample, it was detected by a silicon photodiode. A signal from the photodetector was fed to a TS-8123 storage oscilloscope connected to a computer. The rise time for the

response characteristic in the measuring circuit was about 4 ns. Pulse-to-pulse fluctuations of radiation energy were no larger than ±10%. Before proceeding to a discussion of the data obtained, we should note the following.

In our previous study [2] concerned with the dynamics of annealing of similar implanted Si samples irradiated with ruby laser pulses (τ_p = 70 ns, λ = 694 nm), the recovery of the single-crystal structure (or the CG-Si formation) was shown to occur as a result of a complex sequence of phase transitions: *a*-Si ⟶ l_1-Si ⟶ *FG*-Si ⟶ l_2-Si ⟶ *c*-Si (CG-Si), involving intermediate crystallization with the formation of FG-Si. As the radiation energy decreases to ~0.5 J/cm^2 (E_{ma}), the ensuing melting of FG-Si is ruled out of the process and the laser influence is reduced to the following transformations: *a*-Si ⟶ *l*-Si ⟶ FG-Si. FG-Si is formed according to the mechanism of explosive crystallization [1], with a liquid phase being supercooled considerably since the *a*-Si melting temperature T_{ma} is ~200 K lower than the equilibrium point T_{mc} = 1685 K of the crystal–melt transition in Si. The formation of *pc*-Si at the radiation energies $E_{ma} < E < E_{ec} \approx 1.6$ J/cm^2, which is confirmed by TEM data [6], can be visually observed due to a specific tint of the irradiated area. In this case (Fig. 1), the microscope study of the sample surface with lateral illumination dearly indicates the presence of an irradiated zone 2.5 mm in diameter, which stands out against the general *a*-Si background as a result of scattering of incident light by the *pc*-Si layer microprofile; if $E > E_{ec}$, the area of epitaxially crystallized silicon is encircled by an easily distinguishable thin polycrystalline ring. In the experiment with the excimer laser, a similar pattern appeared upon the formation of *pc*-Si.

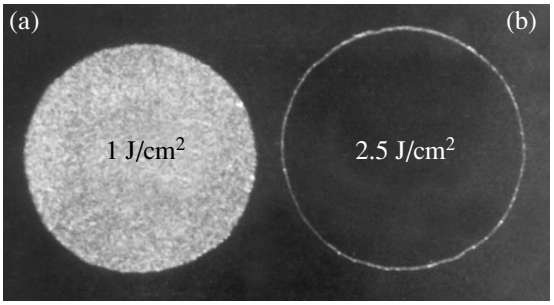

Fig. 1. Irradiated zone at the laser energy (a) below and (b) above the epitaxial-crystallization threshold in implanted silicon.

THE DYNAMICS OF AN IMPLANTED Si SURFACE UNDER SINGLE-PULSE LASER IRRADIATION

Studying the dynamics of the reflection of a probing beam from the samples irradiated by the excimer laser showed that irradiation with an energy 0.16 J/cm^2 < *E* < $E_{ec} \approx 0.75$ J/cm^2 (1 < *A* < 4.7, parameter $A = E/E_{ma}$) results in the phase transformations a_1-Si ⟶ *l*-Si ⟶ a_2-Si, rather than in the formation of a polycrystalline structure. In this situation (Fig. 2, curves *1–6*), the final value of the reflection coefficient *R* appears to be equal to its initial value and the lifetime of the liquid phase (i. e., the duration of phase transitions), characterized by an increased reflectance, amounts to τ_m < 50 ns. As *E* increases within the interval specified above, the time dependence *R*(*t*) changes radically: at *E* > 0.4 J/cm^2 (*A* > 2.5), the establishment of the final value of *R* becomes nonmonotonic (Fig. 2, curves *4–6*). This effect is most pronounced when *E* approaches the epitaxial threshold and can be explained by the fact that, during solidification, the silicon layer becomes amorphous not only from the substrate side but also from the surface of the melted layer; as a result, the reflection coefficient *R* first drops below the initial value, then

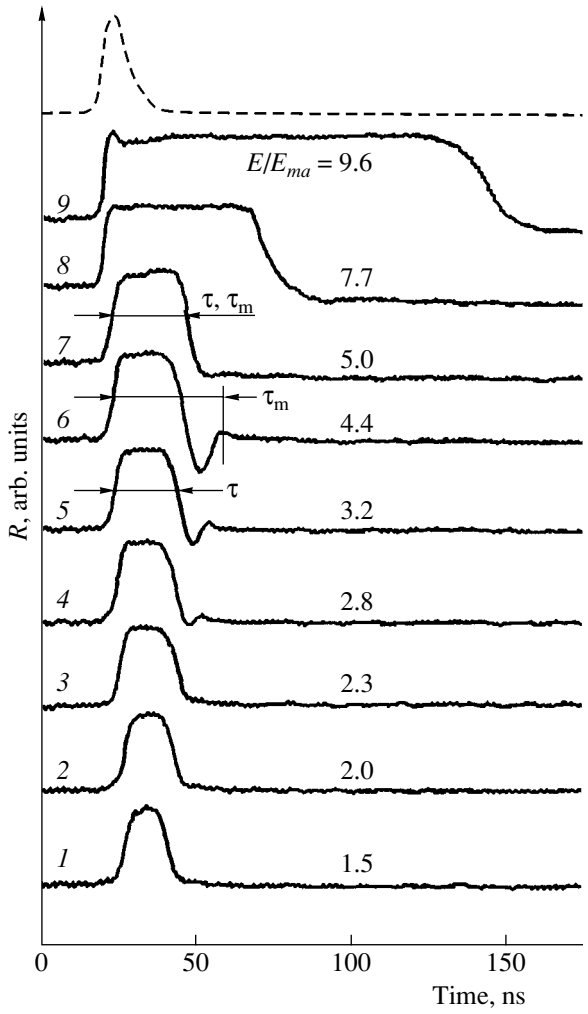

Fig. 2. Dynamics of the probing beam reflection from ion-implanted silicon. Dashed line shows the pulse of the excimer ArF laser.

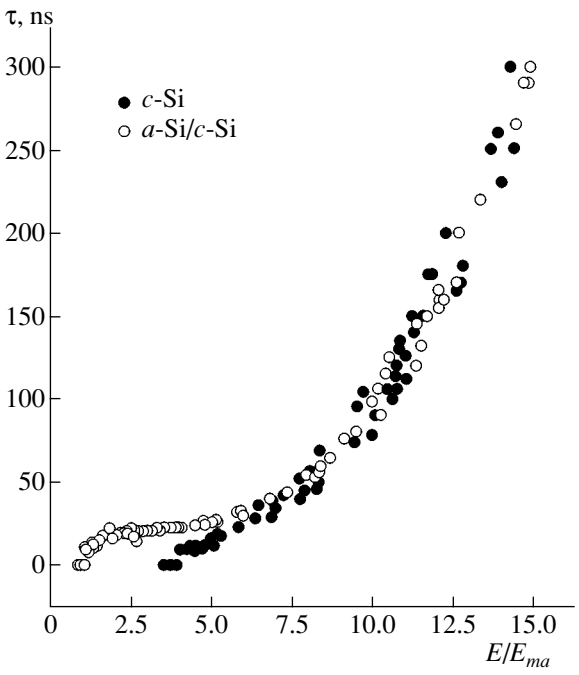

Fig. 3. Silicon liquid-phase lifetime vs. the energy density of the laser.

passes through a weak maximum, and finally again approaches its initial value. Such changes in R are caused by the interference of the probing radiation as it reflects from the a-Si/l-Si system with an increasing thickness of the a-Si surface layer. A similar reflectance dynamics $R(t)$ was derived from a theoretical analysis of the model of an electromagnetic wave propagating in a multilayer media [7] (under the assumption that amorphization starts from the surface and the interphase boundaries propagate towards each other). Similar dependences $R(t)$ and analogous interpretation also follow from [8], which dealt with the effect of picosecond laser pulses on thin amorphous germanium films on silicon.

Laser radiation with $E \geq E_{ec}$ ($A \geq 4.7$) initiates the epitaxial crystallization of a molten layer, and the reflectivity of the sample drops to the value corresponding to c-Si (Fig. 2, curves *7*–*9*), which is lower than the initial value of R. As the energy density increases to 1.5 J/cm^2 ($A = 9.4$), the value of τ_m grows to 0.12 μs; at the stage when quasistationary R (reflectivity of l-Si) is becoming established, a reversible decrease in the reflectance is observed, which can be attributed [9] to a considerable heating of the melt surface (Fig. 2, curve *9*). When the solidification (amorphization) of Si occurs from both the substrate and the melt surface sides, the duration of the enhanced-reflectivity phase $\tau < \tau_m$; in contrast, these time intervals are equal in the case of solidification from the substrate side only. It should be noted that the liquid phase involved in the phase transi-

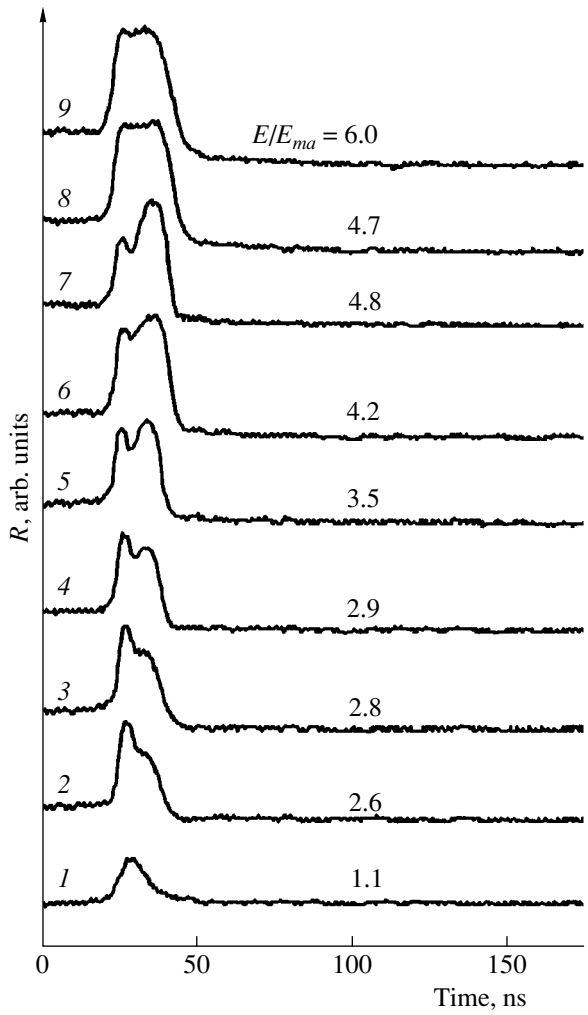

Fig. 4. Dynamics of the probing beam reflection from the implanted Si surface during the second exposure to radiation.

tions a_1-Si ⟶ l-Si ⟶ a_2-Si appears to have a noticeably shorter duration when there is a small excess of E over E_{ec} (Fig. 2, curve *7*) than at the energies slightly below E_{ec} (Fig. 2, curve *6*). The longer time period required for the phase transitions to occur in the latter case can be attributed to the lower thermal conductivity of a-Si compared to that of c-Si (the difference amounts to about two orders of magnitude), which lowers the efficiency of heat removal to the substrate and, thus, prolongs the liquid phase lifetime relative to that corresponding to the epitaxial process. The dependences $\tau(E)$ obtained for the a-Si/c-Si and c-Si samples (Fig. 3) practically coincide at $E \geq 1$ J/cm^2 ($A \geq 6.3$). As E increases, the time τ grows nonlinearly and reaches 300 ns at the energies close to the ablation threshold in silicon $E_a \approx 2.3$–2.4 J/cm^2. The measured melting thresholds of the a-Si/c-Si layer and the single-crystal Si surface differ by a factor of about 4.

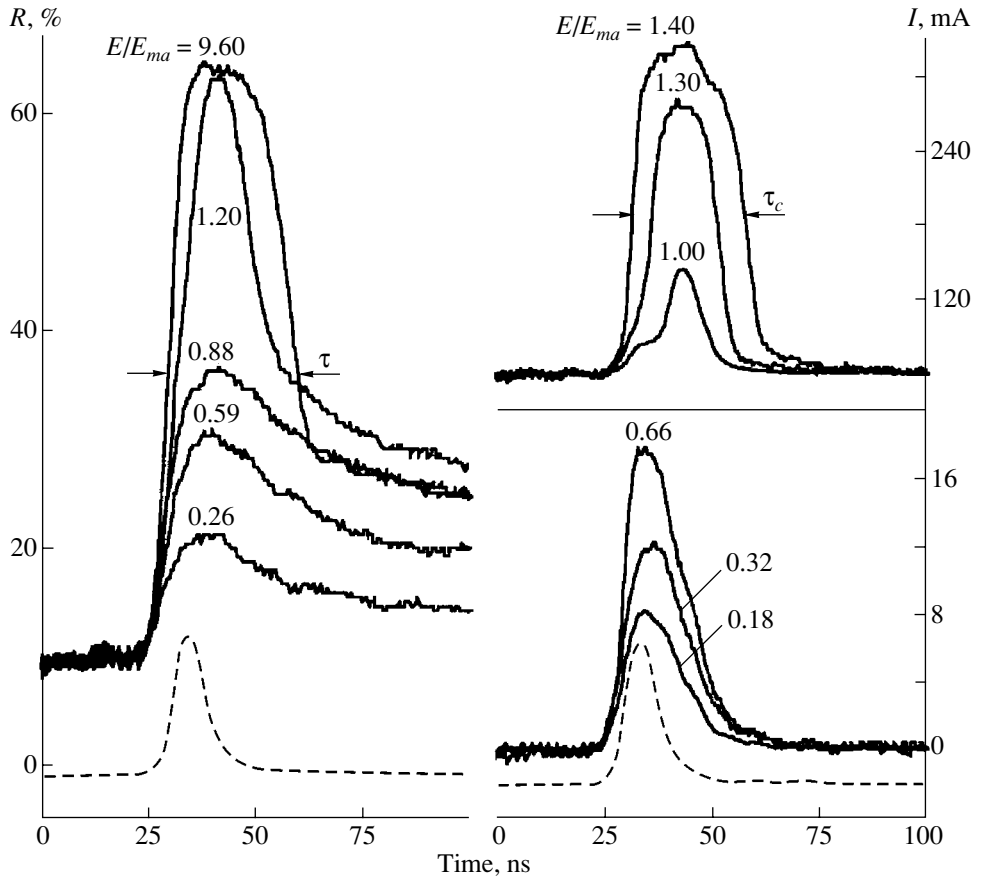

Fig. 5. Dynamics of reflectivity and electrical conduction of *a*-Si/glass films at the irradiation energies below and above the *a*-Si melting threshold. Dashed line shows the pulse of the excimer ArF laser.

THE DYNAMICS OF PROBING-RADIATOH REFLECTION FROM THE IMPLANTED Si SURFACE UNDER REPEATED LASER IRRADIATION

The reflectivity behavior ($E_{ma} < E < E_{ec}$) of the implanted silicon subjected to the second laser irradiation (Fig. 4) differs radically from the time dependence $R(t)$ in the conditions of the first irradiation; i. e., the preliminary exposure ($E = E_1$) has an effect on the kinetics of phase transformations initiated by the second pulse ($E = E_2$). This influence is insignificant if the radiation energy is close to E_{ma} (Fig. 4, curve *1*). However, at higher values of E_2 (E_1 = 0.2–0.3 J/cm^2), the observed dependences $R(t)$ (Fig. 4, curves *2–7*) do not resemble those obtained after the first irradiation of the sample (Fig. 2, curves *3–6*) within approximately the same energy range E_2 = 0.4–0.7 J/cm^2 (A = 2.5–4.4). This circumstance can be explained by the formation of a polycrystalline structure due to the second pulse and the corresponding drop of R below the initial value, as well as by the intermediate crystallization of silicon, which is possible during an induced sequence of phase transformations; as a result, the reflectance increases or decreases nonmonotonically.

By way of example, let us examine oscillogram *5* in Fig. 4. Melting of the *a*-Si layer leads to an increase in R and the subsequent reduction of the reflection coefficient due to the unoriented crystallization of highly supercooled l_1-Si, which seems, most likely, to cause the formation of FG-Si. The polycrystalline material then melts, and the reflection coefficient peaks again for, after which it drops below the initial value because of the crystallization process l_2-Si $\longrightarrow$ FG-Si. A decrease in the energy density E_2 reduces the role of repeat melting (Fig. 4, curves *2–5*). At $E_{ma} < E < 0.4$ J/cm^2 ($1 < A < 2.5$), the phase transitions a_2-Si $\longrightarrow$ l-Si $\longrightarrow$ FG-Si occur and no repeat melting is observed. With an increase in E_2, the intermediate crystallization shifts in time towards the onset of R growth (Fig. 4, curve *7*) or does not develop at all (Fig. 4, curves *8*, *9*) because of the decay of the crystal nuclei at a high rate of l-Si heating, which is typical of the energy densities $E_2 > E_{ec}$ (at a lower laser energy, the growth of crystal nuclei results in FG-Si formation). At $E_2 \approx E_{ec}$, the initiation of intermediate crystallization is stochastic; i. e., it does not always happen (compare oscillograms *7* and *8* in Fig. 4).

It is interesting to compare the results of the current study of the *a*-Si/*c*-Si system with those obtained in [5]

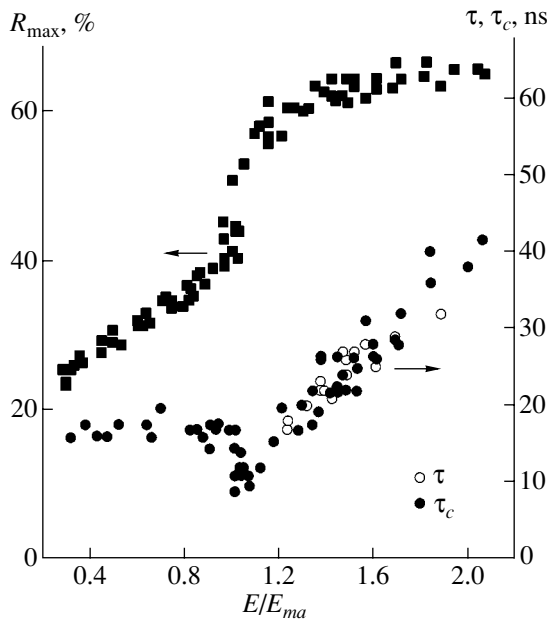

Fig. 6. Maximal reflection coefficient R_{max} and the duration of the pulsed signals obtained from *a*-Si/glass samples vs. the energy density of the laser.

for the annealing dynamics of thin hydrogenated *a*-Si films on glass substrates under similar conditions of excimer laser irradiation.

THE EFFECT OF PULSED LASER RADIATION ON THIN FILMS OF HYDROGENATED AMORPHOUS SILICON

In study [5], *a*-Si films with a thickness of 70 nm (close to the thickness of the amorphous layer in *a*-Si/*c*-Si samples) were formed on glass substrates by the decomposition of pure silane (SiH_4) in glow-discharge plasma. The laser-induced modification of the films was ascertained by the dynamics of optical reflectance $R(t)$ in the experimental conditions similar to those for *a*-Si/*c*-Si samples and from the dynamics of their electrical conduction. The latter value was derived from measurements of current $I(t)$ across a 0.5-mm-wide (and 6-mm-long) gap between deposited thin-film electrodes of Cr or Au; the applied voltage was 20 V. From the oscillograms for the $R(t)$ and $I(t)$ signals (Fig. 5), the melting threshold of the *a*-Si/glass was determined as $E_{ma} \approx 0.1$ J/cm^2. This appears to be markedly lower than the corresponding value E_{ma} for *a*-Si/*c*-Si samples, since a smaller amount of heat is removed during the laser pulse to the glass substrate (Corning 7059), whose thermal diffusivity is substantially lower than that of *c*-Si. It should be noted that, in both cases, the emission of heat due to the absorption of laser radiation occurs in a 10-nm-thick surface layer of *a*-Si, as the absorption coefficient of UV radiation α in *a*-Si (as well as in *c*-Si and in the melt) is on the order of 10^6 cm^{-1}.

The absorption coefficient of the probing radiation in *a*-Si (~5×10^4 cm^{-1} [10]) is appreciably smaller than $\alpha = 10^6$ cm^{-1}, which leads to a considerable difference in the initial values of R for the *a*-Si/glass and *a*-Si/*c*-Si samples. In the former case, the reflection coefficient (~10%) is defined not only by the optical parameters of *a*-Si:H but also by the interference of radiation due to the contribution from the film–substrate interface. In the latter case, the interference is virtually insignificant because of the close refractive indices of *a*-Si and *c*-Si, and the value of R (close to 40%) is mostly defined by the optical parameters of *a*-Si. The maximal reflection coefficient R_{max}, achieved at $E > E_{ma}$, is ~65% in both cases, which corresponds to the reflectivity of Si melt ($\alpha \approx 10^6$ cm^{-1}), as in similar experimental conditions [9] for the laser-induced melting of *c*-Si. In each case, however, the dynamics of reflectivity has its special features, which can be seen from a comparison of the oscillograms shown in Figs. 2 and 5.

In the situation with *a*-Si/glass samples, as E increases to E_{ma}, the peak value of R linearly grows (Fig. 6) and the duration of the pulse of current induced by the photoexcitation of silicon, τ_c, remains constant. A further increase in E leads to the leveling off of the energy dependence of R_{max} due to the complete melting of the film, and the dependences $\tau_c(E)$ and $\tau_m(E)$ coincide. These data suggest that the lifetime of the Si melt increases proportionally to E and reaches 40–50 ns near the ablation threshold of the film E_a. The value of E_a exceeds the melting threshold by a factor of only 2–2.5 because of the low thermal diffusivity of the glass substrate. Note for comparison that, in the experiment with *a*-Si/*c*-Si samples, the ratio E_a/E_{ma} (i. e., the parameter A) approaches 15.

Taking into consideration the differences in the parameters of laser interaction with different systems consisting of amorphous film and substrate, we call attention to the remarkable resemblance of the kinetics of the laser-induced phase transformations in both systems. Specifically, neither in the *a*-Si/*c*-Si nor in the *a*-Si/glass systems does single-pulse laser irradiation at $E_{ma} < E < E_{ec}$ lead to the formation of polycrystalline material. In the case of *a*-Si/glass, this conclusion is also supported by the results of Raman studies of the films. For a polycrystalline structure to appear, repeat exposure of both systems to laser radiation with $E < E_{ma}$ is required, which indicates that the kinetics of Si crystallite growth is similar in both cases and is associated with the growth of nanocrystal nuclei initiated by the first irradiation. Therefore, the differences in manufacturing methods and the content of different impurities (phosphorous with a concentration below 1% or hydrogen in *a*-Si/glass films with an initial concentration of 8–10% [11]), as well as the different conditions of heat

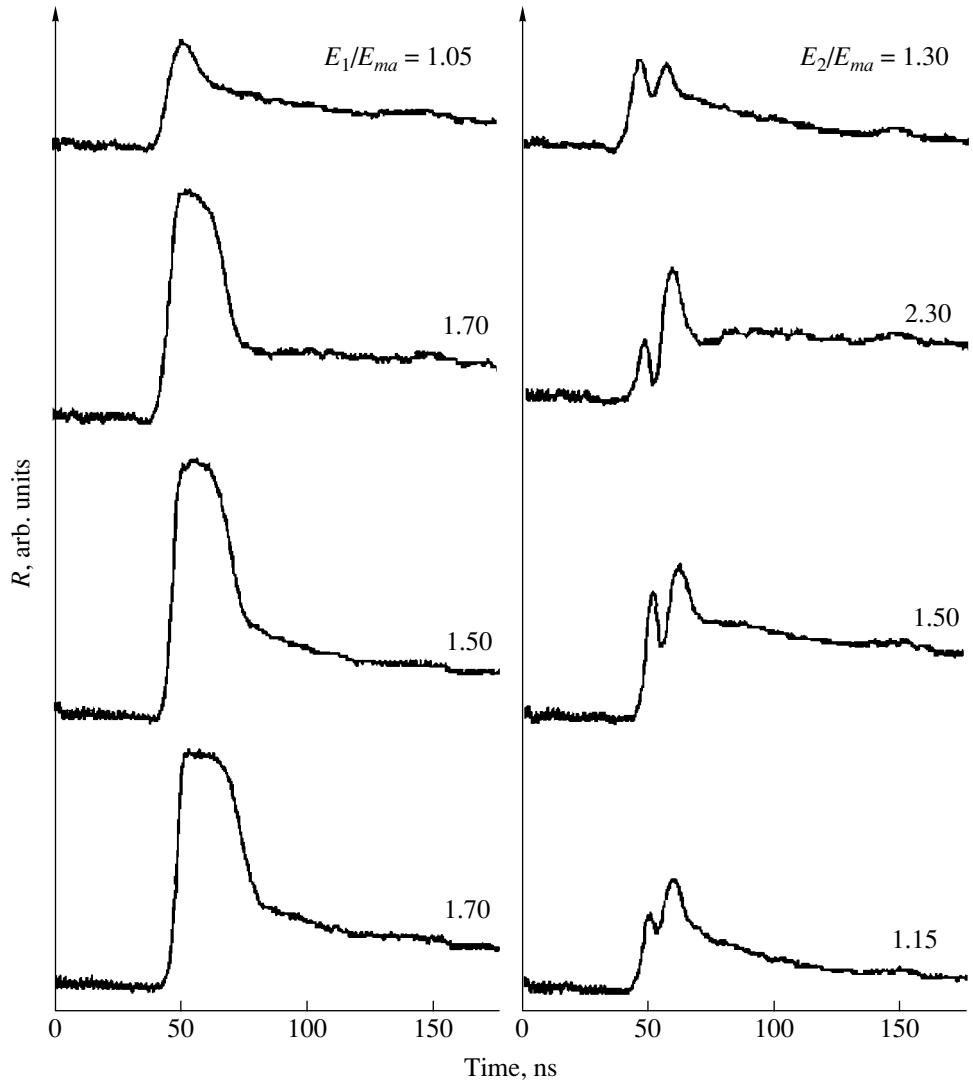

Fig. 7. Dynamics of the probing beam reflection from a_1-Si/glass and a_2-Si/glass films subjected to pulsed laser irradiation. Oscillograms to the left and right were obtained during the first and the second pulse, respectively.

removal to substrate, seem to be of slight influence. Repeat laser irradiation of Si-on-glass samples may result in intermediate crystallization, which manifests itself in the specific dynamics of a change in R (Fig. 7) similar to the dependence $R(t)$ observed upon the irradiation of ion-implanted silicon (Fig. 5).

CONCLUSION

The possibility of nanometer-sized (smaller than 5 nm) single crystals (nanocrystals) forming thin films of *a*-Si/glass under single-pulse UV laser irradiation is supported by the data obtained *ex situ* in study [12], which was carried out with the use of an excimer XeCl laser (λ = 308 nm, τ_p = 5 ns). It was found that the prevailing orientation of the nanocrystals was in the [110] direction perpendicular to the film surface (the film had a thickness of ~100 nm) and their concentration depends on the laser energy density. In our experimental conditions, a similar phenomenon is likely to occur. The formation of nanocrystals leads to the appearance of a polycrystalline phase and allows intermediate crystallization to develop during laser-induced melting of silicon both in the a_2-Si/glass system and in a_2-Si/*c*-Si layers. One of the factors that precludes the crystallization of films as a result of single-pulse irradiation is a fairly rapid rise of the a_1-Si temperature, due to which the nucleation of nanocrystals in the amorphous matrix (a_2-Si) is virtually suppressed. In the experiments with a ruby laser [13], where the heating rate of the *a*-Si/*c*-Si layer was lower due to a substantially longer time of exposure (70 ns), the effective nucleation of nanocrystals in the amorphous phase takes place at the premelting stage and the crystals grow to the size of grains in fine-grained polycrystalline material at the phase tran-

sition l_1-Si ⟶ FG-Si, i. e, during explosive crystallization.

ACKNOWLEDGMENTS

We thank V. Cháb for giving us the opportunity to carry out experiments with the excimer laser.

This study was supported in part by the Belarussian Foundation for Basic Research, project no. F99-184.

REFERENCES

1. W. C. Sinke, A. Polman, and P. A. Stolk, *Physical Research. EPM-89. Energy Pulse and Particle Beam Modification of Materials*, Ed. by K. Hohmuth and E. Richter (Akademie, Berlin, 1990), Vol. 13, p. 94.
2. G. D. Ivlev, Zh. Tekh. Fiz. **61** (1), 195 (1991) [Sov. Phys. Tech. Phys. **36**, 118 (1991)].
3. T. Sameshima and S. Usui, J. Appl. Phys. **70**, 1281 (1991).
4. E. L. Mathe, A. Naudon, M. Elliq, *et al.*, Appl. Surf. Sci. **54**, 392 (1992).
5. G. Ivlev, E. Gatskevich, V. Cháb, *et al.*, Appl. Phys. Lett. **75**, 498 (1999).
6. G. D. Ivlev and N. A. Romanova, Poverkhnost', No. 4, 145 (1989).
7. M. Born and E. Wolf, *Principles of Optics*, 4th ed. (Pergamon Press, Oxford, 1969; Nauka, Moscow, 1970).
8. J. Siegel, J. Solis, and C. N. Afonso, Appl. Surf. Sci. **154–155**, 130 (2000).
9. G. D. Ivlev and E. I. Gatskevich, Fiz. Tekh. Poluprovodn. (St. Petersburg) **34**, 787 (2000) [Semiconductors **34**, 759 (2000)].
10. V. I. Gavrilenko, A. M. Grekhov, D. V. Korbutyak, and V. G. Litovchenko, *Optical Properties of Semiconductors* (Naukova Dumka, Kiev, 1987).
11. C. D. Kim, R. Ishihara, and M. Matsumura, Jpn. J. Appl. Phys. **34**, 5971 (1995).
12. M. D. Efremov, V. V. Bolotov, V. A. Volodin, *et al.*, Fiz. Tekh. Poluprovodn. (St. Petersburg) **36**, 109 (2002) [Semiconductors **36**, 102 (2002)].
13. L. P. Avakyants, G. D. Ivlev, and E. D. Obraztsova, Fiz. Tverd. Tela (St. Petersburg) **34**, 3334 (1992) [Sov. Phys. Solid State **34**, 1784 (1992)].

Translated by A. Sidorova

Semiconductors, Vol. 37, No. 5, 2003, pp. 611–615. Translated from Fizika i Tekhnika Poluprovodnikov, Vol. 37, No. 5, 2003, pp. 629–633.

PHYSICS OF SEMICONDUCTOR DEVICES

Detection of Hydrogen Impurity in Silicon Radiation Detectors

L. F. Makarenko*, F. P. Korshunov, S. B. Lastovskiĭ**, and N. I. Zamyatin*****

** Belarussian State University, Minsk, 220050 Belarus*

*** Institute of Solid-State and Semiconductor Physics, Belarussian Academy of Sciences, ul. Brovki 17, Minsk, 220072 Belarus*

**** Joint Institute for Nuclear Research, Dubna, Moscow oblast, 141980 Russia*

Submitted September 26, 2002; accepted for publication October 4, 2002

Abstract—The behavior of silicon particle detectors irradiated with 2.5-MeV electrons during subsequent annealing is studied. Annealing at 100–250°C was found to result in the formation of two types of traps with the levels E_c – 0.32 eV and E_v + 0.29 eV. Increasing the annealing temperature to 300°C makes both traps disappear. On the basis of data obtained, it was concluded that these traps are related to hydrogen-containing complexes. The presence of hydrogen in a crystal results in a decrease in the annealing temperature for vacancy–oxygen (*V*O) complexes and complexes consisting of carbon and oxygen interstitials (C_iO_i). The reason for this phenomenon is the passivation of these complexes by hydrogen, which results in the formation of electrically active *V*OH centers {with the level E_c – 0.32 eV} in an intermediate stage of this process. It is assumed that hydrogen penetrates the structures under investigation in one of the stages of their fabrication. © *2003 MAIK "Nauka/Interperiodica".*

1. INTRODUCTION

Nowadays, in order to perform experiments in high-energy physics, one needs silicon particle detectors that retain their working capacity even if the content of compensating radiation defects (RDs) exceeds the content of shallow-level impurities in the base region of the detector by more than a factor of 100. The need for such detectors stimulated multiple investigations of the radiation damage in detector-grade silicon (see report [1] and references therein).

One of the principal purposes of these studies was to investigate the possibility of applying the defect-engineering technique for improving the radiation resistance of detectors. This method consists of the purposeful addition of impurities that affect the processes of formation of electrically active defects during irradiation and, thus, make it possible to control the macroscopic parameters of the detector structures.

Some models of defect formation, which served as a basis for using various processing procedures to improve the resistance of detectors with respect to a number of parameters, have been developed [1, 2]. In these models, oxygen and carbon were assumed to be those impurities that completely determine the formation of electrically active complexes in irradiated silicon. However, the available models cannot adequately describe the properties of real structures. Thus, the processes of interaction of RDs both with each other and with impurities are now being studied in more detail.

As recent investigations [3–6] show, hydrogen can penetrate silicon crystals even at room temperature. In this case, conventional processing operations in the fabrication of detector structures may be responsible for the appearance of hydrogen in them. For example, hydrogen penetrates Si structures during wet chemical etching [3–6]. These data make it possible to assume that hydrogen may also be present in silicon detectors. The purpose of this study is to verify the above hypothesis.

2. EXPERIMENTAL

In this study, we investigated detectors fabricated from silicon with a resistivity of 4 kΩ cm and a phosphorus concentration of ~10^{12} cm^{-3} (Wacker Chemitronics, Germany). In fabricating the detector structures, we used conventional stages of planar technology: ion implantation, thermal oxidation, etching, and deposition of metals. In order to introduce radiation defects, we used irradiation with gamma-ray photons from a ^{60}Co source and with fast electrons with an energy of $E \approx 2.5$ MeV. After irradiation, isochronous annealing (30 min) was performed in air in the temperature range of 100–300°C to determine the thermal stability of RDs and study their interaction with the hydrogen impurity.

The defect content was determined by deep-level transient spectroscopy (DLTS). The measurements were carried out in the temperature range of 79–300 K. The bridge operating frequency amounted to 1 MHz.

1063-7826/03/3705-0611$24.00

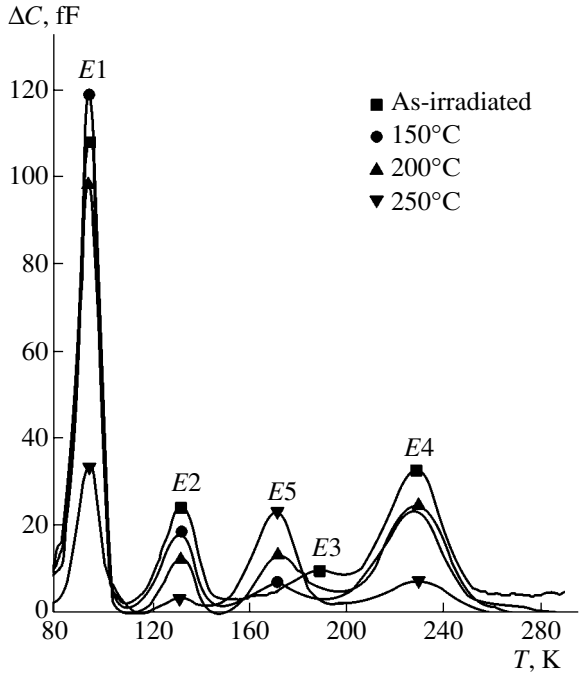

Fig. 1. Energy levels of the traps for majority charge carriers in the DLTS spectra of detectors, as-irradiated (with 2.5-MeV electrons) and isochronously annealed (for 30 min) after irradiation at temperatures T_{ann} indicated in the figure.

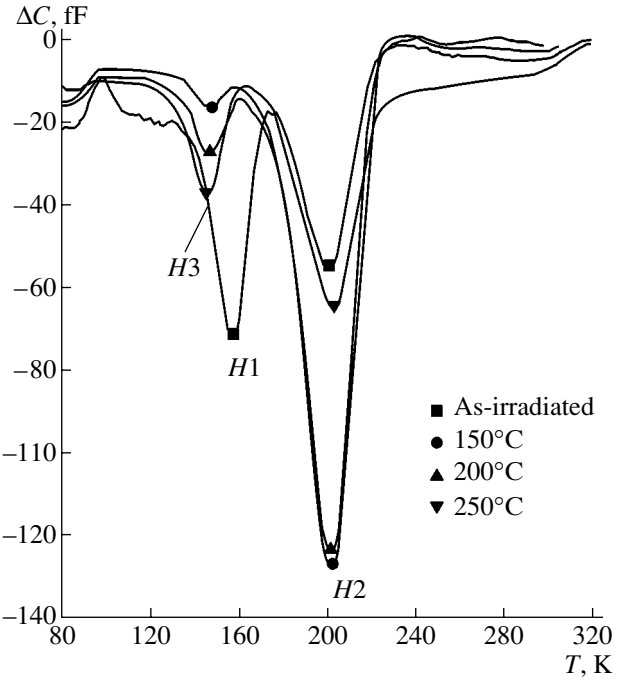

Fig. 2. Energy levels of the traps for minority charge carriers in the DLTS spectra of detectors, as-irradiated (with 2.5-MeV electrons) and isochronously annealed (for 30 min) after irradiation at temperatures T_{ann} indicated in the figure.

3. EXPERIMENTAL RESULTS AND DISCUSSION

3.1. Detection of Hydrogen Centers

The temperature necessary for annealing RDs depends on the presence of hydrogen impurity. One might expect that, during annealing, passivation of vacancy-type defects should occur first [3, 7]. In order to study this effect, we performed isochronous annealing of detector structures irradiated with fast electrons. Figure 1 shows DLTS spectra measured immediately after irradiation and after isochronous annealing at various temperatures for 30 min. Immediately after irradiation, four trapping levels are observed: $E1$ at $\sim E_c$ – 0.17 eV, $E2$ at $\sim E_c$ – 0.25 eV, $E3$ at $\sim E_c$ – 0.37 eV, and $E4$ at $\sim E_c$ – 0.42 eV. The annealing at 150°C leads to an increase in the amplitude of the signal related to the $E1$ trap and to the appearance of a new trapping level $E5$ at (E_c – 0.32 eV). If the annealing temperature increases, the content of $E5$ centers increases, whereas the content of the $E1$ centers decreases. According to [3–6], the $E5$ trap may be related to a vacancy–oxygen–hydrogen complex (*V*OH).

Another center which, according to [8], may also be indicative of the presence of hydrogen is the trapping level at $E_v + 0.28 \pm 0.01$ eV. In order to detect this center, we studied the DLTS spectra related to the traps for minority charge carriers (Fig. 2). As can be seen Fig. 2, in the spectrum recorded immediately after irradiation, two traps are observed: $H1$ at $E_v + 0.30$ eV and $H2$ at $E_v + 0.36$ eV. After annealing at 150°C, the $H1$ trap disappears, while the content of $H2$ centers increases substantially. At higher temperatures, a new trap $H3$ (at E_v + 0.29 eV) appears. The content of these traps increases with an increase in the annealing temperature up to 250°C. The amplitudes of the peaks related to the traps under observation are shown in Fig. 3 as functions of the annealing temperature.

The data we observed may be interpreted as follows. The energy position and the temperature stability of the $H1$ trap indicate that it may be related to the carbon interstitial (C_i) [9]. At $T \approx$ 50–100°C, this atom becomes mobile and migrates through the crystal until it is captured either by an oxygen interstitial (O_i) or by a substitutional carbon atom (C_s) [9, 10]. In this case, either a complex consisting of a carbon interstitial and an oxygen interstitial (C_i–O_i) with a donor level at $\sim E_v$ + 0.35 eV or a complex consisting of a carbon interstitial and a substitutional carbon atom (C_i–C_s) with an acceptor level at $\sim E_c$ – 0.17 eV are formed [9, 10]. In the crystals under investigation, most defects C_i are involved in formation of C_i–O_i complexes, which is indicative of a relatively high content of oxygen impurity.

The centers with energy levels at E_c – 0.32 eV ($E5$) and E_v + 0.29 eV ($H3$) are related to the complexes containing hydrogen [3–6, 8]. In study [8], it was suggested that these two levels represent the acceptor and donor

levels of the complex consisting of an oxygen vacancy and a hydrogen atom (*V*OH). This suggestion is confirmed by our data. The *E*5 and *H*3 centers have similar contents, and both of these centers vanish simultaneously after annealing at 300°C (Fig. 3). Thus, the set of data we obtained makes it possible to conclude that the detector structures under study contain hydrogen impurity.

Presumably, hydrogen penetrated the structures during a certain processing stage. As our experiments showed, the relative content of the *V*O and *V*OH complexes is virtually invariable at distances in the range of 30–90 μm from the *p–n* junction. Hence, we can conclude that either hydrogen penetrated the structure during a high-temperature stage (for example, oxidation) or the structure was subjected to thermal treatment after hydrogen penetrated it.

Previously, the presence of hydrogen in detector structures was reported in [11]. It was observed in that study that a trapping level at $E_v - 0.32$ eV appeared after γ irradiation at 350°C. However, it is well known from the data in the literature [12, 13] that this trap is annealed at 300°C in the same way as in the structures we studied. Therefore, it is worth noting that the data from [11] cannot be unambiguously interpreted and, thus, cannot verify the presence of hydrogen in the silicon detectors.

3.2. Behavior of Divacancies in Detector Structures with Hydrogen

One of the major defects determining the degradation of detectors used in projects in high-energy physics is the divacancy [1, 2]. Therefore, it is of interest, first of all, to investigate the possibility of passivating this defect. As follows from the data reported in [3], a divacancy may be efficiently passivated when doping surface layers with hydrogen during wet etching of silicon. However, in the structures we studied, total passivation of divacancies was not observed. Although our data cannot be interpreted as unambiguously as the data on the formation of the *V*OH complex, nevertheless, it may be concluded that the hydrogen atom and the divacancy interact with each other.

The divacancy is known to have two acceptor levels at $E \approx E_c - 0.24$ eV and $E \approx E_c - 0.42$ eV [14] in the upper half of the band gap of silicon. In the detectors we studied, these levels correspond to the *E*2 and *E*4 traps. However, the contents of these traps are not equal. The largest value of the signal related to the deeper *E*4 trap exceeds that for the *E*2 trap. This fact enables us to conclude that the *E*4 peak is related to at least two centers. As a rule, it is assumed that, in addition to the divacancy, the phosphorus–vacancy complex (*E* center) also contributes to the amplitude of the *E*4 peak. In order to verify this assumption, we irradiated

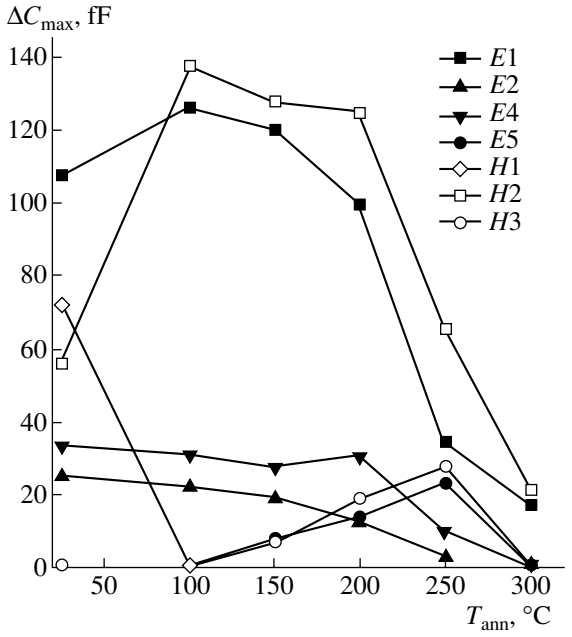

Fig. 3. Variations in the amplitudes of DLTS peaks related to the radiation defects *V*O + C_iC_s (*E*1), *V*OH (*E*5, *H*3?), *VV* (*E*2, *E*4), C_i (*H*1), and C_iC_i (*H*2) as a result of isochronous annealing (for 30 min) and as functions of the annealing temperature T_{ann}.

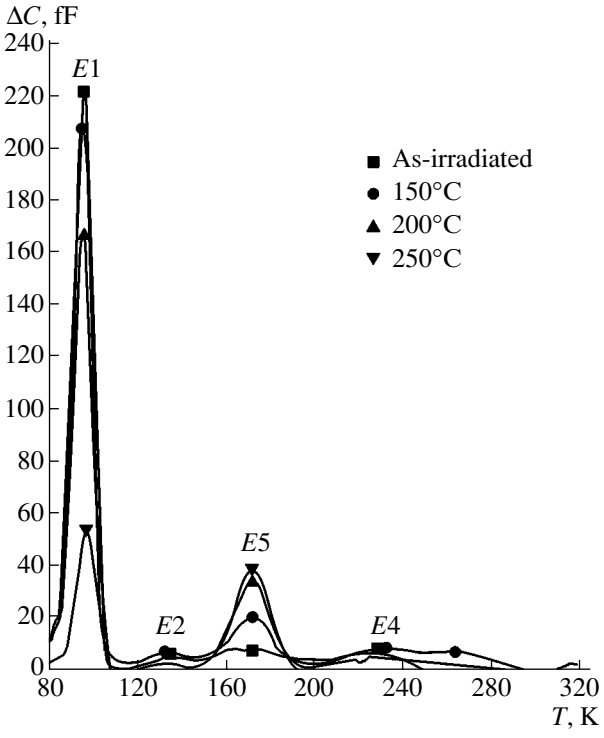

Fig. 4. Energy levels of the traps for majority charge carriers in the DLTS spectra of detectors, as-irradiated (with gamma-ray photons from a ^{60}Co source) and isochronously annealed (for 30 min) after irradiation, at temperatures T_{ann} indicated in the figure.

another detector structure from the same set with γ rays from a ^{60}Co source. The DLTS spectrum of this structure is shown in Fig. 4. It follows from this spectrum that virtually no *E* centers are formed in the structures under investigation due to the γ irradiation. This fact indicates that the oxygen concentration exceeds 10^{15} cm^{-3} in the crystals we studied, and [O]/[P] > 10^3. Thus, the nature of the center that additionally contributes to the amplitude of the *E*4 peak immediately after the electron irradiation is unclear.

The processes of annealing of the *E*2 and *E*4 traps are also somewhat different (Fig. 3). The content of *E*2 centers decreases steadily as the annealing temperature increases and becomes virtually zero at 250°C. The thermal stability of the *E*4 traps is higher. Such a behavior of the traps during annealing can also be explained by the presence of hydrogen in the crystals under investigation. The partial disappearance of divacancies at $T_{ann} < 250$°C, which manifests itself in a decrease in the content of *E*2 traps, can be explained by the interaction of divacancies with hydrogen, with the formation of divacancy–hydrogen complexes. According to [13], such a complex has an acceptor level at ~E_c – 0.43 eV, which is close to the level of the divacancy *E*(0/–). Therefore, the peaks in the DLTS spectra related to the levels of the divacancy *E*(0/–) and the divacancy–hydrogen complex are virtually indistinguishable.

Consequently, we may suggest that it is the interaction between the divacancy and hydrogen atom (V_2 + H ⟶ V_2H) that is responsible for the virtual constancy of the height of the *E*2 peak after annealing at T = 200°C. The content of divacancies decreases, which results in a decrease in the amplitude of the *E*2 peak. However, the content of V_2H complexes increases, and the total content [V_2] + [V_2H] remains invariable in this case (the amplitude of the *E*4 peak remains virtually constant). According to [13], the V_2H complex, as well as the divacancy, is stable up to 250°C, which agrees with our data. Thus, the interaction between hydrogen atoms and divacancies results in the formation of electrically active divacancy–hydrogen complexes in the structures under investigation. It is the *E*4 trap, which is as stable in our structures as in the crystals containing no hydrogen, that is related to this complex.

For practical purposes, it is important to estimate the influence of the observed transformations of the defect complexes on the detector characteristics. Evidently, the total passivation of the *V*O and C_iO_i complexes should result in a decrease in the full-depletion voltage (V_{FD}) in the irradiated detectors. When the passivation is incomplete, the characteristics may degrade due to an increase in V_{FD}. According to [15], the closer the defect level to the midgap, the stronger its influence on the value of V_{FD} in heavily irradiated detectors. Consequently, if most *A* centers (with a level at E_c – 0.17 eV) are incompletely passivated and convert to *V*OH complexes (with a deeper acceptor level at E_c – 0.32 eV), this may lead to increasing V_{FD}. If the interaction of hydrogen with divacancies results only in the formation of V_2H complexes, hydrogen also does not positively affect the detector characteristics, in particular, the value of V_{FD}.

No hydrogen was deliberately introduced into the structures investigated in this study. For this reason, its content appears to be not very high and only partial passivation of radiation defects was observed. One might expect that a larger fraction of radiation defects will be passivated if the hydrogen content is increased, and this will occur at lower temperatures than that at which it was observed in this study. However, additional investigations are necessary to find out whether hydrogen can improve the radiation resistance of radiation detectors operating at temperatures close to room temperature.

4. CONCLUSION

Thus, the results we have obtained indicate that hydrogen is present in silicon detectors and that it actively interacts with primary radiation defects. The presence of hydrogen in the crystal results in the decreasing of the annealing temperature for the *V*O and C_iO_i complexes, which are stable under conventional conditions up to 300°C. The decrease in the annealing temperature is explained by the interaction of these centers with hydrogen and by the formation of electrically active *V*OH centers in an intermediate stage of this process. The interaction between the radiation defects and hydrogen must be taken into account when developing an optimal technology for the fabrication of radiation-resistant silicon radiation detectors.

ACKNOWLEDGMENTS

We are grateful to V. P. Markevich and L. I. Murin for their helpful participation in numerous discussions.

This study was supported in part by the Republic of Belarus Foundation for Basic Research, project no. F-00-226.

REFERENCES

1. CERN LHCC 2000-009 LEB Status Report/RD48 (1999), http://rd48.web.cern.ch/RD48/.
2. B. C. MacEvoy, A. Santocchia, and G. Hall, Physica B (Amsterdam) **273–274**, 1045 (1999).
3. O. V. Feklisova and N. Yarykin, Semicond. Sci. Technol. **12**, 742 (1997).
4. O. V. Feklisova, N. Yarykin, E. B. Yakimov, and J. Weber, Physica B (Amsterdam) **273–274**, 235 (1999).
5. Y. Tokuda, Jpn. J. Appl. Phys. **37**, 1815 (1998).
6. Y. Tokuda and T. Seki, Semicond. Sci. Technol. **15**, 126 (2000).

7. S. J. Pearton, J. W. Corbett, and T. S. Shi, Appl. Phys. A **43**, 153 (1987).
8. O. V. Feklisova, N. Yarykin, E. B. Yakimov, and J. Weber, Physica B (Amsterdam) **308–310**, 210 (2001).
9. L. W. Song and G. D. Watkins, Phys. Rev. B **42**, 5759 (1990).
10. L. W. Song, X. D. Zhan, B. W. Benson, and G. D. Watkins, Phys. Rev. B **42**, 5765 (1990).
11. C. Da Via and S. J. Watts, Nucl. Instrum. Methods Phys. Res. B **186**, 111 (2002).
12. K. Irmscher, H. Klose, and K. J. Mass, J. Phys. C **17**, 6317 (1984).
13. K. Bonde Nielsen, L. Dobaczewski, K. Goscinski, *et al.*, Physica B (Amsterdam) **273–274**, 167 (1999).
14. S. D. Brotherton and P. J. Bradley, J. Appl. Phys. **53**, 5720 (1982).
15. V. Eremin, E. Verbitskaya, and Z. Li, Nucl. Instrum. Methods Phys. Res. A **476**, 537 (2002).

Translated by V. Bukhanov